# Corrosion Assessment and Mechanisms of Materials in Advanced Thermal Energy Production Systems

by

Kaiyang Li

A thesis submitted in partial fulfillment of the requirements for the degree of

Doctor of Philosophy

in

Materials Engineering

Department of Chemical and Materials Engineering

University of Alberta

**Abstract**

Advanced pressurized oxy-fuel combustion and subsequent supercritical $CO_2$ (s-$CO_2$) transportation technologies are being developed for high energy conversion efficiency and significant reduction of greenhouse gas emission at advanced thermal power plants. However, materials knowledge gaps exist on the deployment of these technologies, particularly the selection of suitable alloys for the core components (heat exchangers and flue gas sub-systems) and the upper limits of impurities in the s-$CO_2$ for safe pipeline transportation. This study intends to fill these gaps by investigating the corrosion performance of candidate alloys under various service conditions and advancing the fundamental understanding of how alloys corrode.

The s-$CO_2$ streams captured from the oxy-fuel combustion plants contain certain amounts of impurities $H_2O$, $O_2$, and $SO_2$, which may cause serve corrosion damages on the transportation pipeline steels. Current study finds that $SO_2$ in $H_2O$-saturated s-$CO_2$ can lead to highly active general corrosion by electrochemical reactions instead of gas chemical reactions, but has a marginal influence on stress corrosion cracking susceptibility of pipeline steel. The maximum allowable limits of impurity contents are also proposed based on a comprehensive literature review and current testing results.

At the advanced oxy-fired pressurized fluidized bed combustion plants, the flue gas (composed of $CO_2$, $H_2O$, $O_2$, $SO_2$ and HCl) could introduce potential condensed and hot gas chemical corrosion damage on the flue gas components. To address these issues, the corrosion performances of P91 and DSS 2205 steels were investigated in the simulated flue gas condensates at 60-150 °C, and the results reveal that the dominant reactions are

considerable oxide formation and high chemical dissolution of the formed oxides. Increasing temperature leads to an exponential increase in the long-term corrosion rates of the steels. DSS 2205 exhibited acceptable resistance to the condensates at elevated temperatures because of its high Cr and Mo contents. Besides, the hot flue gas chemical corrosion of 2205 steel was studied in a simulated pressurized hot flue gas environment at 270-320 °C. The oxidation kinetics of DSS 2205 follows parabolic law. $O_2$ and $H_2O$ act as oxidants while $SO_2$ and HCl are the pitting inducers. In general, DSS 2205 is a suitable candidate for the construction of flue gas components.

High-temperature s-$CO_2$ Brayton cycle has been recognized as a promising heat transfer method. The corrosion performance of two candidates, SS310 and Alloy 740, were studied in 30 MPa s-$CO_2$ streams with 100 ppm $H_2O$ or $O_2$ impurities at 600 °C. The addition of $H_2O$ remarkably enhances general and localized oxidations while the presence of $O_2$ leads to the opposite change. Compared with $H_2O$, impurity $O_2$ exhibits a more negative impact on the carburization of SS310. Alloy 740 shows much better resistance to carburization than SS310. The two alloys follow near parabolic oxidation law and show acceptable long-term corrosion resistance.

Depending on the fuel types used, different high-temperature corrosion modes will occur on the fireside of the heat exchangers in the combustion chambers. In pressurized oxy-fuel natural gas-fired system, the fireside of heat exchangers will suffer the attack from high-temperature, high-pressure flue gas mixture ($H_2O$ + $CO_2$ + $O_2$). It is found that $O_2$ is the dominant oxidant and has a threshold content (~2%), above which the nodule oxidation of

SS347, Alloy 800AT and Alloy 825 will be remarkably suppressed at 600 °C and 15 MPa. The three alloys exhibit acceptable corrosion resistance due to the relatively compact $Cr_2O_3$ layer. Among them, Alloy 825 shows the best corrosion performance due to its high contents of Cr, Al and Ti.

For the pressurized oxy-fuel plants fed with coal/biomass, high-temperature molten salt corrosion shall be the dominant reactions on the fireside. Under such service conditions (flue gas + salt mixture of $NaCl/KCl/Na_2SO_4/K_2SO_4$), the corrosion performance of Alloy 800AT and Alloy 740 were studied at 650 °C. The alloys suffer oxidation, sulfidation and chlorination attack with porous and fragile corrosion products. Alloy 740 exhibits better corrosion resistance than Alloy 800 AT, as the latter also experience serious internal and intergranular corrosion damage.

# Preface

This thesis presents original works completed by Kaiyang Li under the supervision of Prof. Jingli Luo and Dr. Yimin Zeng. It includes 8 chapters.

Chapter 1 is the introduction of research background on pressurized oxy-fuel combustion and s-$CO_2$ pipeline transportation systems, including corrosion features of different parts, material selection strategies and corrosion challenges. Part of the chapter has been published as Zeng Yimin, Li Kaiyang, Hughes Robin, Luo Jing-Li. Corrosion Mechanisms and Materials Selection for the Construction of Flue Gas Component in Advanced Heat and Power Systems. *Industrial & Engineering Chemistry Research*. 2017;56(48):14141-54. Dr. Zeng provided useful comments and revised the manuscript. Hughes Robin provided some data and suggestions. Prof. Luo gave useful suggestions and guidance. Kaiyang Li carried out the literature survey, analyzed the data and wrote the manuscript.

Chapter 2 has been published as Yimin Zeng, Kaiyang Li, Influence of $SO_2$ on the Corrosion and Stress Corrosion Cracking Susceptibility of Supercritical $CO_2$ Transportation Pipelines. *Corrosion Science* 165 (2020): 108404. Dr. Zeng contributed to conceptualization, data curation and suggestions. Kaiyang Li did the experiments, data analysis and paper-writing.

Chapter 3 has been submitted to *Materials and Corrosion* under review (Kaiyang Li, Yimin Zeng, Jing-Li Luo, Corrosion of P91 and DSS 2205 in simulated flue gas condensates of oxygen-fired pressurized fluidized bed combustion system). Prof. Luo and Dr. Zeng contributed to conceptualization, insightful suggestions, useful discussions and reviewing of paper. Kaiyang Li carried out the experiments, analyzed the results and wrote the paper.

Chapter 4 has been published as Kaiyang Li, Yimin Zeng, Jing-Li Luo, Corrosion of Duplex Stainless Steel 2205 in Hot Flue Gas Environments produced at Advanced Oxy-fired Pressurized Fluidized Bed Combustion Plants. *International Journal of Greenhouse Gas Control*. 100 (2020): 103108. Prof. Luo and Dr. Zeng provided useful suggestions,

discussions, and feedback for the manuscript writing and revision. Kaiyang Li carried out the experiments, analyzed the results and wrote the paper.

Chapter 5 has been accepted by *Corrosion Science* (Kaiyang Li, Yimin Zeng, Jing-Li Luo, Corrosion of SS310 and Alloy 740 in High Temperature Supercritical $CO_2$ with Impurities $H_2O$ and $O_2$). Prof. Luo and Dr. Zeng made contributions by revising the manuscript and providing useful guidance. Kaiyang Li carried out the experiments, analyzed the results and wrote the manuscript.

Chapter 6 has been accepted by *Energy* (Kaiyang Li, Yimin Zeng, Jing-Li Luo, A study of Corrosion Performance of Candidate Boiler Tube Alloys under Advanced Pressurized Oxy-fuel Combustion Conditions). Prof. Luo and Dr. Zeng provided useful suggestions, feedbacks, recommendations and manuscript revision. Kaiyang Li carried out the experiments, analyzed the results and wrote the manuscript.

# Acknowledgments

First of all, I would like to express my sincere gratitude to my supervisors, Dr. Jing-Li Luo and Dr. Yimin Zeng, for their continuous support, timely guidance and invaluable encouragement. They teach me how to carry out research work, how to think creatively and critically, and how to become a researcher by conquering all the difficulties in the Thorny Road of Honor.

I want to express appreciation to my supervisor committee members, Dr. Thomas H. Etsell and Dr. Hongbo Zeng, for their insightful suggestions and assistance during my research.

I would like to thank my group members and colleagues at U of A, Dr. Yashar Behnamian, Dr. Hongqiang Fan, Dr. Chen Shen, Dr. Yifei Sun, Dr. Qinying Wang, Dr. Chong Sun, Dr. Subiao Liu, Dr. Yaqian Zhang, Dr. Li Zeng, Dr. Tengfei Li, Mr. Jiankuan Li, Dr. Xianzong Wang, Mr. Shuo Shuang, Mr. Minkang Liu, Mrs Xueyuan Chen and Miss Caitlin Guzzo, for their help and collaboration during my research.

I am grateful to my colleagues in CanmetMATERIALS, Dr. Jian Li, Mrs. Pei Liu, Mrs. Renata Zavadil, Mrs. Catherine Bibby, Mrs. Jennifer Collier, Dr. Babak Shalchi, Mr. Jie Liang, Dr. Xin Pang, Dr. Xue Han, Mr. Chao Shi, Mr. Elliott Asare, Mrs. Magdalene Matchim, Dr. Nicholas Senior, Mr. Maciej Podlesny, Dr. Taylor Martino and Dr. Liting Shi. Besides, I want to thank the technical supports by Jarvis Victoria and Hui Yuan from McMaster University.

I appreciate the supports of my family and friends. I benefit a lot from the useful discussion with Mr. Chao Qi. Thanks for the encouragement, suggestions and inspiration from Dr. Guiqin Chen. Very grateful to my parents' love and support.

# Table of contents

# List of Tables

# List of Figures

xviii

# List of Symbols

| | |
|---|---|
| $T_{dew\ point}$ | dew point |
| $\Delta W_g$ | mass gain value |
| $\Delta W_l$ | mass loss value |
| $\tau$ | mass ratio of alloying element to oxygen in the formed oxide |
| A | surface area |
| t | time |
| $\rho$ | density of alloy |
| $K_0$ | pre-exponential factor |
| T | temperature |
| R | gas constant |
| $\Delta G$ | Gibbs free energy |
| CR | corrosion rate |
| $\Delta E$/E/Q | activation energy |
| $\sigma$ | stress |
| y | displacement |
| $E_m$ | Young's modulus |
| $\theta$ | thickness |
| H | distance between two outer alumina rods |
| U | distance between inner and outer alumina rods |
| n | reaction order |
| D | diffusion coefficient |
| P | partial pressure |
| k, b | fitting contant |
| a | activity |
| $K_{sp}$ | solubility product |

# List of Abbreviations

| | |
|---|---|
| AD | Anodic dissolution |
| CBED | Convergent beam electron diffraction |
| CCS | $CO_2$ capture and storage |
| DIC | Digital image correlation |
| DSS | Duplex stainless steel |
| EDS | Energy-dispersive X-ray spectrometer |
| EDTA | Ethylenediaminetetraacetic acid |
| FIB | Focused ion beam |
| FPB | Four point bending |
| GHG | Greenhouse gas |
| GIXRD | Grazing incidence X-ray diffraction |
| HE | Hydrogen embrittlement |
| oxy-fired PFBC | Oxy-fired pressurized fluidized bed combustion |
| PTFE | Polytetrafluoroethylene |
| SAED | Selected area electron diffraction |
| SCC | Stress corrosion cracking |
| s-$CO_2$ | Supercritical $CO_2$ |
| SEM | Scanning electron microscope |
| SS | Stainless steel |
| STEM | Scanning transmission electron microscopy |
| TEM | Transmission Electron Microscopy |
| XPS | X-ray photoelectron spectroscopy |
| XRD | X-ray diffraction |

# Chapter 1.  Introduction

## 1.1.  Carbon capture and storage technology

Although innovative clean and renewable energy generation technologies have been well developed over the past years, fossil fuel combustion, the primary source of anthropogenic $CO_2$, remains to be a reliable main source to meet our daily increasing demands on power, heat and steam supply [1]. To achieve environmentally sustainable economic growth, numerous studies have been carried out to develop applicable solutions that can significantly improve thermal energy conversion efficiency and reduce $CO_2$ emissions at fossil fuel power plants [2, 3]. In this scenario, Carbon Capture and Storage (CCS) technology has been developed as one of the most promising pathways available today, which can utilize fossil fuels as reliable energy feedstock while significantly reduce greenhouse gas emissions [4, 5].

As shown in Figure 1-1, CCS technology can be divided into three categories: post-combustion capture, pre-combustion capture and oxy-fuel combustion capture [6]. The post-combustion capture is the process to separate $CO_2$ from flue gas after the combustion of fuel in air, while pre-combustion capture is achieved through gasification or partial oxidation shift before combustion. Different from them, oxy-fuel combustion capture refers to supplying $O_2$ instead of air for combustion, consequently leading to high concentrations of $CO_2$ in the exhaust gas for later efficient purification, transportation and storage of high dense $CO_2$ streams [7, 8]. After captured from combustion plants, the $CO_2$ stream will be transported under supercritical state to specific sites for either permanent storage or further utilization (e.g., waste mining tailing discharge, enhanced oil recovery, and the conversion of $CO_2$ into valuable raw chemical products) [9, 10]. Pipeline steels (e.g., API grade 5 L X65, X70, and X80 steels) are suitable candidate materials for transportation due to their low cost, acceptable mechanical strength, and wide availability.
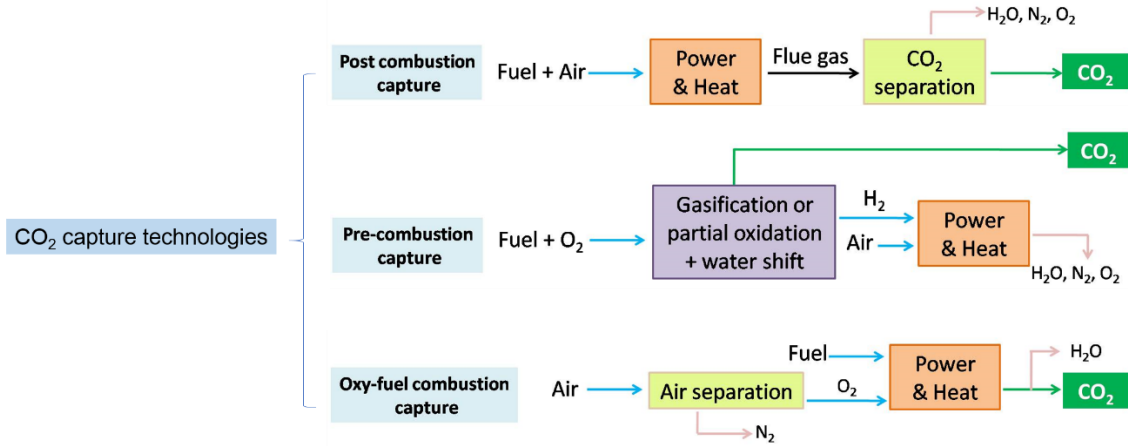
Figure 1-1. Different pathways for $CO_2$ capture technologies.

## 1.2. Pressurized oxy-fuel combustion and supercritical $CO_2$ transportation

Besides the CCS technology, a suite of advanced pressurized oxy-fuel combustion technologies, including oxy-pressurized fluid bed combustion (oxy-PFBC) [11], high-pressure oxy-combustion (HiPrOx) [12], and oxy-fuel pressurized generation two (G2) burner systems [13], are also being developed for clean and efficient utilization of fossil fuels, as schematically shown in Figure 1-2. Figure 1-2(a) is the schematic diagram of the oxy-PFBC system, pressurized pure $O_2$ and solid fuels (coal, biomass) are simultaneously injected into the combustion chamber to produce heat, which was collected by steam, supercritical water (s-$H_2O$) or supercritical $CO_2$ (s-$CO_2$) inside the heat exchangers to drive steam turbine for electricity production. Meanwhile, the generated hot flue gas, which is composed of $CO_2$, $H_2O$, $O_2$, $SO_x$, HCl, etc., is emitted from the combustion chamber under pressure. After dust removal or other cleaning treatments, heat in the hot, pressurized flue gas will be recovered by the heat recovery steam generator (HRSG) system for more electricity generation. Then, part of the flue gas is recycled back into the combustor to make up the flue gas volume and modulate flame temperature for optimum heat transfer efficiency, consequently resulting in high concentrations of $CO_2$ in the exhaust gas for efficient $CO_2$ separation and capture [14]. Figure 1-2(b) is the schematic diagram of the pressurized oxy-fuel natural gas-fired system, in which solid fuels are replaced by natural gas with fewer fly ashes upon combustion. Therefore, the generated hot flue gas, mainly composed of $CO_2$, $H_2O$ and $O_2$, is emitted from the combustion chamber under high pressure to run the gas turbine for more power generation. After dehydration, part of the

flue gas is recycled back into the combustor for high concentrations of $CO_2$ in the exhaust gas [15].
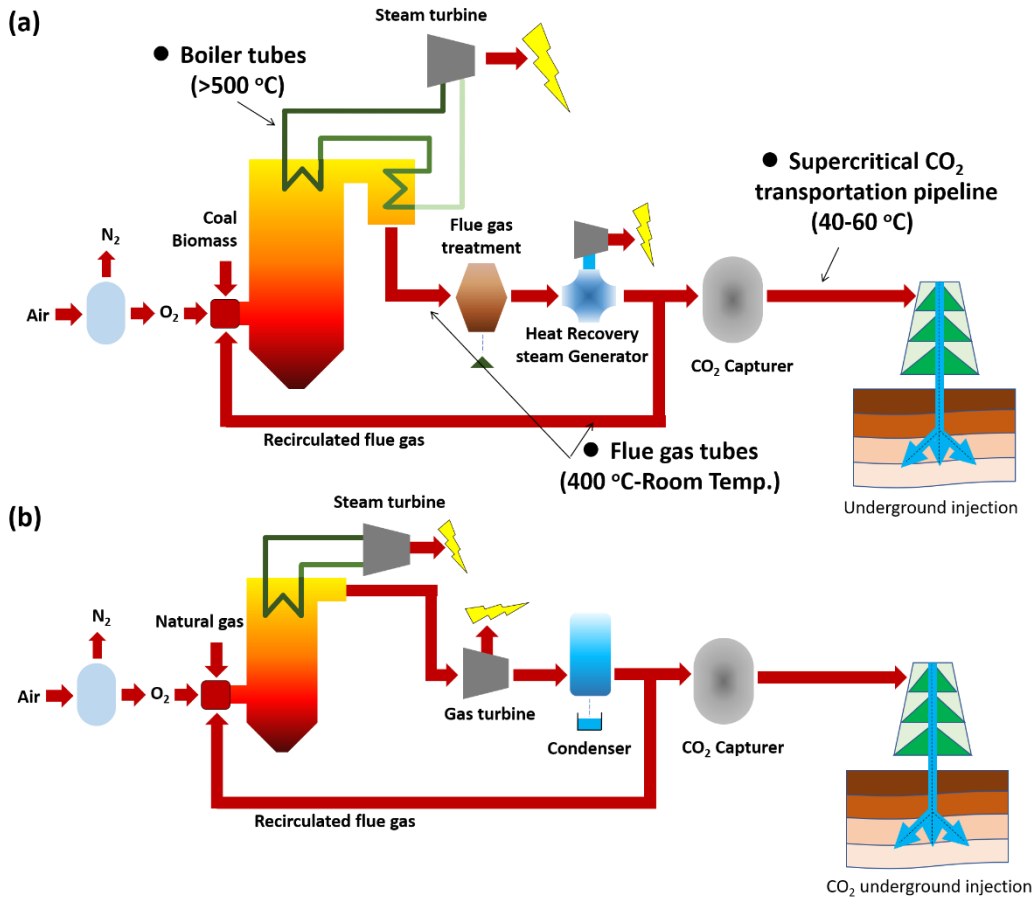


Figure 1-2. Schematic of (a) oxy-fired pressurized fluid bed combustion and (b) pressurized oxy-fuel natural gas-fired systems and $CO_2$ transportation systems.

The advantages of the pressurized oxy-fuel combustion system with CCS technology are obvious. Firstly, the power plant equipped with these technologies could achieve near-zero $CO_2$ emission with a relatively acceptable cost and short implementation period, since the high concentration of $CO_2$ in flue gas makes $CO_2$ capture and separation possible [16]. In fact, negative $CO_2$ emission might occur when renewable biomass fuels are introduced into the systems [17]. Secondly, the combustion efficiency will be improved because of the absence of the burden of heating up nitrogen, the higher flame temperature, and better utilization of the generated heat [18, 19]. Thirdly, the total volume of flue gas in an oxy-fuel

3

combustion system is only about one-fifth of that in a conventional air combustion system [20]. The reduced flue gas shall result in not only higher thermal energy conversion efficiency, but also a smaller size of flue gas treatment equipment. Fourthly, because of the cryogenic removal of $N_2$ in the air separation unit, much less $NO_x$ which is a notorious air pollutant, will be generated in the flue gas [21]. Furthermore, the higher concentration of other pollutants (such as $SO_2$, HCl and Hg) in flue gas makes the following separations easier. Lastly, diverse fuel sources, including fossil fuels (such as hard coal, lignite, crude oil, natural gas) and renewable resources (like biomass), can be used for combustion [22]. The disadvantages of the systems include extra energy cost on air separation. To deal with this issue, robust and cost-effective $O_2$ separation technologies, such as membranes, adsorptions and chemical-looping, are being developed with great progress [23].

### 1.3. Existing materials technology gaps

Despite their promising advantages, material technology gaps exist on the successful commercialization of the advanced pressurized oxy-fuel combustion and s-$CO_2$ transportation technologies. The core components of the developed systems will be operated in harsh environments, introducing the challenge on the selection of suitable alloys of construction and corrosion control strategy development for cos-effective capital investment and long-term safe operation. According to our comprehensive literature review, very few efforts have been employed to investigate corrosion and stress corrosion cracking of steels and alloys under these specific conditions. In the following parts, the corrosion challenges on the construction of the pressurized oxy-fuel combustion systems and $CO_2$ transportation pipeline are briefly reviewed.

### 1.3.1. Supercritical $CO_2$ transportation system

To avoid the formation of two phases (liquid and gas) during transportation and remarkably increase the transportation efficiency with low cost, the $CO_2$ is usually transported in the pipeline under supercritical state in the temperature and pressure ranges of 40-60 °C and high pressure up to 17 MPa, respectively [24]. Note that the supercritical point of $CO_2$ is 31.1 °C and 7.38 MPa. The s-$CO_2$ streams from the oxy-fuel combustion plants always contain certain amounts of aggressive impurities, such as $H_2O$, $O_2$, $SO_2$, and acids,

depending on fuel sources and the capture/separation technologies applied [25-28]. The presence of these corrosive impurities may promote the general/localized corrosion and even stress corrosion cracking (SCC) of s-$CO_2$ pipes [29-31], as shown in Figure 1-3. In fact, typical general corrosion and localized corrosion damages have been found on the internal surfaces of some s-$CO_2$ transportation pipelines [1, 32-36]. Comprehensive literature reviews have been done by us [37] and other groups to clarify the effects of impurities, temperature, pressure, time, flow rate, and other related factors on corrosion of pipeline steels [25, 38]. However, the influence of impurities on corrosion and SCC remains a significant challenge because of limited field operation experience and somewhat controversial laboratory testing results reported [39].
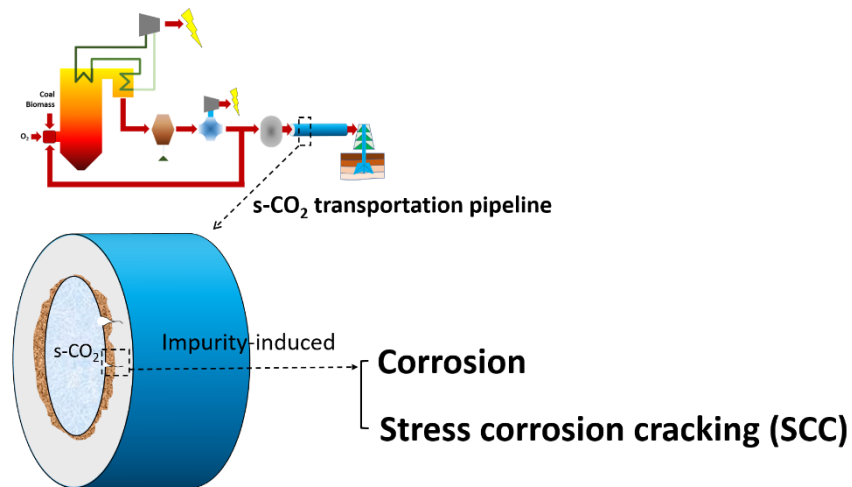


Figure 1-3. Illustrating diagram of corrosion and stress corrosion cracking occurred on s-$CO_2$ transportation pipelines.

### 1.3.2. Corrosion challenge of flue gas components

Due to flue gas recirculation and removal of $N_2$, the contents of $CO_2$, $H_2O$, $SO_x$ and HCl present in the flue gas of pressurized oxy-fuel system are noticeably higher than those produced at conventional air combustion plants [40]. Depending on its temperature, the flue gas generated can introduce two different types of corrosion: hot gas corrosion and condensed phase corrosion (as shown in Figure 1-4) [40]. The hot gas corrosion originates from aggressive gaseous attacks on the component surfaces at high temperatures. The

corresponding corrosion rate is a function of temperature and the concentrations of the corrosive gases (such as steam, HCl and $SO_x$) present. At the oxy-fuel plants, it takes place at the temperature range of 400 °C-dew point of the flue gas. At temperatures lower than the dew point, the condensation of corrosive gases ($SO_x$, HCl, $NO_x$ and $CO_2$) occurs on the surfaces of some components (such as recirculated tube and desulfurization device) and results in unwanted condensed phase corrosion. The formed condensed phase films are acidic solutions at the pH range of 2-4, featuring electrochemical reaction-controlled corrosion process [40]. The hot gas and condensed phase corrosion of flue gas components at conventional air and oxy-fuel combustion plants have been reviewed and analyzed in one of our published papers [40]. It is found that available information is insufficient to determine which alloys are suitable for the construction of flue gas components at the pressurized oxy-fuel plants because the pressure and chemistry of the flue gas are remarkably different from those produced at conventional air combustion plants [40].
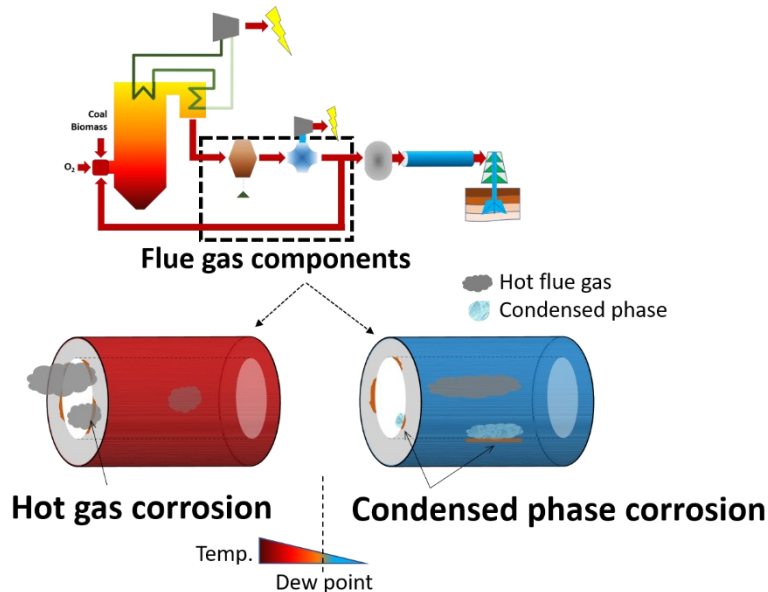


Figure 1-4. Illustrating diagram of hot gas corrosion and condensed phase corrosion occurred on the inside surface of flue gas components.

### 1.3.3. Corrosion challenge of heat exchangers

In the combustion chamber of the oxy-fuel combustion plants, the heat exchanger materials must be able to resist high-temperature attacks from both inside heat transfer fluids (steam,

s-$H_2O$ or s-$CO_2$) and fireside flue gas/molten salts, as shown in Figure 1-5. Over the past few decades, s-$H_2O$ for Rankine cycle or s-$CO_2$ for Brayton cycle has been developed as promising heat transfer fluid to achieve high energy conversion efficiency (>50%), compact turbomachinery, reduced capital investment and operating cost, and significant reduction on Greenhouse Gas (GHG) emission [41, 42]. These high-temperature, high-pressure fluids introduce serious concern on the selection of heat exchanger alloys because of their highly aggressive nature. A number of researches have been carried out in describing the corrosion behavior of alloys in s-$H_2O$ and summarizing the affecting factors, including temperature, pressure, time and impurities[43-47]. Compared with s-$H_2O$, s-$CO_2$ has higher thermodynamic cycle efficiencies as a transfer fluid [48]. However, s-$CO_2$ could cause not only oxidation but also carburization of constructional alloys. It is found that the corrosion behavior (oxidation and carburization) of metallic components in high-temperature s-$CO_2$ will be related to temperature, pressure, alloying elements and impurity contents [49-52]. But the related corrosion mechanisms are far from clear, and it is urgently needed to define the maximum allowable limits of impurities $H_2O$ and $O_2$.
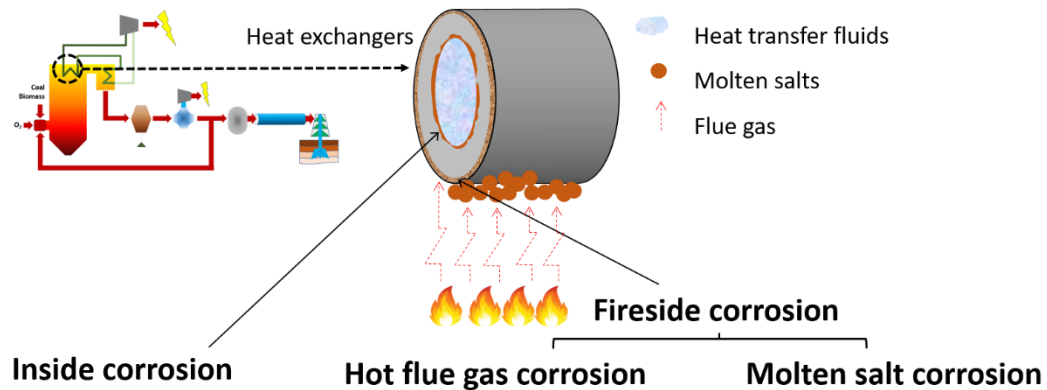


Figure 1-5. Illustrating diagram of inside and fireside corrosion of heat changer at pressurized oxy-fuel combustion plants.

Depending on the fuels charged, the fireside of heat exchanger alloys will suffer high-temperature flue gas corrosion and/or high-temperature molten salt corrosion [53-55]. At the pressurized oxy-fuel natural gas-fired plants, the generated pressurized flue gas is composed of $CO_2$ (up to 33%) and $H_2O$ (60%) as well as certain amounts (about 2-7%) of

7

$O_2$ at the temperature range of 550-750 °C [56]. According to our literature review [40], no data is available to describe the alloy performance under such specific conditions. For the oxy-fuel plants using coal/biomass as fuel feedstock, molten or partially molten particles as combustion residuals can deposit on the fireside of the heat exchangers, leading to high-temperature molten salt corrosion damages. Biomass is a renewable and environmentally friendly energy feedstock. The introduction of biomass as fuels will make the deposited salts as a mixture of sulfates and chlorides. Comprehensive reviews on the fireside molten salt corrosion in conventional air-coal combustion systems could be found in related books and review papers [57-59]. However, the studies of molten salt-induced corrosion in co-combustion of coal/biomass, especially in oxy-fuel environments, are still insufficient. It is unclear how the synergistic effect of sulfates, chlorides and oxy-fuel flue gas will affect the fireside corrosion behavior of alloys.

### 1.4. Candidate alloys for construction of flue gas and heat exchanger components

To advance the deployment of the oxy-fuel combustion technologies, it is crucial to select proper constructional materials with acceptable long-term corrosion resistance and mechanical strength. Fe-based alloys are the most widely used metallic components in the combustion systems of existing fossil fuel-fired power plants due to their good mechanical strength, moderate cost, good thermal conductivity and corrosion resistance [60]. Iron-based alloys include carbon steels (0.05-2.1% C), ferritic steels (with Cr up to 12%), stainless steels (12% or higher Cr) and duplex stainless steels. Ni-based alloys also attract a lot of attention due to their high mechanical strength and the excellent corrosion resistance in harsh high-temperature environments. The following content gives a general review of the alloy types, compositions, mechanical behaviors and corrosion resistance of Fe-based and Ni-based alloys, which aims at providing profound background information on the pre-selection of alloys for our study.

**Carbon steels:**

Carbon steels are the steels with C content up to 2.1 wt%. They are the most widely used materials in engineering areas, including marine environments, power plants, transportation, pipelines and so on [60]. However, the low content of alloying elements

8

and resulting limited corrosion resistance makes carbon steel cannot survive in the high-temperature combustors or flue gas environments, especially in the presence of corrosive components like chlorine and sulfur [61]. Or else, severe corrosion and structural integrity damage are expected to occur as the formed surface oxide scales are ineffective to retard the environmental attack.

**Ferritic steels:**

Ferritic steels are of interest to power plant operation primarily because of the low thermal expansion coefficient, high thermal conductivity, moderate oxidation resistance and good mechanical behavior, such as high creep strength and high resistance to thermal fatigue. The excellent mechanical behavior mainly lies in the inhomogeneous phases and complex structure. Precipitated carbides, including $M_{23}C_6$, NbC, and VC, distribute along the grain or subgrain boundaries and result in a high dislocation density, which inhibits creep deformation. Based on Cr content, the ferritic steels can be further categorized into two groups, low-Cr (1-3%) and high-Cr (9-12%) ferritic steels. Common low-Cr ferritic steels include T11, T12, NFIH, T22, T23 (HCM2S), Tempaloy F-2W and so on [62]. T22 is a typical low-Cr ferritic steel with 2.25% Cr and 1% Mo. It has very high creep strength, good weldability and relatively low cost [63]. Based on T22, T23 was made with the extra addition of 1.6W, V and Nb, leading to a higher creep strength.

In 9-12% Cr steels, different elements, including solution-strengthening elements (W, Co and Mo) and precipitation-strengthening elements (V, Nb and N), have been added to improve the mechanical behavior. Grade P91 and P92 steels are two typical ferritic steels extensively used in modern coal-fired power plants [64]. P91 was originally designated as enhanced creep strength ferritic steel with martensitic structure achieved by normalizing, quenching and tempering at an intermediate temperature. P92 steel is a mechanically improved version of 9% Cr steels through the addition of about 1.8% tungsten. Other ferritic steels, include E911, HT91 (12Cr1MoV), HCM12, P122, NF12, SAVE12, VM12, MARB, have the addition of W, Mo, Cu, Co, and V (usually below 3%) to improve the weldability and creep strength [62, 65-67].

Ferritic steels are used in boilers and flue gas components in existing coal-fired power plants. Due to the relatively low Cr content compared with stainless steel, the application as heat exchangers is restricted to a relatively low temperature. For example, according to ASTM codes, the maximum allowable operation temperatures of P91 and P92 in steam are 593 and 620 °C respectively [68]. The maximum temperature will be further reduced in more corrosive environments [40]. Therefore, in this thesis, P91 steel was examined for the construction of flue gas component at the oxy-fuel combustion plants.

**Stainless steels:**

Stainless steels (SS) are a family of iron-based alloys that contain a certain amount of chromium to prevent the iron from rusting as well as providing heat resistant properties. Increasing amounts of alloying elements like Cr and Ni will help to improve the corrosion resistance of Fe-based alloys. These alloying elements participate in the formation of a protective oxide on the alloy surface and reduce the metal loss to a lower extent.

Based on Cr content, stainless steels are divided into three categories, namely 18Cr-8Ni, 15Cr-15Ni, and high Cr (20-25%) stainless steels. 18Cr-8Ni stainless steels include grade 304 (304L, 304H, Super 304H), 316H, grade 347 (347H and 347HFG), 321H, and Tempaloy A-1 [69]. Grade 304 SS is a typical 18Cr-8Ni stainless steel used for high-temperature boiler components with austenitic structure. Based on grade 304, 2-3% Mo is added to increase corrosion resistance and creep strength as grade 316 SS. Ti and Nb are also added as precipitation-strengthening elements, resulting in SS321 and SS347, respectively [70]. 15Cr-15Ni stainless steels, including 17-14CuMo, Esshete 1250 and Tempaloy A-2, have higher Ni content (10-14%) than 18Cr-8Ni stainless steels (8-10%). These alloys usually show high creep strength. For example, owing to its good corrosion resistance and creep resistance up to 650 °C, Esshete 1250 is extensively used in British power stations as heat exchangers [71]. High Cr stainless steels contain SS310, HR3C, NF707, NF 709(a), Alloy 800H, and Tempaloy A-3 [72]. In these alloys, high content of Cr (20-25%) is added to acquire sufficient oxidation and corrosion resistance, which are quite desired in high-temperature heat exchangers, although the high Cr content increases the cost.

In combustion systems, stainless steels have been widely used in boilers as heat exchangers (superheaters/reheaters) ever since the 1970s [73]. Besides, they have also been used in flue gas systems to resist both hot gas corrosion and condensed phase corrosion [74]. In this thesis, SS347, SS310 and Alloy 800AT were used as candidate heat exchanger materials in the pressurized oxy-fuel combustion systems.

**Duplex stainless steels:**

Duplex stainless steels (DSSs) are composed of austenite and ferrite through the precise control of alloying elements and processing. These types of materials have a combination of acceptable mechanical strength, high corrosion resistance, moderate weldability and relatively low cost compared with austenitic stainless steels [40]. Typical DSSs, including 2507 and 2205, have 22-25% Cr, ~5% Ni and ~3% Mo, providing them with high resistances to both general and localized corrosion, especially to pitting and crevice corrosion in chlorine-containing aqueous environments [75, 76]. The good mechanical behavior of DSSs originates from the dual-phase matrix with very fine lamella and the addition of nitrogen [77]. Because of spinodal decomposition at 375-500 °C and the precipitation of carbides, nitrides, and intermetallic phases at 600-900 °C [78, 79], which are believed to induce embrittlement and mechanical degradation, DSSs are usually recommended to be used at temperatures below 400 °C as the structural components for long-term service [80], i.e. flue gas components in the power plants. In this thesis, DSS 2205 was tested as a candidate flue gas component in the pressurized oxy-fuel combustion system.

**Ni-based alloys**

Based on the predominant strengthening mechanism, Ni-based alloys can be divided into two groups: precipitation-strengthening alloys and solid solution-strengthening alloys. In precipitation-strengthening alloys, Al, Ti, and Nb are added as alloying elements to form an ordered intermetallic compound $Ni_3$(Ti, Al, Nb), which is also called gamma prime phase ($\gamma'$) and improves the creep strength. In solid solution-strengthening alloys, Cr, Co, Mo, and W are added as alloying elements. The addition of these alloying elements also

results in precipitates, such as carbides and nitrides in these alloys, to strengthen the alloys during high-temperature exposures [81].

By far, Ni-based alloys are widely used as high-temperature heat exchanger materials, including Alloy 230, Alloy 282, CCA 617, Alloy 600, Alloy 625, Alloy 693, Nimonic 75, Nimonic 263, Allvac 718plus, Alloy 740, HR6W, GH2984, and so on [62, 72, 73, 82, 83]. These Ni-based alloys tend to show excellent mechanical behaviors and corrosion resistance in the harsh combustion environments [84]. Besides heat exchanger materials, Ni-based alloys, like Alloy C-276 and Alloy 22, have also been used in certain parts of flue gas components to resist the highly acidified condensates. In this thesis, Alloy 740 and Alloy 825 were used as candidate heat exchanger materials in the pressurized oxy-fuel combustion system.

Table 1-1 lists the relative cost ratio (based on SS304) of some candidate alloys for different parts in the system [85]. It is found that the price of different parts generally follows the trend: transportation pipeline < flue gas components < heat exchangers.

Table 1-1. Relative cost ratio of different types of alloys.

| Parts in the system | Material type | Alloy | Relative cost ratio (304L=1.0) |
|---|---|---|---|
| s-CO$_2$ transportation pipeline | Carbon steel | 516 Gr.60 | 0.23 |
| | | 516 Gr.70 | 0.25 |
| Heat exchangers | Stainless steel | 304/304L | 1.00 |
| | | 347 | 1.21 |
| | | 310 | 2.01 |
| | | Alloy 800 | 3.65 |
| Flue gas components | Duplex stainless steel | 2205 | 1.20 |
| Heat exchangers | Ni-based alloys | Alloy 825 | 4.13 |
| | | Alloy 625 | 7.75 |
| | | Alloy G30 | 10.16 |

### 1.5. Objectives and contents of the thesis

The main objectives of the thesis are presented as follows:

- Evaluate corrosion performance of candidate constructional alloys under the designed pressurized oxy-fuel combustion conditions to fill knowledge gaps on materials selection and support the deployment of these advanced thermal power technologies.

- Investigate the effect of impurities in s-$CO_2$ streams captured from the oxy-fuel combustion plants and define the maximum upper limit of the impurities to support the commercialization of CCS technology.

- Advance fundamental understanding of how steels and alloys corrode in $CO_2$-enriched environments at the temperature range of 60-650 °C and what are the roles of alloying elements (Fe, Cr, Co and Ni) and gaseous species ($H_2O$, $O_2$, and $SO_2$) on corrosion.

To achieve these objectives, the following investigations have been completed. Firstly, in the s-$CO_2$ pipeline transportation, the effect of $SO_2$ and other impurities ($O_2$ and $H_2O$) on the corrosion and stress corrosion cracking (SCC) of pipeline steels were studied. The related corrosion mechanism and the maximum allowable contents of impurities are proposed. The detailed information is presented in **Chapter 2**.

Secondly, as mentioned above, the flue gas components of the oxy-fuel power plants will suffer from both hot gas chemical and condensed phase corrosion. For the condensed phase corrosion, two candidate constructional alloys, P91 and DSS 2205, were tested in simulated flue gas condensates containing $Cl^-$, $NO_3^-$, $HCO_3$, and $SO_4^{2-}$ ions at pH=2 at 60-150 °C. The experimental methodology and obtained results are shown in **Chapter 3**. As P91 does not exhibit acceptable resistance to the condensed phase corrosion, only DSS 2205 was tested in simulated hot flue gas with a total pressure of 1.50-1.64 MPa at 270 and 320 °C. The corrosion products formed on the steel were characterized and the related long-term corrosion rates were also evaluated. The roles of aggressive species ($CO_2$, $H_2O$, $O_2$, $SO_2$ and HCl) in the hot gas corrosion of the steel were analyzed. Detailed information can be found in **Chapter 4**.

Thirdly, the heat exchanger will experience both inside and fireside corrosion. Two candidate constructional alloys, SS310 and Alloy 740, were studied as candidate materials in high-temperature, high-pressure s-$CO_2$ with impurity $H_2O$ or $O_2$. The influences of $H_2O$ and $O_2$ on oxidation and carburization are identified, as described in **Chapter 5**. For the gaseous fireside corrosion, the corrosion performances of three Cr-bearing alloys, including SS347, Alloy 800AT and Alloy 825, were investigated in the simulated pressurized oxy-fuel natural gas-fired environment at 600 °C, and obtained results are shown in **Chapter 6**. When coal/biomass are used as fuel feedstocks, high-temperature molten salt corrosion shall be a dominant process on the fireside corrosion of heat exchanger. The molten salt corrosion of two alloys, Alloy 800AT and Alloy 740, was studied in simulated oxy-fuel co-combustion of coal/biomass environments at 650 °C and the methodology applied and the results obtained are present in **Chapter 7**. **Chapter 8** is the summary and future work. To avoid duplication, some similar statements in the introduction sections in Chapter 3, Chapter 4, Chapter 6 and Chapter 7 have been replaced by "referred to corresponding sections in Chapter 1". Similarly, some descriptions of experimental details in Chapter 4, Chapter 5, Chapter 6 and Chapter 7 have been replaced by "referred to the descriptions in previous sections".

# Chapter 2. Influence of $SO_2$ on the Corrosion and Stress Corrosion Cracking Susceptibility of Supercritical $CO_2$ Transportation Pipelines

**Abstract**

The impacts of $SO_2$ on corrosion and stress corrosion cracking (SCC) of supercritical $CO_2$ (s-$CO_2$) pipeline steels are unclear because of limited field operation experience and somewhat controversial reported results. Comprehensive literature review and corresponding tests in the s-$CO_2$ streams from advanced oxy-fuel plants were performed to fill significant knowledge gaps. The presence of $SO_2$ leads to severe general corrosion but does not initiate SCC of the steels in $H_2O$-saturated s-$CO_2$. $SO_2$ induced corrosion is likely dominated by electrochemical reactions. It is necessary to control $H_2O\% < 2000$ ppm and $SO_2\% < 100$ ppm to avoid potential catastrophic disaster.

**Keywords**: Carbon steel; SEM; XRD; Weight loss; Acid corrosion; Stress corrosion.

## 2.1. Introduction

Background information on CCS technology and the corrosion issues in s-$CO_2$ transportation system are referred to Section 1.1 and Section 1.3.1, respectively.

Among all the impurities, $SO_2$ is possibly the most notorious corrodent [86-88]. $SO_2$ originates from the combustion of sulfur-containing fossil fuels and is always found in the s-$CO_2$ streams captured from oxy-fuel or post-combustion power plants with the concentration up to 5000 ppm [89]. Thorough removal of $SO_2$ will lead to an unaffordable cost on CCS operation. A more practical way is to mitigate its toxicity and corrosivity by constraining its content within a safe range. However, the maximum allowable limits of $SO_2$ in transported s-$CO_2$ streams have not been defined yet. For example, DYNAMIS guidance recommends controlling the $SO_2$ content $< 100$ ppm [90], while NETL reports that the content could be in the range of 10-50000 ppm [91]. Besides, the influence of $SO_2$ in s-$CO_2$ on corrosion, especially in the simultaneous presence of other impurities (such as $H_2O$ and $O_2$), is really complicated and far from clear. A number of studies have been conducted to assess the corrosion modes and rates of pipeline steels in s-$CO_2$ streams

containing $SO_2$ and other impurities [86, 92]. The general finding is that $SO_2$ can directly attack pipeline steels via oxidation and sulfidation reactions [80]. Meanwhile, the dissolution of $SO_2$ in liquid water could produce a strong acidic film on pipeline steels and consequently cause severe corrosion damage [93]. However, the results reported from these previous studies are somewhat controversial and the accumulated corrosion databases are insufficient to formulate a clear image of describing $SO_2$ effect on general corrosion and pitting [37]. Moreover, $SO_2$-induced SCC of the pipeline steels is also a serious safety concern [94]. The occurrence of SCC relies on the co-existence of crack-inducing chemical environments, applied stress, and the materials susceptible to SCC [95]. $SO_2$ could create crack-inducing chemical environments through electrolyte acidification [96]. As the designed operating pressure of s-$CO_2$ can be up to 15.3 MPa, the transportation pipes shall be subjected to the high hoop and longitudinal stresses [97, 98]. The candidate pipeline steels are susceptible to SCC in sweet/sour environments as previously reported [99]. Thus, these factors could make s-$CO_2$ transportation pipeline under a situation with a high risk of SCC [100]. Surprisingly, there are very few investigations on this issue [101, 102].

In this paper, most previous studies about the effects of $SO_2$ on corrosion were reviewed to form a general concept and identify knowledge gaps about $SO_2$-induced corrosion in s-$CO_2$ transportation environments. Corresponding laboratory corrosion studies were performed to further examine the previous results and identify the influence of $SO_2$ in the s-$CO_2$ streams captured from advanced pressurized oxy-fuel combustion systems, such as oxy-pressurized fluid bed combustion (oxy-PFBC) and pressurized oxy-fuel generation two (G2) burners, which are being developed to meet greenhouse gas regulation requirements and to significantly improve energy conversion efficiency in a cost-competitive fashion [12]. Related mechanistic corrosion models were subsequently proposed to advance the fundamental understanding of how pipeline steels corrode in $SO_2$-containing s-$CO_2$ and whether SCC cracking occurs in the pipes during the transportation of $SO_2$-containing s-$CO_2$. It is anticipated that this study can support the development of national and international standards of s-$CO_2$ pipelines and help industry engineers to construct and operate s-$CO_2$ pipelines in a safe and cost-effective manner.

## 2.2. Materials and methods

### 2.2.1. Test specimens preparation

Corrosion testing coupons (75 mm long × 20 mm wide × 3 mm thick) were machined from commercial X65, X70 and X80 pipes (API grade) for corrosion study in related s-$CO_2$ streams. The chemical compositions of these steels are listed in Table 2-1. For SCC investigations, bent-beam samples (115 mm long × 18 mm wide × 3 mm thick) with their longitudinal direction parallel to the hoop stress direction of pipeline were also prepared from the same pipes. Prior to each test, the surfaces of each sample were well polished using a series of silicon carbide papers up to 600 grit, degreased with ethanol in an ultrasonic cleaner, washed with distilled water, and finally dried with pressurized air. After that, the samples were weighted (with a precision of 0.1 mg) and the dimensions measured to the nearest 0.01 mm.

Table 2-1. Chemical compositions of tested pipeline steels (wt.%).

| Element | Tested pipeline steels | | |
|---|---|---|---|
| | X65 | X70 | X80 |
| C | 0.075 | 0.051 | 0.062 |
| Si | 0.21 | 0.21 | 0.12 |
| Mn | 1.36 | 1.16 | 1.82 |
| Cr | 0.023 | 0.027 | 0.025 |
| Ni | 0.012 | 0.200 | 0.140 |
| Mo | 0.0026 | 0.0080 | 0.1900 |
| Cu | 0.024 | 0.015 | 0.250 |
| Al | 0.030 | 0.030 | 0.016 |
| Nb | 0.062 | 0.067 | 0.060 |
| V | 0.0040 | 0.049 | 0.0043 |
| Ti | 0.034 | 0.0014 | 0.011 |
| P | 0.013 | 0.010 | 0.006 |
| S | <0.001 | <0.001 | <0.001 |
| Fe | Bal. | Bal. | Bal. |

### 2.2.2. Corrosion and SCC test methodologies

The methodology and apparatus described in ASTM G202-0939 [103] were adapted to conduct corrosion testing under flowing s-$CO_2$ conditions in a 5.5 L Parr autoclave made of Alloy C-276. Driven by a motor shaft, the rotating cage testing is a well-established methodology used for corrosion studies under flow conditions, which can be encountered across the CCS chain. Figure 2-1(a) shows how corrosion coupons were accommodated on a PTFE rotating cage. Three freshly-prepared identical coupons of each steel were installed on the rotating cage in a corrosion test.

Four Point Bending (FPB) method was employed to assess the SCC susceptibility of the pipeline steels in the s-$CO_2$ streams based on ASTM G39 [104]. The image of FPB apparatus is shown in Figure 2-1(b). The loading frame is made of Hastelloy C-276 and four alumina rods are used as electrical insulators between the bent-beam and the fixture during the tests. Required stress/strain can be applied on the bent beam when the center screw is tightened to a certain level, and the stress distribution is believed to be uniform on the bent-beam surface between the two inner alumina rods (i.e., L region in Figure 2-1(b)). The applied stress is calculated based on NACE TM1077 [105]:

$$\sigma = \frac{12E_m\theta y}{3H^2-4U^2} \qquad\qquad \text{Equation 2-1}$$

where $\sigma$ is the uniform loading stress on the mid-portion of the specimen surface; $y$ is the indentation depth with an accuracy of 0.001 mm; $E_m$ is the elastic modulus of test steels; $\theta$ is the thickness of the beam sample; $H$ is the distance between two outer ceramic supports; $U$ is the distance between inner and outer ceramic supports. Moreover, advanced Digital Image Correlation (DIC) method was also used to measure the strains applied on the bent-beam sample surface. DIC measurements were conducted by comparing the digital images of speckle pattern on steel surface before and after beam deformation. The speckle pattern on the beam surface was obtained by successively painting a continuous layer of flat white paint and a light mist of black paint in a fine speckle pattern. The digital images were taken using CCD cameras and analyzed using ARAMIS software to identify the strain levels applied. After DIC measurements, the painted patterns were thoroughly removed using acetone, and the FPB fixtures with loaded beam samples were stored in a vacuum container for subsequent SCC tests in the Parr autoclave.
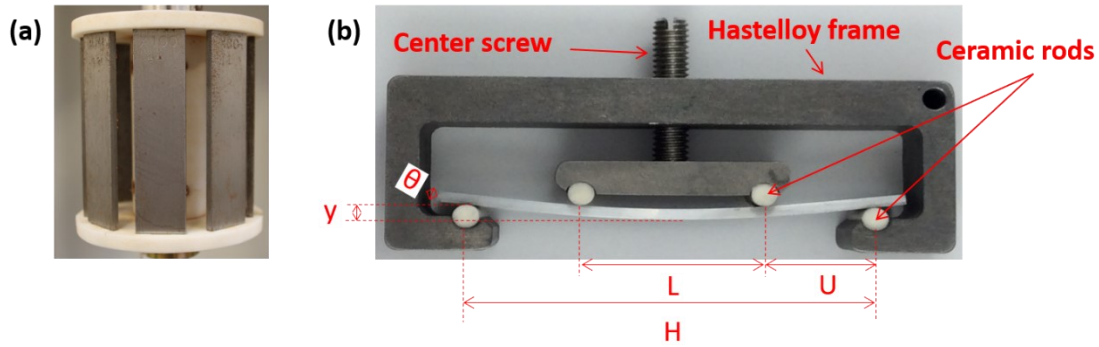
Figure 2-1. (a) Corrosion coupons installed on a home-made rotating cage; (b) Bent-beam specimen loaded on a Four Point Bending (FPB) fixture.

### 2.2.3. Corrosion test matrix and autoclave experimental procedures

Pilot-scale inspections show that the s-$CO_2$ streams captured from the advanced pressurized oxy-fuel combustion systems are likely composed of $O_2$ (1-6 vol.%,), $SO_2$ (up to 4500 ppm), and $H_2O$ (up to its maximum solubility in s-$CO_2$), which are different from those produced at conventional air-fired plants [40, 91, 106]. Thus, the contents of these impurities, as shown in Table 2-2, were set for corrosion study. Note that $SO_2$ can quickly react with water to form $H_2SO_4$ in the presence of oxygen, consequently reducing their concentrations in the test s-$CO_2$ mixture. Thus, in Tests #2-4, it was imperative to control the amount of $H_2O$ added to ensure that the tests were carried out exactly under the required conditions. To achieve the target, a combination of simulation results from ASPEN REFPROP (NIST-based databases) [107] and experimental data published in the reference [108] was applied to determine the $H_2O$-saturation values in the s-$CO_2$ mixtures. Following that, HYSYS simulations utilizing Peng-Robinson fluid package were employed to determine the required pressures of impurities $O_2$ and $SO_2$ in following gas charging process to achieve the desired testing environmental chemistry.

Table 2-2. Corrosion Testing Matrix.

| Test # | T (°C) | P (MPa) | t (h) | $H_2O$ (%) | $O_2$ (vol.%) | $SO_2$ (ppm) | Rotating rate (rpm) | Sample type |
|--------|--------|---------|-------|------------|---------------|--------------|---------------------|-------------|
| 1 | 45 | 10 | 120 | Sat. | 3.0 | - | 100 | Coupons |
| 2 | 45 | 10 | 120 | Sat. | 3.0 | 100 | 0 | Coupons |
| 3 | 45 | 10 | 120 | Sat. | 3.0 | 100 | 100 | Coupons |
| 4 | 45 | 10 | 137 | Sat. | 3.0 | 100 | 0 | Beam |

Note: Sat.—saturated.

Figure 2-2(a) is a photographic image showing the experimental setup for s-$CO_2$ corrosion and SCC tests. A home-made apparatus was applied for delivering $CO_2$-saturated water into the autoclave. A digital pressure gauge was used to monitor and control the pressure of added gaseous impurities, as well as the $CO_2$ phase. A supercritical $CO_2$ pump was used for liquid $CO_2$ charging. To start the test, the autoclave was sealed after sample loading and purged with $CO_2$ gas for at least one hour. Then, the required amounts of $CO_2$-saturated water and gases were charged into the autoclave as schematically shown in Figure 2-2(b). Note that $SO_2$ charging was achieved through charging the mixture of $CO_2$ + 774 ppm $SO_2$. The time at which the system reached the desired condition of a test was recorded as the start point. After the designed exposure time, the autoclave was powered off and cooled down to room temperature. The gaseous mixture was discharged through a home-made specific rig to neutralize the toxic impurities before being released into the air. All the samples were then taken out for further characterization.
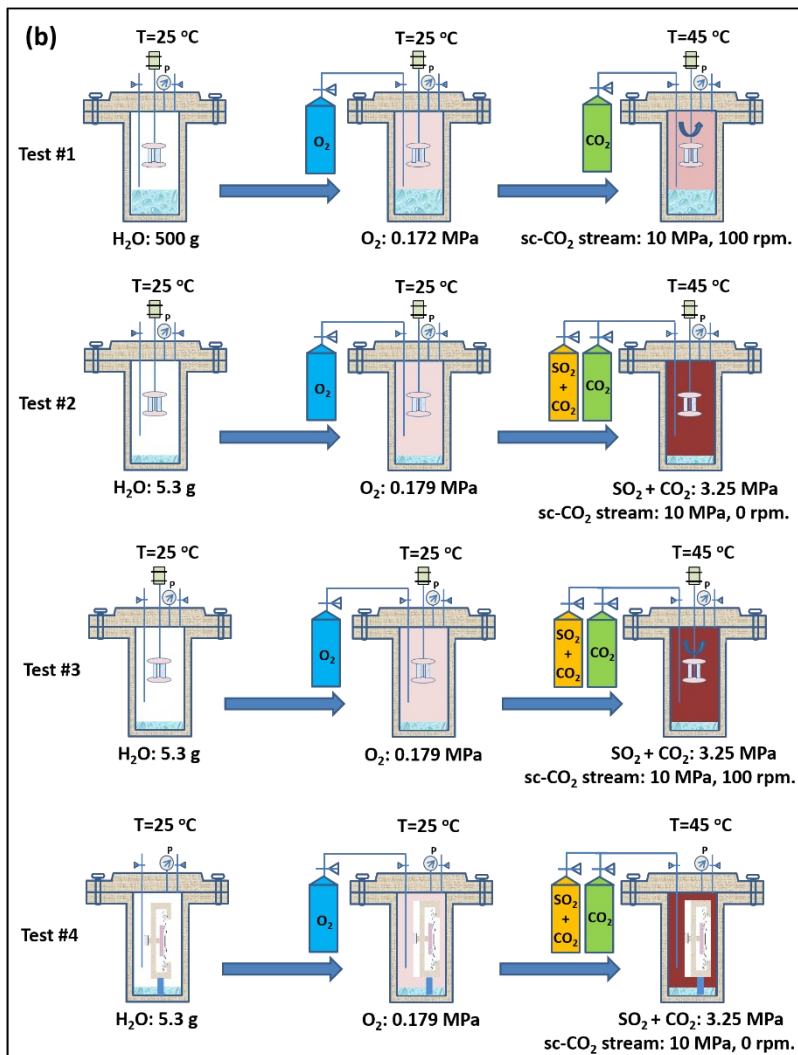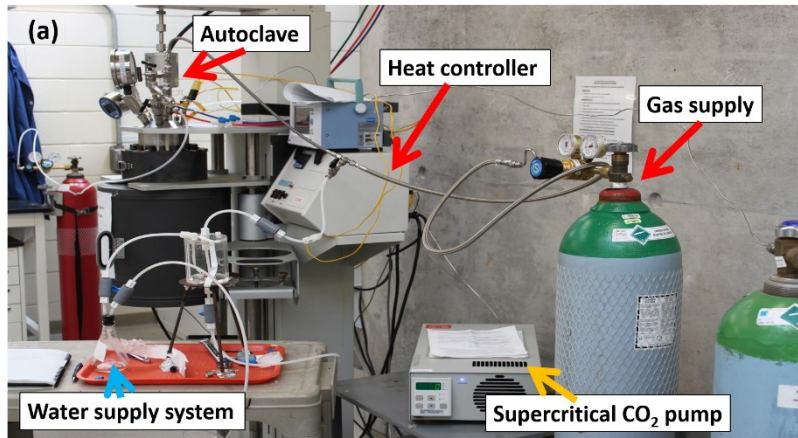
Figure 2-2. (a) Image of work station for s-CO$_2$ corrosion tests; (b) Schematic of experimental procedures of the planned tests.

### 2.2.4. Corrosion rate assessment and corrosion product characterization

The photographic images of all test samples were recorded to identify the obvious changes on surfaces before and after a test. To advance the understanding of how the steels corrode in the s-$CO_2$ environments, a field-emission FEI NOVA NANOSEM 650 Scanning Electron Microscope (SEM) machine equipped with Energy Dispersive X-ray Spectroscopy (EDS) technique was used to characterize the corrosion products formed on the steels. X-ray diffraction (XRD) characterization was also used to identify the phase compositions of the formed corrosion products using a Bruker D8 Discover diffractometer equipped with Co-Kα radiation.

Weight loss measurements were performed on corrosion coupons to evaluate corrosion rates in the s-$CO_2$ media. According to ASTM G1-03 [109] and other references [110, 111], the corrosion products formed on the samples can be completely removed using a pickling solution with 100 ml hydrochloric acid and 900 ml deionized water. The corrosion rate in μm per year was then calculated as [112]:

$$\text{Corr. Rate} = \frac{8.76 \times 10^7 \cdot \Delta W}{dAt} \qquad \text{Equation 2-2}$$

where $\Delta W$ is the mass loss in grams of the sample after an autoclave test and the descaling of formed corrosion products; d is the density of materials in g/cm$^3$ (carbon steels: 7.86 g/cm$^3$); A is the surface area of tested sample in cm$^2$ and t is the test duration in hours.

### 2.3. Results and discussion

### 2.3.1. Previous results about the effect of SO$_2$ on corrosion in s-CO$_2$ streams

In s-$CO_2$ streams, the impact of $SO_2$ on corrosion is still unclear because of relatively complicated chemical environments, limited database and somewhat controversial results. Most studies were conducted in autoclaves at lab-scale to investigate the corrosion performance of steels in simulated s-$CO_2$ environments with different levels of impurities. The results show that the simultaneous presence of $H_2O$, $O_2$ and $SO_2$ is very likely to introduce severe corrosion damage, and the corrosion rates of pipeline steels increase with an increase in $SO_2$ content [88, 113]. Iron sulfites, iron sulfates and iron oxides are typical corrosion products formed on pipeline steels [113]. Figure 2-3 summarizes most published corrosion rate data about the effect of $SO_2$ in s-$CO_2$ mixtures with impurities $H_2O$ and/or

$O_2$ [86, 88, 113-125]. As shown in Figure 2-3(a), the synergistic effect of $O_2$ and $SO_2$ could cause noticeable corrosion damage on pipeline steels in $H_2O$-saturated s-$CO_2$. However, no clear image is available to depict the effect of $SO_2$ on the corrosion rates of pipeline steels because of the limited studies and some conflicting results reported. For example, several research groups reported that the corrosion rate of pipeline steels in $H_2O$-saturated s-$CO_2$ streams containing $O_2$ and $SO_2$ was unlikely to be more than 1500 μm/y [88, 113], while one group found that the rate could be up to 6000 μm/y [114].

Figure 2-3(b) shows that the effect of $SO_2$ on corrosion is also related to the contents of dissolved $H_2O$ in the s-$CO_2$ streams with $O_2$. In s-$CO_2$ with low oxygen contents (< 100 ppm) and dissolved $H_2O$% < 2000 ppm, $SO_2$ only exhibits a marginal effect on corrosion. When $H_2O$% is above 2000 ppm, however, severe corrosion damage may occur as the corrosion rates noticeably increase with an increase in $SO_2$ content. According to our literature review, only one publication pointed out that serve corrosion could also happen in the s-$CO_2$ containing 650 ppm $H_2O$ and 10000 ppm $SO_2$ [114]. In s-$CO_2$ with high oxygen contents (>100 ppm), the influence of $SO_2$ also depends on the content of $H_2O$ dissolved. A notable increase in the corrosion rate is observed when $H_2O$% is more than about 2000 ppm [125].
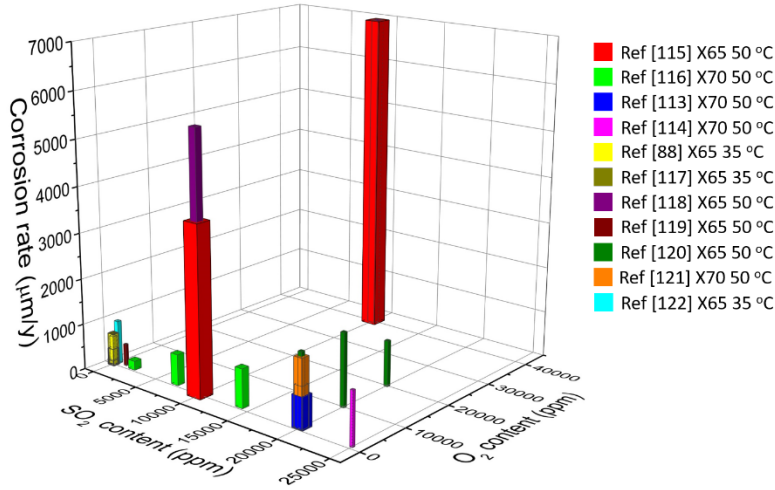
(a) Effect of $SO_2$ and $O_2$ in $H_2O$-saturated s-$CO_2$
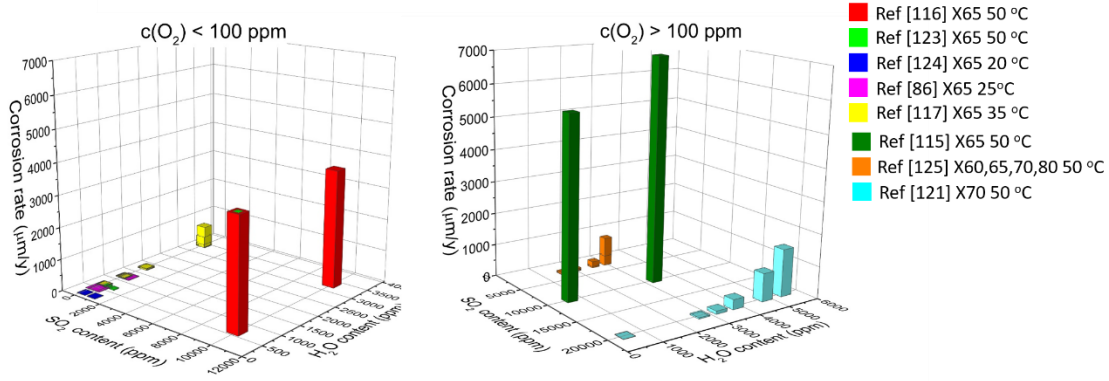


(b) Effect of $SO_2$ and $H_2O$ with different $O_2$% (< or > 100 ppm) in s-$CO_2$

Figure 2-3. Previous results about the influence of $SO_2$, $O_2$ and $H_2O$ on the corrosion rates of different steels in s-$CO_2$ at the pressure range of 8-10 MPa and different temperatures [86, 88, 113-125].

### 2.3.2. Effect of $SO_2$ on corrosion in s-$CO_2$ captured from advanced oxy-fuel combustion plants

The photographic images of corrosion coupons before and after Tests #1-3 are shown in Figure 2-4. During exposure to $H_2O$-saturated s-$CO_2$ containing 3% $O_2$ (Test #1), the surface of the steel samples only developed light brown color, implying the formation of relatively thin surface iron oxides. When exposed to the s-$CO_2$ streams with 100 ppm $SO_2$ and 3% $O_2$, dark red color was developed on the sample surfaces, suggesting that the samples experienced severe corrosion damage. In Tests #1-2, the surface scale was visibly

compact and relatively uniform. In Test #3, however, a noticeable amount of corrosion products was spalled and found at the autoclave bottom, indicating the remarkable effect of flow rate on corrosion.
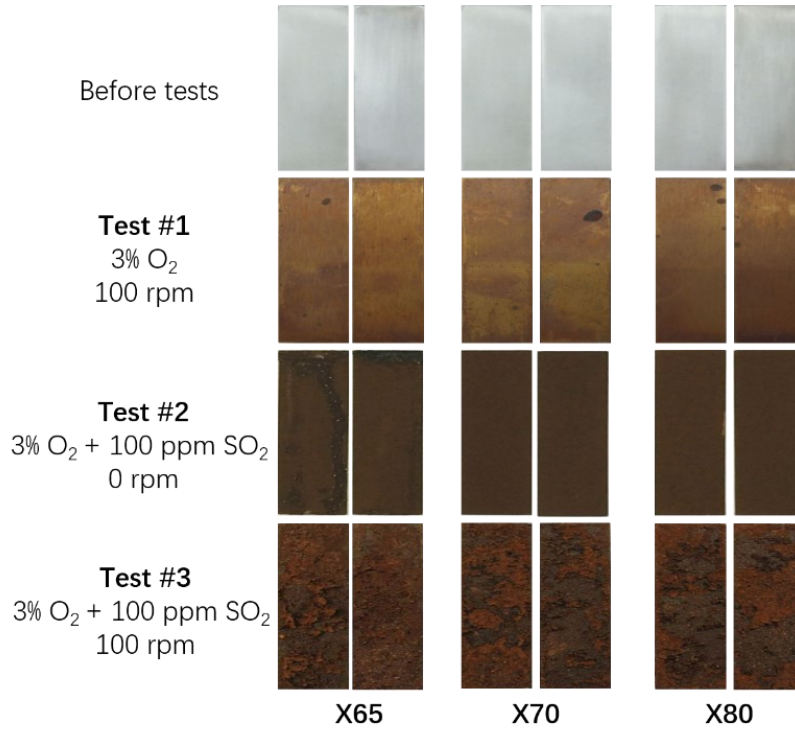


Figure 2-4. Photographic images of steel coupons before and after being tested in 10 MPa $H_2O$-saturated s-$CO_2$ with different contents of impurities at 45 °C.

SEM images and corresponding EDS analyses of X65 and X80 steels after Tests #1-3 are shown in Figure 2-5. In $H_2O$-saturated s-$CO_2$ containing 3% $O_2$ (Test #1), SEM and EDS results indicated the formation of iron oxide and iron carbonate scales on the steels (Figure 2-5(a)). In Tests #2-3, with the addition of 100 ppm $SO_2$, severe corrosion occurred as the surface was covered with quite thick corrosion products. Microcracks were found within the corrosion scales. Spheral corrosion products with worm-like and opening-like shape were observed in Figure 2-5(c), and they were mainly composed of iron oxyhydroxide (FeOOH), iron carbonate ($FeCO_3$) and iron sulfate ($FeSO_4$), as confirmed by XRD measurements in Figure 2-6(a). As shown in Figure 2-5(b), (d), (f) and Figure 2-6, the morphology, chemical composition and phase composition of corrosion products on X80

steel in Tests #1-3 are similar to those formed on X65 steel, indicating the steel should have no noticeable influence on corrosion performance in the s-CO₂ media.



(a) X65 steel after the exposure to H₂O-saturated s-CO₂ with 3% O₂, 100 rpm (Test #1)

(b) X80 steel after the exposure to H₂O-saturated s-CO₂ with 3% O₂, 100 rpm (Test #1)

(c) X65 steel after the exposure to H₂O-saturated s-CO₂ with 3% O₂ +100 ppm SO₂, 0 rpm (Test #2)

(d) X80 steel after the exposure to H₂O-saturated s-CO₂ with 3% O₂ +100 ppm SO₂, 0 rpm (Test #2)

(e) X65 steel after the exposure to H₂O-saturated s-CO₂ with 3% O₂ +100 ppm SO₂, 100 rpm (Test #3)

(f) X80 steel after the exposure to H₂O-saturated s-CO₂ with 3% O₂ +100 ppm SO₂, 100 rpm (Test #3)

Figure 2-5. SEM and EDS results collected on X65 and X80 steel coupons after the exposure to 10 MPa H₂O-saturated s-CO₂ streams with different impurities and rotation rates at 45 °C for 120 h.

The corrosion rates of pipeline steels in the s-CO₂ environments are shown in Figure 2-7. In H₂O-saturated s-CO₂ with 3% O₂ (Test #2), the addition of 100 ppm SO₂ resulted in more than 10 times increase in corrosion rates, which were high enough to cause serious pipeline integrity problems. Moreover, the corrosion rates were further enhanced about twice when a flow rate of 100 rpm was applied (Test #3), suggesting that the flow rate of s-CO₂ steam shall be a factor to consider on pipeline corrosion control. The effect of flow rate on corrosion may be attributed to that increasing flow rate can promote the reactions of impurities with the steels and produce high shear stress to erode the corrosion layers formed on steels [25]. Note that increasing flow rate is unlikely to change corrosion modes

26

of the steels in the simulated s-$CO_2$ media, as indicated in Figure 2-4 and Figure 2-5. Furthermore, consistent with SEM/EDS results, the corrosion rates did not noticeably vary with the steel grades even though the steels have the different contents of alloying elements Mn and Si. Note that X65 steel exhibited somewhat higher corrosion rates compared to X70 and X80 steels after Test #2. It is likely that such a higher rate is partially from unexpected damage during discharging $CO_2$ mixture after the corrosion test as water flow lines were observed on the X65 samples. In general, the findings of this study and some previous reports [88, 113] show that it is important to control the $SO_2$ content below 100 ppm through flue gas desulfurization (FGD) system [126] or other advanced sulfur-capture technologies [127] before injecting the s-$CO_2$ streams from the advanced pressurized oxy-fuel combustion power plants into transportation pipelines from both corrosion and public health point of views. Furthermore, based on the results shown in Figure 2-3 and Figure 2-7, and the assumption that 5 mpy (127 μm/y) is the maximum acceptable corrosion rate of s-$CO_2$ pipelines [128], it is also necessary to control $H_2O\%$ less than 2000 ppm in the s-$CO_2$ streams with $O_2$ (3-6 vol.%) and $SO_2$ (<100 ppm) to meet long-term safe operation requirements of the s-$CO_2$ pipelines based on current and previous studies.
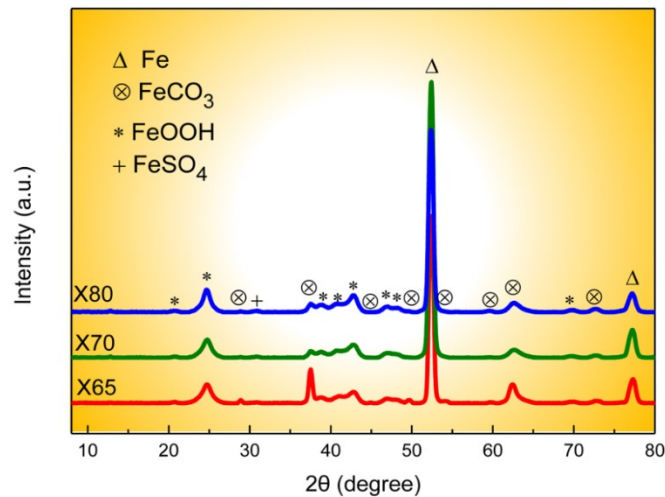


Figure 2-6. XRD spectra of steels after exposure to 10 MPa $H_2O$-saturated s-$CO_2$ stream with 3.0% $O_2$ + 100 ppm $SO_2$ (Test #2).
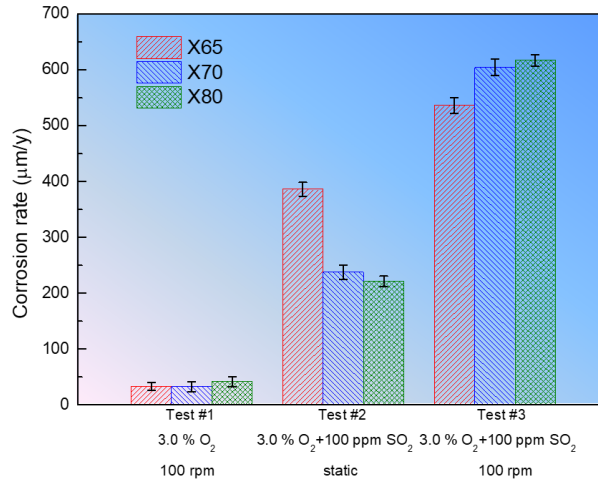
Figure 2-7. Average corrosion rates of the steels exposed to 10 MPa H₂O-saturated s-CO₂ streams with different impurity contents and rotation rates at 45 °C for 120 h.

### 2.3.3. Possible corrosion reactions occurred in s-CO₂ with SO₂

Previous studies [86, 113-116, 118-121, 123, 124, 129-132] and current work show that a mixture of iron oxides, iron carbonates, iron sulfates and iron sulfides might be formed on pipeline steels when exposed to s-CO₂ stream containing impurities SO₂, O₂ and H₂O. However, it is unknown whether the corrosion products are formed through electrochemical or gas chemical reactions. SO₂ has a strong affinity to water to generate an acidic film of H₂SO₃ on steel surfaces via either the reaction between SO₂ and H₂O dissolved in the s-CO₂ stream or the dissolution of SO₂ in water phase condensed on the steel surface [25, 133-136]. Once the aqueous acidic film was formed, the following anodic reaction could occur:

$$Fe \rightarrow Fe^{2+} + 2e^- \hspace{3cm} \text{Equation 2-3}$$

Without the presence of impurity O₂, the cathodic reaction accompanied should be hydrogen evolution. The generated cations ($Fe^{2+}$) and anions ($SO_3^{2-}$) could combine to form a non-protective FeSO₃ layer on the steels [88]:

$$Fe^{2+} + SO_3^{2-} \rightarrow FeSO_3 \hspace{3cm} \text{Equation 2-4}$$

If s-CO₂ contains a certain amount of O₂, the cathodic reaction is likely to be dominated by the oxygen reduction process. Meanwhile, $SO_3^{2-}$ could further be oxidized into $SO_4^{2-}$ and then react with $Fe^{2+}$ [115, 137]:

$$2SO_3^{2-} + O_2 \rightarrow 2SO_4^{2-} \qquad\qquad \text{Equation 2-5}$$

$$Fe^{2+} + SO_4^{2-} \rightarrow FeSO_4 \qquad\qquad \text{Equation 2-6}$$
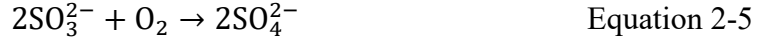
From the gas chemical corrosion point of view, iron sulfites and sulfates could be produced via the following direct gaseous reactions [138]:

$$Fe + SO_2 + H_2O(g) \rightarrow FeSO_3 + H_2 \qquad\qquad \text{Equation 2-7}$$

$$2FeSO_3 + O_2 \rightarrow 2FeSO_4 \qquad\qquad \text{Equation 2-8}$$
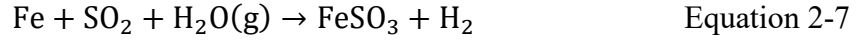
In the presence of impurity $O_2$, $FeSO_4$ might be further oxidized [137]:

$$4FeSO_4 + O_2 + 6H_2O \rightarrow 4FeOOH + 4H_2SO_4 \qquad\qquad \text{Equation 2-9}$$

$$\text{or} \quad 4FeSO_4 + O_2 + 6H_2O \rightarrow 2Fe_2O_3 \cdot H_2O + 4H_2SO_4 \quad \text{Equation 2-10}$$
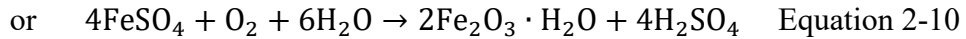
The generated $H_2SO_4$ could work with $O_2$ to attack the steels, leading to the regeneration of $FeSO_4$, which is known as the acid regeneration cycle [137]:

$$2H_2SO_4 + O_2 + 2Fe \rightarrow 2FeSO_4 + 2H_2O \qquad\qquad \text{Equation 2-11}$$
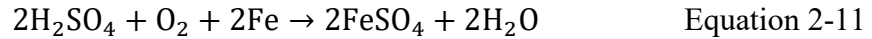
Up to now, the results reported are insufficient to reveal dominant corrosion pathways in the $SO_2$-containing s-$CO_2$ environments due to the lack of in-situ testing evidence. One interesting finding is that the presence of $SO_2$ might decrease the maximum solubility of $H_2O$ in s-$CO_2$, subsequently facilitating the formation of the acidic film on pipeline steels [117]. But more works are still needed to confirm this observation and to identify the critical condition where the acidic film can be formed. Moreover, the analyses of corrosion rates of steels obtained in $SO_2$-contained gaseous and aqueous environments may provide a clue to explain the effect of $SO_2$. When exposed to the $SO_2$ gas flow with 90% relative humidity, the corrosion rate of iron was about 532 μm/y [139]. In such a gaseous environment, an aqueous film was expected to be formed on the iron, making the corrosion process mainly controlled by electrochemical reactions. Meanwhile, in-situ electrochemical measurements showed that the corrosion rate of X80CrSiMoW152 steel was 401 μm/y in a solution saturated with $CO_2$ and 100 ppmw $SO_2$ [140]. These reported corrosion rates are close to the rates obtained from the current study, implying that the corrosion process in the s-$CO_2$ streams captured from the advanced oxy-fuel combustion plants is likely to be dominated by the electrochemical reactions instead of gas chemical reactions. For future clarification, more studies, such as in-situ electrochemical impedance

and noise measurements are required to determine whether an aqueous acidic film is formed on steels in the s-CO$_2$ conditions.

### 2.3.4. SCC susceptibility of pipeline steels in SO$_2$-containing s-CO$_2$ environments

As three tested steels exhibit similar corrosion performance in SO$_2$-containing s-CO$_2$ environments, the SCC investigations were conducted only on X65 steel, which is the most widely used pipeline material in the oil and gas field [141]. Figure 2-8(a) shows the stress-strain curve of X65 steel and the deduced mechanical properties. The 0.2% offset yield point of X65 steel corresponds to 450 MPa and 0.4% strain rate. For SCC studies, the bent-beams were loaded with 35% and 100% of the 0.2% offset yield strength, which corresponded to 0.14% and 0.4% stains, respectively (indicated by the two red dots in Figure 2-8(a)). From an integrity point of view, the operating pressure of pipelines is usually designed below 72% of the specified minimum yield strength [142]. However, the localized stress level on the pipeline steel might go to 100% of the yield strength after long term service under the corrosive conditions. Thus, 100% of the yield strength was applied as an accelerated SCC cracking evaluation. In addition, the DIC-measured surface strains are shown in Figure 2-8(b). The color reflects the degree of strains, and the measured average strains are shown on the left side of each map and represented as the nominal strain applied on the bent-beam samples. Clearly, the DIC measured strains well match the designed strain using FPB loading, confirming that the applied strains are accurate.
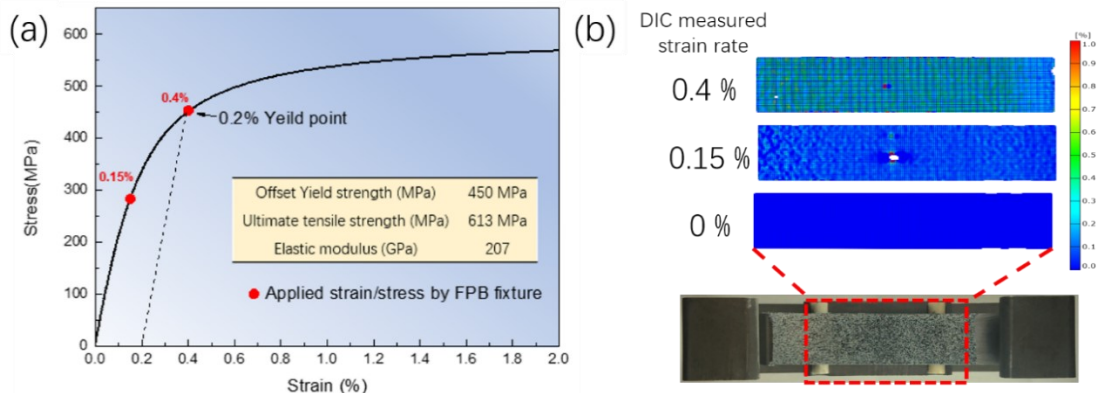


Figure 2-8. (a) Stress-strain curve of X65 steels and the strain pre-applied for the SCC test and (b) DIC strain maps of loaded X65 steel specimens in Test #4.

Figure 2-9 shows the photographic and SEM images of loaded bent-beams after the exposures to $H_2O$-saturated s-$CO_2$ containing 100 ppm $SO_2$ + 3% $O_2$ in static condition (Test #4). The surfaces of loaded bent-beams showed dark reddish color, similar to those on the corrosion coupons in Test #2 (Figure 2-4). No visible crack was found on the bent-beams loaded with different strains. However, high magnification SEM images (Figure 2-9(b) and (d)) showed some micro-cracks formed within the corrosion products. Typical cross-sectional images (Figure 2-9(c) and (e)) revealed that these cracks were developed only within the surface corrosion layer, and didn't penetrate into the steel substrate. The cross-sectional examinations were conducted across the transverse section of two bent-beams and no crack was found in the steel substrates, indicating that the SCC did not occur on the steel even loaded with 100% of the yield strength.
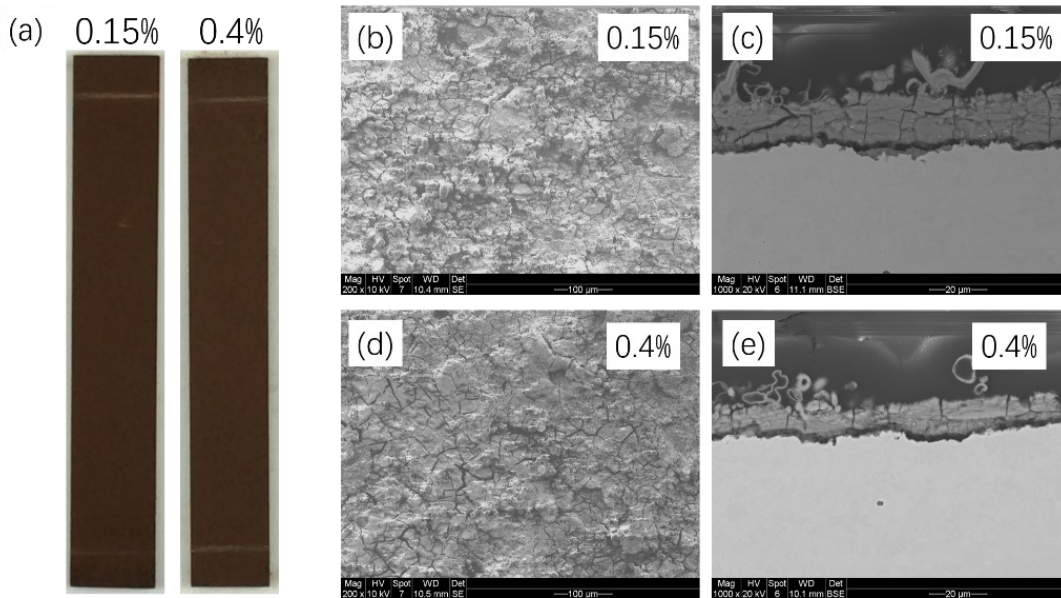


Figure 2-9. (a) Photographic images of the two bent-beam specimens, (b, d) surface and (c, e) cross-sectional morphology of 0.15% and 0.4% strained X65 steels after the exposure to 10 MPa $H_2O$-saturated s-$CO_2$ containing 100 ppm $SO_2$+3% $O_2$ at 45 °C for 137 h (Test #4).

$SO_2$-induced SCC of pipeline steels can occur via two main pathways: anodic dissolution and hydrogen-induced cracking [143-146]. The dissolution of $SO_2$ in water will form

sulfurous acids, which can accelerate the steel dissolution and/or enhance their hydrogen absorption by generating hydrogen atoms via cathodic reactions [146, 147]. Once exceeding a threshold value under external loading, the trapped hydrogen could weaken the metallic bonding of substrate metals and cause local embrittlement [148].

Despite the above factors that may contribute to SCC cracking, however, no SCC crack was found in the steel substrates after Test #4. One explanation is that the testing duration (around 137 hours) may be shorter than the incubation period of SCC crack. For example, the SCC incubation time of pure iron steel loaded with 95% yield stress in NS4 solution was longer than 50 days [95]. Zhang et al. [148] found that the incubation time of C-ring made of Al-based alloy exposed to $SO_2$-rich environment could go up to 103 days. Long-term SCC tests are needed to validate the findings.

Another possible explanation of the absence of SCC cracks is the lack of localized stress concentration. Localized breakdown of surface corrosion layer, like pitting, will act as the precursor of macroscopic crack because of the concentrated stress level [29, 149]. In the current studies, the steel samples only experienced active general corrosion instead of pitting in the simulated s-$CO_2$ media, as indicated in Figure 2-9. The high general corrosion is unlikely to support the formation of localized stress concentration and advance the initiation of SCC cracks. In addition, the observed cracks within the surface corrosion products were possibly formed during the cooling/degassing process of the corrosion tests as these corrosion products are brittle in nature.

## 2.4. Conclusions

All the results indicate that the presence of $SO_2$ in transported s-$CO_2$ streams can induce severe corrosion damage on conventional pipeline steels. In $H_2O$-saturated s-$CO_2$ containing $SO_2$ and $O_2$, the corrosion products formed on the steels are composed of iron sulfites, sulfates, carbonates and oxides. To achieve long-term safe transportation of s-$CO_2$ captured from advanced oxy-fuel combustion plants, it is necessary to control $H_2O$% (< 2000 ppm) and $SO_2$% (< 100 ppm) in the s-$CO_2$ streams based on previous and current work. Possible corrosion reaction analyses and corrosion rate comparison show that the

corrosion of pipeline steels in $H_2O$-saturated s-$CO_2$ with $SO_2$ is very likely controlled by electrochemical reactions instead of gas chemical reactions. In the s-$CO_2$ media, short-term FPB test shows the SCC susceptibility of the X65 steel strained up to 0.4% is lower than expected.

# Chapter 3.  Condensed Phase Corrosion of P91 and DSS 2205 Steels at Advanced Oxygen-fired Pressurized Fluidized Bed Combustion Plants

**Abstract**

Condensed phase corrosion of flue gas components has been recognized as a critical challenge on the structural integrity of existing fossil fuel combustion plants. To achieve the targets of high energy efficiency and reduced $CO_2$ emission, advanced oxy-fired pressurized fluidized bed combustion (oxy-fired PFBC) technology is being developed. Although the condensates generated at the oxy-fired PFBC plants seem to be more corrosive, very limited information is available to select appropriate alloys for the cost-effective construction and long-term safe operation of flue gas components. Thus, this study investigated the corrosion performance of P91 and DSS 2205 steels in the simulated condensates of the oxy-fired PFBC plants at 60-150 °C. The dominant reactions on the two steels were relatively high oxide formation and chemical dissolution instead of pitting. Increasing temperature leads to an exponential increase in the long-term corrosion rates of the steels. Benefited from its high Cr mad Mo contents, DSS 2205 steel exhibited much better resistance to corrosion in the condensed solution, and the formed surface scales consisted of inner Fe-enriched and outer Cr-enriched oxides in which $Cr_2O_3$ was transformed into $Cr(OH)_3$ with increasing temperature. The corrosion products grown on P91 steel consisted of inner Cr-Fr-Mo oxides and outer Fe-enriched oxides which were porous and unable to protect the steel from environmental attack.

**Keywords**: Oxy-fired PFBC; Condensed phase corrosion; Fe-Cr steels; Temperature.

## 3.1.  Introduction

The background information of oxy-fuel PFBC is referred to Section 1.2. Materials challenge and corrosion issues are referred to Section 1.3.2.

The condensed phase corrosion has been seen as a serious challenge on the structural integrity of the flue gas components at existing fossil fuel combustion plants, since the condensates are usually the mixtures of highly corrosive acids, including $H_2SO_4$, HCl,

$H_2CO_3$ and/or $HNO_3$ [150, 151]. As the contents of $CO_2$, $SO_x$ and HCl present in the flue gas of oxy-fired PFBC are noticeably higher than those produced at conventional air combustion plants, the extent of condense phase corrosion is likely to be more severe [152]. For instance, the concentration of $SO_x$ at oxy-fired PFBC may be up to 5 times higher than that at the conventional plants [152, 153]. Moreover, given the pressurized operating design, the dew points of flue gas at oxy-fired PFBC shall be higher than those at conventional plants [11, 154-157], leading to an unclear effect of temperature on the condense phase corrosion. Note that the dew point of the flue gas at the oxy-fired PFBC plants will be up to 150 °C as described later. Therefore, all these changes consequently introduce a serious concern of which alloys are appropriate for the flue gas components at oxy-fired PFBC.

According to our literature review [40], very limited information is available to describe the condensed phase corrosion of steels and alloys under the oxy-fired PFBC operating conditions. Over the past decades, with the development of innovative materials technologies, many Fe- and Ni-based alloys, including carbon steels, ferrite/martensite steels, austenite stainless steels, Ni-based alloys, etc., have been employed for the flue gas components at the conventional plants [158, 159]. It is generally accepted that Cr-containing steels are the primary candidates since the formed chromium oxide scales on the alloys may act as barriers to effectively resist aggressive condensates at temperature < 100 °C [40]. Ni-based alloys with high Cr and Mo, such as Alloy C-276 and Alloy 22, usually have excellent resistance to acidic corrosion at elevated temperatures [160]. However, their application is limited because of the cost. Thus, Fe-Cr steels are affordable candidates. In fact, ferrite-martensite steels (P91 and P92) have been used for the flue gas components at the conventional plants due to their good mechanical strength, moderate corrosion resistance and relatively low cost [161, 162]. Moreover, Duplex Stainless Steels (DSS), such as DSS 2205 and DSS 2207, also show their great potential because of their strong mechanical strength, high corrosion resistance, moderate weldability and relatively low cost compared with austenitic stainless steels [74, 163].

Therefore, this study investigated the corrosion performance of P91 and DSS 2205 in simulated flue gas condensates of oxy-fired PFBC at 60-150 °C. It is expected to fill some

35

knowledge gaps and help the energy sectors with the development of materials selection strategy for the successful construction and long-term safe operation of the oxy-fired PFBC plants.

## 3.2. Experimental procedure

### 3.2.1. Test sample preparation

Corrosion test samples (20 mm long × 10 mm wide × 2 mm thick ) were machined from commercial P91 and DSS 2205 plates, and their chemical compositions are listed in Table 3-1. Before performing condensed phase corrosion testing, all the surfaces and edges of each sample were well polished with SiC papers up to 600 grit, followed by rinsing with deionized water, degreasing with acetone in an ultrasonic bath, and completely drying with pressurized air. After that, each freshly-prepared sample was weighed using a micro-balance with a precision of 1 µg and measured to the nearest 10 µm on dimensions.

Table 3-1. Normalized chemical composition of P91 and DSS 2205 steels (in wt.%).

| Alloy (wt.%) | Cr | Ni | Mo | Fe | C | Si | Mn | P | S |
|---|---|---|---|---|---|---|---|---|---|
| P91 | 8.36 | 0.07 | 0.90 | 89.74 | 0.109 | 0.33 | 0.47 | 0.024 | 0.002 |
| DSS 2205 | 22.54 | 5.61 | 3.03 | 67.18 | 0.020 | 0.42 | 1.17 | 0.028 | 0.001 |

### 3.2.2. Condensed phase corrosion testing methodology and procedure

According to pilot-scale experience, the flue gas at the oxy-fired PFBC is usually pressurized (about 0.7-1.5 MPa) and enriched with $CO_2$ (~66%) and $H_2O$ (~30%) along with certain amounts of $SO_2$, $NO_2$ and HCl [164]. The formed condensed phase is the mixture of dilute $H_2SO_4$, $HNO_3$, HCl and $H_2CO_3$ acids with a pH of ~2. Thus, the condensed phase solution used in this study was prepared from corresponding analytic grade reagents, and its composition is shown in Table 3-2.

Table 3-2. Chemistry of simulated condensed phase solution used for the tests.

| Ions | $SO_4^{2-}$ | $Cl^-$ | $NO_3^-$ | $HCO_3^-$ | $H^+$ |
|---|---|---|---|---|---|
| Concentration (mol/L) | 0.001 | 0.005 | 0.005 | <0.002 | 0.01 |

Previous studies have well demonstrated that the dew point of flue gas is coherently related to the partial pressure and concentration of each gas phase present, such as [156, 165]:

$$T_{\text{dew point}} = 116.5515 + 16.06329 \cdot \lg P_{SO_3} + 1.05377(\lg P_{SO_3})^2 \qquad \text{Equation 3-1}$$

For the mixture of two different gases, the dew point can be estimated by [166]:

$$T_{HCl} = \frac{1000}{\{3.7368 - 0.1591*\ln(P_{H_2O}) - 0.0326*\ln(P_{HCl}) + 0.00269*\ln(P_{H_2O})*\ln(P_{HCl})\}} \qquad \text{Equation 3-2}$$

$$T_{HNO_3} = \frac{1000}{\{3.6614 - 0.1446*\ln(P_{H_2O}) - 0.0827*\ln(P_{HNO_3}) + 0.00756*\ln(P_{H_2O})*\ln(P_{HNO_3})\}} \text{Equation 3-3}$$

$$T_{SO_2} = \frac{1000}{\{3.9526 - 0.1863*\ln(P_{H_2O}) + 0.000867*\ln(P_{SO_2}) - 0.00091*\ln(P_{H_2O})*\ln(P_{SO_2})\}} \qquad \text{Equation 3-4}$$

As the flue gas produced at the oxy-fired PFBC is quite complicated, its dew points were evaluated using commercial software, VMG-Sim, with its in-build database [167], and the results are shown in Figure 3-1. Different from the dew points (usually 40-80 °C) of conventional combustion plants [163, 168], the dew points of flue gas at the oxy-fired PFBC are predicted to be around 120-150 °C due to the designed pressurization operation. To meet industrial application demands, the condensed phase corrosion tests were thus conducted at 60, 90, 120 and 150 °C, respectively.
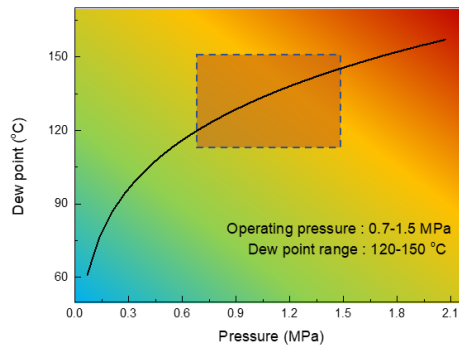


Figure 3-1. Variation of the dew point of flue gas with pressure at oxy-fired PFBC plants.

As schematically shown in Figure 3-2, two different experimental set-ups were used for the testing. At 60 and 90 °C, the tests were carried out in a glass flask containing 1 L simulated condensed solution and with a connection to the air through a water-cooled condenser. The solution temperature was controlled by using an oil bath. The tests at 120

and 150 °C were conducted in an autoclave made of Alloy C-276 in which 1 L simulated solution was added and pressurized with air to introduce an aerated environment. To avoid potential contamination of different dissolved metal ions, only four freshly-prepared coupons of a steel were hung on a custom-made glass holder and then immersed in the condense solution at each temperature. After 120 hours of exposure, the coupons were removed for the direct mass change measurements and surface morphology examinations, and then set back into the testing rig with refreshed condense solution for next exposure. To identify the long-term condensed phase corrosion of the steels, the tests of 6 cycles (total 720 hours of exposure) were performed at one temperature. After all the tests, the corroded coupons were collected, rinsed with deionized water, cleaned with alcohol, and finally dried with pressurized air.
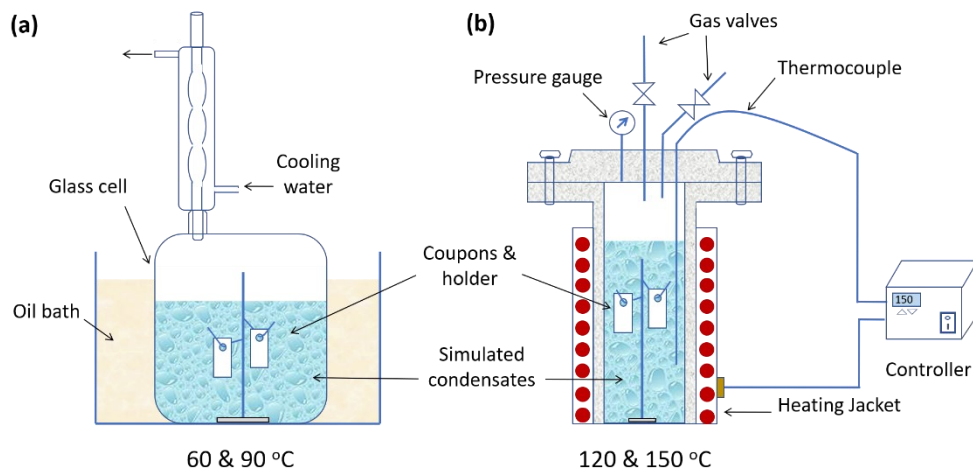


Figure 3-2. Schematic of testing set-ups: (a) glass container used for condense tests at 60 and 90 °C, and (b) autoclave for the tests at 120 and 150 °C.

### 3.2.3. Long-term corrosion rate determination and corrosion products characterization

After the designed tests at each temperature, the coupon with the direct mass change closest to the average one in a given replicate set was selected for subsequent corrosion product characterization. The other three coupons of a steel were used for long-term corrosion rate assessment.

As described in the following section, the two steels experienced negative mass change instead of positive gain in the condensed solution and considerable corrosion products were formed after the tests. Thus, to accurately obtain the long-term corrosion rates of the steels, the corrosion rates were determined using mass loss measurement method involving two major steps: (a) descaling the corrosion product formed on a steel coupon and (b) weighing the mass change of the coupon before corrosion testing and after descaling. According to ASTM-G1 [109], descaling surface corrosion products can be achieved via immersing the coupons in specific solutions that are safe to steel substrates but can effectively remove the formed corrosion products through chemical dissolution reactions. In this study, the descaling of P91 was carried out by immersing corroded coupons in the solution of 500 mL HCl + 3.5 g hexamethylene tetramine + 500 mL deionized water at room temperature for 10 min. The descaling of DSS 2205 was carried out at 90 °C by immersing the corroded coupons in the solution of 2% $KMnO_4$ + 4% NaOH for 5 minutes and in the solution of 2% citric acid + 5% dibasic ammonium citrate + 0.5% disodium EDTA for 30 minutes, followed by ultrasonic cleaning in alcohol for 15 minutes. The long-term corrosion rate (CR) of each coupon was thus estimated by [169]:

$$CR = \frac{87.6 \times \Delta W}{A \rho t}$$

Equation 3-5

where CR (mm/y) is the corrosion rate, $\Delta W$ (mg) is the mass change of the coupon before a test and after descaling treatment; A ($cm^2$) is the surface area of the coupon; $\rho$ ($g/cm^3$) is the steel density (note the values of P91 and DSS 2205 steels are 7.76 and 7.82, respectively); t (h) is the immersion time in condensed solution.

The morphology and chemistry of the corrosion products grown on the steels were characterized using FEI NOVA230 Field Emission Scanning Electron Microscope (SEM) equipped with Energy Dispersive Spectroscopy (EDS). As the corrosion products formed on P91 were quite thick, their phase compositions were also identified using X-ray diffraction (XRD) with a Co Kα X-ray source at 40 kV and 150 mA. Different from P91 steel, the surface scales formed on DSS 2205 were relatively thin and thus, examined using X-ray photoelectron spectroscopy (XPS) on a PHI Quantera II Scanning XPS Microprobe. To obtain depth chemistry profiles, the surfaces of corroded DSS 2205 coupons were also sputtered with $Ar^+$ ion bombardment per 15 s using an ion beam of 1 kV and current of 1

μA. All the obtained XPS peaks were normalized to the standard carbon C 1s binding energy (284.8 eV) and then analyzed using MultiPak software (version 9.9.0).

## 3.3.  Results and discussions

### 3.3.1.  Nature of corrosion products grown on steels in condensed phase

The photographic images of the steels after each exposure were shown in Figure 3-3. Before the corrosion testing, the freshly prepared steel coupons showed neat surfaces with shining luster. After the exposure to the condensed phase solution at different elevated temperatures, the surface color of P91 became dark brown, implying that active corrosion process could occur. On the contrary, the surface color of DSS 2205 coupons remained almost unchanged with time at 60-120 °C, but turned into light yellow after 720 hours immersion at 150 °C. Interestingly, no visible pit was found on the two steels.
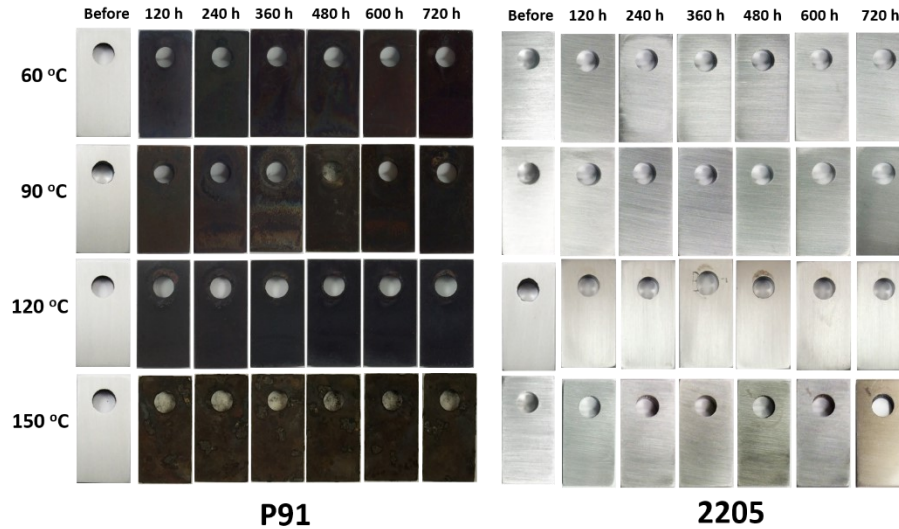


Figure 3-3. Photographic images of P91 and DSS 2205 before and after condensed phase tests at 60, 90, 120 and 150 °C.

Top-view SEM images of the two steels after the 720 hours of exposure to condensed phase solution at 60-150 °C are shown in Figure 3-4. Accumulation of corrosion products was observed on P91. XRD characterization showed that the corrosion products were composed of FeOOH, $FeCr_2O_4$, $MoFe_2O_4$, and $Fe_2O_3$ (see Figure 3-5). The XRD peaks of $Fe_2O_3$ were more remarkable on the sample corroded at temperature >120 °C, which could be attributed

to the transformation of FeOOH to $Fe_2O_3$ at elevated temperatures [163, 170]. Moreover, as shown in Figure 3-4, micro-cracks were found within the corrosion product layers on P91 at all the temperatures, suggesting that the formed oxide layers could not effectively protect the steel from the environment attack. Different from P91 steel, the surface scales grown on DSS 2205 are quite thin as the mechanical polishing lines generated during the sample preparation were still visible after all the tests. Increasing temperature did not cause a noticeable change of the steel surface morphology.
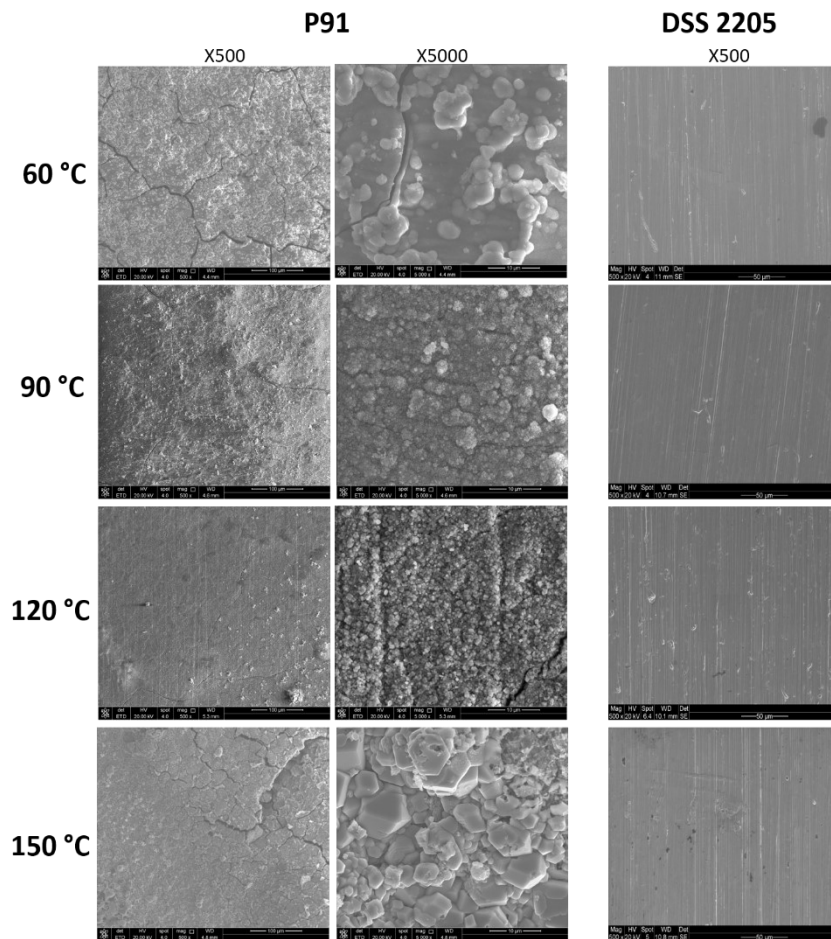


Figure 3-4. Top-view SEM images of P91 and DSS 2205 steels after the 720 hours of immersion in condensed phase solution at 60, 90, 120 and 150 °C.
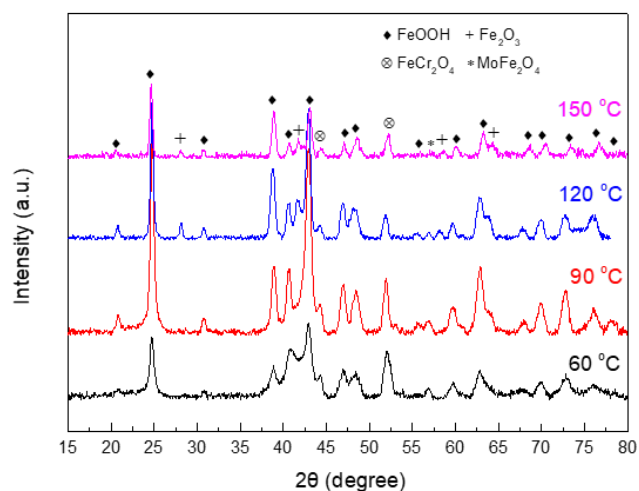
Figure 3-5. X-ray diffraction patterns recorded on corroded P91 steels after the 720 hours of immersion in condensed phase solution at 60, 90, 120 and 150 °C.

Both the photographic and top-view SEM images clearly showed that pitting corrosion did not occur on these two steels. But field inspections at the conventional combustion plants have reported that pits are usually observed on the flue gas components exposed to condensates due to the coupling effect of chloride and protons [169, 171]. The absence of severe pitting on the steels in this study could be from the following aspects:

(1) The $Cl^-$ concentration in the simulated condensed phase (0.005 mol/L) is insufficient to trigger pitting since the previous studies show that pitting occurs only in the solution with $Cl^-$ concentration higher than 0.07 mol/L [74].

(2) The presence of $HCO_3^-$ could somewhat inhibit pitting by modifying $H^+$ ion concentration inside the pit due to its buffer properties [172, 173]. Moreover, the simultaneous presence of $SO_4^{2-}$ and $NO_3^-$ cations could enhance the homogeneous degradation of surface scales [174-176]. For example, $SO_4^{2-}$ was found to induce surface complexation to facilitate the dissolution of chromium oxides by turning surface chromium oxy-hydroxide into soluble chromium sulfates and $CrOH^{2+}$ [175].

(3) As described later, the relatively quick chemical dissolution of surface oxide scales

on the steels could bypass the synergistic effect of Cl$^-$ and H$^+$ on pitting in the condensed phase solution.

The cross-sectional SEM/EDS analyses of the oxide layers formed on P91 steels after 720 hours of immersion in condensed phase solution are shown in Figure 3-6. These cross-sectional views further confirmed that no pitting occurred on P91. Clearly, two typical surface oxide layers, including outer thin and porous iron oxide and inner relatively compact and thick Cr-Fe-Mo oxides, were formed on the steel. Given its features of porosity and scarce of a strong connection with the inner layer, the outer iron oxide layer was very likely from the deposition of Fe$^{2+}$/Fe$^{3+}$ ions dissolved in the solution instead of the direct growth from the inner Cr-Fe-Mo oxide layer. As shown in Figure 3-8, such an iron oxide layer was also found on a pure Zr sample which was simultaneously exposed to the solution during the condense corrosion test of P91 steel at 90 °C. For the inner layer, the average concentrations of cations (Cr, Fe, and Mo) were roughly estimated based on EDS line scanning analyses and the results are shown in Figure 3-7. Increasing temperature led to an increase in Cr % and a decrease in Fe %, which might be attributed to the higher dissolution rate of iron oxide than that of Cr oxide in the condensed solution. An enrichment of Mo in the oxide layer was also observed, and its concentration was kept in the range of 17.4-21.5 at.% and did not significantly vary with temperatures. The enrichment of Mo in the inner oxide layer could promote the enrichment of Cr cations [177], suppress the diffusion of cation vacancies in the oxide layer [178], and/or reduce surface active sites [179].

As shown on Figure 3-6, the average thickness of inner Cr-Fe-Mo oxide layer increased with temperature, i.e, from ~40 μm at 60 °C to ~258 μm at 120 °C, suggesting an enhanced growth of oxides with temperature increase. Such an enhancement could be related to the existence of micro-cracks within the oxide layer (see Figure 3-4 and Figure 3-6), which could act as pathways to support the inward diffusion of aggressive ions into the interface of oxide/steel substrate for direct reactions with the steel and hinder the outward diffusion of the formed cations into the solution. However, further increasing temperature to 150 °C resulted in a decrease in the thickness of the inner oxide layer, suggesting that the influence

43

of temperature on the chemical dissolution of the oxides would become more dominant compared to its impact on the oxide growth. Therefore, increasing temperature can remarkably enhance not only the formation of surface oxides but also the chemical dissolution of oxides, consequently leading to high corrosion rates of the steel in the condensed phase solution at oxy-fired PFBC.
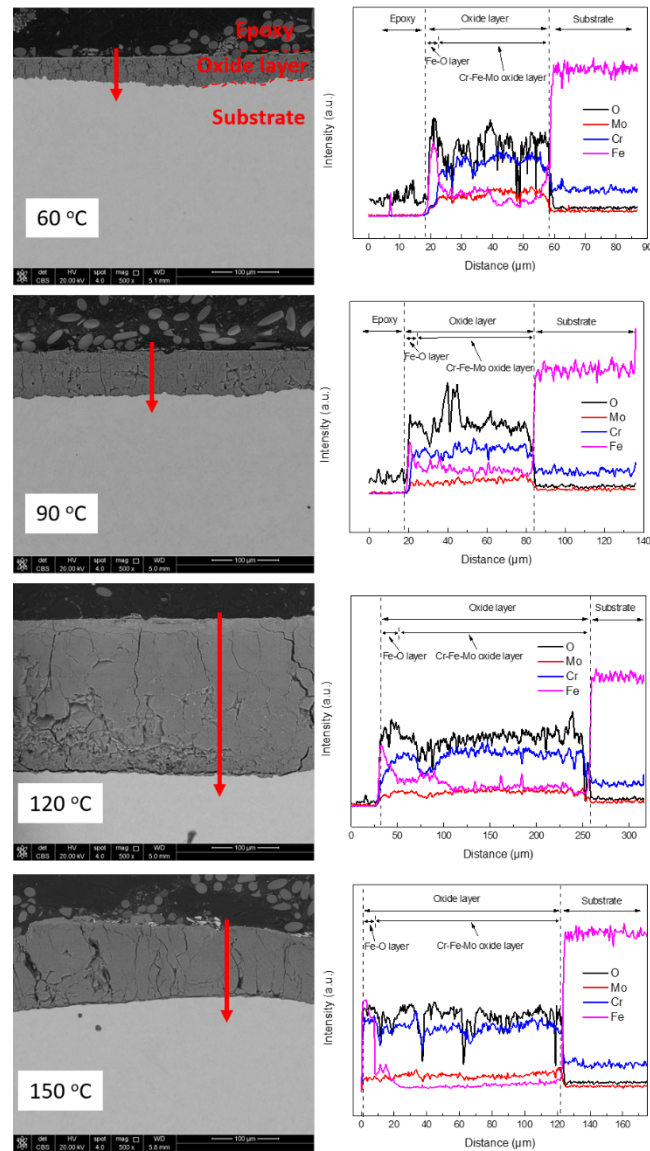


Figure 3-6. Cross-sectional SEM images and EDS line scans of P91 steels after the 720 hours of immersion in condensed phase solution at 60, 90, 120 and 150 °C.
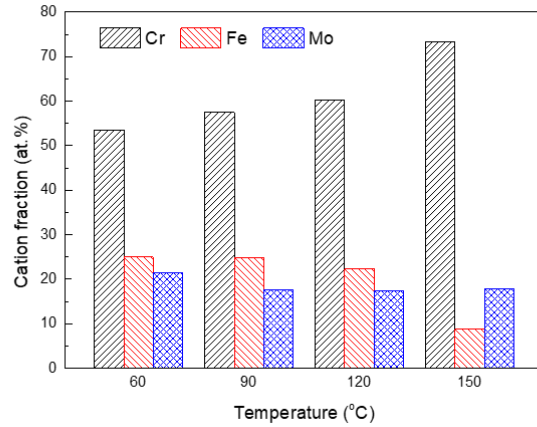
Figure 3-7. Atomic fractions of cations (Cr, Fe and Mo) present in the inner oxide layer on P91 after the 720 hours of exposure to condensed phase solution at 60, 90, 120 and 150 °C.
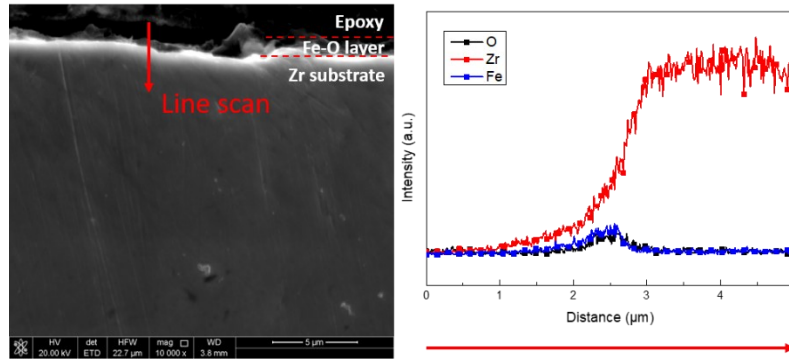


Figure 3-8. SEM cross-sectional image and EDS line scan results of pure Zr after immersion in simulated flue gas condensates together with P91 steel at 90 °C for 120 h.

The nature of the corrosion products formed on P91 shall originate from its relatively low Cr content. According to the previous studies, at least 12 wt.% Cr is needed in Fe-Cr alloys for the formation of a protective Cr-based oxide layer in acid solutions [180, 181]. In the condensed phase solution, major alloying elements in P91 (Fe, Cr and Mo) could be oxidized through [182, 183]:

$$2Fe + 3H_2O \rightarrow Fe_2O_3 + 3H_2 \qquad \text{Reaction 3-1}$$

$$2Cr + 3H_2O \rightarrow Cr_2O_3 + 3H_2 \qquad \text{Reaction 3-2}$$

$$Mo + 2H_2O \rightarrow MoO_2 + H_2 \qquad \text{Reaction 3-3}$$

The estimated negative standard Gibbs energy value of each reaction (shown in Table 3-3) suggests that the oxidation of these alloying elements would be thermodynamically favored. Fe could also react with Mo or Cr to form spinel through the following reactions [184, 185]:

$$Fe + 2Cr + 4H_2O \rightarrow FeCr_2O_4 + 8H^+ + 8e^- \qquad \text{Reaction 3-4}$$
$$2Fe + Mo + 4H_2O \rightarrow MoFe_2O_4 + 8H^+ + 8e^- \qquad \text{Reaction 3-5}$$

Table 3-3. Standard Gibbs energy of Reactions 3-1, 3-2, and 3-3 at 60 and 150 °C, respectively.

|  | $\Delta G^{\emptyset}_{60\,°C}$ | $\Delta G^{\emptyset}_{150\,°C}$ |
|---|---|---|
| Reaction 3-1 | -36.98 | -54.63 |
| Reaction 3-2 | -341.69 | -367.10 |
| Reaction 3-3 | -57.80 | -73.89 |

As a dominant corrosion product, $Fe_2O_3$ could further react with water to form iron oxy-hydroxide, or dissolve into solution via the reaction with $H^+$ [186]:

$$Fe_2O_3 + H_2O \rightarrow 2FeOOH \qquad \text{Reaction 3-6}$$
$$Fe_2O_3 + 6H^+ \rightarrow 2Fe^{3+} + 3H_2O \qquad \text{Reaction 3-7}$$

Since the surface scales formed on DSS 2205 were too thin to be well examined using above cross-sectional SEM/EDS and XRD techniques, XPS technique was thus employed to identify the chemistry of these scales formed after the 720 hours of exposure to condensed phase solution at 60-150 °C. The recorded XPS spectra of Fe 2p$_{3/2}$, Cr 2p$_{3/2}$, Ni 2p$_{3/2}$, Mo 3d are shown in Figure 3-9, respectively. The Fe 2p$_{3/2}$ peaks revealed the presence of three chemical states, including $Fe^0$ (707.5 ± 0.1 eV), $Fe^{2+}$ (708.4 ± 0.1 eV) and $Fe^{3+}$ (710.8 ± 0.2 eV). The $Fe^0$ peak suggests that the thickness of formed surface scales should be at nanometer scale. Increasing temperature resulted in a decrease of $Fe^0$ state and an increase of $Fe^{2+}$ and $Fe^{3+}$ cations. The Cr 2p$_{3/2}$ peaks indicated the formation of $Cr_2O_3$ (576 ± 0.1 eV) and $Cr(OH)_3$ (577.2 ± 0.2 eV), and increasing temperature led to a decrease in $Cr_2O_3$ but an increase in $Cr(OH)_3$. At 150 °C, $Cr(OH)_3$ was the primary oxide present in

the surface scale. The double Mo 3d peaks in Figure 3-9 are related to the spin-orbit coupling of Mo $3d_{5/2}$ and Mo $3d_{3/2}$ [187]. The Mo peaks indicated the two oxidization states, including $Mo^{4+}$ ($229.3 \pm 0.1$ eV for $Mo^{4+}$ $3d_{5/2}$ and $232.4 \pm 0.1$ eV $Mo^{4+}$ $3d_{3/2}$) and $Mo^{6+}$ ($232.5 \pm 0.1$ eV for $Mo^{6+}$ $3d_{5/2}$ and $235.6 \pm 0.1$ eV $Mo^{6+}$ $3d_{3/2}$) in the surface scales on DSS 2205 steel. The $Mo^{6+}$ concentration increased with temperature and became dominant at 150 °C. As for element Ni, only NiO ($853.5 \pm 0.2$ eV) was found. Different from other alloying elements, the increasing temperature only had a marginal effect on the ratio of $Ni^{2+}/Ni^0$ ($852.6 \pm 0.2$ eV). This may be because Ni is less readily oxidized compared to Fe and Cr [188], and also part of NiO could be reduced to Ni during the $Ar^+$ ion sputtering.
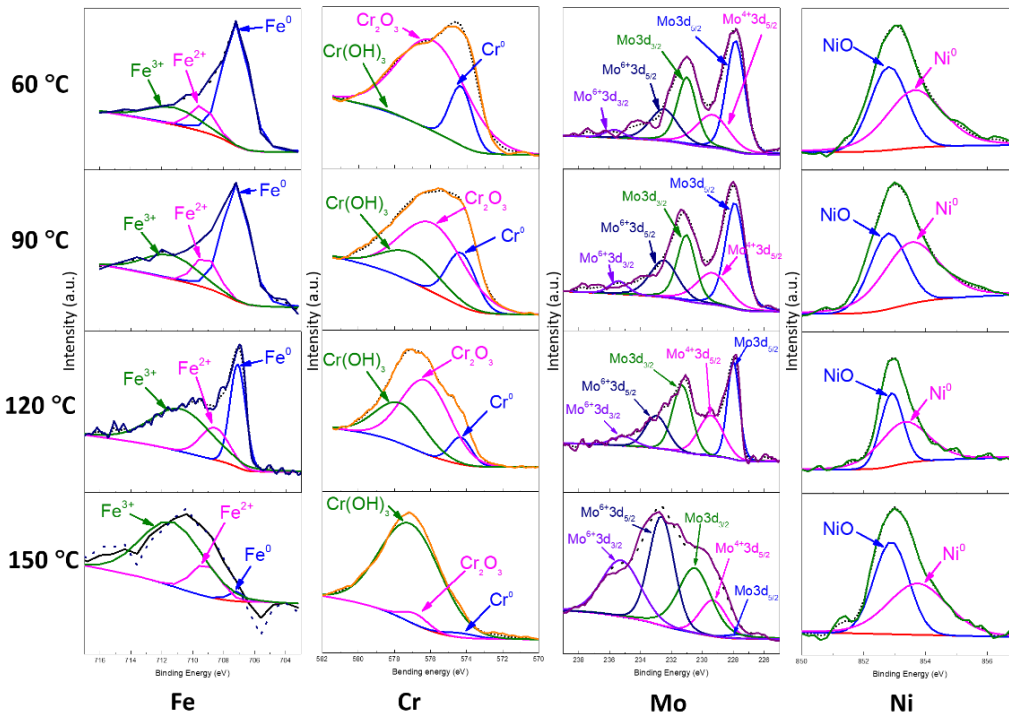


Figure 3-9. XPS spectra of Fe $2p_{3/2}$, Cr $2p_{3/2}$, Ni $2p_{3/2}$, and Mo 3d in the surface scales formed on DSS 2205 after the 720 hours of exposure to condensed phase solution at 60, 90, 120 and 150 °C, respectively.

The XPS spectra of O 1s in Figure 3-10 indicate the existence of three different states, including $O^{2-}$ ($530.1 \pm 0.1$ eV), $OH^-$ ($531.6 \pm 0.1$ eV) and $H_2O$ ($532.7 \pm 0.1$ eV). Note that $H_2O$ may originate from the adsorbed water molecules on the surface [189]. At 60 °C, $O^{2-}$

was the dominant state. Increasing temperature resulted in a decrease of $H_2O$ and an increase in $OH^-$ concentration. At 150 °C, $OH^-$ replaced $O^{2-}$ to be the major state, which was consistent with the observation of high $Cr(OH)_3$ content in the formed surface scale. As $Cr(OH)_3$ is much less protective than $Cr_2O_3$ to the steel substrate [190], the transformation of $Cr_2O_3$ into $Cr(OH)_3$ would result in a remarkable increase in the corrosion rate of the steel.
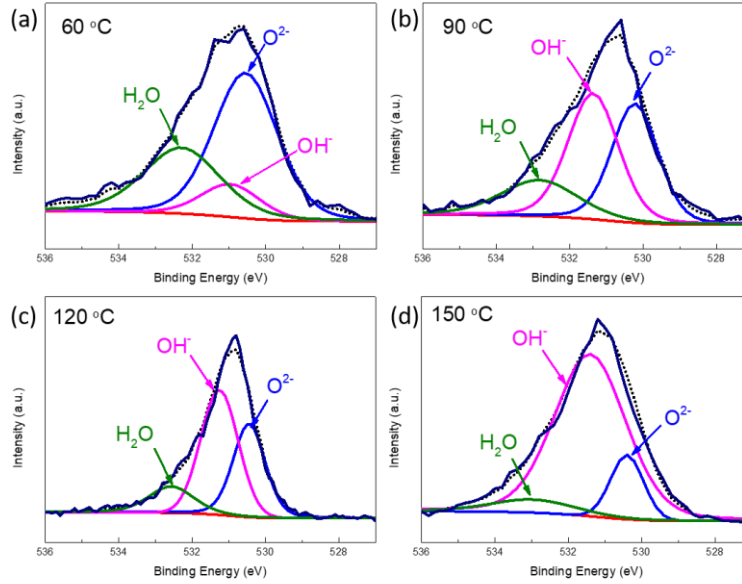


Figure 3-10. XPS spectra of O 1s in the surface scales formed on DSS 2205 steel in condensed phase solution for 720 hours at (a) 60 °C, (b) 90 °C, (c) 120 °C, (d) 150 °C, respectively.

To obtain the depth distribution of cations and anions along the formed oxide layer on DSS 2205, $Ar^+$ ion bombardment technique was applied as mentioned earlier, and the collected depth profiles are shown in Figure 3-11. The following major observations are made:

(1) The surface scales formed are with a double-layer structure including outer Cr-enriched oxide and inner Fe-enriched oxide. The high Cr content (~22.5 wt.%) in DSS 2205 and relatively lower dissolution rate of Cr oxide compared to Fe oxides resulted in the formation of such an outer Cr-enriched oxide layer as a barrier, which was also observed on other Cr-containing steels [191, 192]. Moreover, because of the relatively higher solubility of Fe cations in Cr oxide compared to Ni and Mo cations

[193], part of Fe cations could penetrate into the outer Cr-enriched oxide layer and then partially dissolve into the condensed phase solution via Reaction 3-7, resulting in certain amount of Fe distributed in the outer layer.

(2) Increasing the temperature from 60 to 90 °C only had a marginal effect on the thicknesses of the outer and inner oxide layers. However, further increasing temperature led to a remarkable increase in the thicknesses of the two layers, indicating an enhanced oxide formation. As shown in Figure 3-9, increasing temperature enhanced the transformation from $Cr_2O_3$ into $Cr(OH)_3$, which is with less resistance to the inward oxygen diffusion [194]. Meanwhile, the chemical dissolution of Cr-enriched oxide could also be increased with temperature, especially at temperature > 90 °C, resulting in the increase of cation vacancies in the surface scales and enhancing the outward diffusion of cations. Note that more information about the oxide chemical dissolution can be found in the following section. Based on the Point Defect Model [195], the above two factors would facilitate the oxide formation and growth at higher temperatures.

(3) Accumulation of Ni at the interface of the outer and inner oxide layer was found on the steel corroded at temperature ≤ 120 °C. This may be due to the low solubility of Ni in Cr oxide [193], and such accumulation can hinder the outward diffusion of Fe and Cr [178]. At 150 °C, no Ni accumulation was obverted, possibly due to the relatively high solubility of Ni in $Cr(OH)_3$ and enhanced dissolution of Ni oxide at the interface of oxide/solution. In addition, different from Ni, trace amount of Mo cations was evenly distributed in the formed surface scales. As described above, the presence of Mo in the oxide layers can help increase their stability in the condensed phase solution. The formation of $Mo^{6+}$ could be achieved through the following reaction [196]:

$$Mo + 3H_2O \rightarrow MoO_3 + 3H_2 \qquad \text{Reaction 3-8}$$
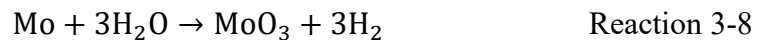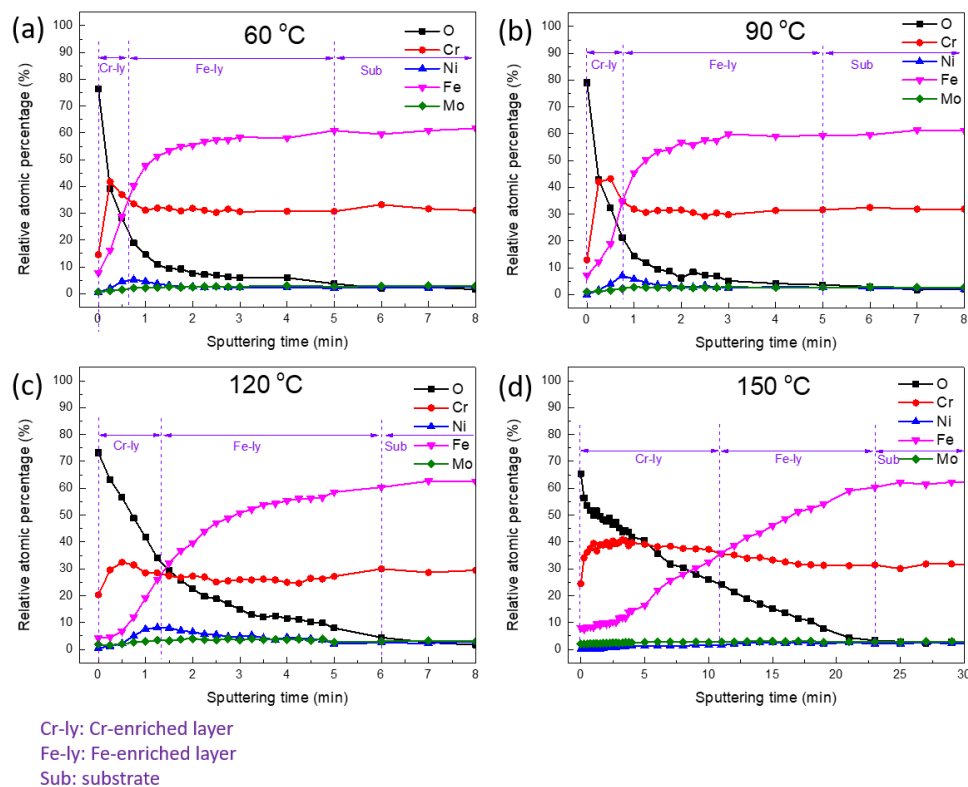
Figure 3-11. XPS depth profiles of O, Cr, Ni, Fe and Mo in the surface oxide scales formed on DSS 2205 after the 720 hours of exposure to simulated flue gas condensates at (a) 60, (b) 90, (c) 120 and (d) 150 °C, respectively.

Because of the high Cr content, a continuous layer of chromium oxides, mainly composed of $Cr_2O_3$ and $Cr(OH)_3$, could be formed on the surface of DSS 2205 in the condensed phase solution. $Cr_2O_3$ could be formed via Reaction 3-2 as described above. The interaction between $Cr_2O_3$ and $H_2O$ would result in the formation of $Cr(OH)_3$ [197]:

$$Cr_2O_3 + 3H_2O \rightarrow 2Cr(OH)_3 \qquad\qquad \text{Reaction 3-9}$$
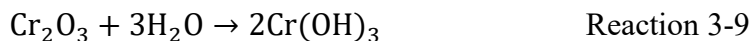
As Reaction 3-9 is an endothermic process, increasing temperature would facilitate the transformation of $Cr_2O_3$ into $Cr(OH)_3$, leading to more $Cr(OH)_3$ in the surface scales.

As the Cr oxides are thermodynamically unstable in the acidic solution with pH=2 [190], considerable chemical dissolution of $Cr_2O_3$ and $Cr(OH)_3$ would occur [198]:

$$Cr_2O_3 + 6H^+ \rightarrow 2Cr^{3+} + 3H_2O \qquad\qquad \text{Reaction 3-10}$$

$$Cr(OH)_3 + 3H^+ \rightarrow Cr^{3+} + 3H_2O \qquad\qquad \text{Reaction 3-11}$$

Due to the presence of $Cr(OH)_3$ and relatively high chemical dissolution of the Cr oxides, the initially formed Cr oxide cannot effectively retard the inward flux of oxygen anions into the interface of the oxide/substrate. With prolonged time, the accumulated oxygen anions would be able to oxidize other alloying elements (Fe, Ni and Mo). Because of the limited solubility of Fe, Ni and Mo cations in Cr oxides, inward diffusion of oxygen anions would be the dominant process [195]. Therefore, these factors would facilitate the formation of inner Fe-enriched oxide layer after the long-term exposure to the condensed phase solution at elevated temperatures, as shown in Figure 3-9 and Figure 3-11.

### 3.3.2. Condensed phase corrosion rates of the steels at oxy-fired PFBC

Figure 3-12 shows the variation of direct mass change of P91 and DSS 2205 with time in simulated flue gas condensates at 60, 90, 120 and 150 °C, respectively. The two steels experienced continuous negative mass change instead of positive mass gain with prolonged time, confirming the occurrence of relatively high chemical dissolution of surface oxide scales, especially on P91 steel, in the condensed phase environments. Moreover, increasing temperature resulted in a remarkable increase in direct mass change, especially at temperatures > 90 °C. After 720 hours of exposure at 150 °C, the direct mass change of P91 was about -186.9 $mg/cm^2$ while that of DSS 2205 only about -0.099 $mg/cm^2$, consistent with previous optical and SEM observations. Based on the corresponding corrosion reactions occurred on the two steels as described earlier, the variation of direct mass change with time was simply fitted by [199]:

$$\frac{\Delta m}{A} = kt^n + b \qquad\qquad \text{Equation 3-6}$$

where $\Delta m$ (mg) is the weight loss of steel during corrosion tests, A ($cm^2$) is the surface area, t (h) is the time, n is the reaction order, k ($mg \cdot cm^{-2} \cdot h^{-n}$) and b ($mg/cm^2$) are the fitting constants. In most cases, the variations followed linear law (n=1) except that of DSS 2205 at 150 °C. At 150 °C, the direct mass change of DSS 2205 exponentially increased with time (n=1.8), which could be attributed to the poor stability and remarkably enhanced dissolution of $Cr(OH)_3$ formed on the steel. Moreover, the k value of P91 was significantly higher than that of DSS 2205 at each temperature, further suggesting that more severe corrosion should occur on P91.
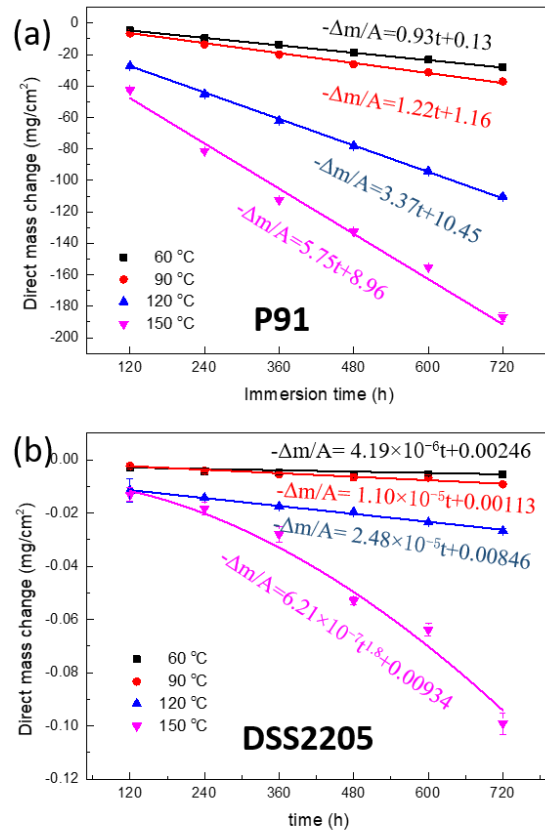
Figure 3-12. Variations of direct mass changes of P91 and DSS 2205 steels with time in condensed phase solution at the temperature range of 60-150 °C.

As described above, the average long-term corrosion rates ($CR_T$) of the steels at different temperatures were determined based on the mass loss measurement results, i.e., the mass changes of the steels before corrosion testing and after 720 hours of exposure and descaling treatment, and the results are shown in Figure 3-13. The corrosion rates of P91 and DSS 2205 increased exponentially with temperature. In aqueous solution, the variation of corrosion rates with temperature is usually governed by Arrhenius law [200]:

$$CR_T = A \cdot e^{-\frac{\Delta E}{RT}}$$
Equation 3-7

where $CR_T$ (mm/y) is the long-term corrosion rate at testing temperature T (K), A is the Arrhenius constant, $\Delta E$ (kJ/mol) is the activation energy and R (8.314 J·K$^{-1}$·mol$^{-1}$) is the gas constant. Thus, the Arrhenius constants and activation energy of the two steels in the condensed solution were estimated by:

For P91, $$CR_T = 12583.75 \times \exp\left(-\frac{28.15}{RT}\right)$$ Equation 3-8

For DSS 2205, $$CR_T = 3228.11 \times \exp\left(-\frac{50.28}{RT}\right)$$ Equation 3-9

Previous studies found that the typical activation energy of diffusion in water was 10-45 kJ/mol [172, 201]. Thus, the obtained apparent active energy of P91 steel further suggested that the corrosion rate-determining step would be the diffusion of certain species through micro-cracks within the surface products (as shown in Figure 3-6). Compared to P91, the higher apparent active energy of DSS 2205 confirmed that the formed surface oxide scales should be able to protect the steel from severe corrosion under the designed operating conditions. This is also consistent with the previous results of Alloy 31 (with 26.75% Cr) for the formation of surface chromium oxide in brine solution [202]. Given that 0.1 mm/y is as the acceptable maximum long-term corrosion rate of flue gas component at power plants [203], the results in Figure 3-13 show that DSS 2205 steel is a promising candidate while the application of P91 shall result in unwanted integrity damage of the components during long-term service.

The noticeable difference between the long-term corrosion rates of the steels with temperature is attributed to the contribution of alloying elements Cr/Mo/Ni to the stability of the formed surface corrosion scales in the condensed phase solution. Cr oxides/hydroxides have much lower dissolution rates compared to iron oxides/hydroxides. For instance, the dissolution rate of $Cr(OH)_3$ ($1.5 \times 10^{-9}$ mol·m$^{-2}$·s$^{-1}$) was found to be almost ten times lower than that of $Fe_2O_3$ ($1.2 \times 10^{-8}$ mol·m$^{-2}$·s$^{-1}$) in 0.01 mol/L $H_2SO_4$ at 65 °C [176]. Thus, Fe oxides would easily dissolve into the condense solution while at least part of Cr-enriched oxide layer could remain on the steels as a protective barrier [204]. Moreover, as shown in Figure 3-13, a sharp increase in the corrosion rates of the steels occurred at temperature > 90 °C. Previous studies also reported that some Cr-bearing alloys suffered enhanced corrosion in acidic solutions at temperatures above critical points [163, 205, 206]. For example, Sanicro 28 steel, a high-alloy austenitic stainless steel originally developed for use in the manufacture of phosphoric acid, experienced accelerated corrosion in 50 wt.% $H_3PO_4$ solution at temperature > 60 °C [205]. In HCl/$H_2SO_4$/$HNO_3$ mixed

solution, the corrosion rate of Alloy 22 increased almost linearly once the temperature exceeded 50 °C [206]. Thus, the critical temperature point in the condensed phase solution is likely to be around 100 °C.

As mentioned previously, increasing temperature led to a remarkable increase in the oxidation of P91 steel due to the presence of micro-cracks within the oxide and considerable enhancement of DSS 2205 steel because of the transition of surface oxides into the less stable ones. Besides, increasing temperature may change related electrochemical reaction pathways (such as cathodic hydrogen or oxygen reduction) and consequently result in higher corrosion rates of steels [163, 206]. For example, the previous study found that the oxygen reduction became more pronounced on DSS 2507 with increasing temperature in an acid solution [163]. However, these factors are insufficient to formulate the relationship of corrosion rates with temperature as shown in Figure 3-13. In fact, the influence of temperature on the chemical dissolution of the oxides cannot be ignored, especially when the solution temperature is higher than 90 °C. Previous investigations indicated that the variation of dissolution rates of Fe oxides and Cr oxides with temperature could follow [207]:

$$D_{rate} = kc(H^+)^n e^{-\frac{E}{RT}} \hspace{2cm} \text{Equation 3-10}$$

where $D_{rate}$ is the dissolution rate of a metal oxide, k is the rate constant, $c(H^+)$ is the concentration of $H^+$, n is the order of reaction, E (J/mol) is the active energy, R (8.314 kJ/mol) is the gas constant and T (K) is the temperature. It suggests that the influence of temperature on the chemical dissolution of surface oxides would be a dominant factor in the long-term corrosion rates of the steels in the condensed phase solution.
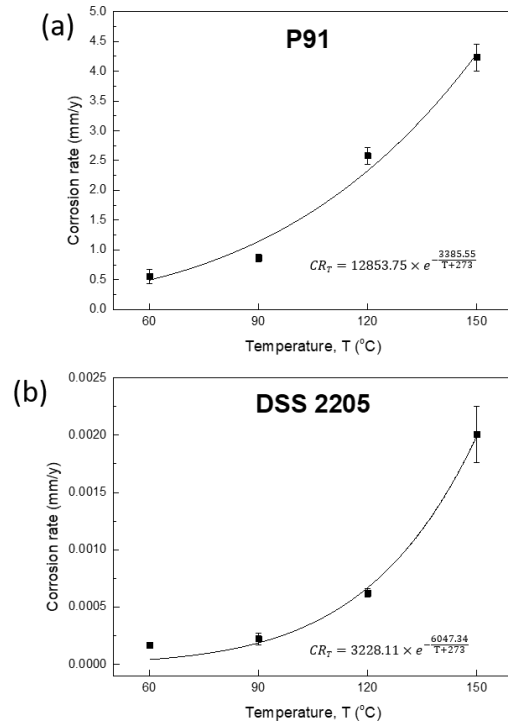
Figure 3-13. Variations of long-term corrosion rates of (a) P91 and (b) DSS 2205 steels with temperature in simulated condensed phase solution of oxy-fired PFBC.

## 3.4. Conclusions

Long-term condensed phase corrosion behaviors of P91 and DSS 2205 at oxy-fired PFBC plants were investigated, and it is found that the two steels experience considerable oxide formation and chemical dissolution in the simulated condensed phase solution at 60-150 °C. No obvious pits are found on the steels even after the 720 hours of exposure to the solution at 150 °C. The porous oxide layer formed on P91 was mainly composed of outer Fe-enriched and inner Cr-Mo-Fe enriched oxides (including FeOOH, $Fe_2O_3$, $FeCr_2O_4$ and $MoFe_2O_4$). The relatively compact oxide scales on DSS 2205 are composed of an outer Cr-enriched and inner Fe-enriched oxide. Increasing temperature facilitates the transformation of $Cr_2O_3$ to $Cr(OH)_3$. Both Cr and Mo are helpful to improve the corrosion resistance. Increasing temperature results in an exponential increase in their long-term corrosion rates. Compared with P91, DSS 2205 exhibits a much better long-term corrosion resistance and is a promising candidate for the construction of flue gas components at oxy-fired PFBC system.

# Chapter 4. Corrosion of Duplex Stainless Steel 2205 in Hot Flue Gas Environments Produced at Advanced Oxy-fired Pressurized Fluidized Bed Combustion Plants

**Abstract**

The selection of appropriate alloys for the construction of flue gas components is one of the crucial steps for the successful deployment and long-term safe operation of the newly developed oxy-fired pressurized fluidized bed combustion (oxy-fired PFBC) plants. In this study, the corrosion performance of a candidate steel, duplex stainless steel 2205 (DSS 2205) was investigated in simulated flue gas mainly composed of $CO_2/H_2O/O_2/N_2/SO_2/HCl$ with a total pressure of 1.50-1.64 MPa at 270 and 320 °C, respectively. In the hot gas, the oxidation kinetics of DSS 2205 followed parabolic law, and the formed surface oxide layer was a double-layer structure with outer Fe-rich oxide and inner Cr-rich oxide layer along with the enriched Si distributed at the interface of oxide and substrate. Besides general oxidation, $SO_2$ and HCl-induced pitting also occurred on the steel. Increasing temperature led to an increasing general oxidation rate and accelerated pitting. Extending exposure duration resulted in an increase in pit density, but did not noticeably affect the maximum pit depth. These results indicate that the steel is a promising candidate for further pilot- and industrial-scale assessments.

**Keywords**: Hot flue gas; Corrosion; Pressurized oxy-fuel combustion; Duplex stainless steel.

## 4.1. Introduction

Background information of oxy-fired PFBC system is referred to Section 1.2.

The hot flue gas emitted from an oxy-fired PFBC plant is mainly composed of $CO_2$ and $H_2O$, along with certain amounts of oxygen (up to 4%), sulfur oxides and HCl [208]. Results of campaign operations at pilot-scale oxy-fired PFBC plants indicated that the pressure and chemistry of the exhaust flue gas were noticeably different from that produced from conventional air combustion plants [209, 210], introducing the concern of which

alloys are suitable for the construction of plant flue gas components [40]. At the oxy-fired PFBC plants, the flue gas components behind the combustion chamber, such as E-filter and hot recirculation path, likely experience the hot gas corrosion in the temperature range of 200-400 °C [208]. According to our literature review, very little information is available to describe alloys' performance in such flue gas environments. Only one group studied the corrosion of several ferrite steels (P11, T24) and ferrite-martensite steels (T91, T92, X20 and VM12) in simulated oxy-fuel flue gas mixtures composed of $CO_2$-$H_2O$-$O_2$-$SO_2$ (67-30-2-1 mol%) or $CO_2$-$H_2O$-$O_2$-$SO_2$ (46.7-50.9-1.9-0.5 mol%) at the temperature range of 170-650 °C [208, 211]. Some low alloyed steels with Cr contents less than 10%, like P11, T24, T91 and T92, show poor corrosion resistance in the hot gas mixture at 300 °C due to the direct reaction between steels and corrosive agents ($SO_2$, $H_2O$ and $O_2$) in the hot gas [208]. Therefore, it is necessary to assess the candidate alloys with higher Cr contents since the corrosion-induced failure of flue gas components remains one of the serious concerns for the long-term safe operation of the combustion plants [212].

High Cr% duplex stainless steels (DSSs) with a balanced austenitic-ferritic crystal structure are likely the promising candidates for the construction of oxy-fired PFBC flue gas components behind the combustion chamber. Background information of DSS could be found in Section 1.4. In recent years, corrosion behaviors of DSSs have been intensively investigated in low-temperature (<200 °C) aqueous solutions and high-temperature (800-1200 °C) gaseous environments. Generally, in acid or Cl$^-$ containing solutions, DSSs have the ability to form a stable passive film, which is mainly composed of chromium oxide or hydroxide to resist aggressive ion attack [213, 214]. Inclusions (such as MnS) could reduce the corrosion resistance by advancing the formation of weak points on surface oxide film and consequently enhancing pitting susceptibility. Till today, some high-temperature studies have been carried out at the temperatures > 900 °C for several hours to simulate the industrial hot processing environments. In high-temperature air (900-1100 °C), the synergistic effects of $MoO_3$ volatilization, molten molybdate dissolution reaction and air-nitriding can promote catastrophic oxidation of DSS S32707 [215]. Another study found that the oxidation behaviors of DSSs S32101 and S2304 in air or simulated industrial reheating atmosphere at 1050 °C likely followed either parabolic

law or breakaway oxidation, which was inherently related to Mn contents in the steels [216]. After about 2 h oxidation at 1050 °C, the oxide formed on S32101 was a triplex layer structure (inner: $\alpha$-$Fe_2O_3$ + $Mn_3O_4$ + $Fe_3O_4$ and $\gamma$-$Fe_2O_3$, middle: $Cr_2O_3$ + $Fe_3O_4$, and outer: $\gamma$-$Fe_2O_3$ + $Fe_3O_4$ + $Mn_3O_4$) while the surface scale grown on S32304 was a duplex layer (inner: $Cr_2O_3$, outer: $Fe_3O_4$) [216]. In 1220 °C air, the variation of weight gain of DSS 2205 with time initially followed parabolic law and then changed to a linear relationship [217]. Surprisingly, few studies have been performed on DSSs in the temperature range of 200-400 °C. One study reported that DSS 2205 only experienced imperceptible oxidation after the 2 h exposure to air at 350 °C [209]. Donik et al. [77] found that iron oxide ($Fe_2O_3$) was the major product formed on DSS 2205 after the 100 s exposure to 75 Pa oxygen plasma. Clearly, the information is insufficient to determine whether DSS 2205 is suitable for the hot flue gas environments from a corrosion perspective.

Therefore, the main objectives of this study are to investigate corrosion performance of a typical DSS, DSS 2205, in the simulated hot flue gas at the oxy-fired PFBC plant to determine whether it is suitable for the flue gas component construction, and to advance fundamental understanding of how DSS corrode in the temperature range of 200-400 °C and what roles the gas species ($H_2O$, $CO_2$, $O_2$, HCl and $SO_2$) play in the corrosion process. It is anticipated to support, at least in part, the development of materials selection strategy for the successful deployment of oxy-fired PFBC technologies in global and Canadian energy sectors.

## 4.2. Experimental procedure

### 4.2.1. Testing sample preparation

The material used in this study was cut from a commercial 26 mm thick DSS 2205 plate with the fabrication history of hot rolling + 1 h of solution annealing at 1338 K + water quenching and the chemical composition of 22.54% Cr, 3.03% Mo, 5.61% Ni, 1.17% Mn, 0.42% Si, 0.02% C, 0.001% S, 0.08% Co, 0.11% Cu, 0.001% S and bal.% Fe (all in wt.%). Detailed coupon preparation methods could be seen found in Section 3.2.1.

### 4.2.2. Autoclave corrosion testing methodology and procedure

Hot gas corrosion tests were carried out in a 2 L Parr autoclave made of SS 316L. Figure 4-1 is a schematic of the experimental setup. Sixteen freshly-prepared coupons were accommodated on a custom-made holder made of alumina. A vial with 3.44 mL HCl solution (0.018 mol/L) was also set on the holder to supply the required amounts of HCl and $H_2O$ at testing temperatures. After that, the autoclave was sealed for leaking testing. If no leaking occurred, the autoclave was purged with $N_2$ to remove the air and then charged with required amounts of gases, including $N_2$, $CO_2$, $SO_2$ and $O_2$, as shown in Table 4-1. A digital pressure gauge was applied to monitor and control the pressure of each charged gas. The total pressure of flue gas was designed to be 1.50 MPa at 270 °C and 1.64 MPa at 320 °C, respectively, to simulate the operating conditions of pressurized flue gas at pilot-scale oxy-fired plants [218]. After about 150 h exposure at a designed temperature, the autoclave was powered off and cooled down to room temperature. The gas mixture was quickly analyzed using a portable toxic gas monitor, purified using 1 M NaOH solution, and discharged into the air. After the degassing, $N_2$ was used to purge the autoclave for about 10 minutes. Finally, the autoclave was opened and the steel coupons were taken out for direct mass change measurement. Four coupons were selected for subsequent corrosion product characterizations and mass loss measurements. The remaining coupons were allocated back into the autoclave for the next exposure (150 hours) under the same condition. To investigate the long-term corrosion of the steel, the tests of four thermal cycles (total 600 h exposure) were conducted at 270 °C and 320 °C, respectively.
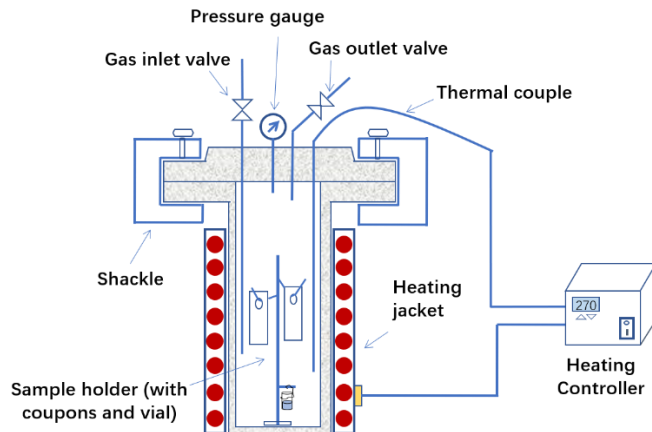


Figure 4-1. Schematic of autoclave experimental setup. Sixteen coupons were used for a test of four thermal cycles. 4 coupons were removed from the autoclave after each cycle.

Table 4-1. Chemical composition of flue gas used for the tests at 270 and 320 °C.

| Gas types | $CO_2$ | $H_2O$ | $N_2$ | $O_2$ | $SO_2$ | HCl |
|-----------|--------|--------|-------|-------|--------|-----|
| Content (mol.%) | 66.4 | 31 | 0.45 | 2 | 0.05 | 0.1 |

### 4.2.3. Corrosion rate assessment and corrosion products characterization

Two mass change measurement techniques were applied to evaluate the corrosion rates of the steel in the hot flue gas. The first is a direct mass change measurement conducted directly on each coupon before and after an autoclave test. This method developed for corrosion rate evaluation is based on the assumption that surface oxide formation would be the dominant reaction on the steel during autoclave testing. The mass gain rate of a test coupon is calculated as the amount of mass gain per exposure duration and surface area unit. In this study, the coupon with the mass gain rate closest to the average one in a given replicate set after an autoclave exposure was selected for subsequent corrosion product characterization.

The second method of mass change measurement is to measure mass loss, which involves two major steps: (a) descaling the formed surface corrosion product on an alloy coupon based on ASTM-G1 (standard practice for preparing, cleaning, and evaluating corrosion test specimens) [109, 219]; and (b) weighing the mass change of the coupon before autoclave testing and after descaling. Descaling can be achieved by immersing the coupons in specific chemical solutions which do not corrode the coupon substrates, but effectively remove the formed corrosion products through chemical dissolution reactions. In this study, the descaling was achieved by immersing the corroded coupons in solution A (2% citric acid + 5% dibasic ammonium citrate + 0.5% disodium EDTA) for 30 minutes at 90 °C and solution B (0.5% potassium permanganate + 2% caustic soda) for 5 minutes at 90 °C, followed by 15 minutes of ultrasonic cleaning in methanol. The coupons were then immersed in solution A again at 90 °C for 15 minutes and weighed. The above immersion treatment process was applied repeatedly until the mass of the coupon reached a constant value. Note that the descaling procedure has been demonstrated to effectively remove the oxide scale formed on Fe-based and Ni-based alloys in other corrosion tests [220]. The

average corrosion rate (in μm/y) of the steel was thus calculated by [221]:

$$\text{Corr. rate} = \frac{8.76 \times 10^7 \times \Delta W}{A\rho t} \qquad \text{Equation 4-1}$$

where $\Delta W$ (g) is the mass loss of coupon before autoclave testing and after descaling; $A$ (cm$^2$) is the exposed surface area of each coupon; $\rho$ (g/cm$^3$) is the density of the alloy; $t$ (h) is the testing duration.

After an autoclave test, light optical microscopy was employed primarily to quickly examine the surface morphology of corroded coupons. The coupons were then selected based on the direct mass change measurement results and characterized using Scanning Electron Microscope (SEM) with Energy Dispersive Spectroscopy (EDS), Focused Ion Beam (FIB), and Transmission Electron Microscopy (TEM) techniques. SEM/EDS characterizations were conducted using a field-emission SEM machine (FEI NOVA230) equipped with a thin window energy-dispersive X-ray spectrometer. TEM samples were prepared using FIB operation from the top surface of the coupon. Before FIB operation, a Pd+Au layer, followed by a Pt layer, was plated on the coupons in vacuum to protect the formed surface oxide layer. High-angle annular dark-field (HAADF), element distribution mapping and EDS analyses were performed on the TEM samples by a FEI TECNAI OSIRIS machine equipped with super X-field emission gun (FEG) and X-ray detection technology at 200 kV.

## 4.3. Results and discussion

### 4.3.1. Post-mortem characterization of corroded steels

Figure 4-2 shows the photographic images of DSS 2205 coupons before and after exposure to the simulated flue gas at 270 and 320 °C, respectively. All before-exposure images readily show mechanical abrasion features from the surface preparation that was applied to each coupon. In contrast, all after-exposure images show the formation of a relatively adherent yellow surface scales, implying that the samples would experience oxidation in the hot gas. Moreover, several dark brown spots were observed on the corroded steel coupons, which may be attributed to localized corrosion induced by HCl and SO$_2$. Furthermore, the steel surface became dark yellow with an increase in exposure duration or temperature. The color roughly reflected the thickness of formed corrosion products, i.e.,

dark yellow color implied the formation of thicker oxide compared to light yellow color. Increasing temperature or exposure time also likely resulted in an increase in the density of localized corrosion spots.
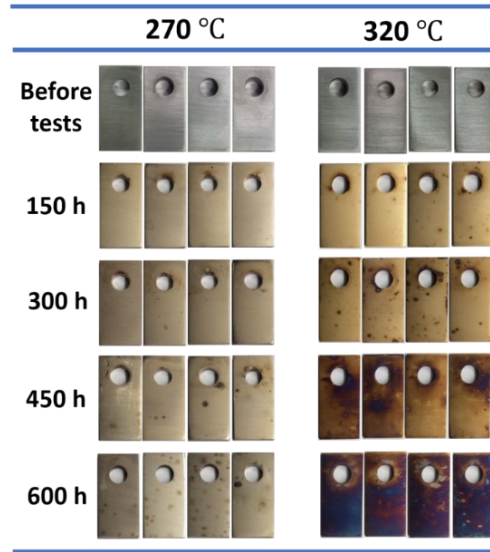


Figure 4-2. Photographic images of DSS 2205 coupons before and after exposure to simulated flue gas at 270 and 320 °C, respectively.

The SEM images of corroded DSS 2205 samples are shown in Figure 4-3. On the surfaces of all tested samples, the lines generated by mechanically polishing prior to corrosion testing are still visible even after 600 hours exposure at 320 °C, suggesting that the steels would experience relatively slow general oxide formation processes in the hot flue gas and such processes should unlikely introduce severe integrity damage of the steel. Besides general oxidation, pitting, a form of localized corrosion (as shown with the red arrow in Figure 4-3), also took place on DSS 2205 and intensified with increasing temperature or extending exposure time. Based on ASTM G46-94 (Standard guide for examination and evaluation of pitting corrosion) [222], the pit density, maximum pit depth and pit diameter at different temperatures were determined from at least three randomly chosen areas on the surface and their variations with time are shown in Figure 4-4. In Figure 4-4(a), the pit density exhibited exponential increase with time, and increasing temperature also resulted in higher density. Besides, the maximum pit depth (Figure 4-4(b)) and average pit diameter (Figure 4-4(c)) also increased with temperature [222]. For instance, the maximum pits

formed at 320 °C was about 2.8 μm in depth and 18.6 μm in diameter, while the one formed at 270 °C was about 2.4 μm in depth and 9.2 μm in diameter. Previous studies also found that stainless steels tend to experience an intensified pitting attack with increasing temperature [223, 224]. However, the maximum pit depth and pit diameter did not change significantly with time.
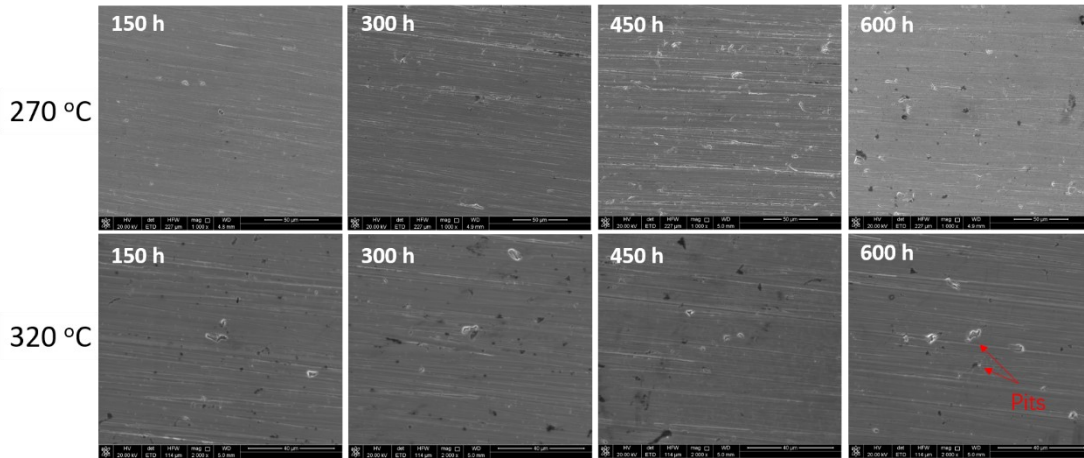


Figure 4-3. SEM images of DSS2205 steels corroded in the simulated flue gas environment at 270 and 320 °C, respectively.
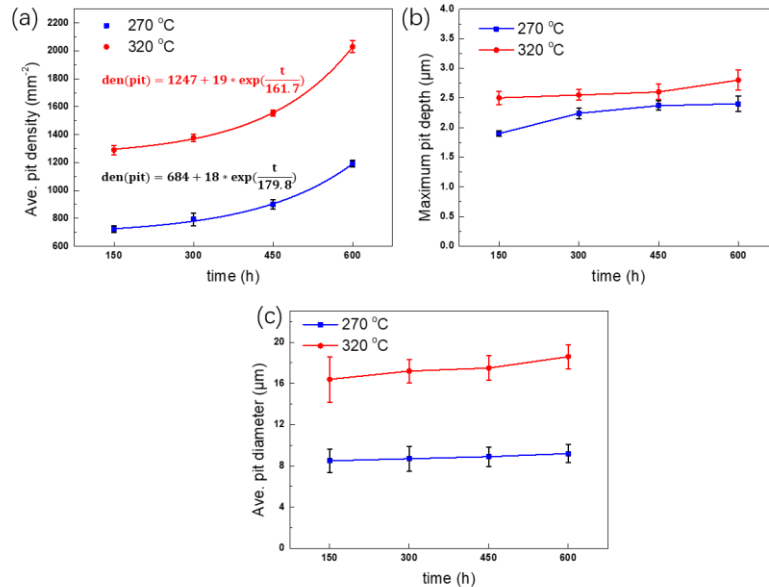


Figure 4-4. Variation of (a) average pit density, (b) maximum pit depth and (c) average pit diameter with time in the simulated hot flue gas mixture at 270 and 320 °C.

Further, SEM/EDS examinations were conducted on the pits formed on DSS 2205 after 600 hours tests at 270 and 320 °C and the results are shown in Figure 4-5. At both temperatures, EDS mapping images show that the elements S, Cl and O are enriched at pits while the alloying elements are noticeably scarce, suggesting that pitting may be initiated and propagated because of the presence of $SO_2$ and HCl at elevated temperatures.
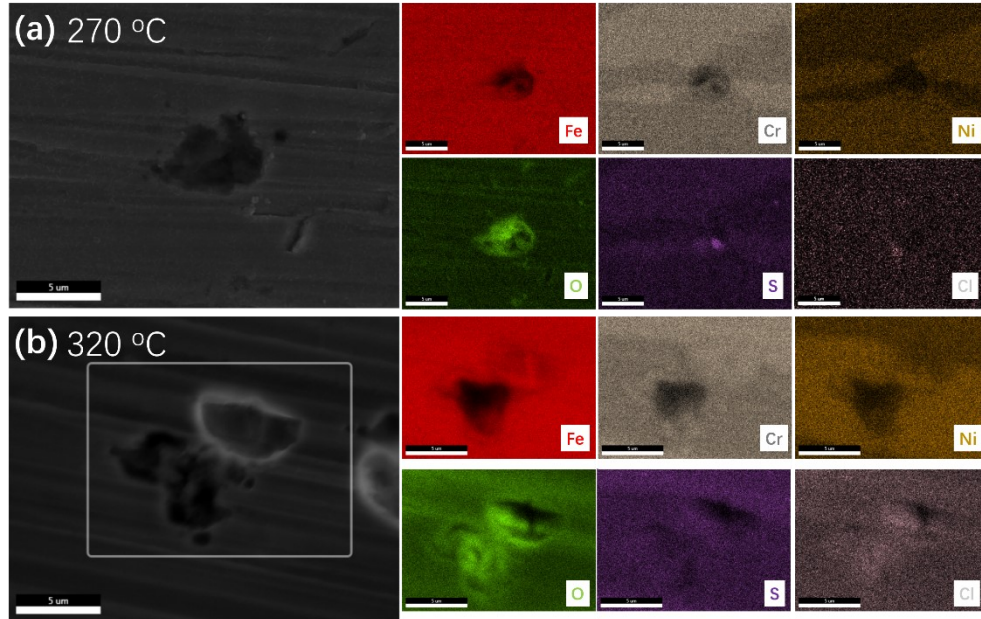


Figure 4-5. EDS mapping analyses of typical pitting on DSS 2205 after 600 hours exposure at different temperatures (a) 270 °C and (b) 320 °C.

Previous studies show that HCl could induce localized corrosion by reacting with metal or metal oxides [40]. Based on the temperature range and gas concentration in the present test, thermodynamic calculation shows that HCl in flue gas could only react with metal instead of metal oxides, as shown in Table 4-2 (calculated with HSC software [225]). Further comparison of Gibbs Free Energies of metal + HCl and metal + $O_2$ (ΔG values are shown in Table 4-7 as below) shows that the reactions between metal and $O_2$ will be more favorable than those between metal and HCl in current testing environments. However, HCl might penetrate into the underlying substrate through some weak points on the steel surface, like grain boundaries and inclusions where the formed oxides are nonprotective [174], resulting in the formation of metal chlorides [226]. Besides, in the presence of excess

$O_2$, HCl could be oxidized into $Cl_2$, which might also corrode metal through a series of processes called active oxidation [227]. Once the $Cl_2$ is formed, it may attack the metal substrate by penetrating the oxide scale, leading to the formation of metal chlorides. These metal chlorides could be further oxidized by oxygen to form corresponding metal oxides at the interface of oxide/flue gas [228]. According to previous studies, the Cl-induced corrosion is prominent at the temperatures higher than 500 °C [229]. In the testing temperature range, the Cl-induced attack causes only limited pitting and shall not be a big concern.

Table 4-2. Gibbs Free Energy of reactions between HCl and metal or metal oxides in the simulated flue gas environment at 270 and 320 °C.

| Reaction | $\Delta G$ (kJ/mol) | |
|---|---|---|
| | 270 °C | 320 °C |
| $\frac{1}{2}Fe + HCl(g) \rightarrow \frac{1}{2}FeCl_2 + \frac{1}{2}H_2(g)$ | -18.94 | -14.20 |
| $\frac{1}{3}Cr + HCl(g) \rightarrow \frac{1}{3}CrCl_3 + \frac{1}{2}H_2(g)$ | -31.39 | -25.95 |
| $\frac{1}{6}Fe_2O_3 + HCl(g) \rightarrow \frac{1}{3}FeCl_3 + \frac{1}{2}H_2O(g)$ | 30.10 | 34.42 |
| $\frac{1}{8}Fe_3O_4 + HCl(g) \rightarrow \frac{1}{4}FeCl_3 + \frac{1}{2}H_2O(g) + \frac{1}{8}FeCl_2$ | 23.46 | 27.95 |
| $\frac{1}{6}Cr_2O_3 + HCl(g) \rightarrow \frac{1}{3}CrCl_3 + \frac{1}{2}H_2O(g)$ | 28.26 | 33.33 |

Sulfur oxides are also the corrosive components in flue gas. $SO_2$ could penetrate into the oxide layer through solution-diffusion or molecular gas permeation mechanisms [230], causing corrosion of alloy by oxidation and sulfidation [40] and turning metals into their corresponding oxides, sulfides and sulfates [231, 232], as shown in Table 4-3. Although $SO_2$ could cause sulfidation and oxidation on metallic components like Fe and Cr, it cannot react with metal oxides such as $Fe_2O_3$ and $Cr_2O_3$ since these reactions are thermodynamically unfavored. Therefore, $SO_2$ might induce corrosion to substrate metal by penetration through the active sites (inclusions and grain boundaries) on the surface

[174]. A comparison of $\Delta G$ from the reactions induced by $SO_2$ (Table 4-3) and HCl (Table 4-2) reveals that $SO_2$ is likely to be more aggressive than HCl due to more negative Gibbs Free Energy.

Table 4-3. Gibbs Free Energy of reactions between $SO_2$ and metal or metal oxides in the simulated flue gas environments at 270 and 320 °C.

| Reactions | $\Delta G$ (kJ/mol) | |
| --- | --- | --- |
| | 270 °C | 320 °C |
| $\frac{7}{3}Fe + SO_2(g) \rightarrow \frac{2}{3}Fe_2O_3 + FeS$ | -230.19 | -220.52 |
| $\frac{5}{2}Fe + SO_2(g) \rightarrow \frac{1}{2}Fe_3O_4 + FeS$ | -245.13 | -236.09 |
| $2Cr + SO_2(g) \rightarrow \frac{2}{3}Cr_2O_3 + \frac{2}{3}Cr_2S_3$ | -456.45 | -445.98 |
| $Fe + SO_2(g) + O_2(g) \rightarrow FeSO_4$ | -410.12 | -391.02 |
| $\frac{2}{3}Fe + SO_2(g) + O_2(g) \rightarrow \frac{2}{3}Fe_2(SO_4)_3$ | -337.19 | -317.42 |
| $\frac{2}{3}Cr + SO_2(g) + O_2(g) \rightarrow \frac{1}{3}Cr_2(SO_4)_3$ | -439.30 | -419.17 |
| $\frac{2}{9}Fe_2O_3 + SO_2(g) \rightarrow \frac{2}{9}Fe_2(SO_4)_3 + \frac{1}{3}1.5S$ | 29.14 | 39.81 |
| $\frac{2}{9}Cr_2O_3 + SO_2(g) \rightarrow \frac{2}{9}Cr_2(SO_4)_3 + \frac{1}{3}S$ | 30.55 | 41.7 |

The detected Cl and S in Figure 4-5 from pitting sites are believed to come from the corrosion products. The entire pitting process could be depicted as follows: metal oxide layer forms on the surface of DSS 2205 upon exposure to hot flue gas. The formed continuous metal oxide layer could serve as a protective barrier to prevent the substrate from further attack. However, $SO_2$ and HCl might penetrate into the substrate through the active sites on the surface and react with substrate metals like Fe and Cr. Increasing temperature will facilitate the attack from $SO_2$ and HCl due to higher diffusivity of gaseous

SO$_2$ and HCl, higher tendency of the oxide layer to incorporate acid gas molecules and higher localized defect density in the oxide layer [174], thus resulting in higher pitting density, larger pit diameter and deeper maximum pit depth [233]. Increasing time, however, could only cause higher pitting density while the pit diameter and maximum pit depth did not vary too much. One possible explanation is that the high Cr content in DSS 2205 could help to resist the attack from SO$_2$ and HCl. Even with the localized breakdown, a new protective oxide layer could be quickly formed on the inner surface of the pit to restrict the further attack.

Besides the HCl and SO$_2$-induced localized breakdown as pitting, general oxidation occurs in the major area of the surface. FIB/TEM examinations were thus conducted to examine the nature of formed oxide scales on DSS 2205, and the results are shown in Figure 4-6. In the hot flue gas, the thin oxide scales formed under all conditions were below 50 nm with a duplex structure, which was composed of an outer Fe-rich oxide and an inner Cr-rich oxide. It is found that increasing temperature has an impact on the oxide layer, including its thickness, chemistry and sublayer. As shown in Table 4-4, increasing temperature from 270 to 320 °C resulted in the almost doubled thickness of both outer Fe-rich and inner Cr-rich oxide layers. Meanwhile, both the Fe-rich oxide and Cr-rich oxide layers exhibit limited growth of less than 2 nm with the testing time extended from 300 to 600 h.

Table 4-4. The thickness of surface oxide layer formed on DSS 2205 after corrosion at 270 and 320 °C for different times.

| Thickness (nm) | 270 °C | | 320 °C | |
|---|---|---|---|---|
| | 300 h | 600 h | 300 h | 600 h |
| Fe-rich oxide | 12.6 | 13.6 | 24.6 | 26.9 |
| Cr-rich oxide | 5.0 | 5.4 | 9.6 | 10.2 |
| Whole scale | 17.6 | 19.0 | 34.2 | 37.1 |

Fe-O: Fe-rich oxides
Cr-O: Cr-rich oxides
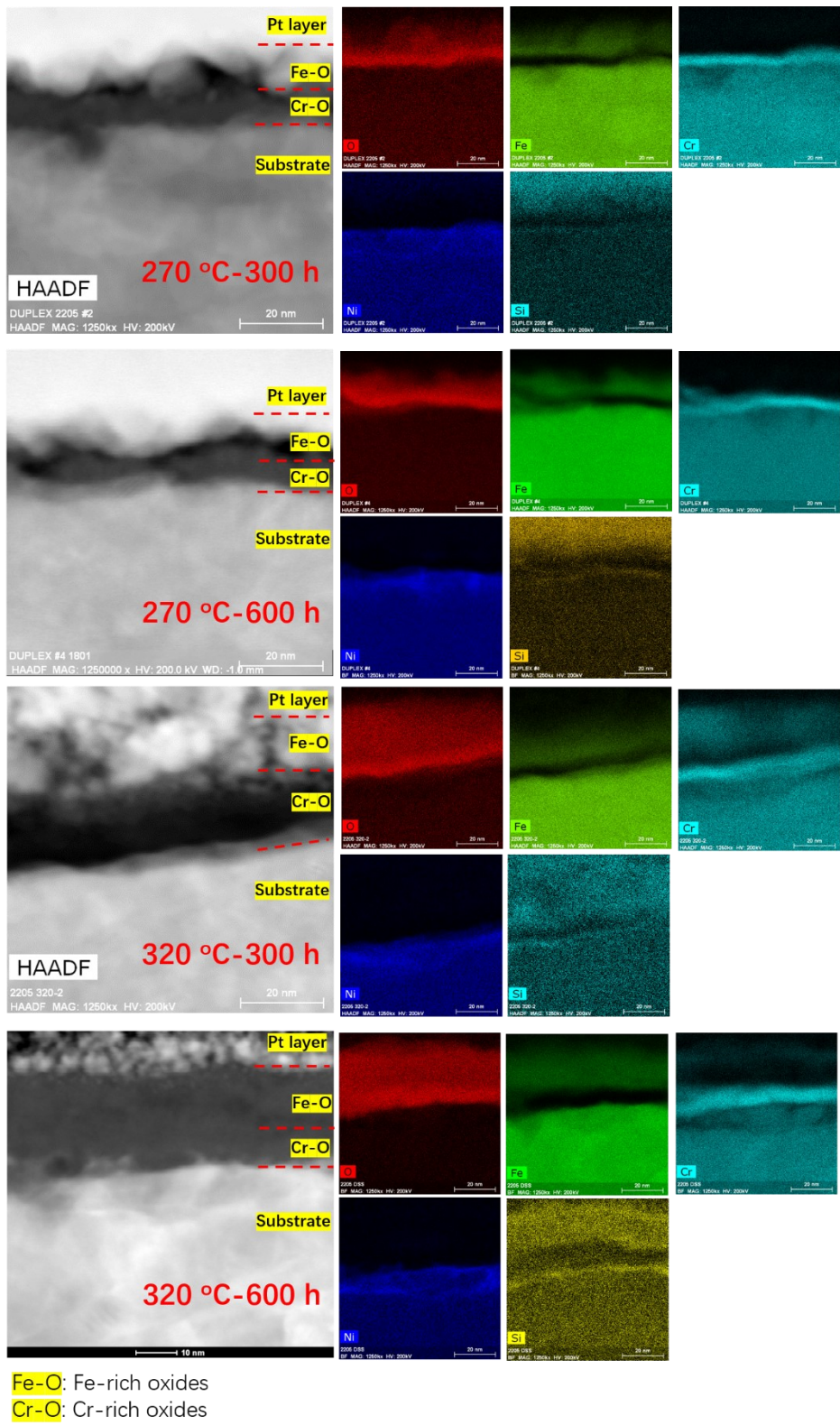
Figure 4-6. TEM cross-sectional images and EDS mappings of DSS 2205 after 600 hours' corrosion in simulated flue gas at 270 °C and 320 °C.

The phases of oxide scales were also identified. Selected area electron diffraction (SAED) showed that the whole oxide layer was amorphous in nature, so EDS point analyses were applied to identify the phase from stoichiometry point of view and the results are shown in Table 4-5. The inner chromium-rich oxide layers formed at both temperatures have an approximate Cr/O atomic ratio of 2:3, indicating the formation of $Cr_2O_3$. On the other hand, the Fe/O ratio of the iron-rich oxide layers increased from 0.67 to 0.79 when the temperature raised from 270 to 320 °C. Based on the Fe/O ratio of several iron-oxides, it is concluded that the iron-rich oxide formed at 270 °C is predominantly $Fe_2O_3$ and increasing temperature led to the transition from $Fe_2O_3$ to $Fe_3O_4$. Besides, a Cr-depletion layer was formed underneath the interface of oxide scale/substrate, and its thickness increased from < 5 nm to ~10 nm when the temperature increased from 270 to 320 °C. During oxidation, while chromium diffused toward the oxide interface to form the chromium oxide, the chromium from the substrate materials failed to diffuse outward at the same rate, forming a lower Cr concentration zone as Cr-depleted layer. It can be concluded that the thicker Cr-depleted layer at 320 °C is related to the higher outward diffusion rate of Cr with elevated temperature.

Table 4-5. Fe/O ratio of several iron oxides and the outer iron-rich oxide layer of DSS 2205 after 600 hours' corrosion at 270 and 320 °C.

| Oxide type | FeO | Fe₃O₄ | Fe₂O₃ | Fe-rich oxide | |
|---|---|---|---|---|---|
| | | | | 270 °C | 320 °C |
| Fe/O ratio | 1.0 | 0.75 | 0.67 | 0.67 | 0.74 |

The formations of outer Fe-rich oxide and inner Cr-rich oxide are interpreted from two possible aspects. One hypothesis is that the outer iron oxide formed due to deposition from the flue gas environments. Upon exposure to the oxidizing hot gas environment, iron oxides may form on the surface of inner wall of the SS316-made autoclave [234]. The simultaneous presence of $H_2O$ and $O_2$ in flue gas, however, may induce the evaporation of surface iron oxides as volatile metal hydroxides [235]. These metal hydroxides have high volatility and may re-deposit on the surface of DSS 2205 coupons as iron oxides during

the cooling process of autoclave test. To examine this, a pure Zr sample was also exposed to the simulated flue gas with other DSS 2205 coupons at 320 °C for 600 h. TEM cross-sectional characterization on Zr sample showed the absence of a continuous layer of Fe or Cr in the surface scale (as shown in Figure 4-7), indicating that the outer iron-rich oxide layer is not from deposition but should be an in-situ grown corrosion product. Therefore, another explanation is proposed: the outer Fe-rich oxide layer comes into being via the diffusion of iron cations through the chromium oxide layer and the following oxidation process. Originally, a chromium oxide layer was formed upon the exposure to hot flue gas (formation of $Cr_2O_3$ is thermodynamically favored over iron oxides, as proved in Section 3.2). Then, iron cations may diffuse outwardly through the grain boundaries in $Cr_2O_3$ layer and oxidized upon the exposure to hot flue gas [236]. This process is kinetically favorable since Fe has a high solubility in $Cr_2O_3$ [193]. Besides, the diffusion coefficient of Fe is much higher than that of Cr in $Cr_2O_3$, and the value was improved by two orders of magnitude with the temperature increased from 270 to 320 °C, as shown in Table 4-6. This could not only support the statement of the formation of outer Fe-rich oxide over Cr-rich oxide, but also explain the transition from $Fe_2O_3$ to $Fe_3O_4$ on the outer iron-rich oxide layer with increasing the temperature since more iron cations diffuse outward for oxidation. A.P. Greeff et al. [237] also found that between room temperature and 600 °C, iron oxides grew more rapidly than the initially formed $Cr_2O_3$ and eventually developed on the top of Cr oxide on FeCrMo steel, which is in agreement with our results. It is generally acknowledged that for the oxidation of stainless steel below 400 °C, iron is the predominant surface oxide with a chromium-rich oxide layer underneath it [238]. Only at very low oxygen pressure ($< 10^{-3}$ Pa) and temperature above 350 °C could chromium predominate throughout the oxide layer. Given that the oxy-fired PFBC environment is featured with excess $O_2$, such outer Fe-rich oxide + Cr-rich oxide are expected to be found on high Cr duplex stainless steels.
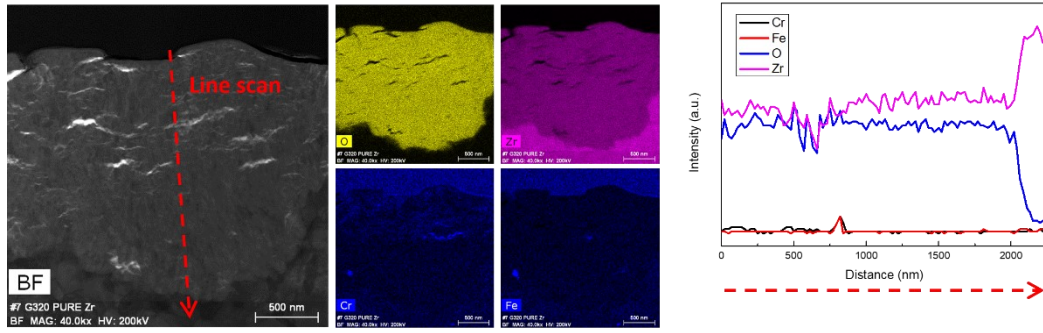
Figure 4-7. TEM cross-sectional images and EDS mappings of pure Zr after corrosion in simulated flue gas at 320 °C for 600 h.

Table 4-6. The diffusion coefficients of Cr, Fe and O ions in $Cr_2O_3$.

| Diffusing ions in $Cr_2O_3$ | D (cm$^2$/s) | | Equation | Ref. |
|---|---|---|---|---|
| | 270 °C | 320 °C | | |
| Cr | 6.77E-36 | 1.26E-33 | $D_{Cr}(cm^2s^{-1}) = 5.84 \times 10^{-9} \cdot \exp\left(-\dfrac{280 \text{ kJ} \cdot \text{mol}^{-1}}{RT}\right)$ | [239] |
| Fe | 6.98E-30 | 5.84E-28 | $D_{Fe}(cm^2s^{-1}) = 4.4 \times 10^{-7} \cdot \exp\left(-\dfrac{237 \text{ kJ} \cdot \text{mol}^{-1}}{RT}\right)$ | [236] |
| O | 4.03E-40 | 1.07E-36 | $D_{O}(cm^2s^{-1}) = 15.9 \cdot \exp\left(-\dfrac{422 \text{ kJ} \cdot \text{mol}^{-1}}{RT}\right)$ | [240] |

Current results show that a relatively compact oxide layer formed on DSS 2205 upon the exposure to hot flue gas of oxy-fired PFBC system, which exhibited limited growth with increasing time and temperature. Thus, the duplex oxide layer was considered comparatively stable. The chromium oxide layer is believed to be the dominant diffusion barrier since the diffusion rates of metal ions (Cr, Fe and Ni) in chromium oxide are much lower than those in iron and nickel oxides [236, 241]. Besides, EDS mappings also exhibit the accumulation of silicia at the interface of oxide scale/substrate on all the tested DSS 2205 in Figure 4-6. A continuous layer of Si oxide at the interface of oxide/metal substrate has long been reported [242], which helps to maintain the integrity of surface oxide layer by serving as a diffusion barrier to the outward diffusion of metallic ions and inward diffusion of oxidizing ions. In a simulated oxy-fuel flue gas environment, Yu et al. [243] found that the addition of 0.5% Si into the Fe-Cr steel can significantly improve its corrosion resistance.

### 4.3.2. Corrosion kinetics of steel in hot flue gas

The average mass gain of DSS 2205 steel in the hot flue gas is shown in Figure 4-8. The variation of mass gain with time followed parabolic law, indicating that the oxidation process is diffusion-controlled. Based on the fact that the diffusion rate of O is much slower than Cr and Fe in the oxide layer (Table 4-6), the oxide growth rate would be controlled by inward oxygen diffusion from the hot flue gas [242]. The mass gain curves with time at different temperatures could be fitted by the following equation [242, 244]:

$$\left(\frac{\Delta m}{A}\right)^2 = k_0 \cdot \exp\left(-\frac{Q}{RT}\right) \cdot t \qquad \text{Equation 4-2}$$

where $\Delta m$ (mg) is the mass gain of coupon during corrosion process, A ($cm^2$) is the surface area of the coupon, $k_0$ is the pre-exponential factor as a constant, Q is the activation energy, T (K) is the temperature, R is the gas constant, t (h) is the testing time. Based on the equation, $k_0$ and Q were estimated to be $1.87 \times 10^{-6}$ $mg^2 \cdot cm^{-4} \cdot h^{-1}$ and 13.19 kJ/mol, respectively. According to Wagner's theory, the migration of ions through the oxide layer is the rate-determining step during parabolic oxidation. The calculated Q (13.19 kJ/mol) from the current study is much lower than the active energy obtained from other studies in oxidizing environments (240-280 kJ/mol) [244]. One possibility is that the presence of high content of steam may reduce the activation energy. The presence of steam could change the diffusion properties of the formed oxide by dissolving hydron in the oxide, which could lower the activation energy and facilitate the diffusion behavior of metal ions through the oxide layer [245]. Another explanation is that the occurrence of pitting can influence the direct weight change value, thus affecting the calculation of activation energy. Even so, the low apparent activation energy could still reflect the trend that the weight change of DSS 2205 with temperature is not rapid in the simulated flue gas environments.
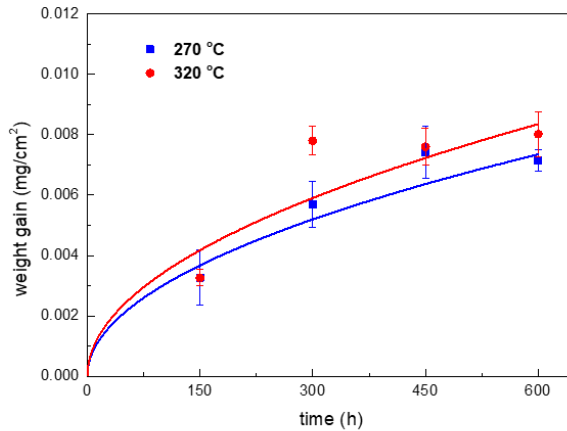
Figure 4-8. Variation of direct mass gain of DSS 2205 with time in flue gas at 270 and 320 °C.

The formation of oxide layer on the surface of DSS 2205 can be caused by one or several oxidizing gases ($CO_2$, $H_2O$ and $O_2$) during the exposure to hot flue gas. Identifying the oxidizing effect of each gas component is important in understanding the corrosion mechanisms in the flue gas environment of oxy-fired PFBC systems. $CO_2$ shall be considered to be inert with steels at temperatures below 400 °C [208]. To identify the effect of $H_2O$ and $O_2$, the Gibbs free energies of several iron and chromium oxides regarding $H_2O$ and $O_2$ were calculated using commercial HSC software [225] and the results are summarized in Table 4-7. Compared with that of Ni, the oxides of Fe and Cr might be the main corrosion products from a thermodynamic point of view. The more negative Gibbs Free Energies of metal oxides with $O_2$ indicate the more important role of $O_2$ in the oxidation process compared with $H_2O$. It is likely that $O_2$ would be responsible for the formation of the oxides during the corrosion process.

Table 4-7. Gibbs Free Energy of several metal oxides regarding $H_2O$ and $O_2$ at 270 and 320 °C.

| Reaction | $\Delta G$ (kJ/mol) | |
|---|---|---|
| | 270 °C | 320 °C |
| $\frac{4}{3}Cr + O_2 = \frac{2}{3}Cr_2O_3$ | -658.61 | -649.94 |
| $\frac{4}{3}Fe + O_2 = \frac{2}{3}Fe_2O_3$ | -450.11 | -441.39 |
| $\frac{3}{2}Fe + O_2 = \frac{1}{2}Fe_3O_4$ | -465.06 | -456.97 |
| $2Ni + O_2 = 2NiO$ | -377.86 | -368.93 |
| | | |
| $\frac{2}{3}Cr + H_2O = \frac{1}{3}Cr_2O_3 + H_2$ | -112.39 | -110.58 |
| $\frac{2}{3}Fe + H_2O = \frac{1}{3}Fe_2O_3 + H_2$ | -8.14 | -6.31 |
| $\frac{3}{4}Fe + H_2O = \frac{1}{4}Fe_3O_4 + H_2$ | -15.61 | -14.10 |
| $Ni + H_2O = NiO + H_2$ | 27.99 | 29.93 |

Despite not being the dominant oxidant, the effect of steam should also be identified in the hot flue gas environments. At elevated temperatures, steam could basically affect the corrosion through two processes: oxidation of metals and facilitating the evaporation of metal oxides. The oxidation could be achieved by the adsorption of water molecules on the scale and their subsequent dissociation into oxygen ions and hydrogen ions. The former could serve as oxidizing species while the latter could transport into the scale as interstitial hydrogens, thus decreasing the diffusion barrier of cations and anions and enhancing the oxidation process [246, 247]. However, in oxidizing environments, the presence of $O_2$ will depress the dissociation of water vapor and inhibit the oxidizing effect [248]. It was then postulated that steam might behave as an oxidant only to a limited degree in the hot flue gas environment. As for the evaporating effect, steam could turn surface metal oxide, including iron oxides ($Fe_2O_3$ and $Fe_3O_4$) and chromium oxide ($Cr_2O_3$), into volatile compounds. Detailed chemical reactions and the corresponding Gibbs Free Energies at

elevated temperatures could be found in other references [249]. Based on our calculation, it is found that the Gibbs Free Energies of these metal hydroxides in the temperature range of 200-400 °C are all positive, indicating that the formation of these metal hydroxides are thermodynamically unfavored and the steam-induced metal oxide evaporation may happen only to a limited degree in the hot flue gas environments. In fact, the lack of iron or chromium oxide on the surface of Zr coupon in Figure 4-7 also proves that the $H_2O$-induced evaporation would be limited.

As mentioned above, HCl and $SO_2$ in the flue gas can initiate localized corrosion like pitting instead of general corrosion, as shown by SEM images (see Figure 4-5). In TEM cross-sectional images, Cl or S is absent throughout the formed oxide layer, further suggesting that Cl and S did not cause the severe general attack to the DSS 2205 in current testing environments. Otherwise, the oxide layer would be porous, and the accumulation of sulfur-containing compounds or metal chlorides could be found at the interface of the oxide layer/substrate, as reported in previous studies [250, 251]. Thermodynamic phase stability diagrams could also provide some useful hints as these diagrams present the thermodynamic stabilities of metal oxides, chlorides, sulfates and sufides at a given temperature with the variation on partial pressures of $O_2$ + $Cl_2$ or $O_2$ + $SO_2$. Thermodynamic phase stability diagrams for the systems Fe-O-Cl, Cr-O-Cl, Fe-O-S and Cr-O-S at 320°C were constructed and are shown in Figure 4-9, in which the equilibrium conditions for the current testing atmosphere containing $O_2$ + $Cl_2$ or $O_2$ + $SO_2$ are marked with red dots. It is found that for the flue gas atmosphere of the current study, metal oxides are the thermodynamically stable phases for Fe and Cr in the presence of $Cl_2$ and $SO_2$, which indicates that the iron oxides and chromium oxide are stable and $SO_2$/HCl could not cause a severe general attack in the hot flue gas environment.
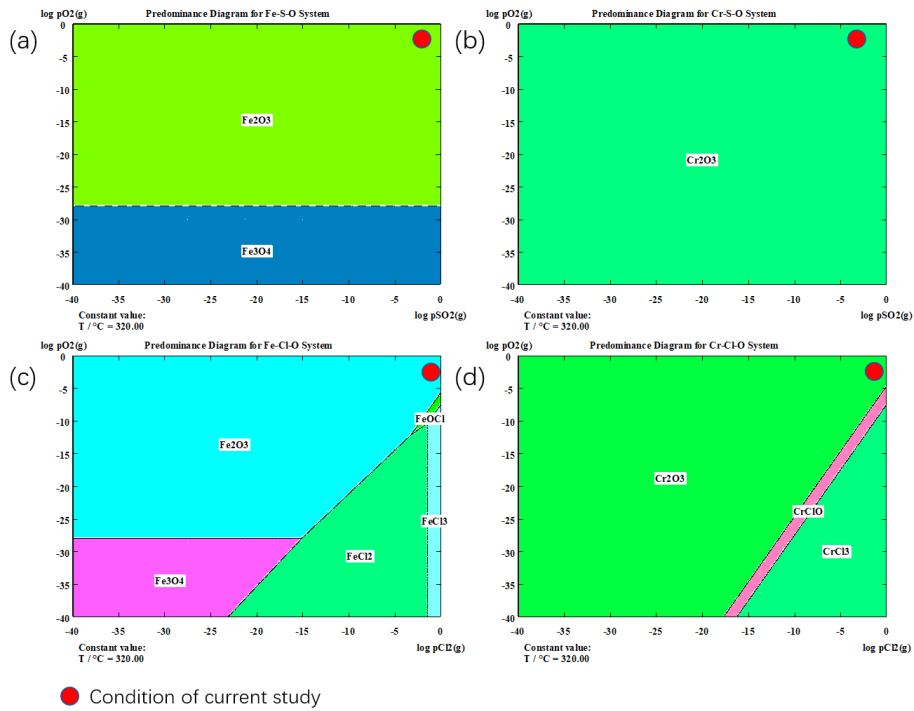
Figure 4-9. Constructed thermodynamic stability diagrams of the systems (a) Fe-S-O, (b) Cr-S-O, (c) Fe-Cl-O, and (d) Cr-Cl-O systems at 320 °C.

Besides the direct mass gain measurements, the mass loss method was also carried out to better characterize the degree of corrosion. The mass gain is the net result of oxygen, sulfur and chlorine mass uptake (due to scaling, sulfidation and chlorization) and metal loss (due to metal oxide spallation and evaporation). To eliminate the effect of steam-induced evaporation (although not much) or pitting-induced oxide spallation, mass loss measurement was carried out by calculating the corrosion rate based on the metal loss after chemically removing the formed corrosion products, and the results are shown in Figure 4-10(a). As expected, increasing temperature resulted in an increase in mass loss of the steel because of enhanced oxidation and pitting processes. At a certain testing temperature, the average mass loss of DSS 2205 only slightly increased with time, which might be attributed to the slow and continuous formation of surface oxide scales. However, a noticeable increase in the mass loss value was observed after 600 hours of exposure. This could be related to the following two factors. The first is the accumulated local attack from $SO_2$ and HCl. As described above, the presence of $SO_2$ and HCl in the hot flue gas can damage the substrate metal by penetrating the surface oxide layer through active sites,

leading to the formation of pit. With extended exposure time (600 h), pitting effect would become more noticeable, leading to a notable increase in steel consumption rate. In fact, this trend is in accordance with the exponentially increased pit density with time (Figure 4-4). The second reason is the stress accumulation from the oxide growth and thermal stress after cyclic oxidation, making the oxide more susceptible to be attacked by the aggressive agents ($SO_2$ and HCl) in the flue gas.

To support the development of materials selection strategy for industrial application, the corrosion rate based on mass loss measurements of DSS 2205 was calculated. As shown in Figure 4-10(b), the average corrosion rate increased with temperature as expected. It also decreased with time at an early stage due to the formation and growth of protective surface scales on the steel. After 450 hours, further extending time led to a slight increase in the average corrosion rate because of the influence of pitting. The highest corrosion rate, 0.13 µm/y, was observed on the samples corroded at 320 °C for 150 h. Currently, there is no criterion specifying the maximum allowable corrosion rate for flue gas components. Previous experience from heat exchangers and gas transportation pipelines may be used as references. For engineering pipeline components, 5 mpy (127 µm/y) is often recommended as the maximum acceptable corrosion rate [128]. For superheater/reheater materials in the combustor, the generally acceptable corrosion rate is 40-50 µm/1000 h [252]. Given that 0.13 µm/y is much lower than the above-mentioned values, DSS 2205 may be a suitable candidate alloy for the flue gas component in oxy-fired PFBC system. However, it should also be noted that $SO_2$/HCl-induced pit with maximum depth below 3 µm could be found on DSS 2205. The depth of the pits didn't increase with time up to 600 h, yet long-term tests are still needed to further examine the pitting propagation on DSS 2205 under the operating conditions.
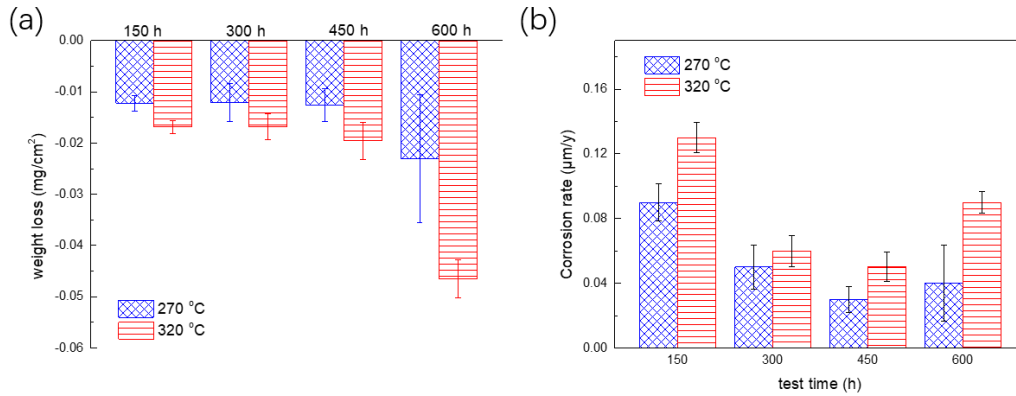
Figure 4-10. (a) Mass loss measurements and (b) corrosion rate measurement of DSS 2205 after corrosion tests at 270 and 320 °C for different times.

## 4.4. Conclusions

Corrosion tests in a simulated oxy-fired PFBC flue gas environment containing $H_2O + O_2 + CO_2 + N_2 + HCl + SO_2$ were carried out on DSS 2205 at both 270 and 320 °C for 600 h. Both general oxidation and pitting were found on the DSS 2205. $O_2$ is believed to be the main oxidant for general oxidation while $H_2O$ may assist the process. At both temperatures, the corrosion behavior of DSS 2205 followed a parabolic law and the corrosion products were mainly composed of the outer iron-rich oxide and inner chromium-rich oxide. The chromium-rich oxide formed first, then iron oxide grew over it due to the higher diffusion rate of iron cations in the chromium-rich oxide. Accumulation of Si was found beneath the oxide layer to improve the corrosion resistance. $SO_2$ and HCl caused pitting by penetrating the surface oxide layer through the active sites/paths like inclusions or grain boundaries. Pit density increased with higher temperatures and longer testing time, but the maximum pit depth and pit diameter only increased with higher temperature but did not change too much with time. Both direct weight change and mass loss were used to evaluate the corrosion, and the highest corrosion rate of DSS 2205 calculated by mass loss method is only 0.13 μm/y at 320 °C, suggesting it may be a promising candidate material for flue gas components in oxy-fired PFBC systems.

# Chapter 5. Corrosion of SS310 and Alloy 740 in High Temperature Supercritical CO₂ with Impurities H₂O and O₂

**Abstract**

This study investigated corrosion performance of SS310 and Alloy 740 in supercritical $CO_2$ streams with 100 ppm $H_2O$ or $O_2$ at 600 °C and 30 MPa up to 1000 h. The addition of 100 ppm $H_2O$ remarkably enhances general and localized oxidations while $O_2$ led to the opposite change. Compared with $H_2O$, impurity $O_2$ exhibited a more negative impact on the carburization of SS310. Alloy 740 had better carburization resistance compared to SS310 despite the addition of $H_2O$ or $O_2$. Both alloys followed near parabolic oxidation law and showed acceptable corrosion resistance in different supercritical $CO_2$ steams.


 **Keywords**: Alloy; Stainless steel; TEM; XRD; Carburization; High temperature corrosion.

## 5.1. Introduction

Over the past decades, high temperature supercritical $CO_2$ (s-$CO_2$) has been recognized as a promising working fluid with great potential in Brayton cycle at advanced solar, thermal, and nuclear power plants. The concept of s-$CO_2$ Brayton cycle was originally proposed by Angelino and Feher in 1968 [253, 254], followed by several innovative modifications to improve its performance and efficiency [255]. Since 2012, the s-$CO_2$ Brayton cycle concept has been tested with a turbine inlet temperature of 343 °C and power output of 20 kW at Sandia National Laboratories [256]. Most recently, a pilot plant with 10 MW s-$CO_2$ recompression closed Brayton cycle is under construction in San Antonio, TX, aiming at a much higher operating temperature and better energy efficiency [257]. However, several materials knowledge gaps, especially the selection of appropriate constructional alloys for compact heat exchangers and joints, hinder the successful deployment of this technology as current available information is still not enough to support the selection of materials with acceptable long-term resistance to high-temperature/high-pressure s-$CO_2$ streams with certain amounts of impurities [47, 258-262].

In the advanced s-CO$_2$ Brayton cycles, the designed operating pressure and temperature of s-CO$_2$ stream are at the ranges of 8-30 MPa and 400-800 °C, respectively [50]. Previous studies indicated that high-temperature pure s-CO$_2$ may cause external oxidation and/or internal carburization damages for different types of steels and alloys including ferrite-martensite steels (e.g., Gr 22, VM12, P/T91, and EBrite), austenite stainless steels (e.g., SS201, SS304H, HR3C, SS316L, SS310, SS347HFG, and 800H), Fe-based alumina-forming alloys (AFA) (e.g., APMT, PM2000 and AFA-OC series), Ni-based alloys (e.g., Alloy 625, Alloy 282, Alloy 740H, Alloy 617, Alloy 600, Alloy 690 and Alloy 230) and Co-based alloys (Alloy 188) [50, 261-269]. These works also revealed that temperature would play a key role in the corrosion process while the pressure only has a marginal effect as long as the CO$_2$ is controlled under the supercritical state [270, 271]. The carburization susceptibility of alloys is coherently related to their chemical composition and microstructure in the high-temperature s-CO$_2$. For instance, ferritic steels and austenitic stainless steels are more prone to carburization compared to Ni-based alloys [272], and increasing Cr and Ni contents in these steels is likely to reduce the carburization damages [50].

Despite the above interesting findings, more efforts are seriously needed to focus on the impacts of trace amounts of impurities and the roles of major alloying elements (such as Cr, Ni and Co) in the steels and alloys on corrosion in high-temperature high-pressure s-CO$_2$ streams. Impurities, such as H$_2$O and O$_2$, are usually found in s-CO$_2$ streams, either with low levels (ppm) in indirect-fired cycles or high levels (%) in the direct-fired cycles [259]. Unfortunately, the results reported are somewhat controversial, and the information accumulated is insufficient for selecting appropriate constructional alloys and developing effective long-term corrosion control strategy [42, 49, 273]. For example, Mahaffey et al. [273] compared the effects of industrial-grade CO$_2$ (99.95%) and ultra-pure CO$_2$ (99.999%), and found that the presence of impurities H$_2$, hydrocarbon, O$_2$ and H$_2$O in the industrial-grade CO$_2$ might be responsible for the enhanced corrosion of Alloy 800H and AFA-OC6 alloy. Kung et al. [49] studied the corrosion behavior of ferritic steels (P91, VM12), austenite stainless steels (Crofer 22H, SS304H, HR3C) and Ni-based alloys (Alloy 617, Alloy 740H) in the s-CO$_2$ with ~3.6 mol.% O$_2$ and ~5.3 mol.% H$_2$O at 650-750 °C;

they found that ferrite and stainless steels suffered severe oxidation and carburization while the Ni-based alloys were relatively safe from carburization embrittlement. Besides general oxidation, several pioneer studies indicated that the presence of 10-100 ppm $O_2$ could enhance localized oxidation (nodule) and degrade surface scale stability of Alloy 230 and Alloy 625 [42, 274]. On the contrary, other investigations reported that $O_2$ and $H_2O$ could only have a negligible effect on the oxidation of several Fe-based (SS25) and Ni-based alloys (Alloy 282, Alloy 740, Alloy 625) at 650-750 °C [275, 276]. A recent study showed that the influence of impurities on corrosion could also be related to s-$CO_2$ pressure [277]. Moreover, according to our literature review, very limited work has been done on the corrosion of Co-based high-temperature alloys in high temperature s-$CO_2$ streams [269], although the alloys have a successful application history in high-temperature environments [278].

Therefore, this study investigated the corrosion modes and extents of two representative candidates, SS310 and Alloy 740, in supercritical $CO_2$ with 100 ppm $H_2O$ or 100 ppm $O_2$ at 600 °C and ~30 MPa for up to 1000 hours exposure. Note that the two candidates exhibit good high-temperature mechanical properties (such as strength and creep resistance) as heat exchanger alloys in Brayton cycle [50, 279]. It is anticipated to clarify the influences of $H_2O$ and $O_2$ impurities and identify the role of element Co on oxidation and carburization in high-temperature s-$CO_2$ to support, in part, the development of applicable materials selection strategy for the deployment of s-$CO_2$ Brayton cycle in the advanced energy generation systems.

## 5.2. Experimental details

### 5.2.1. Test sample preparation

Flat test samples (20 mm long × 10 mm wide × 2 mm thick) were machined from commercial SS310 and Alloy 740 plates, and their chemical compositions are shown in Table 5-1. Please refer to Section 3.2.1 on the details of sample preparation.

Table 5-1. Normalized chemical compositions (wt.%) of SS310 and Alloy 740.

| | Cr | Co | Mo | Ni | Fe | Nb (+Ta) | Al | Mn | Si | Ti | C |
|---|---|---|---|---|---|---|---|---|---|---|---|
| SS310 | 24.2 | 0.1 | 0.2 | 19.2 | 56.3 | - | - | 1.66 | 0.54 | - | 0.043 |
| Alloy 740 | 24.6 | 20.1 | 0.5 | 50.0 | 0.2 | 1.47 | 1.4 | 0.30 | 0.15 | 1.45 | 0.030 |

### 5.2.2. Corrosion testing conditions

To identify the influence of $O_2$ and $H_2O$, the following tests were carried out in different s-$CO_2$ streams: (1) Test #1, ultra-pure s-$CO_2$ (99.999%); (2) Test #2, ultra-pure s-$CO_2$ + 100 ppm $H_2O$; and (3) Test #3, ultra-pure s-$CO_2$ + 100 ppm $O_2$. The result obtained from Test #1 was used as a baseline for comparison to clarify the influence of $H_2O$ and $O_2$. All the tests were conducted in a static autoclave made of Alloy 625 at 600 °C and a total pressure of ~30 MPa for up to 1000 h. Note that the addition of 100 ppm $H_2O$ or $O_2$ was achieved by charging the certified mixtures of $CO_2$ + 141 ppm $H_2O$ or $CO_2$ + 856 ppm $O_2$, respectively.

For each test, four thermal cycles (including 170 h, 340 h, 510 h, and 1000 h exposures) were performed (shown in Figure 5-1(a)), and 16 freshly prepared coupons of an alloy were employed. After carefully allocating the sample holder with alloy coupons, the 1 L autoclave was sealed, purged with ultra-pure $CO_2$ at room temperature, and heated up to 60 °C. At 60 °C, the required gases were charged into the autoclave by using corresponding gas cylinders and a booster pump as indicated in Figure 5-1(b). Note that Clausius-Clapeyron relation is inapplicable for $CO_2$ charging due to the supercritical state of current system. To reach the designed environment (s-$CO_2$ with 30 MPa at 600 °C), the pressure of charged $CO_2$ at 60 °C is determined based on mass balance and NIST $CO_2$ databases [280]. After charging, the autoclave was directly heated up to 600 °C. The start-point was defined as the temperature and pressure of the s-$CO_2$ stream reached 600 °C and about 30 MPa, respectively. At the end of a designed exposure, the autoclave was powered off and cooled down to room temperature. Four corroded coupons of an alloy were removed from the autoclave for short-term corrosion rate assessments and corrosion product characterizations. The other coupons were then loaded back into the autoclave for

the next run in which fresh gases were charged following the same procedure as described above. To avoid the over-consumption of impurities and obtain reliable long-term corrosion results, the s-CO$_2$ streams were re-refreshed after 680 and 850 hours of exposures. After about 1000 h, all the remaining coupons were collected from the autoclave for long-term corrosion mode and rate determination.
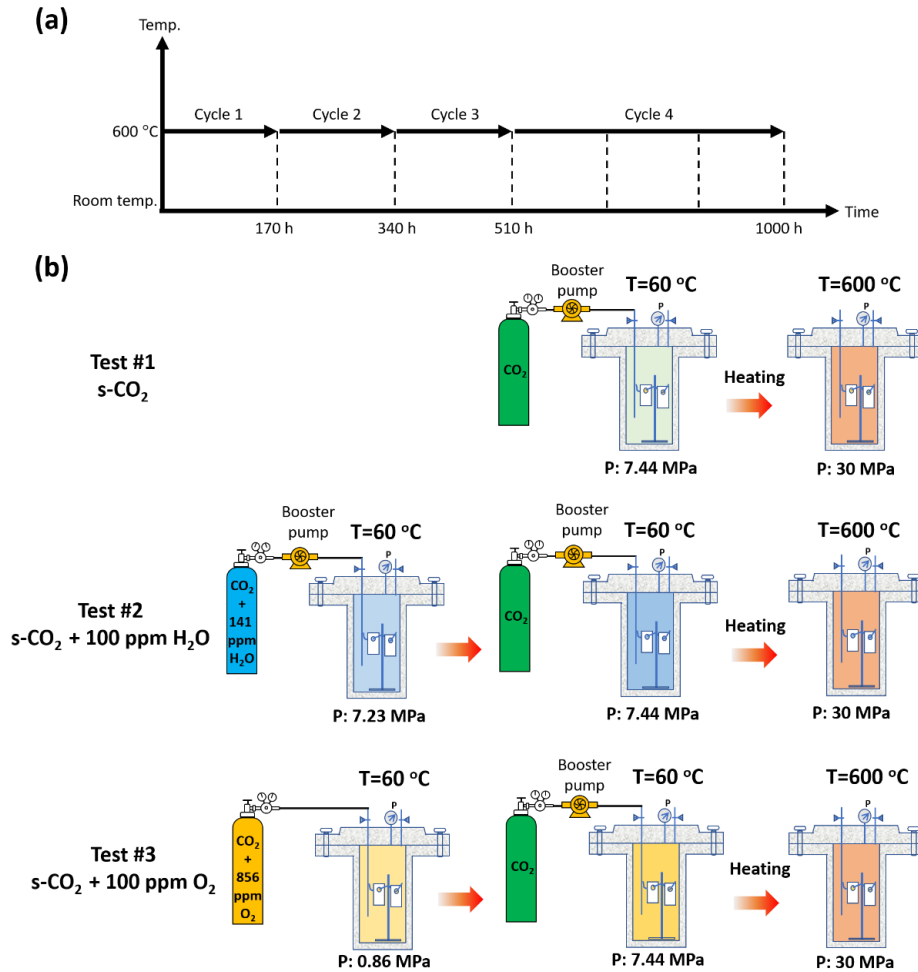


Figure 5-1. (a) Duration of the thermal cycles in each test; (b) Schematic of charging and heating procedures and matrix applied in this study.

### 5.2.3. Corrosion rate assessments and corrosion product characterizations

The short-term and long-term corrosion rates of the two alloys were assessed based on two different methods: (1) direct mass change measurements and (2) mass loss measurements. Please refer to Section 4.2.3 for the experimental details of the two methods.

The phases of corrosion products were identified by Grazing incidence X-ray diffraction (GIXRD) characterization at the incidence angle of 1° to identify the chemical phases of the formed corrosion products on a PANalytical X'Pert Pro high-resolution X-ray diffractometer equipped with Cu-Kα radiation. SEM, TEM, FIB were also carried out, ad the experimental details could be found in Section 4.2.3.

## 5.3. Results and discussions

### 5.3.1. Post-mortem characterization of alloys corroded in different s-CO₂ streams

Figure 5-2 shows the photographic images of SS310 and Alloy 740 after the exposure to three types of s-$CO_2$ streams at 600 °C. All the images before corrosion testing readily showed metallic luster. In contrast, the surface color of corroded coupons turned yellow or dark green, implying the formation of surface oxide scales during the exposure. With prolonged exposure, the coupon surfaces became darker, suggesting the further growth of the surface oxides. Among them, the alloys exposed to s-$CO_2$ + 100 ppm $O_2$ (Test #3) exhibited the slightest color transformation with time while those corroded in s-$CO_2$ + 100 ppm $H_2O$ (Test #2) showed the most obvious change, implying the different effects of $H_2O$ and $O_2$ on oxidation.
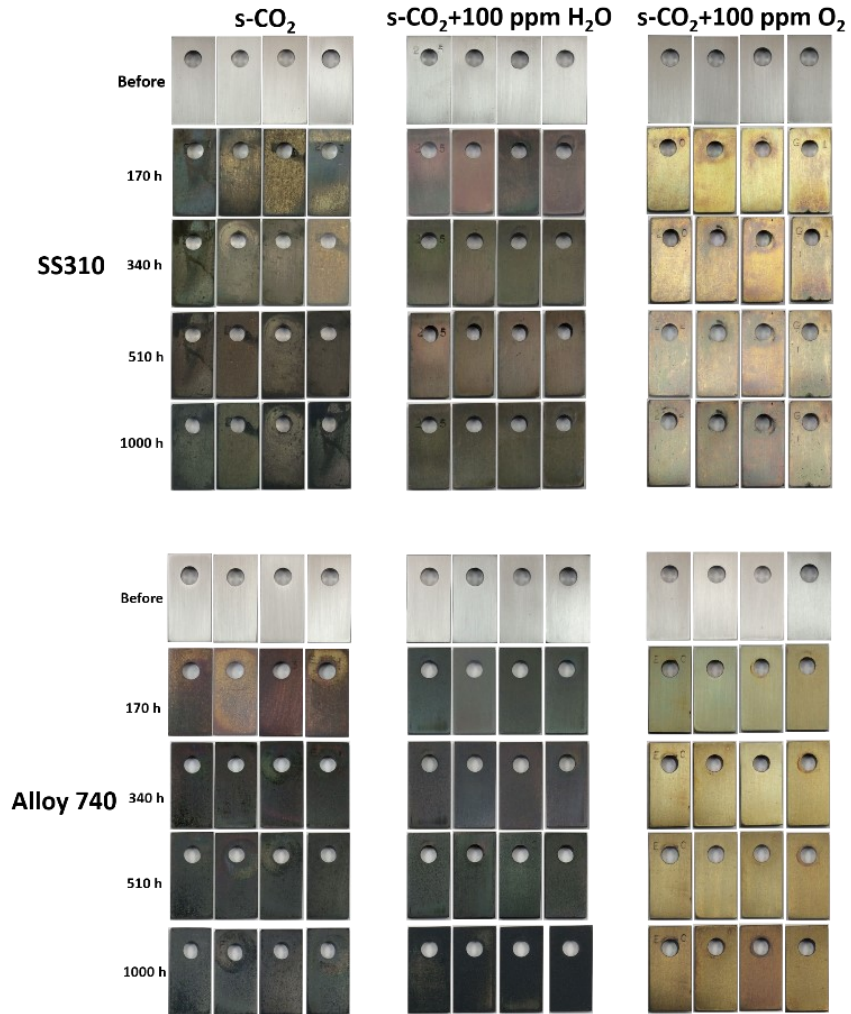
Figure 5-2. Photographic images of SS310 and Alloy 740 before and after various exposure times to different s-CO₂ streams at 600 °C and 30 MPa.

Figure 5-3 shows the XRD spectra of SS310 and Alloy 740 coupons after the exposure to different s-CO₂ streams at 600 °C and 30 MPa for 1000 hours. The results indicate that the surface oxide scales grown on the two alloys in the s-CO₂ streams are composed of dominant $Cr_2O_3$ and some spinels. Previous studies confirmed the formation of $Cr_2O_3$ on Cr-bearing alloys (such as SS310, 800H, Alloy 600, Alloy 690 and Alloy 625) in high-temperature pure s-CO₂ [262, 265, 268], and the mechanism is likely to be via [281]:

$$2Cr + 3CO_2 \rightarrow Cr_2O_3 + 3CO \qquad \text{Reaction 5-1}$$

The Gibbs Free Energy of Reaction 5-1 in current test environment is estimated to be -407 kJ/mol based on the calculation results from HSC software [282]. The generated CO may

85

subsequently be involved in the carburization of the alloys [268]. Moreover, the $Fe_{3-x}Cr_xO_4$ peaks were found on SS310 while those of $Co_{3-x}Cr_xO_4$ were found on Alloy 740, implying the effects of Fe and Co on spinel formation. The peaks of metal substrates were also observed on the XRD spectra, and the intensity seemed to be somewhat higher in $s-CO_2$ + 100 ppm $O_2$ (Test #2) than those in other two $s-CO_2$ streams (Test #1 and #3), implying the formation of a relatively thinner surface oxide scale.
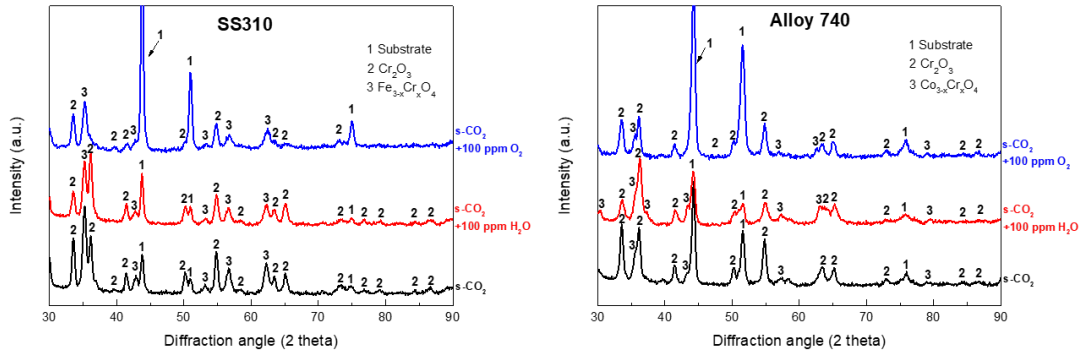


Figure 5-3. XRD spectra for SS310 and Alloy 740 samples corroded in $s-CO_2$ streams at 600 °C and 30 MPa for 1000 hours. Note that Test #1: $s-CO_2$, Test #2: $s-CO_2$+100 ppm $H_2O$, and Test #3: $s-CO_2$+100 ppm $O_2$.

SEM images of SS310 and Alloy 740 surfaces corroded in the $s-CO_2$ streams for 340 and 1000 hours of exposures are shown in Figure 5-4. Even after 1000 hours of exposure, abrasion lines generated by mechanically polishing prior to corrosion testing were still visible on the alloys, indicating the slow general oxide formation processes. Localized nodular oxides with several micrometers in diameter were found on the alloy grain boundaries, and their density increased with the exposure time. The nodule formation and growth were possibly inhibited with the addition of 100 ppm $O_2$ into $s-CO_2$, but enhanced by the introduction of 100 ppm $H_2O$. The $H_2O$-enhanced nodule oxidation was more prominent on Alloy 740 compared to SS310, and exacerbated with the prolonged time. EDS analyses revealed that the nodules formed on SS310 had much higher Fe content than other uniform areas while the nodules on Alloy 740 were enriched with Co and Ni, suggesting the impacts of these alloying elements on nodular oxidation. Both EDS and

86

XRD results indicate that the nodules formed on SS310 and Alloy 740 are likely to be $Fe_{3-x}Cr_xO_4$ and $Co_{3-x}Cr_xO_4$, respectively.
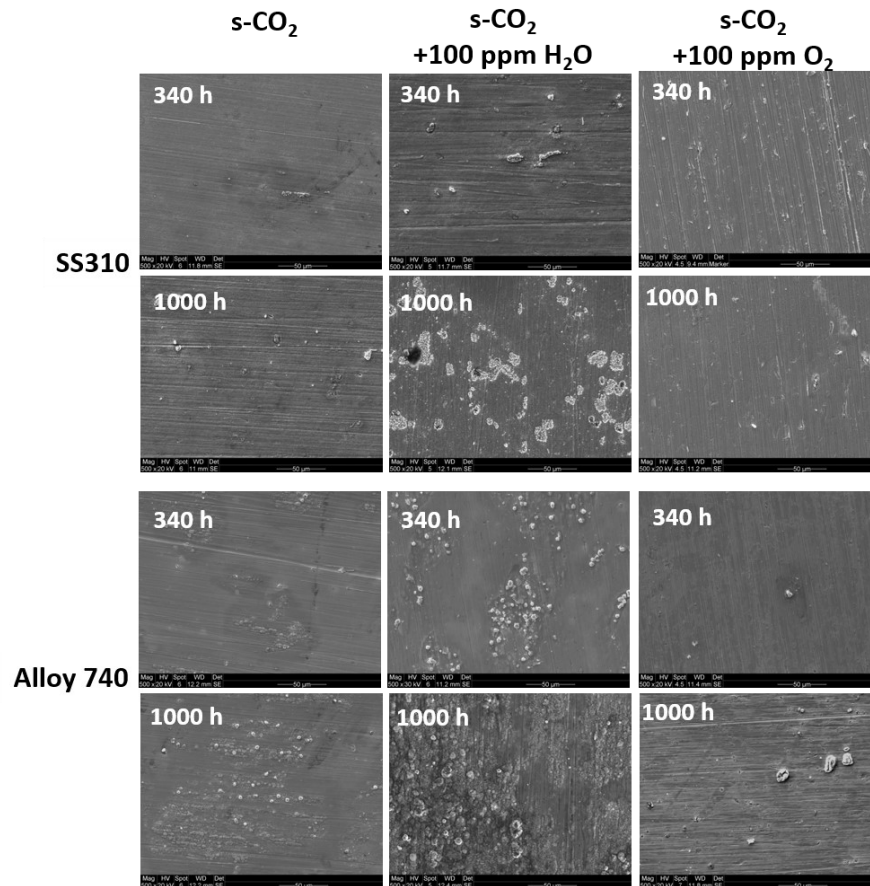


Figure 5-4. Top-view SEM images of SS310 and Alloy 740 corroded in s-CO₂ streams with different impurities for 340 and 1000 hours.

The nodule oxidation originates from the inability of local oxide layer to reheal itself and the consequent fast external growth of non-protective corrosion products on defective spots (such as grain boundaries) [283]. As will be shown later (see Figure 5-5, 5-6, 5-7 and 5-9), underneath Cr depletion zone enriched with the alloying elements (Fe or Ni+Co) was formed in the alloys during the exposure to the s-CO₂ streams. Localized chemical failure (such as the fluctuation of Cr contents) [284] or physical failure (cracks within the surface $Cr_2O_3$ scales) [285] at defects could trigger the outward diffusion of elements from the depletion zone, which would be oxidized into spinel upon the exposure to the corrosive environments [286, 287]:

$$(3 - x)Fe + CO_2 + \frac{x}{2}Cr_2O_3 \rightarrow Fe_{3-x}Cr_xO_4 + CO \qquad \text{Reaction 5-2}$$

$$(3 - x)Co + CO_2 + \frac{x}{2}Cr_2O_3 \rightarrow 2Co_{3-x}Cr_xO_4 + CO \qquad \text{Reaction 5-3}$$
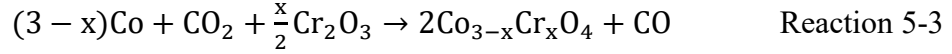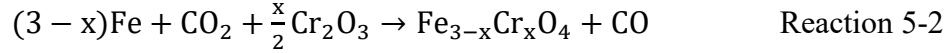
In high-temperature s-$CO_2$, $H_2O$ impurity had a detrimental effect by enhancing the formation of Fe-containing oxide nodules. Previous studies found that $H_2O$ could facilitate the defect formation within the $Cr_2O_3$ scales via an increase in hydrogen absorption into the oxides [246] and/or $H_2O$-assisted volatilization through [288-290]:

$$\frac{1}{2}Cr_2O_3 + H_2O + \frac{3}{4}O_2 = CrO_2(OH)_2 \qquad \text{Reaction 5-4}$$
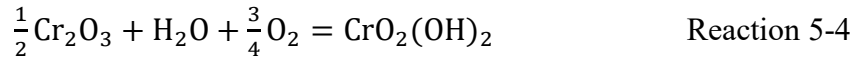
These would consequently generate more local pathways for supporting the outward diffusion of Fe/Ni/Co elements and trigger nodule oxidation. In contrast, the addition of 100 ppm $O_2$ in 30 MPa s-$CO_2$ suppresses nodule oxidation on SS310 and Alloy 740, as shown in Figure 5-4. $O_2$ is supposed to enhance the stability of the $Cr_2O_3$ oxide layer [291] by preferentially adsorbed on the defective spots of the $Cr_2O_3$ layer and facilitating the outward diffusion of chromium for the formation of a more protective oxide. However, Mahaffey et al. [42, 274] found that the addition of 100 ppm $O_2$ in 20 MPa s-$CO_2$ enhanced the formation of nodules on Alloy 230 and Alloy 625. One possible explanation for the difference is the status of testing conditions. In Mahaffey's experiments, the test gas was in flow condition with an average rate of 0.1 kg/h [42, 274], which may either interrupt the preferential adsorption of $O_2$ on defective site, or further enhance the outward diffusion of chromium, leading to suddenly increased stress developed within a short period and the enhanced formation of nodules.

As the continuous surface $Cr_2O_3$ scales formed on the two alloys are quite thin, TEM characterization was thus employed on the cross-sectional areas of the samples using FIB lift-out technique as described above. The TEM results of SS310 samples are presented in Figure 5-5, 5-6, 5-7 and 5-8. As shown in Figure 5-5(a), three different layers were formed on and in the steel after the 1000 hours of exposure to high-temperature pure s-$CO_2$, including outer continuous oxide layer (with the average thickness of ~300 nm thick), internal Cr-Fe-Ni oxide layer (with the thickness in the range of 870-1710 nm) and Cr-depletion zone (830-1460 nm). Note that as mentioned in Section 4.2.3, the top Pt layer

was artificially deposited in a vacuum chamber after the corrosion tests to protect the surface oxide during FIB operation. The outer continuous oxide layer is composed of $Cr_2O_3$ oxide along with a thin $SiO_2$ layer located at the interface of outer/inner oxide layers. In the s-$CO_2$, Cr should have higher reactivity with $CO_2$ molecules compared to other alloying elements (Fe and Ni), and a previous study on Ni-Cr alloys indicated that a thin and continuous chromia layer could be formed on the alloys with Cr contents > 14 wt.% [292]. The formation of silica layer might be from the outward diffusion of Si to the surface through grain boundaries during the exposure and the layer could act as a diffusion barrier and improve the $Cr_2O_3$ stability [289]. The internal Cr-Fe-Ni oxide layer was irregular and thick, in which Cr was completely oxidized while Fe and Ni were only partially oxidized due to their relatively lower affinity to oxygen ions that inward diffused through grain boundaries [261]. Several voids were observed, and their formation might be related to (1) the more rapid outward diffusion of chromium compared to Fe and Ni [274] and/or (2) Kirkendall Effect, i.e., the inward migration of defects generated and accumulated at the interface of gas/scale [42]. Obviously, these voids would act as short-circuit pathways for the inward diffusion of $CO_2$/CO, consequently resulting in the fast growth of internal oxidation layer [293]. The formation of Cr depletion zone could be attributed to the slower diffusion of Cr atoms within the steel than the outward diffusion of Cr for oxide formation, especially at the early exposure stage.

A continuous carbon layer was also found at the interface of the continuous $Cr_2O_3$ layer/internal Cr-Fe-Ni oxide layer, as further examined using EDS line scanning [see Figure 5-5(b)]. Its formation could be either via the outward diffusion of carbon from the substrate or the inward diffusion of CO/$CO_2$ from the environment. Since such a continuous carbon layer was not found on SS310 after the 1000 hours of exposure to the supercritical water (s-$H_2O$) at 625 °C and 29 MPa [294] or other high-temperature s-$H_2O$ environments [295], the carbon layer is likely to be formed from the ingression of $CO_2$/CO through the defect tunnels within the $Cr_2O_3$ layer [289]. Previous studies also reported that the carbon layer could be formed in Ni-based alloys, such as Alloy 600, Alloy 690 and Alloy 800HT, after the exposure to high-temperature s-$CO_2$ [281]. In the substrate, several precipitated Cr carbides (with an average diameter of ~120 nm) were distributed close to

the Cr depletion zone. These carbides could be either formed from carburization or sensitization reactions. In fact, such type of carbides was also found in austenite stainless steels (SS304, SS316 and SS310) exposed to high-temperature s-$H_2O$ [296, 297]. Thus, the carburization risk of SS310 in high temperature s-$CO_2$ is likely to be low.
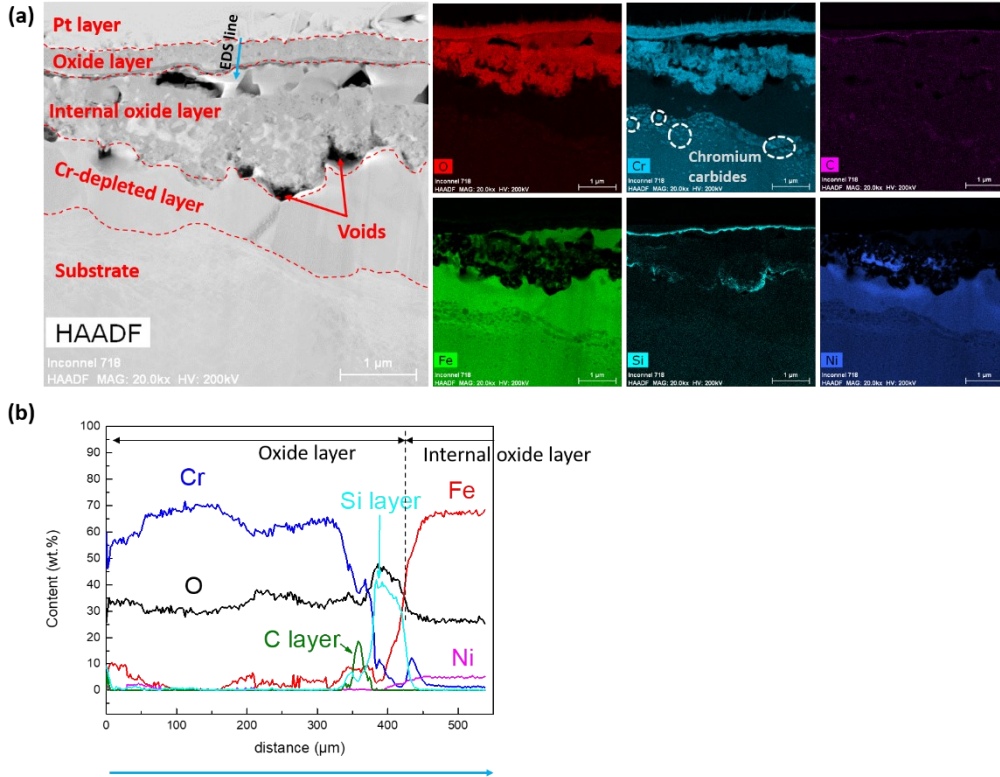


Figure 5-5. TEM results of the cross-sectional sample of SS310 corroded in s-$CO_2$ at 600 °C and 30 MPa for 1000 h: (a) cross-sectional STEM dark field and EDS mapping images, (b) EDS line scanning spectrum taken along the lines as shown in (a).

The TEM results of the steel corroded in s-$CO_2$ + 100 ppm $H_2O$ for 1000 hours are shown in Figure 5-6, including the continuous surface oxide layer and a nodule oxide. Compared with those formed in pure s-$CO_2$, the uniform surface oxide layer only had two distinguished layers, namely continuous oxide layer and Cr-depleted layer [see Figure 5-6(b)]. The absence of the internal oxidation layer was possibly related to the remarkably enhanced general oxidation with the addition of $H_2O$. The formed continuous oxide layer was also composed of $Cr_2O_3$ (major) and $SiO_2$ (minor), but became thicker with the average

thickness of ~427 nm. A previous study showed that the protons generated from $H_2O$ decomposition could penetrate into the $Cr_2O_3$ scale as interstitials, enhancing the diffusion of cations and anions and leading to a higher oxidation rate [246].

The carbon layer just underneath the continuous oxide layer was also observed, and considerable precipitated chromium carbides (with the average diameter of 50-60 nm) were found within the substrate. SAD patterns (Figure 5-7) revealed that the carbides were in the form of $Cr_{23}C_6$ with a cubic structure and a cube-to-cube orientation relationship with the gamma substrate. Compared with the observations in the pure s-$CO_2$, the increased density of carbides suggests that the addition of $H_2O$ would enhance carburization, although not so severe. The carburization affected zone could penetrate into the substrate with a depth of at least 5 μm [see Figure 5-6(c)]. The above findings are quite different from the previous reports that the presence of $H_2O$ in the $CO_2/CO$ mixture could reduce the tendency to carburization in Fe-Cr and Ni-Cr alloys [298]. Depending on its content and related environment chemistry (such as temperature and the presence of other impurities), $H_2O$ could either block some adsorption sites for $CO_2/CO$ species on surface oxide scales [299], or reduce the integrity and stability of $Cr_2O_3$ layer to make it more penetrable to $CO_2/CO$ [245]. In high-temperature s-$CO_2$ streams, the $Cr_2O_3$ scales formed on Cr-bearing alloy cannot stop the penetration of $CO_2/CO$ through micro/nanochannels (such as pores, cracks and grain boundaries) into metals for carbide formation [289, 300, 301]. As mentioned above, $H_2O$ could degrade the $Cr_2O_3$ stability and facilitate the defect formation in the oxides. Thus, it is very likely that the negative effect of $H_2O$ (even at ppm level) on carburization observed in this work could become dominant in high-temperature s-$CO_2$.

In addition, Figure 5-6(c) also reveals the nature of the nodule oxide. The nodule was a double-layer structure with outer Fe-enriched oxides and inner Cr-enriched oxides. As described above, the nodule formation is related to the fast outward diffusion of Fe at the weak area of the $Cr_2O_3$ layer and subsequent oxidation. The results from TEM, XRD (Figure 5-3) and SEM (Figure 5-4) characterization consistently indicate that the nodule shall be composed of $Fe_{3-x}Cr_xO_4$ oxides.
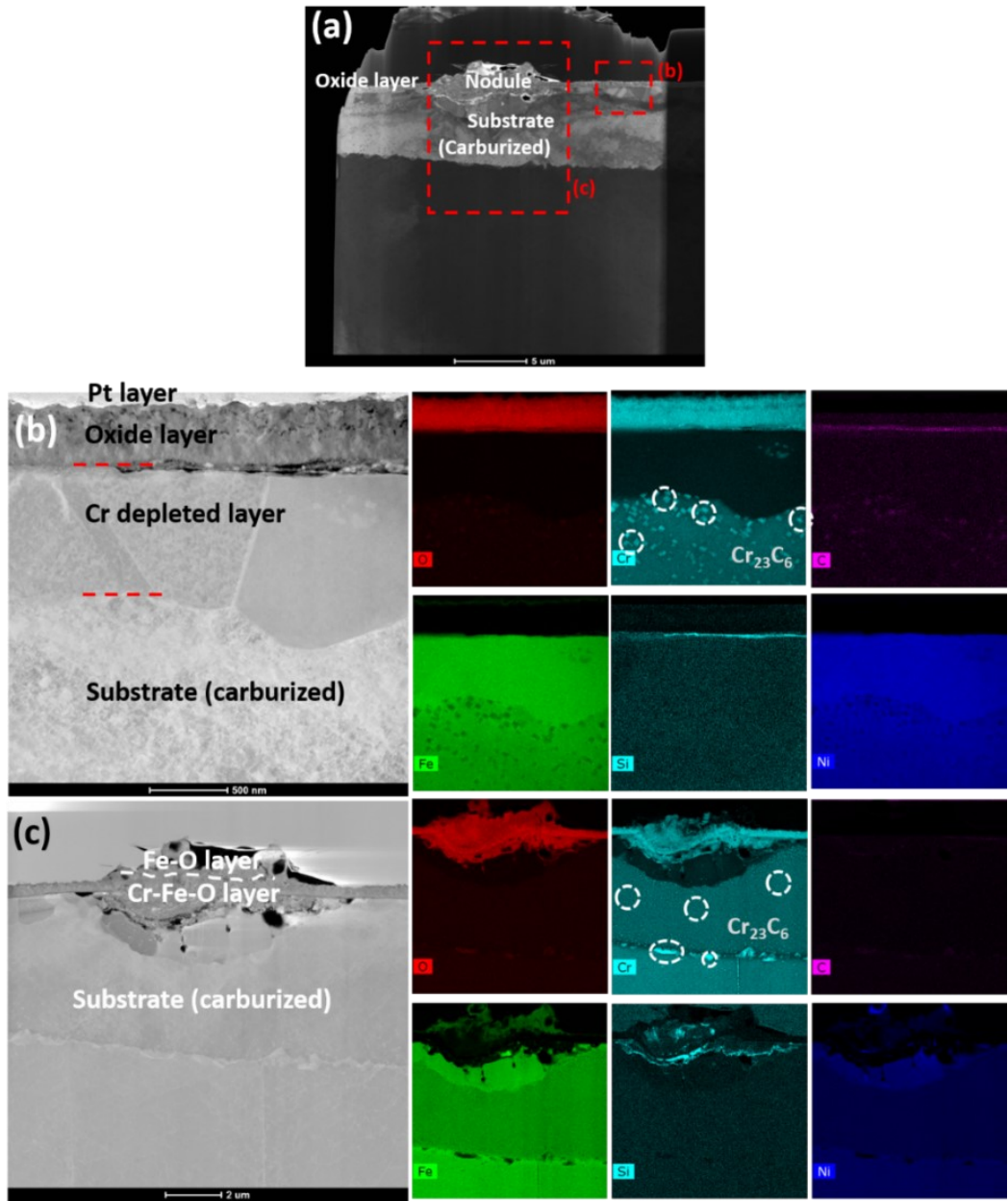
Figure 5-6. TEM results of the cross-sectional areas SS310 corroded in s-$CO_2$+100 ppm $H_2O$ at 600 °C and 30 MPa for 1000 h, including: (a) dark field image of oxide layer and nodule, and amplified cross-sectional dark field and EDS mapping images of (b) continuous $Cr_2O_3$ oxide layer and (c) a localized nodule.
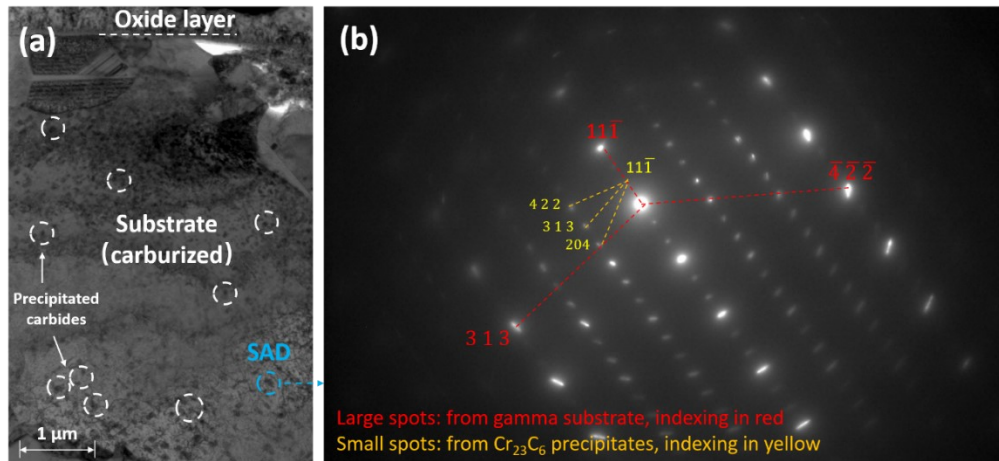
Figure 5-7. TEM characterization results of cross-sectional area of SS310 sample after 1000 hours of exposure to s-$CO_2$+100 ppm $H_2O$ at 600 °C and 30 MPa, including (a) bright field image of corrosion product layer and carburized substrate, (b) SAD pattern of the precipitated carbides and substrate.

The STEM dark field and EDS mapping images of SS310 after 1000 hours of exposure to s-$CO_2$ + 100 ppm $O_2$ are shown in Figure 5-8. Only two different layers were observed, including continuous oxide layer and carburized substrate in which Cr carbide islands were present. Figure 5-8(b) shows that the continuous oxide layer also consisted of $Cr_2O_3$ (major) and $SiO_2$ (minor) with the thinnest thickness (~215 nm) among all the three tests. Based on theoretical calculation from previous study and HSC software (shown in Table 5-2) [281, 282], the addition of 100 ppm $O_2$ could lead to a significant increase in $O_2$ partial pressure, which would be sufficient for the selective oxidation of Cr due to the more negative Standard molar Gibbs Free Formation Energy of $Cr_2O_3$ (as shown in Table 5-3 below). Previous studies found that the addition of $O_2$ (even only at ppb level) into high-temperature $CO_2$ could remarkably improve the oxidation process of Alloy 617 [302], and the formed $Cr_2O_3$ layer was thinner in $O_2$-containing $CO_2$ environments than that in pure $CO_2$ environments [270, 289, 303]. Compared with the $Cr_2O_3$ formed in $O_2$-containing environments, the one formed in pure $CO_2$ environment tends to have the segregated C at grain boundaries, which could restrict the growth of $Cr_2O_3$, leading to finer grain size and more grain boundaries as diffusion paths for the ingression of oxidants and eventually, the thicker scale [289]. Different from those in s-$CO_2$, the disappearance of internal oxides

may be because the formed surface $Cr_2O_3$ scale in s-$CO_2$ + $O_2$ could be more compact and less transparent to inward oxidant penetration. The distribution of carbides in the carburized substrate implies that C might diffuse into the substrate along the grain boundaries.

Table 5-2. The estimated partial pressure of $O_2$ in different environments at 600 $^o$C.

| Environment | 30 MPa pure $CO_2$ | 100 ppm $H_2O$ | 100 ppm $O_2$ |
|---|---|---|---|
| $P_{O_2}$ (atm) | $1.61×10^{-7}$ | $6.62×10^{-10}$ | 0.03 |

Although $O_2$ suppressed general and localized oxidations, its influence on the carburization of steel was really unexpected. Based on the Boudouard reaction [285], the addition of $O_2$ would retard the CO formation and reduce carbon activity on the surface oxide scale. However, as shown in Figure 5-8(c), a number of chromium carbides ($Cr_{23}C_6$) with several hundreds of nanometers in dimension were precipitated in the substrate with the carburization depth of more than 5 μm. EDS analyses on the whole mapping area in Figure 5-8(c) showed that the C content was about 1.29 wt.%, which was much higher than the normalized C content in SS310 (0.043% based on Table 5-1). Compared with those formed in pure s-$CO_2$ and s-$CO_2$ + 100 ppm $H_2O$, the addition of $O_2$ enhanced the inward diffusion of carbon atoms from the testing environment into the steel substrate. In high-temperature s-$CO_2$, the presence of 100 ppm $O_2$ would hinder CO formation and possibly suppress $CO_2$/CO adsorption due to its higher chemical affinity to metal oxides, thereby enhancing the formation and stability of $Cr_2O_3$ scale. Thus, the deleterious influence of $O_2$ on carburization may be attributed to the addition of $O_2$ at ppm level that makes the formed $Cr_2O_3$ thinner, resulting in a relatively shorter barrier for $CO_2$/CO ingression into the steel. Moreover, the reduction in thickness of the $Cr_2O_3$ layer will lower its thermal barrier effect and raise the temperature of the underlying substrate during the high-temperature exposure. Since the segregation of Cr at the grain boundaries of the substrate became more obvious at higher temperatures [304], chromium carbides may form more easily in s-$CO_2$ + $O_2$ environments. Further, previous studies have proposed that the generation of carbon would be achieved through the reactions of CO with alloying elements or CO decomposition beneath the surface oxide scale [300]:

$$xM + yCO \rightarrow M_xO_y + yC \qquad \text{Reaction 5-5}$$

$$2CO(g) \rightarrow CO_2(g) + C \qquad \text{Reaction 5-6}$$

The results in Figure 5-8 suggest that Reaction 5-6 is unlikely to occur in high-temperature s-CO₂ as the disappearance of oxygen below the surface oxide scale. The active carbon generated can be quickly diffuse into the substrate along grain boundaries for carbide formation. Previous studies mentioned that C was almost insoluble in $Cr_2O_3$ [305]. However, the studies were carried out by exposing $Cr_2O_3$ to radioactive $CO_2$-CO mixture rather than active carbon atoms. Thus, it is possible that active carbon might be also generated on the defect sites of surface $Cr_2O_3$, and then quickly pass through the oxide to form the carbide formation, and because of the smaller radius of carbon atom, the active carbon might penetrate $Cr_2O_3$ layer much faster than CO and $CO_2$. It should be noted that TEM confirms the precipitation of carbides within several micrometers, and quantitative analysis on larger area (like EPMA, SEM, or GDOES) are needed to further confirm the carburization behavior.
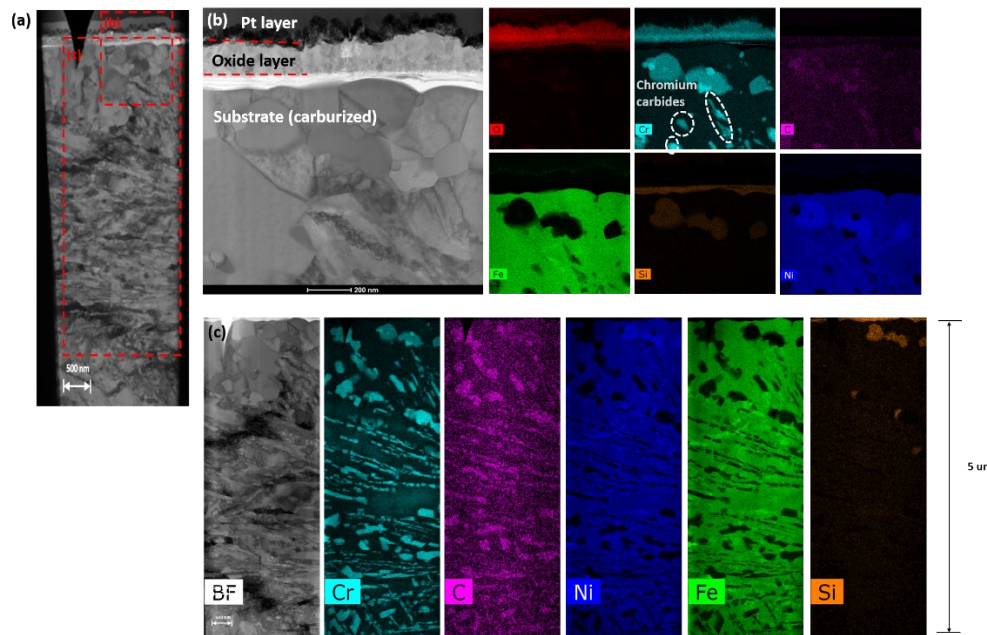


Figure 5-8. TEM results collected on the cross-sectional sample of SS310 corroded in s-CO₂+100 ppm O₂ at 600 °C and 30 MPa for 1000 h, including: (a) dark field image of oxide layer and substrate, and amplified dark field and EDS mapping images of (b) the continuous oxide layer and (c) carburized substrate.

Figure 5-9 shows the cross-sectional TEM results of the general oxidation areas of Alloy 740 after 1000 hours of exposure in different s-$CO_2$ streams at 600 °C. The following major observations are made:

- After the exposure to pure s-$CO_2$, three distinguished layers were also formed over Alloy 740 substrate, including continuous oxide layer, internal oxidation layer and Cr-depleted layer. The addition of 100 ppm $H_2O$ remarkably enhanced the general and internal oxidations while the introduction of 100 ppm $O_2$ resulted in the formations of thinner surface and Cr-depletion zone and the disappearance of internal oxidation layer. Compared with SS310, Alloy 740 generally exhibited better resistance to pure s-$CO_2$ and s-$CO_2$ + 100 ppm $O_2$ environments, but worse oxidation performance in s-$CO_2$ + 10 ppm $H_2O$ at 600 °C.

- In three different s-$CO_2$ streams, the outer surface scales formed on Alloy 740 were mainly composed of $Cr_2O_3$ due to its high Cr content. Minor amounts of $SiO_2$, $TiO_2$ and $Al_2O_3$ were found underneath the $Cr_2O_3$ layer, which may be related to the rejection of Si, Ti and Al from the interface of gas/oxide scale during the selective oxidation of Cr [306] or the outward diffusion of Si/T/Al elements from the substrate to the sub-surface because of a decrease in Cr activity due to surface $Cr_2O_3$ formation [307]. Due to their high affinity to oxygen (as shown in Table 5-3), these accumulated elements could be oxidized at the interface of oxide/substrate and improve the corrosion resistance by reducing the further outward diffusion of alloying elements and inward diffusion of oxidants (such as $CO_2$, CO, $H_2O$ and $O_2$) [265]. In s-$CO_2$ + 100 ppm $H_2O$, part of alumina was also found within the $Cr_2O_3$ layer, indicating that the outward diffusion of Al could be enhanced by the presence of $H_2O$ since the formation of $Al_2O_3$-$Cr_2O_3$ mixture was favored at high diffusion areas [308].

- In pure s-$CO_2$, internal oxidation possibly took place along the grain boundaries and the formed oxides were enriched with $Al_2O_3$ and $TiO_2$ with a small amount of $Cr_2O_3$. With the addition of 100 ppm $H_2O$, the internal oxidation became aggravated and the formed oxide was primarily composed of $Cr_2O_3$ and $TiO_2$ instead of $Al_2O_3$, which

96

were mostly located in the outer continuous $Cr_2O_3$ layer. As described above, $H_2O$ can degrade the properties of the outer $Cr_2O_3$ layer and make it less resistant to the diffusion of oxidants and alloying elements. Voids in the internal oxidation zone were found, which could be due to the fast outward diffusion of metallic cations and the condensation of left metal vacancies within the substrate [309]. Similar to the effect on SS310, the introduction of $O_2$ into s-$CO_2$ rendered the formed surface scale more compact with better resistance to the inward diffusion of oxidants, consequently blocking the internal oxidation.

- In the formed Cr depletion and/or internal oxidation zone, the accumulation of Ni and Co elements was observed. Thermodynamic calculation (Table 5-3) shows that their oxidation is unlikely to occur due to the higher Gibbs Free Formation Energy compared to other alloy elements.

- Compared with SS310, Alloy 740 exhibited much better resistance to carburization since Ni and Co were less likely involved in the carburization due to more positive Gibbs free formation energy of corresponding carbides [80]. For Alloy 740, although carbon could still penetrate through the oxide layer and then accumulated at the interface of continuous oxide layer/Cr-depleted layer, the trapped C appeared as flakes instead of a continuous C layer, indicating that the oxide scale formed on Alloy 740 may act as a better barrier to retard $CO/CO_2$ ingression. The $Al_2O_3$ and $TiO_2$ layers may contribute to the barrier effect. More interestingly, the addition of 100 ppm $H_2O$ or $O_2$ only had a negligible influence on the alloy carburization resistance as shown in Figure 5-9(b) and (c).
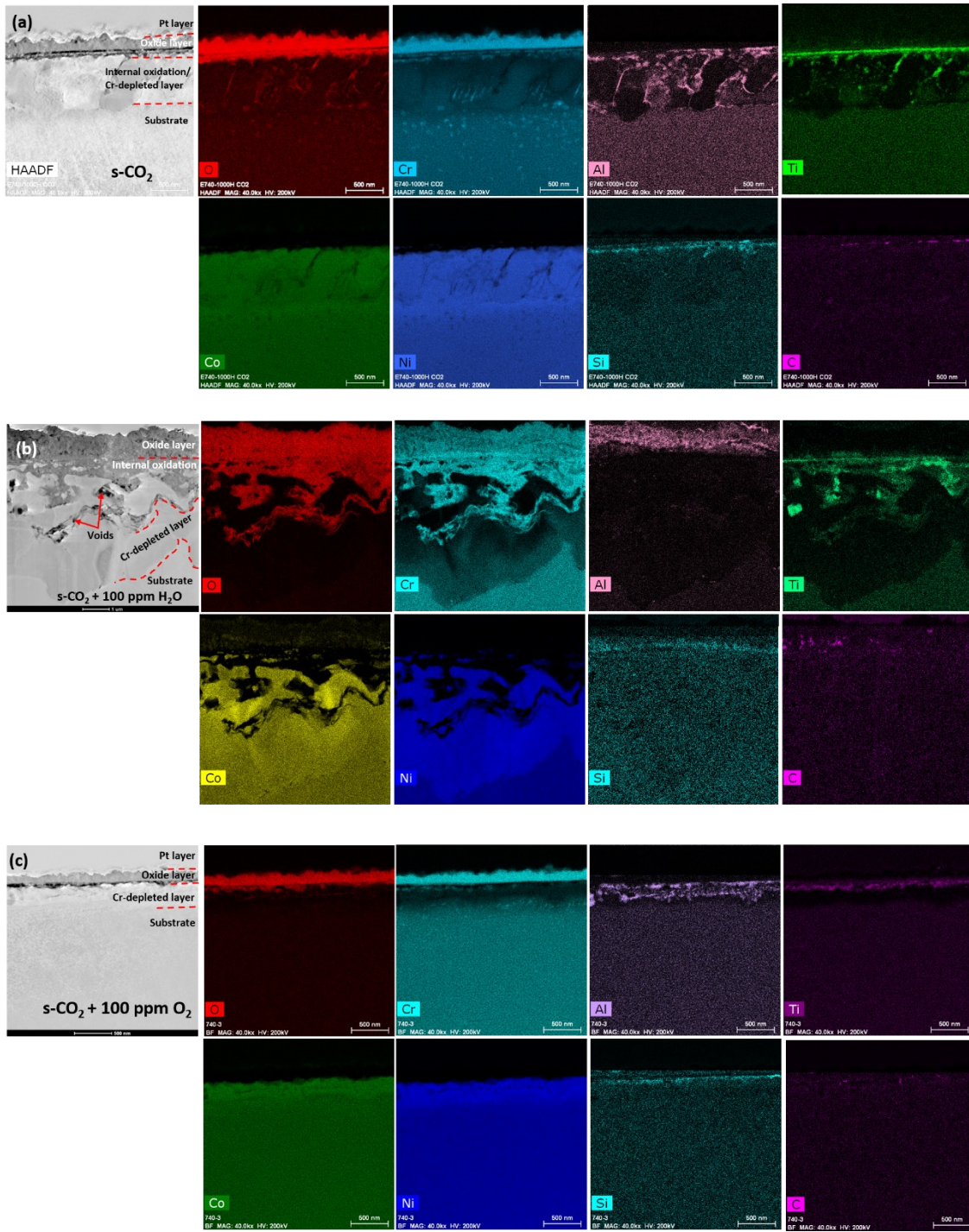
Figure 5-9. Cross-sectional STEM dark field and EDS mapping images of Alloy 740 after 1000 hours exposure to different s-$CO_2$ streams at 600 °C and 30 MPa: (a) s-$CO_2$, (b) s-$CO_2$+100 ppm $H_2O$, (c) s-$CO_2$+100 ppm $O_2$.

Table 5-3. Standard molar Gibbs Free Formation Energy $\Delta G_f^{\emptyset}$ (kJ/mol) of several metal oxides at 600 °C.

| | $Cr_2O_3$ | $Al_2O_3$ | $TiO_2$ | $SiO_2$ | NiO | CoO |
|---|---|---|---|---|---|---|
| $\Delta G_f^{\emptyset}$ (kJ/mol) | -602.20 | -934.6 | -785.13 | -752.54 | -319.3 | -344.7 |

The better resistance of Alloy 740 to carburization could be due to the following factors. Firstly, the accumulated Co in the Cr-depletion zone can retard the diffusion of C from the interface of oxide layer/Cr-depletion layer to the substrate since Co can reduce the tendency of carbide precipitation at grain boundaries [278]. Secondly, the high Ni content in Cr-depletion zone and substrate can help to effectively retard carbide formation. A previous study found that Alloy C-276 required a carbon activity value of two orders of magnitude greater than that for SS316 for $Cr_{23}C_6$ formation even though the two metals had the same Cr content of 17% [310]. Based on related information [285], our calculation (as shown in Table 5-4) also indicates that higher solubility product ($K_{sp}$) and carbon mole fraction ($N_C^{min}$) are needed for $Cr_{23}C_6$ formation in Ni-24Cr compared to Fe-24Cr alloy. Therefore, the synergistic effect of Ni and Co shall provide Alloy 740 with a much lower tendency of carburization in high-temperature s-$CO_2$ streams. As a result, more Cr atoms could be available to support the stability of surface $Cr_2O_3$ scale, resulting in the formation of relatively thinner surface scales and Cr depleted zones in s-$CO_2$ and s-$CO_2$ + 100 ppm $O_2$ than in s-$CO_2$ + 100 ppm $H_2O$. With the addition of $H_2O$ into s-$CO_2$, however, the integrity of surface scale was remarkably degraded and it became less protective, which consequently enhances the outward flux of metallic elements and causes severe oxidation, especially localized nodule growth as shown in Figure 5-4.

Table 5-4. Solubility product ($K_{sp}$) and carbon mole fraction ($N_C^{min}$) for precipitation of $Cr_{23}C_6$ carbide in model Fe-24Cr and Ni-24Cr binary alloys.

| | Fe-24Cr | Ni-24Cr |
|---|---|---|
| $K_{sp}$ | $2.7 \times 10^{-37}$ | $4.7 \times 10^{-34}$ |
| $N_C^{min}$ | $1.6 \times 10^{-4}$ | $4.7 \times 10^{-4}$ |

To further reveal the nodule oxidation mechanism, the cross-sectional TEM examinations were conducted on typical nodules formed on Alloy 740 after 1000 hours of exposure to s-$CO_2$ + 100 ppm $H_2O$, and the results are shown in Figure 5-10. The nodules were composed of $Cr_2O_3$ and $Co_{3-x}Cr_xO_4$ around unoxidized Ni-Co particles. The unoxidized Ni-Co particles had about 82% Ni and 18% Co. During the localized breakdown of the surface oxide scale at defective spots, the fast outward diffusion of alloying elements Co, Ni and Cr would take place. Due to its high chemical affinity to O, Cr would be quickly oxidized. With the depletion of Cr atoms, Co might partially be involved in the nodule formation via Reaction 5-3 for the formation of $Co_{3-x}Cr_xO_4$. Among all the alloying elements, Ni has the least tendency to react with O based on the results shown in Table 5-3. These processes finally led to the formation of nodules which were in the form of unoxidized Ni and Co particles surrounded by $Cr_2O_3$ and $Co_{3-x}Cr_xO_4$.
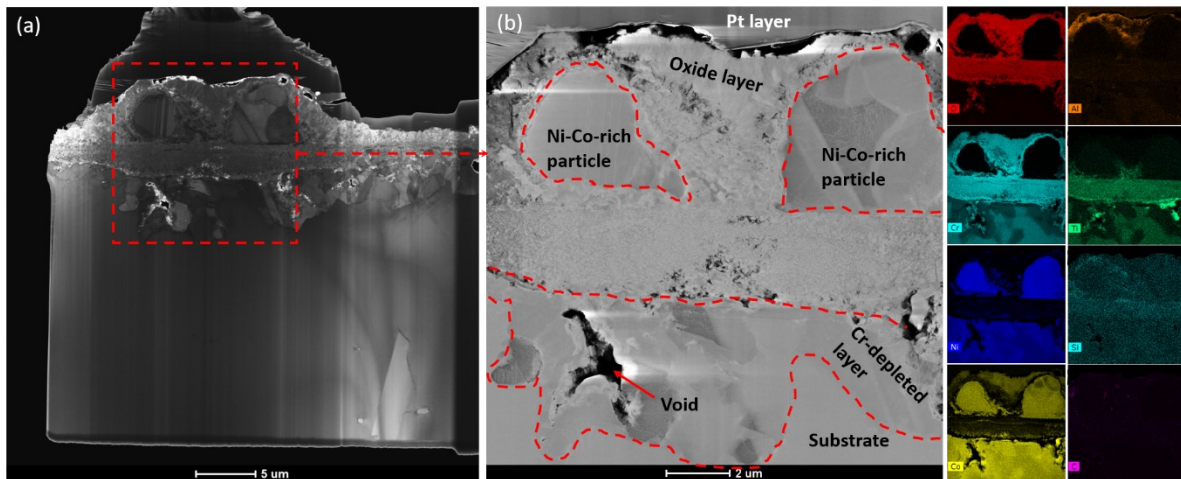


Figure 5-10.  Cross-sectional (a) STEM bright field image and (b) local STEM dark field and EDS mapping images of nodule oxidation area of Alloy 740 in s-$CO_2$ + 100 ppm $H_2O$ at 600 °C and 30 MPa for 1000 h.

### 5.3.2.  Corrosion kinetics of alloys in different s-$CO_2$ streams

Figure 5-11 summarizes the variation of average direct mass change of the two alloys with time in the s-$CO_2$ streams at 600 °C. Based on high-temperature oxidation laws [242], the variation of the mass change with time can be fitted by [311]:

$$\frac{\Delta m}{A} = kt^n \qquad \text{Equation 5-1}$$

where $\Delta m/A$ (mg/cm$^2$) is the weight gain per unit area during time t (h), k (mg·cm$^{-2}$·h$^{-n}$) is the oxidation constant, and n is the reaction order. The positive mass change values of two alloys indicate the formation of oxide layers on the surface, consistent with the previous characterization results of optical, XRD, SEM and TEM. In pure s-CO$_2$, both alloys exhibited near parabolic behaviour (n≈0.5), suggesting that the oxidation process would be controlled by the outward diffusion of Cr [242, 302]. The addition of 100 ppm H$_2$O impurity in s-CO$_2$ increased the mass gain of the alloys with higher k values. The n values decreased to 0.38 for SS310 and 0.35 for the early oxidation of Alloy 740. Note that Alloy 740 exhibited an accelerated mass gain after 510 hours of exposure, very likely due to the enhanced nodule and internal oxidations. In s-CO$_2$ + 100 ppm O$_2$, the n value further decreased to 0.25 on SS310 and 0.27 on Alloy 740, likely due to the improved stability of surface oxide layer and the inhibited internal and nodule oxidations as shown in Figure 5-4.
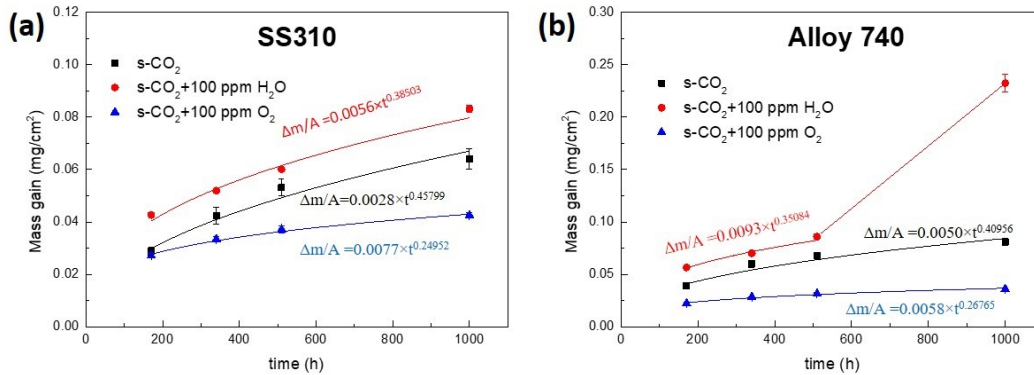


Figure 5-11. Variations of direct mass changes of (a) SS310 and (b) Alloy 740 with time in different s-CO$_2$ streams at 600 °C and 30 MPa.

Because the complicated corrosion processes (such as general oxidation, localized nodule formation, carburization and/or internal oxidation) occurred on the two alloys in the s-CO$_2$ streams, direct mass change results may not provide accurate corrosion rates for the appropriate alloy selection of construction materials from an engineering design perspective. As such, the mass loss measurement method was carried out to meet the industrial demands, and the obtained corrosion rate results are shown in Figure 5-12. The average corrosion rate of SS310 in s-CO$_2$ was in the range of 5.4-5.6 µm/y and also slightly decreased with time. The corrosion rates were increased with the addition of 100 ppm H$_2$O

and further increased with 100 ppm $O_2$. The former could be enhanced because of the nodule and internal oxidations while the latter could be caused by more severe carburization and possible dissolution of carbides/over-etching of the substrate during descaling. Nevertheless, in $H_2O/O_2$-doped s-$CO_2$, the corrosion rates gradually decreased with time because of the further formation of surface oxide scale. The average corrosion rates of Alloy 740 in s-$CO_2$ and s-$CO_2$ + $O_2$ decreased with time from 7.2 to 3.7 μm/y and from 5.1 to 1.1 μm/y, respectively. In s-$CO_2$+100 ppm $H_2O$, the corrosion rates decreased in the early oxidation stage and then increased from 510 to 1000 h due to the accelerated nodule oxidation.
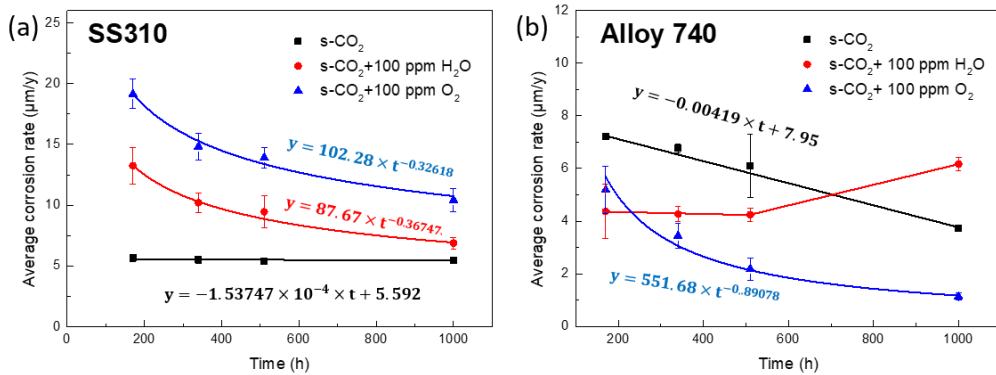


Figure 5-12. Variation of corrosion rate of (a) SS310 and (b) Alloy 740 with time in different s-$CO_2$ streams at 600 °C and 30 MPa.

A comparison of corrosion rates between SS310 and Alloy 740 generally shows that Alloy 740 exhibits better resistance than SS310, especially in s-$CO_2$ with the presence of $H_2O$ or $O_2$. The highest average corrosion rate of SS310 was $19.15 \pm 1.21$ μm/y, which occurred at the early exposure stage. However, it is still much lower than the allowable metal degradation rate of compact heat exchangers as 2 mm in 200,000 hours (87 μm/y) [312]. Thus, both SS310 and Alloy 740 show acceptable long-term corrosion resistance in different s-$CO_2$ streams and appear to be the promising constructional candidates for the Brayton system. However, caution is needed on the application of SS310 in a high-temperature s-$CO_2$ with $H_2O$ and/or $O_2$ because of enhanced carburization.

## 5.4. Conclusions

The corrosion performances of SS310 and Alloy 740 in different s-CO$_2$ streams (s-CO$_2$, s-CO$_2$ + 100 ppm H$_2$O, s-CO$_2$ + 100 ppm O$_2$) were investigated at 600 °C and 30 MPa for up to 1000 h and the following major findings are made:

- In three s-CO$_2$ streams, both general oxidation and localized breakdown (nodules) took place on the tested alloys. During the exposures, the protective continuous chromia (Cr$_2$O$_3$) layers were formed on the two alloys. Besides, minor amount of SiO$_2$ was incorporated into the surface chromia layer on SS310 while SiO$_2$/Al$_2$O$_3$/TiO$_2$ into that on Alloy 740. The nodules formed on SS310 and Alloy 740 consist of Fe$_{3-x}$Cr$_x$O$_4$ and Co$_{3-x}$Cr$_x$O$_4$, respectively.

- The addition of 100 ppm H$_2$O into s-CO$_2$ significantly accelerated the general and nodule oxidations while the presence of 100 ppm O$_2$ improved the stability of the surface Cr$_2$O$_3$ layer and inhibited nodule formation.

- The addition of H$_2$O or O$_2$ into s-CO$_2$ made SS310 more prone to carburation. However, the effect of H$_2$O or O$_2$ on the carburization of Alloy 740 was negligible, possibly due to the high contents of Co + Ni in the Cr-depletion zone and substrate. Still, quantitative analyses on larger areas are needed to further confirm the carburization behavior.

- In different s-CO$_2$ streams, the direct mass gains of SS310 and Alloy 740 generally followed parabolic or near-parabolic behaviors. The average corrosion rates of the two alloys demonstrated their acceptable long-term corrosion resistance in the high temperature s-CO$_2$ streams and Alloy 740 generally exhibited better performance than SS310. In light of its high risk of carbonization, caution needs to be exercised when utilizing SS310 in Brayton cycle system.

# Chapter 6. Corrosion Performance of Candidate Heat Exchanger Alloys under Advanced Pressurized Oxy-fuel Natural Gas-fired Conditions

**Abstract**

Advanced pressurized oxy-fuel combustion technologies have been developed to significantly improve thermal energy conversion efficiency and reduce greenhouse gas emission. However, materials knowledge gaps, especially the selection of appropriate constructional alloys for boiler tubes, retard the commercialization of the technologies. In this study, the corrosion performances of three candidate alloys (SS347, Alloy 800AT and Alloy 825) were investigated in simulated pressurized oxy-fuel natural gas-fired environments at 600 °C and 15 MPa. In the simulated hot flue gas ($H_2O + CO_2 + O_2$), the formed surface oxide scales on the alloys were mainly composed of $Cr_2O_3$ oxides and several alloying elements (including Si, Al and/or Ti) accumulated at the interface of oxide layer/substrate. Among the gas species, $O_2$ acted as a dominant oxidant on oxide formation, and there was a critical $O_2$ content (~2%), above which nodular oxidation and average corrosion rates were remarkably suppressed. The effect role of $H_2O$ was very likely to be on oxide further growth and evaporation, while the presence of $CO_2$ had no influence on the alloy carburization. Compared with the other two alloys, Alloy 825 exhibited the best performance. From a corrosion perspective, the three alloys have acceptable corrosion resistance for boiler tube construction.

**Keywords**: Pressurized oxy-fuel combustion; Hot flue gas; General and localized oxidation.

## 6.1. Introduction

Background information on pressurized oxy-fuel natural gas-fired technology is referred to Section 1.2.

Despite its attractive advantages, significant material technology gaps, particularly the selection of appropriate boiler tube alloys of construction, must be addressed to advance

the successful commercialization of the technology at global energy sectors. Under designed operation conditions, the nature of the flue gas in the combustion chamber of an oxy-fuel natural gas-fired plant is remarkably different from those generated at conventional air combustion plants. In the combustion chamber, the temperature and pressure of the flue gas can be high up to 650 °C and 15 MPa on the fireside surface of boiler tubes [13], thus introducing a concern of whether the tube alloys used at the conventional air combustion plants are still suitable for long-term safe operation at the oxy-fuel plants.

Based on the mechanical property criterion of boiler tube alloys (i.e., 100,000 h creep rupture lifetime at 100 MPa stress) [313], several austenitic stainless steels (such as SS310 and SS347) and high temperature Ni-based alloys (Alloy 617, Alloy 800 and Alloy 625, etc.) are favorable candidates at temperature up to 650 °C [50, 314].

From a corrosion perspective, the boiler tube alloys must be able to resist the attacks from both inside heat transfer fluids and fireside flue gas. Over the past few decades, a number of researches have been initiated to investigate corrosion of steels and alloys in high-temperature supercritical water and $CO_2$ environments for the development of next-generation thermal and nuclear power plants [53, 54]. For example, the results showed that some Cr-enriched alloys, such as SS347 and Alloy 800, exhibited reliable long-term corrosion performance in high-temperature supercritical water environments because of the formation of protective surface $Cr_2O_3$ scales [273, 281, 315]. As for the fireside corrosion, previous studies implied that Cr-bearing steels might experience severe corrosion damage when exposed to high-temperature flue gas composed of $H_2O$ and/or $CO_2$ [53, 54]. For example, the corrosion rates of Fe-Cr steels are usually exacerbated in high-temperature steam due to the formation of Cr-depletion zones under the surface oxide scales and deleterious steam-assisted $Cr_2O_3$ evaporation into gaseous $CrO_2(OH)_2$. Increasing Cr content in the steels may improve the stability of the surface chromia scales. Moreover, the presence of $CO_2$ possibly introduces unwanted carburization risk, which has the potential to retard the outward diffusion of Cr for the formation of protective $Cr_2O_3$ and advance the formation of brittle phases (like $Cr_{23}C_6$ and $Cr_7C_3$) [316]. For instance,

Fe-2.25Cr and Fe-9Cr alloys were found to experience both external oxidation and internal carburization with intergranular $(Fe, Cr)_7C_3$ precipitates after 120 h exposure to 0.2 atm $CO_2$ at 650 °C [317]. However, most of the previous fireside corrosion studies were carried out at atmospheric pressure [303, 318]. As described above, the hot flue gas in the combustion chamber of the oxy-fuel plant is under pressurized conditions. More importantly, the contents of $H_2O$, $CO_2$ and $O_2$ in the flue gas are significantly different from previous testing conditions, and it is unclear whether they have synergistic effects on the fireside corrosion of boiler tubes. For example, the $O_2$ concentration is about 2-4% in the hot flue gas at the oxy-fuel plants, which is different from those shown in previous investigations [319, 320]. According to our comprehensive literature review, very limited information is available about the corrosion of steels and alloys in the pressurized mixture of $H_2O/CO_2/O_2$ at high temperature [321, 322], making the selection of suitable alloys of construction difficult.

Therefore, this study aims at investigating the corrosion modes and extents of three candidate alloys (SS347, Alloy 800AT and Alloy 825) under simulated pressurized oxy-fuel combustion conditions to support the deployment of the oxy-fuel natural gas-fired technology at industrial-scale. Note that SS347 and Alloy 800AT have been approved as the constructional alloys under ASME Boiler and Pressure Valve Code [69]. Alloy 825, a well-known high-temperature welding filler for interconnecting boiler tubes [323], is thus included in the study. It is anticipated to fill some knowledge gaps of how alloys corrode under the pressurized oxy-fuel combustion conditions and partially support the development of cost-effective materials selection strategy for the construction and long-term safe operation of advanced pressurized oxy-fuel power plants at Canadian and international energy sectors.

## 6.2. Experimental Procedure

### 6.2.1. Corrosion sample preparation

The chemical compositions of three alloys are listed in Table 6-1. Please refer to Section 3.2.1 on the details of sample preparation.

Table 6-1. Chemical compositions (wt.%) of tested alloys.

| Alloy | Fe | Cr | Mo | Ni | Mn | Si | S | C | Co | Cu | Ti | Al |
|-------|-----|------|------|------|------|------|--------|-------|------|------|------|------|
| SS347 | 69.7 | 17.7 | 0.31 | 9.7 | 1.64 | 0.65 | 0.004 | 0.057 | - | 0.27 | - | - |
| 800AT | 44.1 | 20.7 | 0.18 | 32.4 | 0.83 | 0.19 | <0.005 | 0.008 | 0.05 | 0.12 | 0.46 | 0.54 |
| Alloy 825 | 30.3 | 22.7 | 3.10 | 39.6 | 0.80 | 0.30 | 0.002 | 0.010 | - | 1.90 | 0.80 | 0.20 |

### 6.2.2. Test methodology and procedures

High-temperature autoclave tests were conducted under simulated pressurized oxy-fuel natural gas combustion conditions in a 1 L autoclave made of Alloy 625. The chemistry of simulated gaseous mixture at each test is shown in Table 6-2. In all the tests, the contents of $H_2O$ and $CO_2$ were controlled as 60 mol.% and 33 mol.%, respectively, to represent major gases in the flue gas produced in the combustion chamber based on pilot-scale campaign results [324]. The concentration of $O_2$ varied from 2 mol.% (in Tests #1-3) to 7 mol.% (in Test #4), based on that 2% represents typical $O_2$% in the pressurized oxy-fuel combustion chamber and 7% is for the case with excess oxygen supply [325]. In Tests #1-3, 5 mol.% Ar gas was supplied as a compensation for the reduced $O_2$ content, making the total testing pressure of the gaseous mixture reaches 15 MPa at 600 °C. Before starting Test #1, the inside surfaces of the autoclave wall and lid were completely polished and cleaned. But the inside surfaces of the autoclave remained in the oxidized state in Tests # 2-4 as it was found that the state of autoclave inside surfaces had an unexpected effect on the chemistry of designed testing environments. Detailed information can be found in Section 6.3.1.

Table 6-2. The gas compositions (mol.%) used in designed tests at 600 °C.

| Test # | $H_2O$ | $CO_2$ | $O_2$ | Ar |
|--------|------|------|------|------|
| 1 | 60 | 33 | 2 | 5 |
| 2 | 60 | 33 | 2 | 5 |
| 3 | 60 | 33 | 2 | 5 |
| 4 | 60 | 33 | 7 | - |

To achieve the required testing conditions in the autoclave, chemical simulations based on Peng-Robinson equations [326] were performed firstly to estimate the desired amount of water and pressure of each gas phase in the sealed autoclave at 25 °C. After that, several blank tests were conducted to further examine and validate the simulation results. Figure 6-1 schematically shows the charging parameter of each component at 25 °C to achieve the required hot flue gas environments at 600 °C.
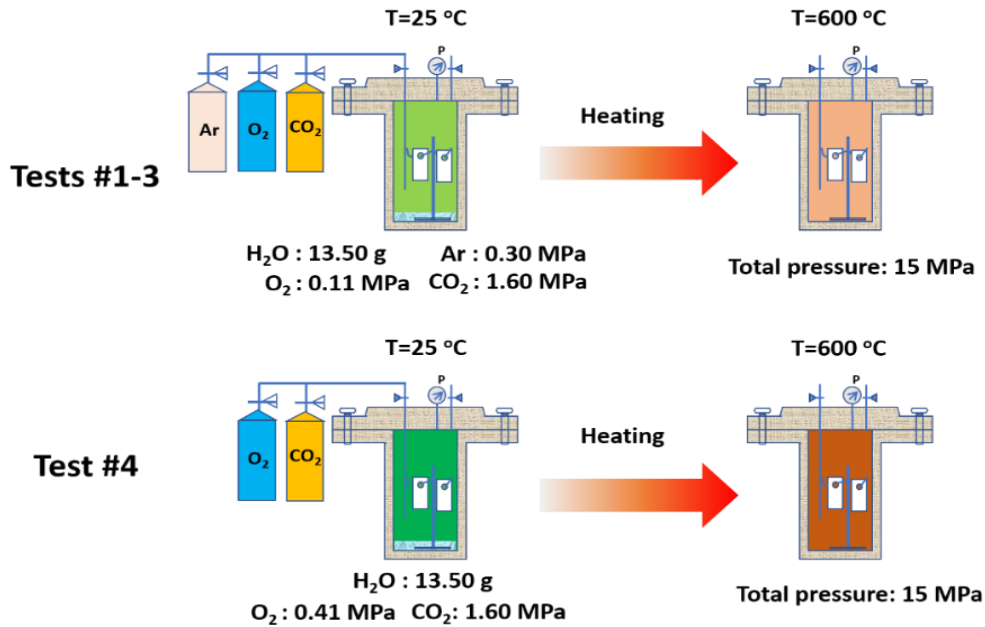


Figure 6-1. Schematic of experimental methodology and procedures used for the designed autoclave tests as shown in Table 6-2.

In each autoclave test, four freshly-prepared coupons of an alloy were carefully accommodated on a custom-made holder and then allocated into the autoclave. After that, the autoclave was sealed and then purged with ultrapure $CO_2$ (99.995%), followed by charging required amounts of water, $O_2$ (or $O_2+Ar$) and $CO_2$ through the inlet/outlet valves at 25 °C. Before charging into the autoclave by syringe injection, the ultrapure water was deaerated with ultrapure $CO_2$ to remove the dissolved $O_2$. After charging, the inlet/outlet valves were closed and the autoclave was heated to 600 °C with a total pressure of about 15 MPa. After 120 h at 600 °C, the autoclave was powered off and cooled down in air to room temperature. The testing gas was purified using 1 M NaOH solution and then

discharged into the air. All the alloy samples were removed from the autoclave for corrosion rate assessments and surface corrosion product characterizations.

### 6.2.3. Corrosion rate assessments

The corrosion rates were evaluated by two different methods, including direct mass change measurement (mass change before and after an autoclave test) and mass loss assessment which involves two major steps: (a) descaling the formed surface corrosion product on an alloy coupon and (b) weighing the mass change of the coupon before autoclave testing and after descaling. For comparison, all the obtained results were converted to the thickness of the consumed alloys in unit time (i.e., μm/y) [112].

The direct mass change method is based on the assumption that oxidation would be the dominant process during high-temperature exposure and the formed surface oxides remain relatively intact without noticeable exfoliation, spallation or evaporation. Thus, the corrosion rate (μm per year) of a coupon can be estimated by :

$$\text{Corr. Rate} = \frac{8.76 \times 10^4 \times \Delta W_g \times \tau}{A\rho t}$$
 Equation 6-1

where $\Delta W_g$ (mg) is the mass change value of the coupon before and after its autoclave exposure; $\tau$ is the mass ratio of the alloying element to oxygen in the formed oxide; A (cm$^2$) is the exposed surface area of each coupon; t (hour) is the testing duration; $\rho$ (g/cm$^3$) is the density of alloy. The densities of SS347, Alloy 800AT and Alloy 825 are 7.96, 7.94 and 8.14 g/cm$^3$, respectively. Note that $\tau$ is ~2.16 for $Cr_2O_3$ with or without trace amounts of element Fe and Ni [295]. In this study, the average corrosion rate of an alloy was obtained from four parallel tested coupons and expressed as "average value ± standard deviation of the average" based on ASTM G16 [327].

For the mass loss assessment, Please refer to Section 4.2.3 for the experimental details.

### 6.2.4. Post-mortem examination of the formed corrosion products

Please refer to Section 4.2.3. on the detailed characterization techniques, including SEM, FIB, and TEM.

## 6.3.  Results and Discussion

### 6.3.1.  Corrosion kinetics of the alloys in simulated high-temperature flue gas

Figure 6-2 shows the direct mass changes of three alloys before and after Tests #1-4. All the alloys exhibited positive mass change, suggesting the formation of oxides on their surfaces. Among them, Alloy 825 exhibited the lowest mass gain after each test. Interestingly, the mass gain of each alloy continuously decreased from Tests #1 to #3 although the initial chemistry of flue gas in these tests was controlled to be identical (Table 6-1), implying that there would be an unexpected consumption of hot gases (especially $O_2$) through the corrosion of autoclave constructional alloy during the exposures. Moreover, increasing the oxygen concentration in the flue gas from 2% in Test #3 to 7% in Test #4 did not lead to a remarkable change in the mass gains of each alloy.
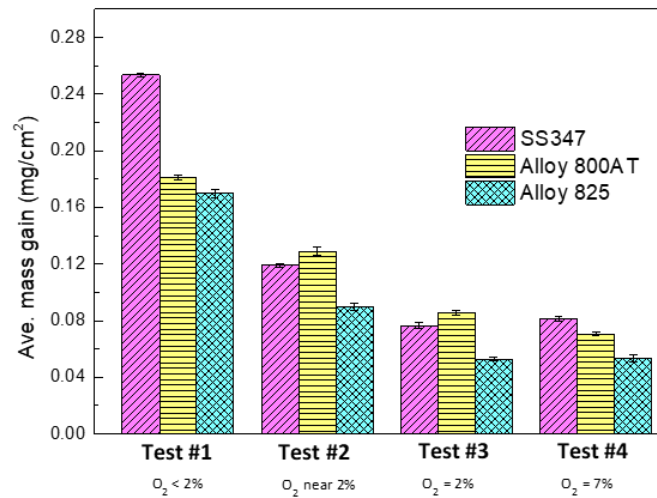


Figure 6-2. Average direct mass change of tested alloys in simulated flue gas environments at 600 °C for 120 h.

To clarify the roles of $O_2$, $H_2O$ and $CO_2$ on oxidation, the Gibbs Free Formation Energy of typical metal oxides at 600 °C were calculated using commercial HSC Chemistry software with its built-in database [225], and the results are shown in Table 6-3. Clearly, $O_2$ should be the dominant oxidant responsible for the initial formation of surface oxide scales on the alloys, while $H_2O$ and $CO_2$ might influence surface oxide growth. Moreover, $Cr_2O_3$ oxide requires the least formation energy compared to Fe and Ni oxides, implying that the surface

scales formed on the three Cr-bearing alloys would likely be Cr-enriched oxides. Note that the consumption of $O_2$ by the autoclave constructional alloy would also occur, especially in Test #1 since the freshly polished inner surface was easily oxidized during high-temperature exposure. Once the surface oxide is formed, the consumption of $O_2$ by the autoclave alloy gradually reduced and the $O_2$ content present in Tests #3 would be very close to 2%. Thus, the $O_2$ concentrations in Tests #1-3 were noted as "< 2%", "near 2%" and "2%", respectively. Table 6-4 shows how the Gibbs Free Formation Energy of $Cr_2O_3$ will vary with $O_2$ content. Even in the condition with 1% $O_2$, the Gibbs Free Formation Energy of $Cr_2O_3$ is still below -600 kJ/mol, indicating that the consumption of $O_2$ by autoclave is unlikely to significantly affect the dominant role of $O_2$ on the oxidation processes of three alloys.

Table 6-3. Calculated Gibbs Free Formation Energy of several typical oxides via the reactions of alloying elements with different oxidants present in the flue gas at 600 °C.

| Oxidants | $\Delta G_f$ (kJ/mol) | | | | |
|---|---|---|---|---|---|
| (mol.%) | $Fe_3O_4$ | $Fe_2O_3$ | FeO | NiO | $Cr_2O_3$ |
| 60% $H_2O$ | -39.84 | -29.94 | -40.33 | 7.34 | -134.12 |
| 33% $CO_2$ | -28.51 | -18.62 | -29.01 | 18.66 | -122.80 |
| 7% $O_2$ | -421.64 | -401.84 | -422.64 | -327.29 | -610.20 |

Table 6-4. Theoretical calculation about the effect of $O_2$ content on Gibbs Free Formation Energy of $Cr_2O_3$ in the flue gas at 600 °C.

| $O_2$ mol.% | $P_{(O2)}$ (MPa) | $\Delta G_f$ of $Cr_2O_3$ (kJ/mol) |
|---|---|---|
| 1 | 0.150 | -602.23 |
| 1.5 | 0.225 | -605.17 |
| 2 | 0.300 | -608.11 |
| 7 | 1.050 | -610.20 |

As described above, descaling and mass loss measurements were also employed to assess the corrosion kinetics of three alloys in the hot flue gas at 600 °C. Figure 6-3 shows the mass loss results of the alloys in each test. After each exposure, the average mass loss of

Alloy 825 was still noticeably lower than those of SS347 and Alloy 800AT, consistent with the results from the direct mass change measurements. The weight loss of each alloy also decreased remarkably from Test #1 to #3, but did not experience obvious change from Tests #3 to #4 in which $O_2$ content varied from 2% to 7%.
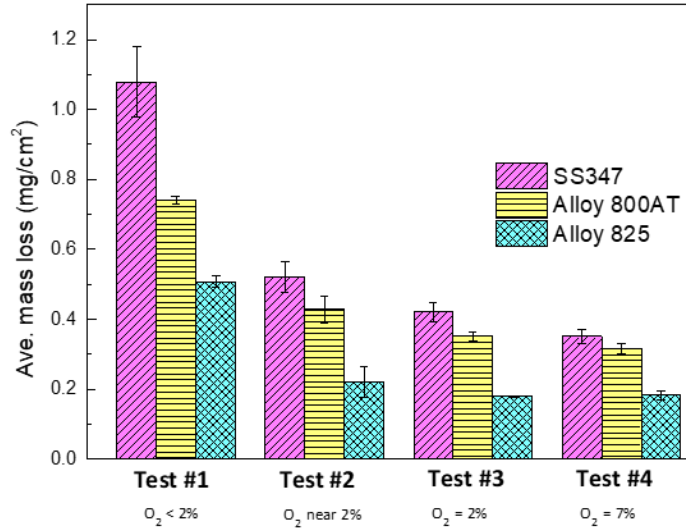


Figure 6-3. Average mass loss of tested alloys in simulated flue gas environments at 600 °C for 120 h.

As mentioned previously, the corrosion rates of three alloys in Tests #1, #3 and #4 were estimated based on direct mass change measurements and mass loss measurements for comparison, and the results are shown in Figure 6-4. In each test, the average corrosion rate of each alloy calculated from direct mass change result is consistently lower than those from mass loss measurements, implying that $H_2O$-assisted evaporation and/or even spalling of surface oxide might also occur in the high-temperature $H_2O$-containing flue gas. $H_2O$ in the hot flue gas might destroy the integrity of surface oxide layer by assisting the volatilization of formed oxide as metal (oxy)hydroxide, especially at the temperatures above 500 °C [54]. The $H_2O$-assisted volatilization reactions of $Cr_2O_3$ and $Fe_2O_3$, the two major oxides formed on the alloys, could be depicted as [54, 328]:

$$\frac{1}{2}Cr_2O_3(s) + \frac{3}{4}O_2(g) + H_2O(g) \rightarrow CrO_2(OH)_2(g) \qquad \text{Reaction 6-1}$$

$$Fe_3O_4(s) + 3H_2O(g) \rightarrow 3Fe(OH)_2(g) + \frac{1}{2}O_2 \qquad \text{Reaction 6-2}$$
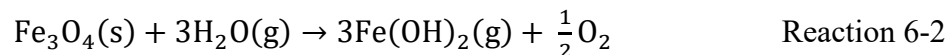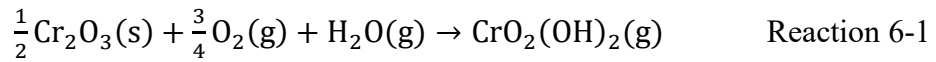
As for $CO_2$-induced carburization, it is unlikely to occur because high contents of $O_2$ and $H_2O$ present in the hot flue gas could significantly inhibit the decomposition of $CO_2$ into carbon-containing species (C/CO) [329]. Moreover, as shown in the TEM analyses below, the formation of a compact and protective $Cr_2O_3$ layer on all the tested alloys could also act as an effective diffusion barrier to retard the penetration of C/CO into the alloys [305, 330].

Thus, the mass loss assessment, as opposed to the direct mass change measurement, is likely to be a more appropriate method to assess corrosion rates of the alloys in the hot flue gas. Based on mass loss calculation, the corrosion rate of the alloys in Test #3 was only about half of those in Test #1, even though the initial $O_2$% in the two tests was controlled to be 2%. The possible reason is that a certain amount of oxygen would be consumed by the oxidation and evaporation of autoclave alloy during the exposure. Further increasing $O_2$ content from 2% (Test #3) to 7% (Test #4) did not result in a remarkable decrease in the corrosion rates of the alloys. These results clearly indicate that there is a critical $O_2$ content (about 2%) in the flue gas, above which a compact and protective oxide layer could grow on the alloys to effectively resist further hot gas attack.

Figure 6-4 shows that the overall ranking of the corrosion resistance of the alloys in Tests #1-4 is:

<div align="center">SS347 < Alloy 800AT < Alloy 825</div>

The difference in corrosion rates could be attributed to the nature of the oxide layer formed on the three alloys. Detailed information about the oxide chemistry and structures can be found in section 6.3.2. Moreover, the highest corrosion rate among the three alloys was $98.97 \pm 9.18$ μm/y which occurred on SS347 in Test #1. This value is much lower than the allowable corrosion rate (350-438 μm/y) of superheater/reheater alloys at conventional coal-fired power plants [331]. Therefore, from the corrosion point of view, three alloys have promising potential for boiler tube construction at the advanced pressurized oxy-fuel combustion plants.
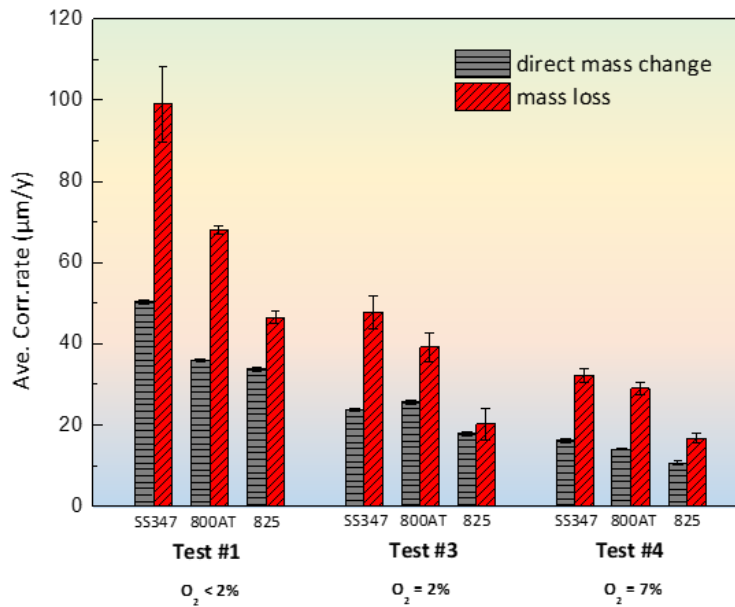
Figure 6-4. Corrosion rates of tested alloys which were calculated based on direct mass change and weight loss methods, respectively.

### 6.3.2. Nature of surface oxide scales formed on the alloys

The photographic images of the alloys after Tests #1-4 are shown in Figure 6-5. All the coupons before corrosion tests readily showed shining and neat surfaces. After exposure, the surfaces of all the coupons became darker with different degrees, indicating the formation of surface corrosion products [209]. Note that the surface color could roughly reflect the thickness of surface corrosion products: darker color often implies thicker oxide formed in comparison with lighter color [332]. The samples in Test #1 exhibited the darkest yellow surface, indicating the formation of the thickest oxide layer among all the tests. From Tests #2 to #4, the surface colour gradually became lighter, implying that the corrosion processes were inhibited with increasing $O_2$ content. The surface color transition tendency is generally in accordance with the above mass gain and mass loss measurement results.

114
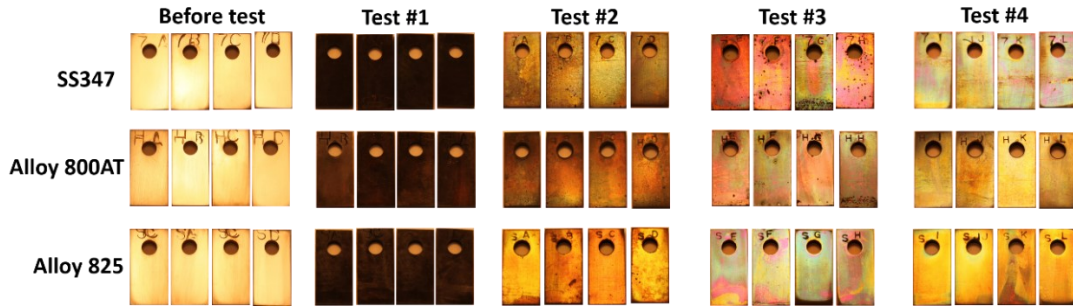
Figure 6-5. The photographic images of three alloys after exposed in simulated flue gas environments at 600 °C for 120 h.

Top-view SEM images of corroded alloy samples are shown in Figure 6-6. After Test #1, the surface scales formed on the three alloys were the mixture of a relatively compact oxide layer and a number of blade-shaped lamella oxides preferentially grew. In fact, such types of lamella oxides have been observed on Fe- or Ni-based alloys after the high-temperature exposure to the environments containing steam [318, 333]. The density of lamella oxides on Alloy 825 was much less than those formed on SS347 and Alloy 800AT.

Surprisingly, after Tests #2-4, nodule oxides instead of lamella were formed on the alloys. The nodule density decreased from Test #2 to #4, indicating that the formation of the nodule oxides would be related to $O_2$ content. Besides nodules, polishing lines generated prior to the corrosion tests were still observed on all the sample surfaces, suggesting that most surface oxide scale formed would be quite thin. The SEM results also indicated that Alloy 825 exhibited better resistance to the hot gas attack because of more obvious polishing lines and a smaller number and size of nodules in Tests #2-4, consistent with direct mass change and mass loss measurement results.
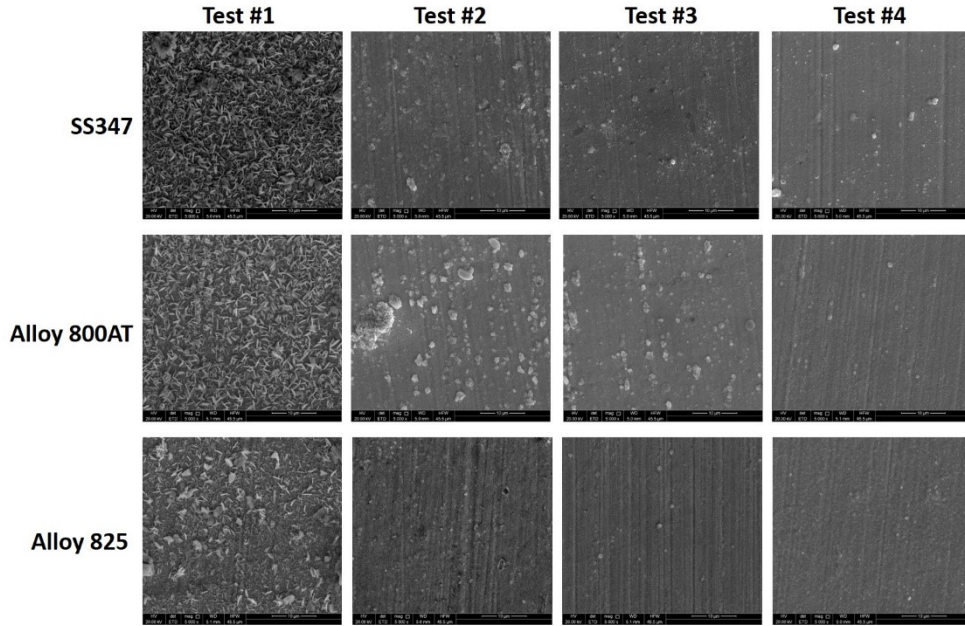
Figure 6-6. Top-view SEM images of SS347, Alloy 800AT, and Alloy 825 samples after exposed in simulated flue gas environments at 600 °C for 120 h.

After FIB operation, the cross-sectional views of the formed oxides/alloy substrates were obtained, and the corresponding SEM images are shown in Figure 6-7. Here, the images of Alloy 800AT are used as a representative of all the alloys. Generally, four typical layers, including Pt layer, oxide layer, sub-layer and alloy substrate, were found on the corroded Alloy 800AT. As mentioned above, the Pt layer was deposited on the corroded sample to protect the surface morphology from potential damages during FIB operation. The grown oxide layer exhibited different features after Tests #1-4. After Test #1, it was found that the lamella oxides grew over a thin and continuous oxide layer. The lamella was outward grown on and coherently connected to the continuous oxide layer, indicating that the lamella would be naturally grown during high-temperature exposure instead of from the deposition of evaporated oxides during autoclave cooldown [334]. After Tests #2-4, the lamella disappeared but nodules were found on the alloy. The nodule width and height were at micrometer level, and they seemed to become smaller from Test #2 to #3, consistent with top-view SEM observation (see Figure 6-6). Underneath the nodules, a continuous and compact oxide layer was also observed. As for the sub-layer under the continuous

oxide layer, its thickness was about several hundred nanometers, which was characterized as Cr-depleted layer with TEM techniques as described in the following paragraphs.
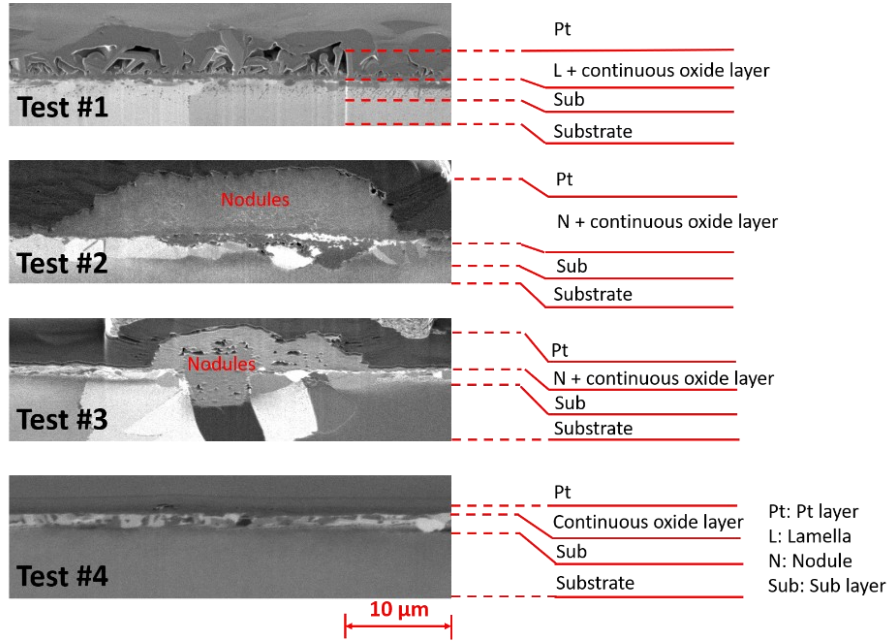


Figure 6-7. Cross-sectional views of corroded Alloy 800AT samples after exposed in simulated flue gas environments at 600 °C for 120 h.

To further characterize the chemistry and microstructures of lamella and continuous oxide layer formed on the alloys after Test #1, STEM and EDS analyses were carried out and the results are shown in Figure 6-8. EDS mapping results indicate that the formed surface scales (including localized lamella and continuous oxide layer) on the three alloys are composed of Cr oxides. The structure of surface oxide scale on SS347 was identified using CBED and SAED techniques, and the results are shown in Figure 6-9. Both the localized lamella and continuous oxide layer are identified as $Cr_2O_3$ structure. This is consistent with the above thermodynamic calculation shown in Table 6-3, i.e., $Cr_2O_3$ shall be the most stable oxide grown on Cr-bearing alloys under the testing conditions.

The preferential formation and growth of localized lamella could be attributed to the following factors. In the formed $Cr_2O_3$ layer, the outward diffusion of cation $Cr^{3+}$ could proceed faster at localized defects, (e.g., screw dislocations or grain boundaries) than in

117

crystalline bulk [335]. Meanwhile, the oxidants ($O_2$ and $H_2O$) in the hot flue gas phase would dissociate at the interface of gas/surface scale to generate $O^{2-}$ for inward diffusion. At the defects, the dissociation of $O_2$ or $H_2O$ could be enhanced due to their higher active energy compared to continuous oxide layer [299]. These would consequently stimulate the preferential formation of lamella at the localized defects. As shown in Figure 6-8the formed localized lamellas are unlikely to protect alloy substrates as they can not block hot flue gas attack. On the contrary, the lamella formation would not only consumes Cr content which is crucial to maintain the stability of the continuous $Cr_2O_3$ layer, but also introduce extra stress within the surface oxide scale due to the impinging effects of orientated lamellas, possibly resulting in the integrity damage of the continuous chromia layer [336, 337]. That is why the three alloys exhibit the highest corrosion rates in Test #1 (see Figure 6-4).
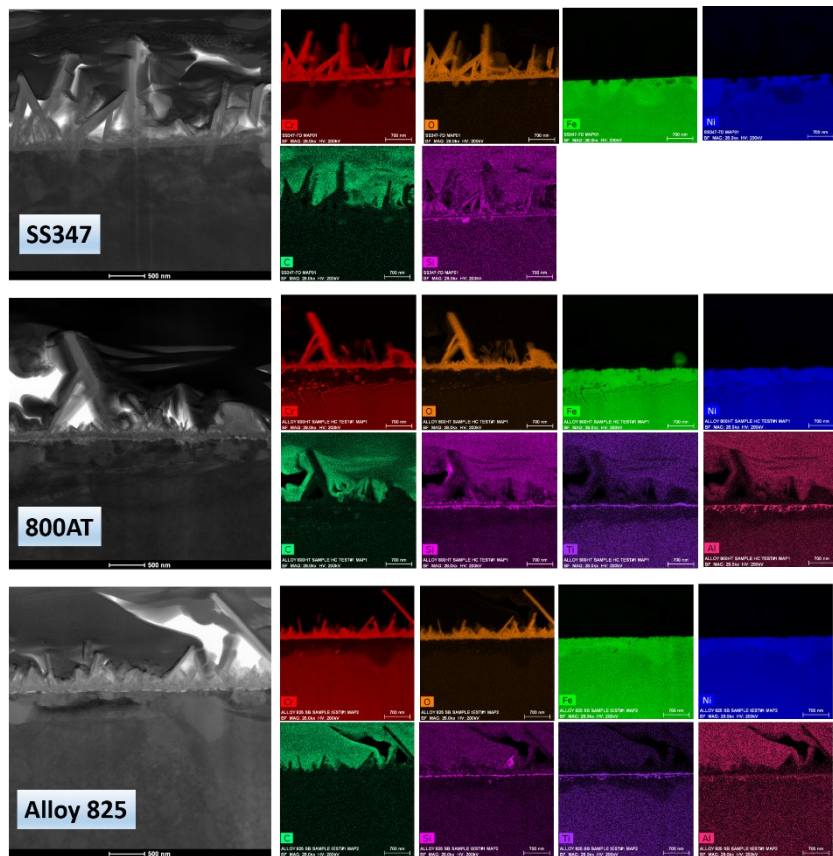


Figure 6-8. Bright field and EDS mapping images of the cross-sections of SS347, Alloy 800AT and Alloy 825 samples after Test #1
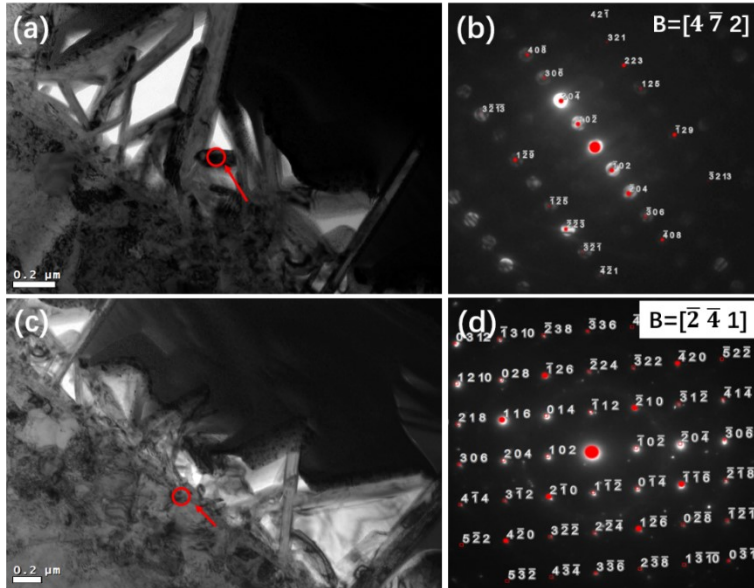
Figure 6-9. TEM results of SS347 steel after Test #1, including (a, b) bright field images of the localized lamella and related CBED pattern, and (c, d) bright field images of the continuous oxide layer and corresponding SAED pattern.

In Tests #2-4, a transition from lamella to nodule oxides took place on the three alloys. To identify the chemical compositions of the nodules, the cross-sectional characterizations of the oxide layers on SS347, Alloy 800AT and Alloy 825 after Tests #3 and #4 were conducted, and the results are shown in Figure 6-10. Note that nodules on the top of the continuous oxide layer are marked by red circles in Figure 6-10. The EDS mapping results indicate that the nodules are consisted of $Cr_2O_3$ without the presence of elements Fe or Ni. Based on the above thermodynamic prediction on the stability of different Cr oxides under this study conditions, the nodules are likely to be $Cr_2O_3$. The transformation from lamella to nodule shapes could be attributed to an increase in nominal oxygen contents in these tests. Higher oxygen content in the flue gas could make the alloys surface more evenly react with oxygen instead of localized adsorption, consequently suppressing the preferential outward growth of lamella. Previous studies also reported that the preferential formation of chromia lamellas occurred in the environments containing a relatively low $O_2$ concentration [299, 338-340]. For example, $Cr_2O_3$ lamellas were found to grow above the dense surface oxide on Fe-20Cr-0.5Si after the exposure to Ar-20CO$_2$-20H$_2$O (vol.%) at 818 °C for 240 h [337]. According to former studies and our current investigation, it is very

likely that there is a critical oxygen content, above which localized preferential growth of $Cr_2O_3$ on Cr-bearing alloys would be significantly suppressed in the high-temperature oxy-fuel combustion environments.
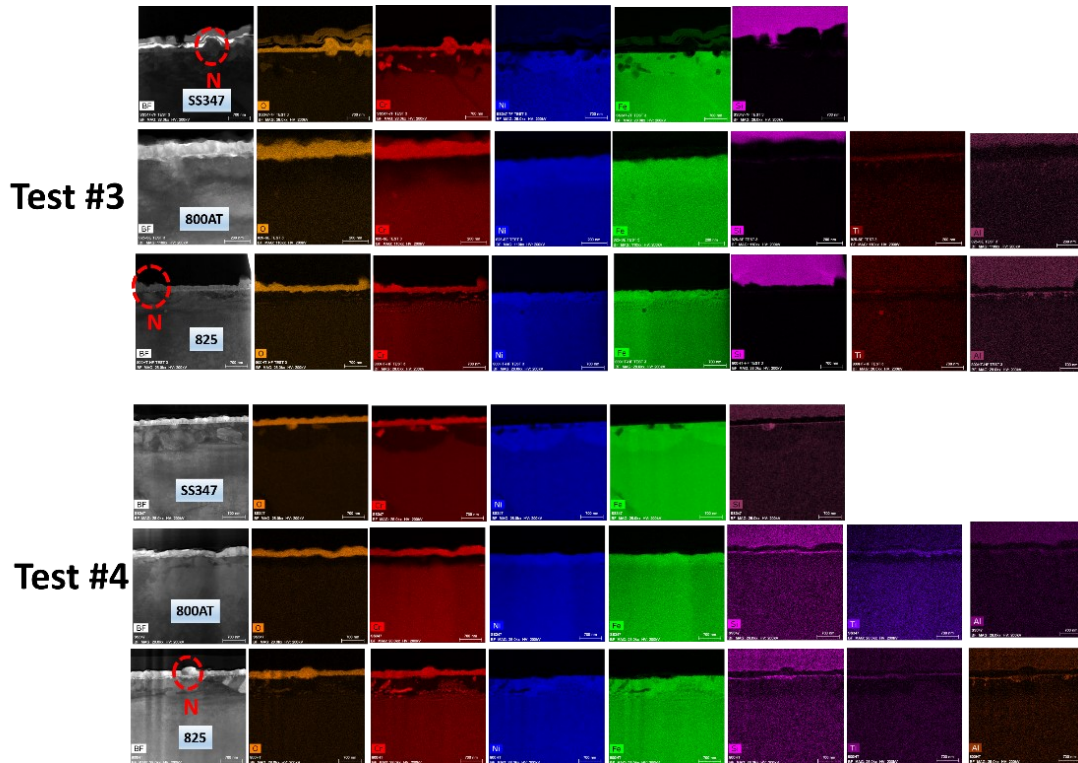


Figure 6-10. Cross-sectional BF and EDS mapping images of the oxides formed on the alloys after Tests #3 and #4. Note that N on the images indicates nodule.

As shown in Figure 6-9 and Figure 6-10, the continuous oxide layer grown on the alloys after Tests #1-4 are also composed of Cr-enriched oxides. It has been reported that at least 10 wt.% Cr is required to form a continuous Cr oxide layer on an alloy even in dry air at 600 ºC [336]. Longer exposure, higher temperature and more aggressive agents under the high-temperature service conditions could need a further increase in the critical Cr % in alloys for the continuous $Cr_2O_3$ layer formation [285]. In steam-containing environments, there is no consensus about the critical Cr% in alloys for the $Cr_2O_3$ layer formation since the results reported from different groups vary a lot. For instance, a study proposed that 20 wt.% Cr was needed for Ni-based alloys at 500-800 °C for 200 h [341], while other group found that with at least 25 wt.% Cr was required to be in Ni-Cr alloys in $Ar-20CO_2-20H_2O$

(vol.%) at 700 and 800 °C for 500 h [342]. Based on this study, a continuous protective Cr oxide layer can be formed on an alloy with Cr content higher than 17 wt.% in the pressurized oxy-fuel combustion environments.

Underneath the continuous Cr oxide layer, a Cr-depleted sub-layer is found. This likely originated from that the diffusion rates of Cr atom within the alloy substrates could be lower than those diffused outward to the oxide/alloy interface for the formation of $Cr_2O_3$ Oxides. In the pressurized oxy-fuel combustion environments, high steam content could induce the evaporation of Cr oxides via the reaction 6-1. However, the accelerated oxidation of the three alloys was not observed yet in this study even though Cr-depleted sub-layers were formed. Note that the current study was conducted under static conditions, and the limited evaporation of Cr oxides might not be sufficient to trigger oxide breakdown [343]. Previous studies found that SS304 and SS310 steels only experienced obvious breakaway oxidation when the flow rate of the $H_2O/O_2$ mixture exceeded 200 mL/min at 600 °C [248, 344, 345]. Therefore, it is still needed to investigate whether the selected alloys experience cyclic breakaway oxidation under flow conditions at the pressurized oxy-fuel natural gas-fired plants for long-term safe operation.

Among the three alloys, the thinnest surface oxide and inner Cr-depleted layers were formed on Alloy 825, consistent with the findings of their overall corrosion resistance ranking. Besides the thin protective oxide layer, the accumulation of alloying elements Si, Al, and Ti were also found just below the oxide/substrate interfaces on Alloy 800AT and Alloy 825. Such accumulation has been recognized for its protective characteristics on the stability of surface Cr-enriched oxide layers [265, 346]. For example, Thuan et al. [347] found that the addition of Si up to 0.5% in Fe-Cr and Fe-Cr-Ni alloys resulted in a remarkable decrease in the oxidation rates of the alloys. It was also found that the addition of 0.1% Si into Fe-20Cr could prevent carburization by reducing the outward diffusion of Fe/Cr and facilitating the rapid formation of $Cr_2O_3$ at the early oxidation stage [243]. Moreover, the accumulation of elements Ti and Al at the interface could act as a diffusion barrier to retard the growth rate of Cr oxide layer [348]. Furthermore, the accumulation of

Si, Al and/or Ti may also help reduce the necessary Cr% for the formation of a continuous and protective Cr-enriched oxide layer on a Cr-containing alloy [291].

## 6.4. Conclusions

The corrosion performance of SS347, Alloy 800AT and Alloy 825 in simulated pressurized oxy-fuel natural gas-fired environments were investigated and following major findings are made:

- In the flue gas of 60% $H_2O$ + 33% $CO_2$ + 2-7% $O_2$ at 600 $^oC$ and 15 MPa, continuous and protective $Cr_2O_3$ oxide layers can be formed on the three Cr-bearing alloys. The accumulation of alloy elements Si, and/or Al and Ti is found at the interface of the oxide/substrate on three alloys.

- Localized formation of Cr oxides in the shape of lamella or nodules occurs on the alloys in the environment with less available oxygen contents. Thermodynamic calculation and testing results indicate that $O_2$ acts as a dominant agent on the alloy oxidation, and there is a critical $O_2$ content (~2%), below which localized preferential growth of Cr oxides (lamella) occurs, leading to a considerable increase in the corrosion rates of the alloys. In addition, the role of $H_2O$ is more likely to support oxide growth and induce surface oxide evaporation, while the presence of $CO_2$ does not cause an obvious carburization determination after 120 hours exposure effect.

- Mass loss measurement instead of direct mass change method is a more accurate method to evaluate the corrosion rates of the alloys. All the alloys exhibit acceptable corrosion resistance to the hot flue gas and have promising potential for boiler tube constructions at the pressurized oxy-fuel natural gas-fired plants. Among them, Alloy 825 shows the best corrosion performance. Future investigations at pilot-scale pressurized oxy-fuel natural gas-fired plants are recommended to examine the long-term application suitability of the three alloys.

# Chapter 7.  Preliminary Study of High Temperature Molten Salt Corrosion of Alloy 800AT and Alloy 740 Under Oxy-fuel Combustion of Coal/biomass Feedstocks

**Abstract**

Oxy-fuel co-combustion of biomass and coal is a promising technology to achieve negative $CO_2$ emission with a relatively low cost. However, the material technology gaps, especially concerning the selection of heat exchanger materials to resist fireside corrosion by flue gas + deposit ashes, must be addressed to ensure the commercial deployment of this technology. In this study, the high-temperature corrosion behavior of Alloy 800AT and Alloy 740 as candidate heat exchanger materials was studied at 650 °C in simulated flue gas + salt mixture environments of oxy-fuel coal and biomass co-combustion system. Due to the synergistic effects of oxidation, sulfidation and chlorination, both alloys developed porous corrosion products with cracks. Alloy 800AT had an outer Fe-enrich oxide and inner Cr-enrich oxide layers and experienced internal oxidation and intergranular corrosion with extended time. The corrosion products formed on Alloy 740 were multi-layered with oxides and sulfides of Cr, Ni and Co. Due to its higher Cr and Ni content, Alloy 740 exhibited better corrosion resistance than 800AT based on both direct mass change and mass loss measurements.

**Keywords**: Co-combustion; Oxy-fuel; Molten salt; Sulfates; Chlorides.


## 7.1.  Introduction

Over the past few decades, pressurized oxy-fuel combustion technologies have been developed to achieve high fuel combustion efficiency and a significant reduction in $CO_2$ emission [349]. Most recently, novel progress has been made by partially replacing coal with biomass as fuel at the oxy-fuel power plants, resulting in a net reduction in atmospheric $CO_2$ [350, 351]. Biomass fuels, such as forestry, energy crops and agriculture residuals, are renewable and environmentally friendly energy feedstocks [352]. Pioneer pilot-scale testing indicates that co-combustion of coal/biomass is a more effective way of reducing $CO_2$ emission and air pollution at a lower cost compared with the dedicated

biomass combustion power plants [353]. More attractively, most modern fossil fuel power plants can accommodate the co-combustion technology without major modification on existing infrastructure. The replacement of coal with biomass can not only reduce the reliance on fossil fuel, but also avoid landfilling biomass as waste disposal [354].

Pilot-scale investigation has been carried out to advance the deployment of this promising technology. For instance, in a retrofitted 100 kW pilot oxy-combustor with biomass and coal co-firing at Cranfield University, the effects of fuel variability and the recycled ratio of flue gas on the flue gas composition, temperature, heat flux and ash deposition has been studied systematically [355]. In a 0.8 MW oxy-fuel circulating fluidized bed combustor, increasing the amount of co-fired wood pellets from 20% to 50% did not noticeably affect the combustion conditions [356]. In a lab-scale reactor, it is found that the addition of corn stover into anthracite for oxy-fuel co-combustion increased the deposition rate and the chlorine content in fly ashes [357]. Besides, the general operating temperature was in the range of 550-631 °C, which was higher than that of air-firing (509-555 °C). Based on previous studies, it is concluded that oxy-fuel coal/biomass co-combustion system generally has different combustion parameters from conventional air-fuel combustion systems.

Despite the progress, however, the available information is still insufficient to formulate a cost-effective material selection guideline for the core components for the system, especially on the applicable heat exchanger alloys. As described in Section 1.3.2, the heat exchangers are supposed to resist the attacks by heat transfer fluids (s-$H_2O$ or s-$CO_2$) from inside and by flue gas and deposit ashes from fireside. From inside, considerable works have been conducted on the corrosion of candidate heat exchanger alloys in high-temperature, high-pressure supercritical fluids for advanced thermal power plant applications [47, 174]. High chromium ferritic steels, austenitic steels and Ni-based alloys generally displayed good corrosion resistance over a wide range of temperatures because of the formation of a protective chromium oxide layer [43, 358]. From fireside, the corrosion-induced damage has always been an on-going concern at the power plants as more severe damage may occur due to the synergistic effects of hot flue gas and salt

deposits [359]. During the oxy-combustion of coal, $O_2$ in the flue gas causes oxidation while the presence of $CO_2$ may result in carburization embrittlement [329, 360, 361]. Because of the high content of S in coals, alkali metal sulfates, combined with other ash components, will deposit onto the heat exchanger surface and lead to high-temperature molten salt corrosion. In the oxy-fuel co-combustion environment, the changes in flue gas chemistry and deposit composition introduce more complicated service environment. Compared with dedicated coal combustion, co-firing biomass and coal brings higher levels of Cl, which could possibly accelerate the molten salt corrosion of superheaters/reheaters at the power plants. The addition of biomass in coal is a conventional way for combustion. However, few public information is available in oxy-fuel combustion environments, making the selection of proper materials for heat exchanger difficult from corrosion perspective [357].

Austenitic stainless steels (such as SS347, Alloy 800) and Ni-based alloys (including Alloy 625, Alloy 740) are two important candidates for the construction of core components at the oxy-fuel plants, such as heat exchangers, headers, steam lines and exhaust gas systems [362, 363]. These alloys exhibit good mechanical behavior by precipitation strengthening and dissolution strengthening, and acceptable oxidation resistance at high temperatures [364, 365]. For instance, as one of the most utilized high-temperature alloy at power plants, Alloy 800 (UNS N08810) has both high strength and corrosion resistance at temperatures up to 760 °C. Based on a recently renewed American Society of Mechanical Engineers (ASME) code [69], Alloy 740 (UNS N08367), a newly-developed low carbon, nitrogen-bearing super-austenitic Ni-based alloy, shows promising corrosion resistance to harsh environments and has been extensively employed in chemical plants and power plants [286, 366]. As described in Chapter 5, this alloy also has good corrosion resistance in high temperature supercritical $CO_2$ streams. However, it is still unclear whether the two alloys are applicable for the oxy-fuel co-combustion processes.

This preliminary study investigates the corrosion behavior of the two candidates heat exchanger materials under simulated oxy-fuel co-combustion, and aims at filling some

knowledge gaps about the corrosion under the oxy-fuel co-combustion conditions and supporting the selection of suitable alloys for the construction of heat exchangers.

## 7.2. Experimental details

### 7.2.1. Testing sample preparation

The chemical compositions of Alloy 800AT and Alloy 740 alloys are shown in Table 7-1. Please refer to Section 3.2.1 on the details of sample preparation.

Table 7-1. Chemical composition of Alloy 800AT and Alloy 740 (wt.%).

| Alloy type | Cr | Ni | Fe | Co | Mo | Al | Ti | Si | Mn | C |
|---|---|---|---|---|---|---|---|---|---|---|
| 800AT | 20.7 | 32.4 | 44.1 | 0.05 | 0.18 | 0.34 | 0.46 | 0.19 | 0.83 | 0.083 |
| 740 | 24.6 | 50.0 | 0.2 | 20.10 | 0.50 | 1.40 | 1.45 | 0.15 | 0.30 | 0.030 |

### 7.2.2. Corrosion testing methodology and procedure

For the purposes of accelerated corrosion evaluation under the oxy-fuel co-combustion conditions, the gas mixture of $CO_2$ + $O_2$ was used to simulate the dry combustion environment with flue gas dehydrated before recycling back to the combustion chamber, and the deposit ash was simplified as the mixture of alkali sulfates and chlorides in this study. The synthetic flue gas was a pre-mixed gas with the identified composition of 4% $O_2$ + bal.% $CO_2$ (vol.%), since 4% is the typical oxygen concentration in the pilot plants operated with recycled hot flue gas [367]. The mixture of alkali sulfates and chlorides was made of $Na_2SO_4$ : $K_2SO_4$ : $NaCl$ : $KCl$ = 5 : 5 : 0.5 : 0.5 in mol.% to ensure the ratio of S/Cl close to those in the ash deposited on the superheater tube fireside surfaces during the co-combustion of 70% peat + 30% woodchip at a pilot fluidized bed combustor [368].

As schematically shown in Figure 7-1, the tests were carried out in a horizontal tube furnace with three heating controlled zone. Sixteen freshly-prepared coupons of each alloy were prepared and embedded in the salt mixture with the salt/sample ratio of 7.5 g/sample in the alumina boat. A glass rod was used to slightly tap the salt to increase its coherence. Following that, the boat was accommodated in the middle section of the furnace tube, where the temperature deviation was controlled to be less than 1 °C. During the tests, the

temperature was controlled at 650 °C and synthetic flue gas was charged with a rate of $\sim 10^{-4}$ $m^3/s$ for atmospheric control. The gas emitted from the tube furnace, which was found to contain ppm level of $SO_2$, was purified using a gas washing bottle with 1 M NaOH solution before being released into the air.
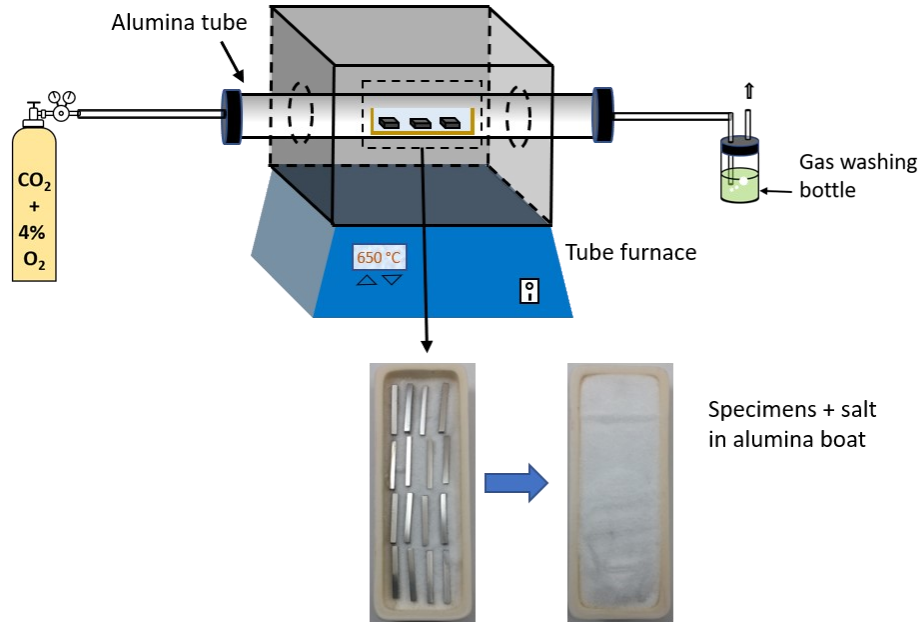


Figure 7-1. Schematic of experimental set-ups and the photo images of how the corrosion specimens were allocated in an alumina boat containing alkali sulfates and chlorides.

After 120 hours of exposure, heating power was turned off and the furnace naturally cooled down to room temperature. All the specimens were taken out, and the deposited salts on most specimens were carefully removed by immersing the specimens in boiling water for 3 min. After that, optical examinations and weight change measurements were performed. One of each alloy didn't experience boiling water immersion but withhold the deposited salts + oxide scales in order to study the morphologies and composition of the corrosion products. For each alloy, four samples (three washed and one with deposited salt) were left for further characterizations while the remaining coupons were sent back into the alumina boat with refreshed salt mixture for the next exposure. To identify the long-term corrosion of the alloys, the tests of 4 cycles (480 hours of exposure in total) were completed.

### 7.2.3. Corrosion rate assessment and corrosion products characterization

Two techniques, including direct mass change and mass loss measurements, were applied to evaluate the corrosion rates of the tested alloys in the simulated oxy-fuel co-combustion environment. Please refer to Section 4.2.3 for the details of direct mass change and mas moss measurements. Note that in this section, the direct mass change of each alloy at each period is acquired from three parallel samples after the removal of surface deposit salt.

After a corrosion test, light optical microscopy was employed primarily to quickly examine the surface morphology of corroded samples. The samples with deposited salts were selected for corrosion product characterization. They were mounted with epoxy, cross-sectioned using a diamond saw-cutter, and polished up to 1 μm diamond grit finish using non-aqueous lubricants. A field-emission scanning electron microscope (SEM) (FEI NOVA230) with energy dispersive X-ray spectroscopy (EDS) was used to investigate the cross-sectional microstructure and identify the distribution of major elements in the corroded samples.

### 7.3. Results and discussions

Figure 7-2 shows the photographic images of Alloy 800AT and Alloy 740 after each exposure to the simulated oxy-fuel co-combustion environment at 650 °C. All before corrosion testing images readily showed metallic luster. In contrast, the surface color of corroded samples turned dark green or grey, implying the occurrence of severe corrosion. In the testing environment, oxidation, sulfidation and chlorination were expected to occur on the alloys. With prolonged exposure time, the sample surfaces became darker, indicating the continuous growth of the surface corrosion products. Besides, localized white spots were also observed on the alloys, indicating the partial spallation of corrosion products occurred.
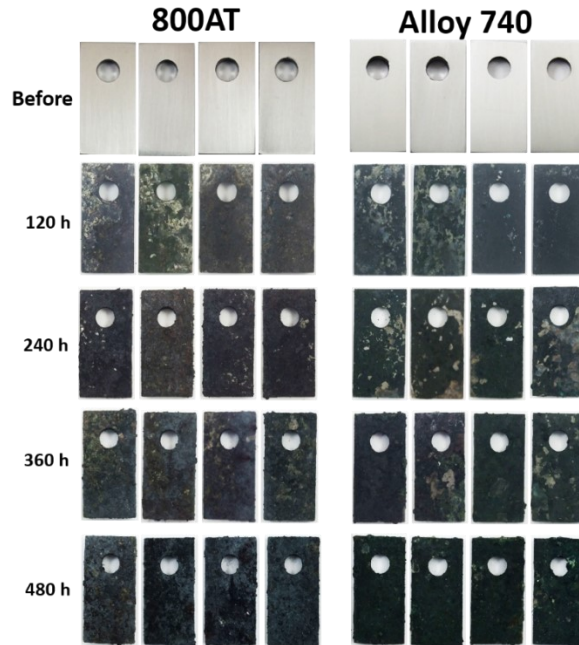
Figure 7-2. Photographic images of Alloy 800AT and Alloy 740 coupons before and after exposure to simulated oxy-fuel co-combustion environments at 650 °C.

Figure 7-3 shows the cross-sectional views of the corroded Alloy 800AT at 650 °C. At the early stage, the formed oxide scale consisted of outer porous and inner relatively compact layers. Further increasing the exposure time to 240 h results in the formation of the thicker outer porous and cracked oxide layer. The presence of pore and cracks in the corrosion layer could be attributed to the internal stress during oxide growth and the thermal stress after cycles of heating and cooling. The pore and cracks would act as localized windows for the ingression of molten salts and gases to the substrate, consequently inducing internal oxidation, sulfidation and chlorination. With the extended exposure time, the inner relatively compact oxide layer disappeared and only a porous and uneven scale was left. Internal oxidation and intergranular corrosion were observed and became more serious with time.
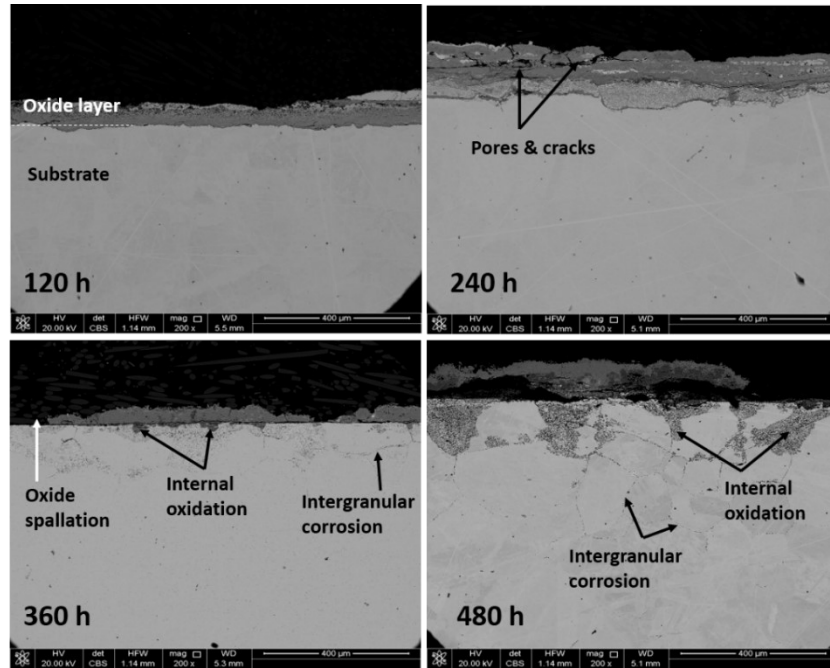
Figure 7-3. SEM cross-sectional images of Alloy 800AT after 120-480 hours of exposure in simulated oxy-fuel co-combustion environment at 650 °C.

EDS maps of the cross-section area of the alloy are shown in Figure 7-4. After 120 hours of exposure, the formed outer porous layer was actually composed of two sub-layers, including outer Ni and Fe oxides, and inner compact and continuous Cr-enriched oxides layer. Slight accumulations of sulfur and chlorine were found within the formed scale. After 480 h, the formed porous and uneven corrosion layer was a mixture of Cr and Fe-enriched oxides. The disappearance of Ni-enriched oxides could be due to spalling effect and/or its higher instability compared to Cr/Fe oxides, as proved by the molar Gibbs Free Formation Energy shown in Table 7-2. As shown in Figure 7-4(b) and (c), the internal oxidation zone was enriched of Ni and depleted of Fe and Cr. It is likely that sulfur involved in internal corrosion. Furthermore, O, S and Cl elements ingressed into the substrate along grain boundaries and contributed to the intergranular corrosion.

Table 7-2. Gibbs Free Formation Energy $\Delta G_f$ of oxides in current testing environments.

|  | $Cr_2O_3$ | $Fe_2O_3$ | NiO |
|---|---|---|---|
| $\Delta G_f$ (kJ/mol) | -853.5 | -541.2 | -142.9 |
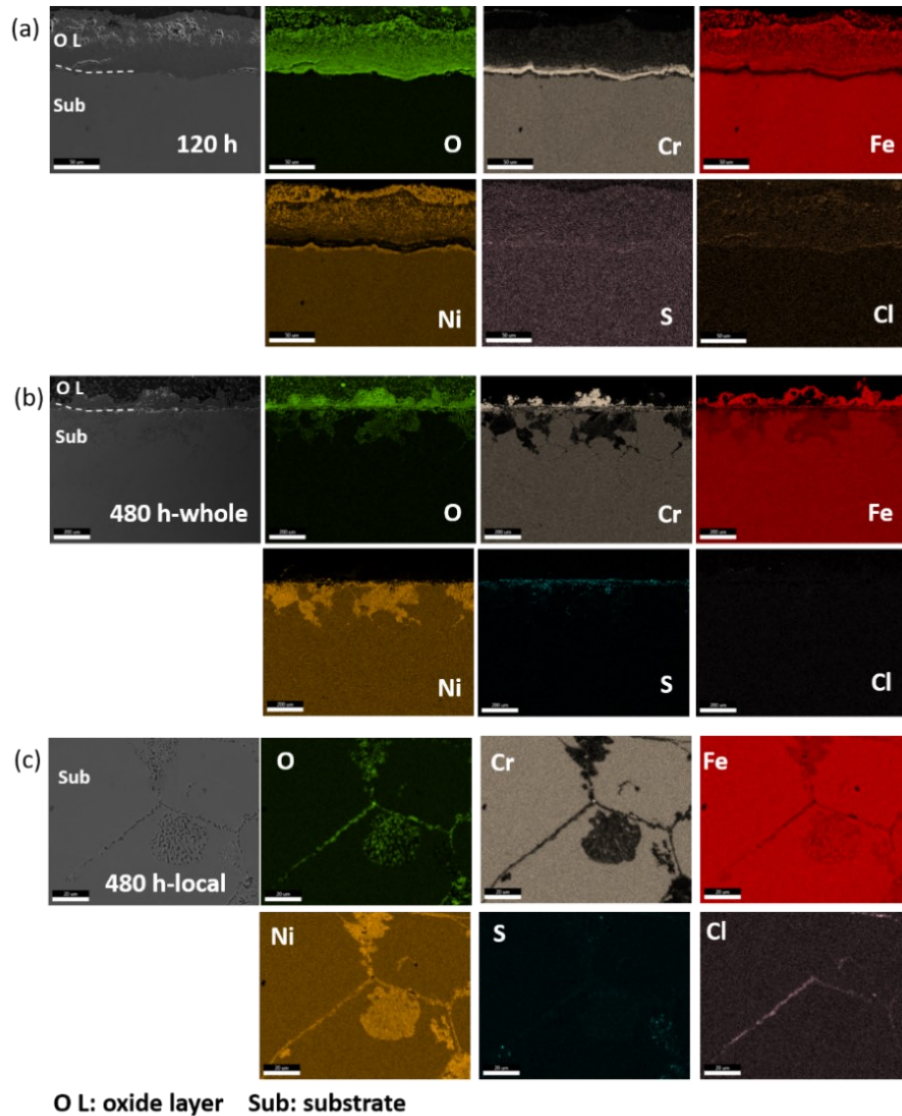
Figure 7-4. Cross-sectional BSE images and EDS maps of Alloy 800AT after (a) 120 and (b, c) 480 hours of exposure in simulated oxy-fuel co-combustion environment at 650 °C.

The cross-sectional views of Alloy 740 corroded in simulated oxy-fuel co-combustion environment at 650 °C are shown in Figure 7-5 and Figure 7-6. In general, the surface scale formed on the alloy was composed of outer unprotective and inner relatively compact and continuous Cr-enriched layer. A Cr-depletion zone under the oxide layer was formed even only after 120 exposure. Sulfur accumulation was observed within the surface oxide scale and Cr-depletion zone. The corrosion layer became thicker and the outer layer transformed

131

into multi-layer structure (a mixture of Cr/Ni/Co oxides and sulfides) with time. After 480 h, Cl accumulation was also found. During the exposure, cracks and pores were developed within the outer oxide layer. One more interesting finding is that different from Alloy 800AT, internal oxidation and intergranular corrosion did not occur on Alloy 740 even after 480 hours of testing, indicating its promising application potential in the co-combustion environments.
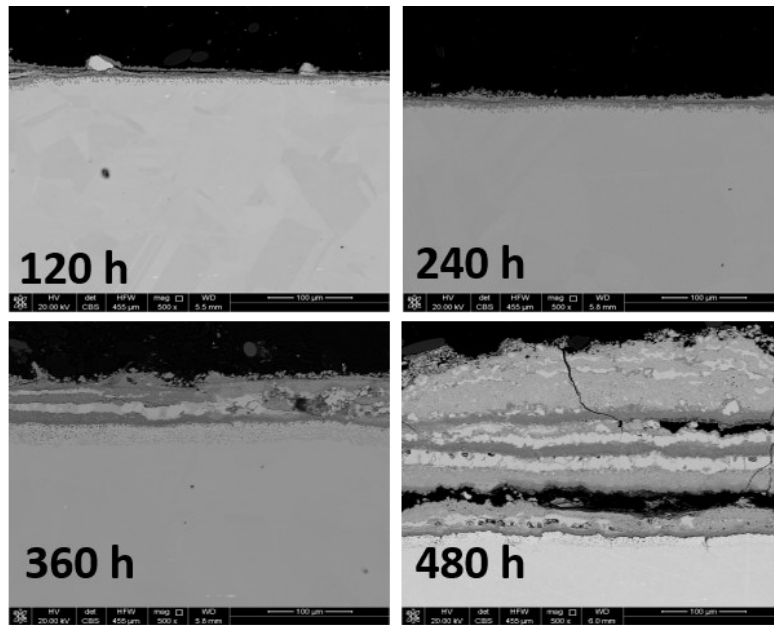


Figure 7-5. SEM cross-sectional views of Alloy 740 after 120-480 hours corrosion in simulated oxy-fuel co-combustion environment at 650 °C.
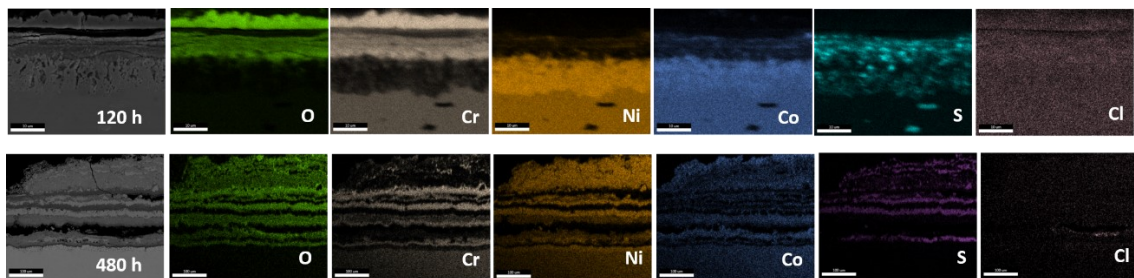


Figure 7-6. Cross-sectional BSE images and EDS maps of Alloy 740 after 120 and 480 h exposures in simulated oxy-fuel co-combustion environment at 650 °C.

It is widely acknowledged that the melting point of the salt mixture is lower than that of a single salt [369]. The melting points of NaCl, KCl, Na₂SO₄ and K₂SO₄ are 801, 770, 884 and 1069 °C, respectively, while the eutectic melting points of NaCl/Na₂SO₄ and KCl/K₂SO₄ are 628 and 694 °C, respectively [370]. Thus, the salt mixture used in the current study shall be at least partially molten at 650 °C, resulting in the corrosion of the alloys dominated by high-temperature molten salt electrochemical reactions, and the typical reactions occurred in the molten salt mixture are shown below [371]:

Anodic: $\qquad M \rightarrow M^{n+} + ne^-$ Reaction 7-1

Cathodic: $\qquad Ox + ne^- \rightarrow Red$ Reaction 7-2
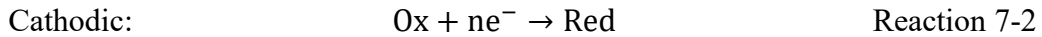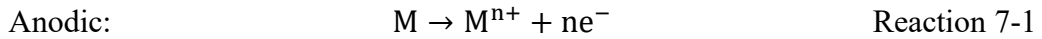
where M represents metallic elements such as Ni, Fe, Cr and Co in the alloy substrate, n represents the number of exchanged electrons. Ox and Red are the oxidant and the corresponding reductant, respectively.

Because of the tested alloys with high Cr content and the presence of oxidizing environment (4% O₂), chromium oxides (Cr₂O₃) would be expected to form on the alloys as the dominant component, similar to the observations of two alloys exposed to air or oxy-fuel flue gas environments [286, 372]. However, further exposure in the molten salt could damage the integrity of Cr₂O₃ layer due to the following reaction [373]:

$$Cr_2O_3 + \frac{3}{2}O_2 + 2SO_4^{2-} = 2CrO_4^{2-} + 2SO_3 \qquad \text{Reaction 7-3}$$
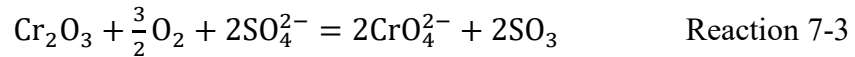
This reaction results in the formation of unprotective outer porous oxide layers and allows sulfates penetrating from the environment into the interface of scale/substrate. Note that S could be formed via [374]:

$$2SO_4^{2-} = 2O^{2-} + 3O_2 + 2S \qquad \text{Reaction 7-4}$$

The released S would react with alloying elements in the substrate to produce sulfides.

Meanwhile, the addition of chlorides in the salt mixture could accelerate the corrosion process. Detailed mechanisms as active oxidation could be depicted as follows. Soon after its formation, molten chlorides could destroy the integrity of the surface chromium oxide layer though the following reactions [375]:

$$8Cl^- + 2Cr_2O_3 + 5O_2 = 4CrO_4^{2-} + 4Cl_2 \qquad \text{Reaction 7-5}$$
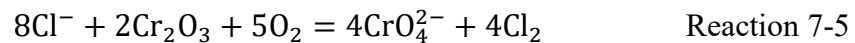
Part of the $Cl_2$ could penetrate through the surface oxide scale and react with substrate metals like Cr to form volatile chlorides, which tend to diffuse outward through the cracks or pores in the oxide and re-oxidized at the interface of scale/gas [369, 376]:

$$2Cr + 3Cl_2 = 2CrCl_3 \qquad \text{Reaction 7-6}$$

$$4CrCl_3 + 3O_2 = 2Cr_2O_3 + 6Cl_2 \qquad \text{Reaction 7-7}$$
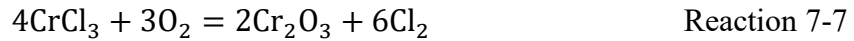
$Cl_2$ is regenerated and the corrosion will continue as a self-sustaining process. It indicates the incorporation of chlorine into the co-combustion system, even with a small amount, could greatly enhance the corrosion degree.

Therefore, the synergistic effects of Cl and S would accelerate the formation of porous oxide layer and even completely damage the whole surface scale on the alloy with "lower" Cr% after long exposure. With the degradation of initially formed $Cr_2O_3$ layer, new chromium oxide layers would be formed on the alloy. The SEM results (from Figure 7-3 to Figure 7-6) suggest that:

(1)  Due to the high Cr content (> 24%), inner relatively compact and continuous Cr-enriched oxide layer is likely to be present on the alloys even after long-term service. Previous studies also indicate that chromium is the most critical alloying element in the alloys to defend the attack of molten sulfates [377].

(2)  Fe might facilitate the corrosion process through the combination with alkali metal and sulfates to form low-melting-point compounds, such as alkali-iron tri-sulfate ($(Na/K)_3Fe(SO_4)_3$, melting point of 550 °C), which would cause consequent severe corrosion. Further characterizations (such as XRD) on the corrosion products are still needed to confirm the formation of alkali-iron tri-sulfate.

(3)  Other alloying elements (Ni and Co) could also play important roles on the stability of the surface oxide layer and the penetration of O, Cl and S for internal and intergranular corrosion. The thermodynamic calculation indicates that Ni and Co have a lower tendency to be oxidized, sulfurized or chlorinated compared to Cr and Fe [377]. It is likely that during the molten salt corrosion, the accumulation of Ni and

Co underneath the $Cr_2O_3$ will defend the ingression of corrodents, thus suppress the internal and intergranular corrosion.

Figure 7-7(a) shows the variation of direct mass change of both alloys with time in simulated molten salt at 650 °C. Both alloys showed positive mass change values, further confirming the incorporation of O, S, and Cl into the corrosion products. The two alloys experienced near parabolic behavior at an early stage (up to 360 h) and then exhibited accelerated mass gain with increasing time. The average mass gain values of Alloy 740 were only about half of that of Alloy 800AT, consistent with SEM/EDS results, i.e., the oxide formed Alloy 740 can protect the metal from severe internal and intergranular corrosion.

As the most conventional and frequently reported method, the direct mass change method could measure the oxidation and corrosion of metals at high temperatures. However, it is not able to provide accurate corrosion rates of the two alloys from engineering design consideration because of the spallation and volatilization of corrosion products, particularly on Alloy 800AT. Thus, the mass loss measurements were performed and the estimated corrosion rates are shown in Figure 7-7(b). The corrosion rates of the alloy peaked at the initial exposure stage and then gradually decreased with time. However, as shown in Figure 7-3 and Figure 7-4, the corrosion rates of Alloy 800AT are likely to be underestimated because of internal and intergranular corrosion occurred, whose influence cannot be precisely estimated from the weight loss measurements. More work is still needed to verify its application for heat exchanger fabrication.
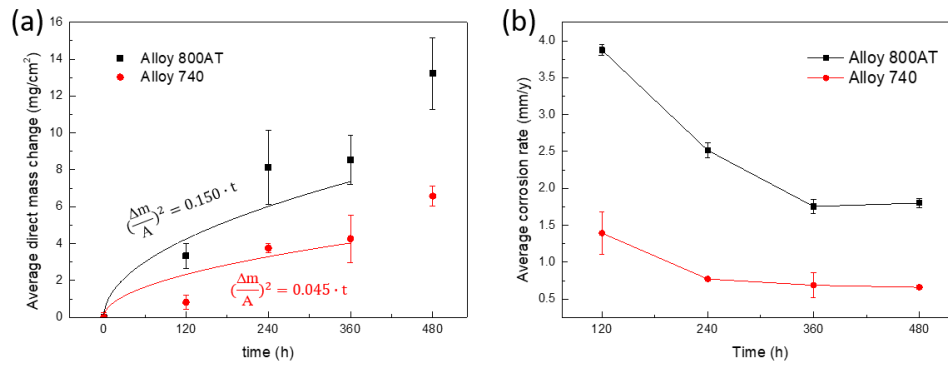
Figure 7-7. Variation of (a) direct mass changes and (b) corrosion rates of Alloy 800AT and Alloy 740 with time in simulated oxy-fuel co-combustion environment at 650 °C.

## 7.4. Summary

This study investigated the application potential of Alloy 800AT and Alloy 740 for heat exchangers under the oxy-fuel combustion of coal and biomass. In the environment of $CO_2$ + 4% $O_2$ flue gas and alkali sulfates and chlorides deposit salts with a S:Cl of 10:1 at 650 °C, both alloys experienced oxidation, sulfidation and chlorination. With extended time, Alloy 800 AT also suffered internal and intergranular corrosion. The oxide layer formed on Alloy 800AT was composed of double-layer structure and heavily degraded with the long-term exposure to the testing environment. The surface scale formed on Alloy 740 has a multi-layered structure containing oxides and sulfides. Mass change measurements also confirmed that Alloy 740 had better resistance to the environmental attack, possibly due to its higher Cr, Ni and Co contents.

# Chapter 8. Conclusions and Future Work

## 8.1. Summary

This thesis aims at selecting the suitable alloys for the construction of heat exchangers and flue gas components in advanced pressurized oxy-fuel combustion plants and identifying the effect of impurities ($SO_2$, $H_2O$ and $O_2$) on the corrosion of pipeline steels used for the transportation of supercritical $CO_2$ captured from the oxy-fuel plants. It is also anticipated to advance the mechanistic understanding of how steels and alloys perform in $CO_2$-enriched environment at the temperature range of 60-650 °C. After the extensive study, the following general conclusions are made:

(1)     The presence of $SO_2$ in the s-$CO_2$ streams captured from the advanced oxy-fuel combustion plants can lead to severe corrosion damage on transportation pipeline steels. The corrosion of pipeline steels in $H_2O$-saturated s-$CO_2$ with $SO_2$ is very likely controlled by electrochemical reactions instead of gas chemical reactions. The SCC susceptibility of X65 steel in the s-$CO_2$ streams is lower than expected. For long-term safe transportation, it is recommended to control $H_2O$% ($< 2000$ ppm) and $SO_2$% ($< 100$ ppm) in the transported s-$CO_2$.


(2)     In simulated condensed phase solution generated at the oxy-fuel combustion plant, both P91 and DSS 2205 experience active corrosion instead of pitting at temperatures up to 150 °C, which is just below the dew point of pressurized flue gas mixture. Increasing temperature results in an exponential increase in the long-term corrosion rates of two steels. Compared with P91, DSS 2205 exhibits much better corrosion resistance to the condensate due to the formation of a compact protective surface oxide scale.


(3)     When exposed to simulated flue gas produced at the oxy-fuel plants, DSS 2205 experiences general oxidation (caused by $O_2$ and $H_2O$) and slight pitting (induced by $SO_2$ and HCl) after exposure at the temperatures of 270-320 °C for 600 h. The corrosion kinetics of DSS 2205 follows a parabolic law and the formed corrosion products have a double-layer structure composed of outer Fe-enriched oxides and inner compact Cr-enriched oxides. Both condensed phase and hot flue gas corrosion

137

testing results show that DSS 2205 shall be a promising candidate for the construction of flue gas components.

(4) For the oxy-fuel plants equipped with s-CO$_2$ Brayton cycle, the inside surface of heat exchanger suffers high-temperature oxidation and carburization. The oxidation and carburization resistance of two candidate construction alloys (SS310 and Alloy 740) is evaluated in three types of s-CO$_2$ streams (ultrapure s-CO$_2$, s-CO$_2$ + 100 ppm H$_2$O, s-CO$_2$ + 100 ppm O$_2$) at 600 °C and the total pressure of 30 MPa for about 1000 hours of exposure. In three s-CO$_2$ streams, general and localized oxidations occur on the tested alloys and the formed surface scale is mainly composed of Cr$_2$O$_3$ oxides. The addition of 100 ppm H$_2$O into s-CO$_2$ significantly enhances the general and nodule oxidations of the steels while the presence of 100 ppm O$_2$ leads to the opposite effect. The addition of H$_2$O or O$_2$ makes SS310 more prone to carburization, but only has a marginal influence on Alloy 740 possibly due to its high contents of Co and Ni. In the high-temperature, high-pressure s-CO$_2$ streams, the direct mass gains of SS310 and Alloy 740 follow parabolic or near-parabolic law. The long-term corrosion rates of the alloys obtained by weight loss measurements are lower than that required for safe operation heat exchanger at the plants.

(5) For the pressurized oxy-fuel natural gas-fired plants, the fireside of heat exchanger suffers ultrahigh temperature flue gas attack. The corrosion performance of three Cr-bearing alloys (SS347, Alloy 800AT and Alloy 825) is investigated in the simulated pressurized flue gas of 60% H$_2$O + 33% CO$_2$ + 2-7 % O$_2$ at 600 °C and the total pressure of 15 MPa for about 120 hours. There is a critical content (~2%) of O$_2$, below which localized preferential growth of Cr oxides occurs, resulting in a considerable increase in the corrosion rates of the alloys. H$_2$O may affect oxide formation and evaporation while CO$_2$ does not exhibit noticeable influence. All the alloys exhibit acceptable corrosion resistance as the constructional materials of heat exchangers. Among them, Alloy 825 shows the best corrosion performance.

(6) For the oxy-fuel combustion of coal/biomass, new type of molten salt mixture can be formed on the fireside of heat exchangers as biomass fuel contains certain amounts of Na, K and Cl elements. The high-temperature molten salt corrosion of Alloy 800AT and Alloy 740 are tested in an environment with continuous $CO_2$ + 4% $O_2$ flue gas and the mixture of alkali sulfates and chlorides with the ration of S/Cl of 10 at 650 °C. All the alloys experience severe oxidation, sulfidation and chlorination. Longer exposure makes internal and intergranular corrosion occurred on Alloy 800AT. Mass change measurements suggest that Alloy 740 has better resistance to the environmental attack compared to Alloy 800AT.

## 8.2. Future work

### 8.2.1. More candidate materials tests under the designed operating conditions

Due to the time limitation, only several typical alloys are assessed under the designed operating conditions. As I introduced in Chapter 1, more candidate materials, including stainless steels, Ni-based alloys, or even Co-based alloys, may also be promising candidates. For example, Co-based alloys may also be applicable for s-$CO_2$ Brayton cycle because of their good mechanical strength, and excellent resistance to carburization in s-$CO_2$ and sulfurization in molten salts at high temperatures. Based on energy sector demands, it is necessary to develop materials selection guidelines for the deployment of the oxy-fuel combustion and CCS technologies.

### 8.2.2. Validation tests required

All the tests in this work are done at lab-scale. It is needed to further examine the long-term corrosion performance of these selected alloys at pilot oxy-fuel combustion plants to validate the results to avoid unwanted capital cost and catastrophic disaster. For example, due to instrumental limitations, most of the current studies employed closed static autoclaves to simulate the hot flue gas and s-$CO_2$ transportation environments. However, the contents of corrodents (such as $SO_2$ and HCl) in these testing environments may drop with time due to corrosion reactions, probably leading to the underestimation of corrosion damage. It shall be more valuable to estimate the long-term corrosion kinetics of the alloys with continuous supply of corrodents.

### 8.2.3. Advanced testing techniques

Advanced techniques are of great importance in revealing related corrosion mechanisms. In s-$CO_2$ environments, *in-situ* electrochemical measurements will be of great help in measuring instantaneous corrosion rate and identifying the corrosion modes (electrochemical reaction or gas chemical reaction). In molten salt environments, corrosion rate measurement with higher accuracy should be developed because current direct mass change or mass loss methods only give an average corrosion rate and could either underestimate or overestimate the degree of corrosion, especially in the presence of intergranular corrosion.

# References

[1] Cole IS, Corrigan P, Sim S, Birbilis N. Corrosion of pipelines used for $CO_2$ transport in CCS: Is it a real problem? International Journal of Greenhouse Gas Control 2011;5:749-56.

[2] Xiang Y. Corrosion issues of carbon capture, utilization, and storage. Materials Performance 2018.

[3] Manan ZA, Nawi WNRM, Alwi SRW, Klemeš JJ. Advances in Process Integration research for $CO_2$ emission reduction–A review. Journal of cleaner production 2017;167:1-13.

[4] Agency IE. Carbon Capture and Storage. 2018.

[5] Huang C-H, Tan C-S. A review: $CO_2$ utilization. Aerosol Air Qual Res 2014;14:480-99.

[6] Jordal K, Anheden M, Yan J, Strömberg L. Oxyfuel combustion for coal-fired power generation with $CO_2$ capture–opportunities and challenges. 7th International Conference on Greenhouse Gas Technologies. Vancouver, Canada2004.

[7] Toftegaard MB, Brix J, Jensen PA, Glarborg P, Jensen AD. Oxy-fuel combustion of solid fuels. Progress in energy and combustion science 2010;36:581-625.

[8] Okawa M, Kimura N, Kiga T, Takano S, Arai K, Kato M. Trial design for a $CO_2$ recovery power plant by burning pulverized coal in $O_2CO_2$. Energy conversion and management 1997;38:S123-S7.

[9] Lackner KS. A guide to $CO_2$ sequestration. Science 2003;300:1677-8.

[10] Liu S, Tao H, Zeng L, Liu Q, Xu Z, Liu Q, et al. Shape-dependent electrocatalytic reduction of $CO_2$ to CO on triangular silver nanoplates. Journal of the American Chemical Society 2017;139:2160-3.

[11] Symonds RT, Hughes RW, De Las Obras Loscertales M. Oxy-pressurized fluidized bed combustion: Configuration and options analysis. Applied Energy 2020;262:114531.

[12] Cairns PE, Clements BR, Hughes R, Herage T, Zheng L, Macchi A, et al. High-Pressure Oxy-Firing (HiPrOx) of Fuels with Water for the Purpose of Direct Contact Steam Generation. Energy & Fuels 2015;29:4522-33.

[13] K. Zanganeh AS, C. Salvador, and A. Beigzadeh. G2 Technology four Production of Power, Water or Steam and Pipeline-ready Pressurized $CO_2$. 5th Oxyfuel Combustion Research Network Meeting. Wuhan, China 2015.

[14] Toftegaard MB, Brix J, Jensen PA, Glarborg P, Jensen AD. Oxy-fuel combustion of solid fuels. Prog Energy Combust Sci 2010;36:581-625.

[15] Corchero G, Timón V, Montanes J. A natural gas oxy-fuel semiclosed combined cycle for zero $CO_2$ emissions: a thermodynamic optimization. Proceedings of the Institution of Mechanical Engineers, Part A: Journal of Power and Energy 2011;225:377-88.

[16] Scheffknecht G, Al-Makhadmeh L, Schnell U, Maier J. Oxy-fuel coal combustion— A review of the current state-of-the-art. International Journal of Greenhouse Gas Control 2011;5:S16-S35.

[17] Möllersten K, Yan J, Moreira JR. Potential market niches for biomass energy with $CO_2$ capture and storage—opportunities for energy supply with negative $CO_2$ emissions. Biomass and Bioenergy 2003;25:273-85.

[18] Lockwood T. Developments in oxyfuel combustion of coal. Report of IEA Clean Coal Centre 2014.

[19] Han SH, Lee YS, Cho JR, Lee KH. Efficiency analysis of air-fuel and oxy-fuel combustion in a reheating furnace. International Journal of Heat and Mass Transfer 2018;121:1364-70.

[20] Uchida T, Yamada T, Watanabe S, Kiga T, Gotou T, Misawa N, et al. Application and Demonstration of Oxyfuel Combustion Technologies to the Existing Power Plant in Australia. Cleaner Combustion and Sustainable World: Springer; 2013. p. 1385-8.

[21] Okazaki K, Ando T. $NO_x$ reduction mechanism in coal combustion with recycled $CO_2$. Energy 1997;22:207-15.

[22] Anthony E. Oxy-fuel firing technology for power generation. Handbook of climate change mitigation 2012:1515-43.

[23] Wu F, Argyle MD, Dellenback PA, Fan M. Progress in $O_2$ separation for oxy-fuel combustion–A promising way for cost-effective $CO_2$ capture: A review. Progress in Energy and Combustion Science 2018;67:188-205.

[24] Mohitpour M, Seevam P, Botros KK, Rothwell B, Ennis C. Pipeline transportation of carbon dioxide containing impurities: ASME Press; 2012.

[25] Xiang Y, Xu M, Choi Y-S. State-of-the-art overview of pipeline steel corrosion in impure dense $CO_2$ for CCS transportation: mechanisms and models. Corrosion Engineering, Science and Technology 2017:1-25.

[26] Xiang Y, Long Z, Li C, Yan W. Neutralization and adsorption effects of various alkanolamines on the corrosion behavior of N80 steel in supercritical $CO_2$ with impurities. Corrosion 2019.

[27] Xiang Y, Huang H, Long Z, Li C, Yan W. Role of residual 2-amino-2-methyl-1-propanol and piperazine in the corrosion of X80 steel within an impure supercritical $CO_2$ environment as relevant to CCUS. International Journal of Greenhouse Gas Control 2019;82:127-37.

[28] Li C, Xiang Y, Song C, Ji Z. Assessing the corrosion product scale formation characteristics of X80 steel in supercritical $CO_2$-$H_2O$ binary systems with flue gas and NaCl impurities relevant to CCUS technology. The Journal of Supercritical Fluids 2019;146:107-19.

[29] Rütters H, Stadler S, Bäßler R, Bettge D, Jeschke S, Kather A, et al. Towards an optimization of the $CO_2$ stream composition—A whole-chain approach. International Journal of Greenhouse Gas Control 2016;54:682-701.

[30] Yevtushenko O, Bettge D, Bäßler R, Bohraus S. Corrosion of $CO_2$ transport and injection pipeline steels due to the condensation effects caused by $SO_2$ and $NO_2$ impurities. Materials and Corrosion 2015;66:334-41.

[31] Yevtushenko O, Bäßler R, Carrillo-Salgado I. Corrosion stability of piping steels in a circulating supercritical impure $CO_2$ environment. CORROSION 2013: NACE International; 2013.

[32] Patchigolla K, Oakey JE. Design overview of high pressure dense phase $CO_2$ pipeline transport in flow mode.  2013.

[33] Paschke B, Kather A. Corrosion of pipeline and compressor materials due to impurities in separated $CO_2$ from fossil-fuelled power plants. Energy Procedia 2012;23:207-15.

[34] Dugstad A, Halseid M. Internal corrosion in dense phase $CO_2$ transport pipelines-state of the art and the need for further R&D. CORROSION 2012: NACE International; 2012.

[35] Mohitpour M. Pipeline transportation of carbon dioxide containing impurities: ASME Press; 2012.

[36] Le Hoa Q, Bäßler R, Bettge D. On the corrosion mechanism of $CO_2$ transport pipeline steel caused by condensate: Synergistic effects of $NO_2$ and $SO_2$. Materials 2019;12:364.

[37] Zeng Y, Li K, Luo J, Arafin M. Impacts of Impurities on Corrosion of Supercritical $CO_2$ Transportation Pipeline Steels. CORROSION 2018: NACE International; 2018.

[38] Cui G, Yang Z, Liu J, Li Z. A comprehensive review of metal corrosion in a supercritical $CO_2$ environment. International Journal of Greenhouse Gas Control 2019;90:102814.

[39] Svenningsen G, Morland BH, Dugstad A, Thomas B. Stress corrosion cracking testing of 13Cr stainless steel in dense phase $CO_2$ with oxygen. Energy Procedia 2017;114:6778-99.

[40] Zeng Y, Li K, Hughes R, Luo J-L. Corrosion Mechanisms and Materials Selection for the Construction of Flue Gas Component in Advanced Heat and Power Systems. Industrial & Engineering Chemistry Research 2017;56:14141-54.

[41] Lee HJ, Kim H, Jang C. Compatibility of candidate structural materials in high-temperature S-$CO_2$ environment. 4th International Symposium-Supercritical $CO_2$ Power Cycles. Pittsburgh, PA2014. p. 1-9.

[42] Mahaffey J, Adam D, Brittan A, Anderson M, Sridharan K. Corrosion of alloy haynes 230 in high temperature supercritical carbon dioxide with oxygen impurity additions. Oxidation of Metals 2016;86:567-80.

[43] Sarver J, Tanzosh J. Steamside oxidation behaviour of candidate USC materials at temperatures between 650 and 800 °C. Energy Materials 2007;2:227-34.

[44] Bermejo M, Cocero M. Supercritical water oxidation: a technical review. AIChE Journal 2006;52:3933-51.

[45] Xie X, Wu Y, Chi C, Zhang M. Superalloys for Advanced Ultra-Super-Critical Fossil Power Plant Application. Superalloys; InTech: Rijeka, Croatia 2015:51-76.

[46] Ennis P. Nickel-base alloys for advanced power plant components. Coal Power Plant Materials and Life Assessment: Elsevier; 2014. p. 147-67.

[47] Sarrade S, Féron D, Rouillard F, Perrin S, Robin R, Ruiz J-C, et al. Overview on corrosion in supercritical fluids. The Journal of Supercritical Fluids 2017;120:335-44.

144

[48] Brun K, Friedman P, Dennis R. Fundamentals and applications of supercritical carbon dioxide ($sCO_2$) based power cycles: Woodhead publishing; 2017.

[49] Kung S, Shingledecker J, Wright I, Tossey B. Oxidation and Carburization of Alloys Exposed to Impure Supercritical $CO_2$. CORROSION 2017: NACE International; 2017.

[50] Pint BA, Brese RG. Chapter 4 - High-temperature materials. In: Brun K, Friedman P, Dennis R, editors. Fundamentals and Applications of Supercritical Carbon Dioxide ($sCO_2$) Based Power Cycles: Woodhead Publishing; 2017. p. 67-104.

[51] Brady MP, Yamamoto Y, Santella ML, Maziasz PJ, Pint BA, Liu C, et al. The development of alumina-forming austenitic stainless steels for high-temperature structural use. Jom 2008;60:12.

[52] Young DJ, Pint BA. Chromium volatilization rates from $Cr_2O_3$ scales into flowing gases containing water vapor. Oxidation of Metals 2006;66:137-53.

[53] Essuman E, Meier GH, Żurek J, Hänsel M, Singheiser L, Quadakkers WJ. Enhanced internal oxidation as trigger for breakaway oxidation of Fe–Cr alloys in gases containing water vapor. Scripta Materialia 2007;57:845-8.

[54] Saunders SRJ, Monteiro M, Rizzo F. The oxidation behaviour of metals and alloys at high temperatures in atmospheres containing water vapour: A review. Progress in Materials Science 2008;53:775-837.

[55] Aaron D, Tsouris C. Separation of $CO_2$ from flue gas: a review. Separation Science and Technology 2005;40:321-48.

[56] K. Zanganeh AS, C. Salvador, A. Beigzadeh. G2 Technology four Production of Power, Water or Steam and Pipeline-ready Pressurized $CO_2$. https://ieaghg.org/docs/General_Docs/5oxy%20presentations/Session%207B/7B-01%20-%20K.%20Zanganeh%20(CANMET).pdf: IEA.

[57] Muktinutalapati NR, Natarajan A, Arivarasu M. Hot Corrosion of Superalloys in Boilers for Ultra-Supercritical Power Plants. Superalloys for Industry Applications 2018:29.

[58] Harb J, Smith E. Fireside corrosion in PC-fired boilers. Progress in energy and combustion science 1990;16:169-90.

[59] Tillman DA, Duong D, Miller B. Chlorine in solid fuels fired in pulverized fuel boilers: Sources, forms, reactions, and consequences: A literature review. Energy & Fuels 2009;23:3379-91.

[60] Finšgar M, Jackson J. Application of corrosion inhibitors for steels in acidic media for the oil and gas industry: a review. Corrosion science 2014;86:17-41.

[61] Drew M, Humphries S, Thorogood K, Barnett N. Remaining life assessment of carbon steel boiler headers by repeated creep testing. International Journal of Pressure Vessels and Piping 2006;83:343-8.

[62] Viswanathan R, Sarver J, Tanzosh J. Boiler materials for ultra-supercritical coal power plants—steamside oxidation. Journal of Materials Engineering and Performance 2006;15:255-74.

[63] Gaus-Liu X. High-Temperature Chlorine Corrosion during Co-Utilisation of Coal with Biomass or Waste: Cuvillier Verlag; 2008.

[64] Mogire E, Higginson R, Fry A, Thomson R. Microstructural characterization of oxide scales formed on steels P91 and P92. Materials at High Temperatures 2011;28:361-8.

[65] Lechtenberg T. The effect of microstructure on the mechanical properties of a commercial 12Cr-1Mo steel (HT-9). Journal of Nuclear Materials 1981;104:1133-7.

[66] Viswanathan R, Coleman K, Shingledecker J, Sarver J, Stanko G, Borden M, et al. Boiler materials for ultrasupercritical coal power plants. US Department of Energy, Report No DE-FG26-01NT411752006.

[67] Gabrel J, Zakine C, Lefebvre B, Vandenberghe B. VM12–a new 12% Cr steel for application at high temperature in advanced power plants. Status of Development. Advances in Materials Technology for Fossil Power Plants: Proceedings from the Fifth International Conference 20072007.

[68] Sun C, Sun J, Wang Y, Sui P, Lin X, Liu H, et al. Effect of impurity interaction on the corrosion film characteristics and corrosion morphology evolution of X65 steel in water-saturated supercritical $CO_2$ system. International Journal of Greenhouse Gas Control 2017;65:117-27.

[69] Farr JR, Jawad MH. Guidebook for the Design of ASME Section VIII Pressure Vessels. ASME; 2010.

[70] Bolt N. FIRESIDE CORROSION PHENOMENA IN SUPERHEATERS OF AISI 347H AND ESSHETE 1250/AISI 310 AT METAL TEMPERATURES OF UP TO 700 degree C.  Proceedings of the 9th International Congress on Metallic Corrosion1984. p. 242-7.

[71] Spindler M, Spindler S. Creep deformation, rupture and ductility of Esshete 1250 weld metal. Materials Science and Technology 2014;30:17-23.

[72] Viswanathan R, Bakker W. Materials for ultrasupercritical coal power plants—Boiler materials: Part 1. Journal of Materials Engineering and Performance 2001;10:81-95.

[73] Viswanathan R, Henry J, Tanzosh J, Stanko G, Shingledecker J, Vitalis B, et al. US program on materials technology for ultra-supercritical coal power plants. Journal of materials engineering and performance 2005;14:281-92.

[74] Phull BS, Mathay WL, Ross R. Corrosion Resistance of Duplex and 4-6% Mo-Containing Stainless Steels in FGD Scrubber Absorber Slurry Environments. CORROSION 2000: NACE; 2000.

[75] Schulz Z, Whitcraft P, Wachowiak D. Availability and economics of using duplex stainless steels.  CORROSION 2014: NACE International; 2014.

[76] Iacoviello F, Casari F, Gialanella S. Effect of "475 °C embrittlement" on duplex stainless steels localized corrosion resistance. Corrosion Science 2005;47:909-22.

[77] Donik Č, Kocijan A, Grant JT, Jenko M, Drenik A, Pihlar B. XPS study of duplex stainless steel oxidized by oxygen atoms. Corrosion Science 2009;51:827-32.

[78] Nilsson J-O. Super duplex stainless steels. Materials Science and Technology 1992;8:685-700.

[79] Revie RW. Uhlig's corrosion handbook. John Wiley & Sons; 2011.

[80] Lai GY. High-temperature corrosion and materials applications: ASM International; 2007.

[81] ENNIS P. Nickel-base alloys for advanced power plant components. Coal Power Plant Materials and Life Assessment: Developments and Applications 2014:147.

[82] Shingledecker J, Evans N. Creep-rupture performance of 0.07 C–23Cr–45Ni–6W–Ti, Nb austenitic alloy (HR6W) tubes. International Journal of Pressure Vessels and Piping 2010;87:345-50.

[83] Natesan K, Park J. Fireside and steamside corrosion of alloys for USC plants. International Journal of Hydrogen Energy 2007;32:3689-97.

[84] Patel SJ, Baker BA, Gollihue RD. Nickel base superalloys for next generation coal fired AUSC power plants. Procedia Engineering 2013;55:246-52.

[85] steeltank. https://www.steeltank.com/Portals/0/Pressure%20Vessels/SSWseminarOct2012/Relative%20Cost%204%2015%202012.pdf.

[86] Dugstad A, Halseid M, Morland B. Effect of $SO_2$ and $NO_2$ on corrosion and solid formation in dense phase $CO_2$ pipelines. Energy Procedia 2013;37:2877-87.

[87] Sun C, Sun J, Wang Y, Lin X, Li X, Cheng X, et al. Synergistic effect of $O_2$, $H_2S$ and $SO_2$ impurities on the corrosion behavior of X65 steel in water-saturated supercritical $CO_2$ system. Corrosion Science 2016;107:193-203.

[88] Hua Y, Barker R, Neville A. Understanding the influence of $SO_2$ and $O_2$ on the corrosion of carbon steel in water-saturated supercritical $CO_2$. Corrosion 2014;71:667-83.

[89] Hu Y, Naito S, Kobayashi N, Hasatani M. $CO_2$, $NO_x$ and $SO_2$ emissions from the combustion of coal with high oxygen concentration gases. Fuel 2000;79:1925-32.

[90] De Visser E, Hendriks C, Barrio M, Mølnvik MJ, de Koeijer G, Liljemark S, et al. Dynamis $CO_2$ quality recommendations. International Journal of Greenhouse Gas Control 2008;2:478-84.

[91] Halseid MC, Dugstad A, Morland BH. Corrosion and bulk phase reactions in $CO_2$ transport pipelines with impurities: review of recent published studies. Energy Procedia 2014;63:2557-69.

[92] Wang W, Shen K, Tang S, Shen R, Parker T, Wang Q. Synergistic effect of $O_2$ and $SO_2$ gas impurities on X70 steel corrosion in water-saturated supercritical $CO_2$. Process Safety and Environmental Protection 2019;130:57-66.

[93] Nesic S, Postlethwaite J, Olsen S. An electrochemical model for prediction of corrosion of mild steel in aqueous carbon dioxide solutions. Corrosion 1996;52:280-94.

[94] Ramamurthy S, Atrens A. Stress corrosion cracking of high-strength steels. Corrosion Reviews 2013;31:1-31.

[95] Choi Y-S, Hassani S, Vu TN, Nešić S, Abas AZB. Effect of $H_2S$ on the corrosion behavior of pipeline steels in supercritical and liquid $CO_2$ environments. Corrosion 2016;72:999-1009.

[96] Ma H, Liu Z, Du C, Li X, Cui Z. Comparative study of the SCC behavior of E690 steel and simulated HAZ microstructures in a $SO_2$-polluted marine atmosphere. Materials Science and Engineering: A 2016;650:93-101.

[97] Onyebuchi VE, Kolios A, Hanak DP, Biliyok C, Manovic V. A systematic review of key challenges of $CO_2$ transport via pipelines. Renewable and Sustainable Energy Reviews 2018;81:2563-83.

[98] Huang F, Cheng P, Zhao X, Liu J, Hu Q, Cheng YF. Effect of sulfide films formed on X65 steel surface on hydrogen permeation in $H_2S$ environments. International Journal of Hydrogen Energy 2017;42:4561-70.

[99] Woodtli J, Kieselbach R. Damage due to hydrogen embrittlement and stress corrosion cracking. Engineering failure analysis 2000;7:427-50.

[100] Sandana D, Dale M, Charles E, Race J. Transport of gaseous and dense carbon dioxide in pipelines: is there an internal stress corrosion cracking risk? CORROSION 2013: NACE International; 2013.

[101] Morana R, Piccolo EL, Scoppio L, Nice PI. Environmental Cracking Performance Of Super Martensitic Stainless Steels "13-5-2"(Grades 110Ksi And 125Ksi) For Tubing Applications In High Chloride Reservoir Fluids Containing $H_2S$/$CO_2$. CORROSION 2010: NACE International; 2010.

[102] Ruhl AS, Göbel A, Kühn H-J, Kranzmann A. Materials Testing under Mechanical Stress, Pressure and Turbulent Flow of Impure Supercritical $CO_2$. Materials Testing 2013;55:158-62.

[103] International A. ASTM G202-09, Standard Test Method for Using Atmospheric Pressure Rotating Cage. West Conshohocken, PA2009.

[104] Wei L, Zhang Y, Pang X, Gao K. Corrosion behaviors of steels under supercritical $CO_2$ conditions. Corrosion Reviews 2015;33:151-74.

[105] Standard N. Laboratory testing of metals for resistance to sulfide stress cracking and stress corrosion cracking in $H_2S$ environments. Houston, TX: NACE2005.

[106] Porter RT, Fairweather M, Pourkashanian M, Woolley RM. The range and level of impurities in CO2 streams from different carbon capture sources. International Journal of Greenhouse Gas Control 2015;36:161-74.

[107] Gallier P, Evans L, Britt H, Boston J, Gupta P. Aspen: Advanced capabilities for modeling and simulation of industrial processes. ACS symposium series1980. p. 293-308.

[108] Tabasinejad F, Moore RG, Mehta SA, Van Fraassen KC, Barzin Y, Rushing JA, et al. Water solubility in supercritical methane, nitrogen, and carbon dioxide: measurement and modeling from 422 to 483 K and pressures from 3.6 to 134 MPa. International Journal of Greenhouse Gas Control 2011;50:4029-41.

[109] ASTM. ASTM G1 Standard practice for preparing, cleaning, and evaluating corrosion test specimens. ASTM international; 2011.

[110] Papavinasam S, Zanganesh K, Li J, Emadi D, Doiron A, Salvador C, et al. Materials Issues In $CO_2$ Capture, Transport, And Storage Infrastructure. CORROSION 2012: NACE International; 2012.

[111] Collier J, Papavinasam S, Li J, Shi C, Liu P, Gravel J-P. Effect of impurities on the corrosion performance of steels in supercritical carbon dioxide: optimization of experimental procedure. CORROSION 2013: NACE International; 2013.

[112] Standard A. Standard practice for laboratory immersion corrosion testing of metals. American Society for Testing and Materials G31-72 2004.

[113] Xiang Y, Wang Z, Li Z, Ni W. Long term corrosion of X70 steel and iron in humid supercritical $CO_2$ with $SO_2$ and $O_2$ impurities. Corrosion Engineering, Science and Technology 2013;48:395-8.

[114] Choi Y-S, Nešić S. Effect of water content on the corrosion behavior of carbon steel in supercritical $CO_2$ phase with impurities. CORROSION 2011.

[115] Xiang Y, Wang Z, Xu C, Zhou C, Li Z, Ni W. Impact of $SO_2$ concentration on the corrosion rate of X70 steel and iron in water-saturated supercritical $CO_2$ mixed with $SO_2$. The Journal of Supercritical Fluids 2011;58:286-94.

[116] Xiang Y, Wang Z, Li Z, Ni W. Effect of exposure time on the corrosion rates of X70 steel in supercritical $CO_2/SO_2/O_2/H_2O$ environments. Corrosion 2012;69:251-8.

[117] Hua Y, Barker R, Neville A. The influence of $SO_2$ on the tolerable water content to avoid pipeline corrosion during the transportation of supercritical $CO_2$. International Journal of Greenhouse Gas Control 2015;37:412-23.

[118] Choi Y-S, Nešic S. Effect of impurities on the corrosion behavior of carbon steel in supercritical $CO_2$-water environments. CORROSION 2010: NACE International; 2010.

[119] Sun C, Wang Y, Sun J, Lin X, Li X, Liu H, et al. Effect of impurity on the corrosion behavior of X65 steel in water-saturated supercritical $CO_2$ system. The Journal of Supercritical Fluids 2016;116:70-82.

[120] Xu M, Zhang Q, Wang Z, Liu J, Li Z. Effect of high-concentration $O_2$ on corrosion behavior of X70 steel in water-containing supercritical $CO_2$ with $SO_2$. Corrosion 2016;73:290-302.

[121] Xiang Y, Wang Z, Yang X, Li Z, Ni W. The upper limit of moisture content for supercritical $CO_2$ pipeline transport. The Journal of Supercritical Fluids 2012;67:14-21.

[122] Hua Y, Jonnalagadda R, Zhang L, Neville A, Barker R. Assessment of general and localized corrosion behavior of X65 and 13Cr steels in water-saturated supercritical $CO_2$ environments with $SO_2/O_2$. International Journal of Greenhouse Gas Control 2017;64:126-36.

[123] Farelas F, Choi Y, Nešić S. Corrosion behavior of API 5L X65 carbon steel under supercritical and liquid carbon dioxide phases in the presence of water and sulfur dioxide. Corrosion 2012;69:243-50.

[124] Dugstad A, Morland B, Clausen S. Corrosion of transport pipelines for $CO_2$–effect of water ingress. Energy Procedia 2011;4:3063-70.

[125] Xu M, Li W, Zhou Y, Yang X, Wang Z, Li Z. Effect of pressure on corrosion behavior of X60, X65, X70, and X80 carbon steels in water-unsaturated supercritical $CO_2$ environments. International Journal of Greenhouse Gas Control 2016;51:357-68.

[126] Rubin ES, Cushey MA, Marnicio RJ, Bloyd CN, Skea JF. Controlling acid deposition: the role of FGD. Environmental Science & Technology 1986;20:960-9.

[127] Srivastava RK, Jozewicz W, Singer C. $SO_2$ scrubbing technologies: A review. Environmental Progress 2001;20:219-28.

[128] Standard N. Preparation and Installation of Corrosion Coupons and Interpretation of Test Data in Oilfield Operations. NACE RP0775-2005, Houston, TX, NACE International Publication, Item2005.

[129] Hua Y, Barker R, Neville A. The influence of $SO_2$ on the tolerable water content to avoid pipeline corrosion during the transportation of supercritical $CO_2$. Int J Greenhouse Gas Control 2015;37:412-23.

[130] Ayello F, Evans K, Thodla R, Sridhar N. Effect of impurities on corrosion of steel in supercritical $CO_2$. CORROSION 2010: NACE International; 2010.

[131] Hua Y, Barker R, Neville A. Understanding the influence of $SO_2$ and $O_2$ on the corrosion of carbon steel in water-saturated supercritical $CO_2$. Corros 2014;71:667-83.

[132] Zanganeh YZABASDEK. The effects of the typical $CO_2$ stream impurities on corrosion of pipeline steels. $CO_2$ QUEST: Summary of achievements2016.

[133] Le QH, Bäßler R, Kratzig A, Bettge D, Kranzmann A, Knauer S. Droplet corrosion of $CO_2$ transport pipeline steels. CORROSION 2018. Phoenix, AZ, USA2018. p. 10845, 1-11.

[134] Hoa LQ, Bäßer R, Knauer S, Kratzig A, Bettge D. Factors Influencing Droplet Corrosion in Dense Phase $CO_2$. CORROSION 2019. Nashville, Tennessee, USA: NACE International; 2019. p. 13.

[135] Hoa LQ, Baessler R, Knauer S, Jaeger P, Kratzig A, Bettge D, et al. Droplet Corrosion of $CO_2$ Transport Pipeline Steels in Simulated Oxyfuel Flue Gas. Corrosion 2018;74:1406-20.

[136] Li C, Xiang Y, Li W. Initial corrosion mechanism for API 5L X80 steel in $CO_2/SO_2$-saturated aqueous solution within a CCUS system: Inhibition effect of $SO_2$ impurity. Electrochimica Acta 2019;321:134663.

[137] Choi Y-S, Nesic S, Young D. Effect of impurities on the corrosion behavior of $CO_2$ transmission pipeline steel in supercritical $CO_2$−water environments. Environmental science & technology 2010;44:9233-8.

[138] Xiang Y, Wang Z, Xu M, Li Z, Ni W. A mechanistic model for pipeline steel corrosion in supercritical $CO_2$–$SO_2$–$O_2$–$H_2O$ environments. The Journal of Supercritical Fluids 2013;82:1-12.

[139] Kilinççeker G, Taze N, Galip H, Yazici B. The effect of sulfur dioxide on iron, copper and brass. Anti-Corrosion Methods and Materials 2011;58:4-12.

[140] Xiang Y, Li C, Long Z, Guan C, Wang W, Hesitao W. Electrochemical behavior of valve steel in a $CO_2$/sulfurous acid solution. Electrochimica Acta 2017;258:909-18.

[141] Tang Y, Guo X, Zhang G. Corrosion behaviour of X65 carbon steel in supercritical-$CO_2$ containing $H_2O$ and $O_2$ in carbon capture and storage (CCS) technology. Corrosion Science 2017;118:118-28.

[142] McLamb M, Hopkins P, Marley M, Nessim M. A justification for designing and operating pipelines up to stresses of 80% SMYS. 4th International Pipeline Conference: American Society of Mechanical Engineers; 2002. p. 745-57.

[143] Ma H, Du C, Liu Z, Li X. Effect of $SO_2$ content on SCC behavior of E690 high-strength steel in $SO_2$-polluted marine atmosphere. Ocean Engineering 2018;164:256-62.

[144] Yi G, Zheng C. Hydrogen permeation through X56 pipeline steel in atmospheric environment and its implication on SCC. International Journal of Electrochemical Science 2012;7:10633-43.

[145] Lynch S. Hydrogen embrittlement (HE) phenomena and mechanisms.  Stress Corrosion Cracking: Elsevier; 2011. p. 90-130.

[146] Oskuie AA, Shahrabi T, Shahriari A, Saebnoori E. Electrochemical impedance spectroscopy analysis of X70 pipeline steel stress corrosion cracking in high pH carbonate solution. Corrosion Science 2012;61:111-22.

[147] Liu ZY, Li XG, Du CW, Zhai GL, Cheng YF. Stress corrosion cracking behavior of X70 pipe steel in an acidic soil environment. Corrosion Science 2008;50:2251-7.

[148] Zhang X, Sun Z, Tang Z, Liu M, Li B. Study on stress corrosion cracking of aluminum alloys in marine atmosphere. Environment-Induced Cracking of Materials: Elsevier; 2008. p. 351-7.

[149] Yevtushenko O, Bettge D, Bohraus S, Bäßler R, Pfennig A, Kranzmann A. Corrosion behavior of steels for $CO_2$ injection. Process Safety and Environmental Protection 2014;92:108-18.

[150] Shoemaker L, Crum J, Maitra D, Muro R, Neighbor M. Recent experience with stainless steels in FGD air pollution control service. CORROSION 2011: NACE International; 2011.

[151] Dahl L. Corrosion in flue gas desulfurization plants and other low temperature equipment. Materials and Corrosion 1992;43:298-304.

[152] Simms N, Kilgallon P, Oakey J. Fireside issues in advanced power generation systems. Energy Materials 2007;2:154-60.

[153] Bordenet B. Influence of novel cycle concepts on the high-temperature corrosion of power plants. Materials and corrosion 2008;59:361-6.

[154] Abel E. The Vapor Phase above the System Sulfuric Acid–Water. The Journal of Physical Chemistry 1946;50:260-83.

[155] Okkes A. Get acid dew point of flue gas. Hydrocarbon Process;(United States) 1987;66.

[156] Xiang B, Zhang M, Yang H, Lu J. Prediction of acid dew point in flue gas of boilers burning fossil fuels. Energy & Fuels 2016;30:3365-73.

[157] Galatro D, Marín-Cordero F. Considerations for the dew point calculation in rich natural gas. Journal of Natural Gas Science and Engineering 2014;18:112-9.

[158] Shoemaker L, Crum JR. Experience in effective application of metallic materials for construction of FGD systems. Special Metals Corporation 2010.

[159] Lee J-S, Fushimi K, Nakanishi T, Hasegawa Y, Park Y-S. Corrosion behaviour of ferrite and austenite phases on super duplex stainless steel in a modified green-death solution. Corrosion science 2014;89:111-7.

[160] Asphahani A, Nicholas A, Silence W, Meyer T. High performance alloys for solving severe corrosion problems in flue gas desulfurization systems. Materials and Corrosion 1989;40:409-17.

[161] Bugge J, Kjær S, Blum R. High-efficiency coal-fired power plants development and perspectives. Energy 2006;31:1437-45.

[162] Hernas A, Imosa M, Pasternak J, Fudali S. New experience in field of application of corrosion resistance protection in flue gas desulphurisation plant absorbers. Energy Materials 2006;1:256-62.

[163] Cui Z, Wang L, Ni H, Hao W, Man C, Chen S, et al. Influence of temperature on the electrochemical and passivation behavior of 2507 super duplex stainless steel in simulated desulfurized flue gas condensates. Corrosion Science 2017;118:31-48.

[164] Fitzsimmons M, Heim DM, Follett W, Jovanovic S, Byron M, Hughes RW, et al. Final Report, Project: Advanced Oxy-Combustion Technology Development and Scale Up for New and Existing Coal-Fired Power Plants (Phase II). Gas Technology Institute, Des Plaines, IL (United States); 2019.

[165] Xiang B, Tang B, Wu Y, Yang H, Zhang M, Lu J. Predicting acid dew point with a semi-empirical model. Applied Thermal Engineering 2016;106:992-1001.

[166] Huijbregts W, Leferink R. Latest advances in the understanding of acid dewpoint corrosion: corrosion and stress corrosion cracking in combustion gas condensates. Anti-Corrosion Methods and Materials 2004.

[167] Inc. VMG. VMGSim Process Simulator, Version 9.0,. Calgary, Alberta, Canada2015.

[168] Kivisäkk U. A test method for dewpoint corrosion of stainless steels in dilute hydrochloric acid. Corrosion science 2003;45:485-95.

[169] Xiang Y, Li C, Hesitao W, Long Z, Yan W. Understanding the pitting corrosion mechanism of pipeline steel in an impure supercritical $CO_2$ environment. The Journal of Supercritical Fluids 2018;138:132-42.

[170] Inouye K, Shibata K, Ozeki S, Kaneko K. Ferromagnetic Iron Oxides from Synthetic β-FeOOH by Vacuum Thermal Decomposition. Journal of The Electrochemical Society 1984;131:2435.

[171] Marcus P. Corrosion mechanisms in theory and practice: CRC press; 2011.

[172] Takasaki S, Yamada Y. Effects of temperature and aggressive anions on corrosion of carbon steel in potable water. Corrosion Science 2007;49:240-7.

[173] Olmedo A, Villegas M, Alvarez M. Corrosion behaviour of Alloy 800 in high temperature aqueous solutions: Electrochemical studies. Journal of nuclear materials 1996;229:102-14.

[174] Kritzer P. Corrosion in high-temperature and supercritical water and aqueous solutions: a review. The Journal of Supercritical Fluids 2004;29:1-29.

[175] Reartes GB, Morando PJ, Blesa MA, Hewlett PB, Matijevic E. Reactivity of chromium oxide in aqueous solutions. 2. Acid dissolution. Langmuir 1995;11:2277-84.

[176] Rodenas LG, Morando PJ, Blesa MA, Duhalde S, Saragovi C. Acid and oxidative dissolution of coprecipitated iron–chromium oxides. Canadian journal of chemistry 1993;71:771-8.

[177] Tan MW, Akiyama E, Habazaki H, Kawashima A, Asami K, Hashimoto K. The effect of molybdenum on the stability of passive films formed on amorphous Fe-Cr-Mo-P-C alloys by potentiostatic polarization in deaerated 1 M HCl. Corrosion Science 1997;39:589-603.

[178] Montemor MF, Simões Amp, Ferreira MGS, Belo MDC. The role of Mo in the chemical composition and semiconductive behaviour of oxide films formed on stainless steels. Corrosion Science 1999;41:17-34.

[179] Hashimoto K, Asami K, Teramoto K. An X-ray photo-electron spectroscopic study on the role of molybdenum in increasing the corrosion resistance of ferritic stainless steels in HCl. Corrosion Science 1979;19:3-14.

[180] Asami K, Hashimoto K, Shimodaira S. An XPS study of the passivity of a series of iron—chromium alloys in sulphuric acid. Corrosion Science 1978;18:151-60.

[181] Holliday JE, Frankenthal RP. Characterization of Passivating Films on Fe-Cr Alloys by Soft X-Ray Spectroscopy. Journal of The Electrochemical Society 1972;119:1190.

[182] Lu Y, Clayton C. An XPS study of the passive and transpassive behavior of molybdenum in deaerated 0.1 M HCl. Corrosion science 1989;29:927-37.

[183] Pourbaix M. Atlas of Electrochemical Equilibria in Aqueous Solutions. Houston, TX: National Association of Corrosion Engineers; 1974.

[184] Yue X, Zhang L, Wang Y, Xu S, Wang C, Lu M, et al. Evolution and characterization of the film formed on super 13Cr stainless steel in $CO_2$-saturated formation water at high temperature. Corrosion Science 2020;163:108277.

[185] Schimek GL, McCarley RE, Chumbley LS. Synthesis and superstructural characterization of $Fe_{1.89}Mo_{4.11}O_7$. Journal of materials research 1994;9:891-7.

[186] Li L, Chu Y, Liu Y. Synthesis and characterization of ring-like $\alpha$-$Fe_2O_3$. Nanotechnology 2007;18:105603.

[187] Gardin E, Zanna S, Seyeux A, Allion-Maurer A, Marcus P. Comparative study of the surface oxide films on lean duplex and corresponding single phase stainless steels by XPS and ToF-SIMS. Corrosion Science 2018;143:403-13.

[188] Olsson COA, Landolt D. Passive films on stainless steels—chemistry, structure and growth. Electrochimica Acta 2003;48:1093-104.

[189] Finšgar M, Kek Merl D. An electrochemical, long-term immersion, and XPS study of 2-mercaptobenzothiazole as a copper corrosion inhibitor in chloride solution. Corrosion Science 2014;83:164-75.

[190] Beverskog B, Puigdomenech I. Revised pourbaix diagrams for chromium at 25–300 °C. Corrosion Science 1997;39:43-57.

[191] Fu Y, Wu X, Han E-H, Ke W, Yang K, Jiang Z. Effects of cold work and sensitization treatment on the corrosion resistance of high nitrogen stainless steel in chloride solutions. Electrochimica Acta 2009;54:1618-29.

[192] Kumagai M, Myung S-T, Kuwata S, Asaishi R, Yashiro H. Corrosion behavior of austenitic stainless steels as a function of pH for use as bipolar plates in polymer electrolyte membrane fuel cells. Electrochimica Acta 2008;53:4205-12.

[193] Young DJ. Chapter 5 - Oxidation of Alloys I: Single Phase Scales. In: Young DJ, editor. High Temperature Oxidation and Corrosion of Metals (Second Edition): Elsevier; 2016. p. 193-260.

[194] Shimizu H, Omori E, Ikeda M. Anomalous behavior of Schottky barrier-type surface photovoltages in chromium-contaminated n-type silicon wafers exposed to air. Japanese journal of applied physics 2006;45:4982.

[195] Macdonald DD. The history of the point defect model for the passive state: a brief review of film growth aspects. Electrochimica Acta 2011;56:1761-72.

[196] Nikolaychuk P, Tyurin A. The revised pourbaix diagram for molybdenum. Butlerov Commun 2011;24:101-5.

[197] Rasheed RT, Easa HA, Jassim LS. Preparation and characterization of $Cr_2O_3$ nanoparticle prepared by chemical method.  AIP Conference Proceedings: AIP Publishing LLC; 2020. p. 020202.

[198] Korshunov V, Safonov V, Vykhodtseva L. Structural features of the electrode/solution interface at the reduction of $Cr^{3+}$ (aq) cations on liquid mercury and solid indium electrodes in acidic media. Russian Journal of Electrochemistry 2008;44:255-64.

[199] Carvalho DS, Joia CJB, Mattos OR. Corrosion rate of iron and iron–chromium alloys in $CO_2$ medium. Corrosion Science 2005;47:2974-86.

[200] Popova A, Sokolova E, Raicheva S, Christov M. AC and DC study of the temperature effect on mild steel corrosion in acid media in the presence of benzimidazole derivatives. Corrosion Science 2003;45:33-58.

[201] Case B. The diffusivity of oxygen in dilute alkaline solution from 0 °C to 65 °C. Electrochimica Acta 1973;18:293-9.

[202] Blasco-Tamarit E, Igual-Muñoz A, Antón JG, García-García D. Effect of temperature on the corrosion resistance and pitting behaviour of Alloy 31 in LiBr solutions. Corrosion Science 2008;50:1848-57.

[203] Pettersson R, Ekman S, Bergquist A, Flyg J, Carinci G. Corrosion of austenitic and duplex stainless steels in flue gas cleaning systems for waste combustion processes. CORROSION 2013: NACE International; 2013.

[204] Ziemniak S. Metal oxide solubility behavior in high temperature aqueous solutions. Journal of solution chemistry 1992;21:745-60.

[205] BenSalah M, Sabot R, Triki E, Dhouibi L, Refait P, Jeannin M. Passivity of Sanicro28 (UNS N-08028) stainless steel in polluted phosphoric acid at different temperatures studied by electrochemical impedance spectroscopy and Mott–Schottky analysis. Corrosion Science 2014;86:61-70.

[206] Gray J, Hayes J, Gdowski G, Viani B, Orme C. Influence of solution pH, anion concentration, and temperature on the corrosion properties of alloy 22. Journal of The Electrochemical Society 2006;153:B61-B7.

[207] Crundwell F. The mechanism of dissolution of minerals in acidic and alkaline solutions: Part I—A new theory of non-oxidation dissolution. Hydrometallurgy 2014;149:252-64.

[208] Kranzmann A, Neddemeyer T, Ruhl AS, Hünert D, Bettge D, Oder G, et al. The challenge in understanding the corrosion mechanisms under oxyfuel combustion conditions. Int J Greenhouse Gas Control 2011;5:S168-S78.

[209] Sánchez-Tovar R, Leiva-García R, García-Antón J. Characterization of thermal oxide films formed on a duplex stainless steel by means of confocal-Raman microscopy and electrochemical techniques. Thin Solid Films 2015;576:1-10.

[210] Huczkowski P, Olszewski T, Schiek M, Lutz B, Holcomb G, Shemet V, et al. Effect of $SO_2$ on oxidation of metallic materials in $CO_2$/$H_2O$-rich gases relevant to oxyfuel environments. Materials and Corrosion 2014;65:121-31.

[211] Ruhl AS, Kranzmann A. Corrosion behavior of various steels in a continuous flow of carbon dioxide containing impurities. International Journal of Greenhouse Gas Control 2012;9:85-90.

[212] Li M-J, Tang S-Z, Wang F-l, Zhao Q-X, Tao W-Q. Gas-side fouling, erosion and corrosion of heat exchangers for middle/low temperature waste heat utilization: a review on simulation and experiment. Applied Thermal Engineering 2017;126:737-61.

[213] Luo H, Dong C, Xiao K, Li X. Characterization of passive film on 2205 duplex stainless steel in sodium thiosulphate solution. Applied Surface Science 2011;258:631-9.

[214] Olsson C-OA. The influence of nitrogen and molybdenum on passive films formed on the austenoferritic stainless steel 2205 studied by AES and XPS. Corrosion Science 1995;37:467-79.

[215] Zhang S, Jiang Z, Li H, Zhang B, Chang P, Wu J, et al. Catastrophic oxidation mechanism of hyper duplex stainless steel S32707 at high temperature in air. Materials Characterization 2018;145:233-45.

[216] Jin Q, Li J, Xu Y, Xiao X, Zhang W, Jiang L. High-temperature oxidation of duplex stainless steels S32101 and S32304 in air and simulated industrial reheating atmosphere. Corrosion Science 2010;52:2846-54.

[217] Li L-F, Jiang Z-H, Riquier Y. High-temperature oxidation of duplex stainless steels in air and mixed gas of air and $CH_4$. Corrosion Science 2005;47:57-68.

[218] Follett W. Oxy-combustion pressurized fluidized Bed with carbon dioxide purification. 2017 NETL CO 2017;2.

[219] ASTM ASfTaM. G1-03. Standard Practice for Preparing, Cleaning, and Evaluating Corrosion Test Specimens. Philadelphia, Pennsylvania2003.

[220] Zeng Y, Amirkhiz BS, Pang X, Podlesny M, Matchim M. Corrosion Assessment of Nickel-Based Alloys for SCWR Fuel Cladding Application. CORROSION 2016: NACE International; 2016. p. 1.

[221] Zeng Y, Shi C, Arafin M, Zavadil R. Influence of Impurity Hydrogen Sulfide on the Corrosion Performance of Pipeline Steels in Supercritical Carbon Dioxide Stream. Corrosion 2016: NACE International; 2016. p. 1.

[222] G46-94 A. Standard guide for examination and evaluation of pitting corrosion. 2005.

[223] Laycock NJ, Newman RC. Temperature dependence of pitting potentials for austenitic stainless steels above their critical pitting temperature. Corrosion Science 1998;40:887-902.

[224] Carranza RM, Alvarez MG. The effect of temperature on the passive film properties and pitting behaviour of a FeCrNi alloy. Corrosion Science 1996;38:909-25.

[225] Roine A. HSC Chemistry 5.11. Outokumpu Research Oy, Pori, Finland 2002;76.

[226] Tokuda S, Muto I, Sugawara Y, Hara N. Pit initiation on sensitized Type 304 stainless steel under applied stress: Correlation of stress, Cr-depletion, and inclusion dissolution. Corrosion Science 2020:108506.

[227] Persdotter A, Sattari M, Larsson E, Olivas Ogaz MA, Liske J, Jonsson T. Oxidation of Fe-2.25Cr-1Mo in presence of KCl(s) at 400 °C – Crack formation and its influence on oxidation kinetics. Corrosion Science 2020;163:108234.

[228] Grabke HJ, Reese E, Spiegel M. The effects of chlorides, hydrogen chloride, and sulfur dioxide in the oxidation of steels below deposits. Corrosion Science 1995;37:1023-43.

[229] Zahs A, Spiegel M, Grabke HJ. Chloridation and oxidation of iron, chromium, nickel and their alloys in chloridizing and oxidizing atmospheres at 400–700 °C. Corrosion Science 2000;42:1093-122.

[230] Singh P, Birks N. Mechanism of sulphur transport through preformed oxide scales. Materials and Corrosion 1980;31:682-8.

[231] Young DJ. Chapter 8 - Corrosion by Sulphur. In: Young DJ, editor. High Temperature Oxidation and Corrosion of Metals (Second Edition): Elsevier; 2016. p. 393-430.

[232] Kladkaew N, Idem R, Tontiwachwuthikul P, Saiwan C. Corrosion behavior of carbon steel in the monoethanolamine−$H_2O$−$CO_2$−$O_2$−$SO_2$ system: Products, reaction pathways, and kinetics. Ind Eng Chem Res 2009;48:10169-79.

[233] Sánchez Pastén M, Spiegel M. High temperature corrosion of metallic materials in simulated waste incineration environments at 300–600 °C. Materials and Corrosion 2006;57:192-5.

[234] Costa GCC, Jacobson NS, Lukco D, Hunter GW, Nakley L, Radoman-Shaw BG, et al. Oxidation behavior of stainless steels 304 and 316 under the Venus atmospheric surface conditions. Corrosion Science 2018;132:260-71.

[235] Kishi K, Ikeda S. X-ray photoelectron spectroscopic study for the reaction of evaporated iron with $O_2$ and $H_2O$. Bulletin of the Chemical Society of Japan 1973;46:341-5.

[236] Sabioni ACS, Huntz AM, Silva Fd, Jomard F. Diffusion of iron in $Cr_2O_3$: polycrystals and thin films. Materials Science and Engineering: A 2005;392:254-61.

[237] Greeff AP, Louw CW, Swart HC. The oxidation of industrial FeCrMo steel. Corrosion Science 2000;42:1725-40.

[238] Vesel A, Drenik A, Mozetic M, Zalar A, Balat-Pichelin M, Bele M. AES investigation of the stainless steel surface oxidized in plasma. Vacuum 2007;82:228-31.

[239] Sabioni A, Lesage B, Huntz A, Pivin J, Monty C. Self-diffusion in $Cr_2O_3$ I. Chromium diffusion in single crystals. Philosophical Magazine A 1992;66:333-50.

[240] Hagel WC. Anion Diffusion in $\alpha$-$Cr_2O_3$. Journal of the American Ceramic Society 1965;48:70-5.

[241] Kelley M, Ponec V. Surface composition of alloys. Progress in Surface Science 1981;11:139-244.

[242] Birks N, Meier GH, Pettit FS. Introduction to the high temperature oxidation of metals: Cambridge University Press; 2006.

[243] Yu C, Zhang J, Young DJ. High temperature corrosion of Fe-Cr-(Mn/Si) alloys in $CO_2$-$H_2O$-$SO_2$ gases. Corrosion Science 2016;112:214-25.

[244] Tung H-M, Stubbins JF. Incipient oxidation kinetics of alloy 617 and residual stress of the oxide scale formed in air at temperatures between 850 and 1000 °C. Journal of Nuclear Materials 2012;424:23-8.

[245] Saunders S, Monteiro M, Rizzo F. The oxidation behaviour of metals and alloys at high temperatures in atmospheres containing water vapour: A review. Progress in Materials Science 2008;53:775-837.

[246] Luo L, Su M, Yan P, Zou L, Schreiber DK, Baer DR, et al. Atomic origins of water-vapour-promoted alloy oxidation. Nature materials 2018;17:514.

[247] Suzuki T, Sawado Y, Fujii Y. Characterization of oxide films generated on stainless steel in water vapor and oxygen plasmas. Surf Coat Technol 2005;200:284-7.

[248] Asteman H, Svensson JE, Johansson LG. Oxidation of 310 steel in $H_2O/O_2$ mixtures at 600 °C: the effect of water-vapour-enhanced chromium evaporation. Corrosion Science 2002;44:2635-49.

[249] Young DJ. Chapter 11 - Effects of Water Vapour on Oxidation. In: Young DJ, editor. High Temperature Oxidation and Corrosion of Metals (Second Edition): Elsevier; 2016. p. 549-601.

[250] Singh V, Kachhawaha J, Tare V. Corrosion Behavior of 9Cr-1Mo Steel in Sulfur Dioxide Environment. Journal of Materials Engineering and Performance 2014;23:3285-98.

[251] Kawahara Y. High temperature corrosion mechanisms and effect of alloying elements for materials used in waste incineration environment. Corrosion Science 2002;44:223-45.

[252] Hussain T, Simms NJ, Nicholls JR, Oakey JE. Fireside corrosion degradation of HVOF thermal sprayed FeCrAl coating at 700–800 °C. Surface and Coatings Technology 2015;268:165-72.

[253] Angelino G. Carbon dioxide condensation cycles for power production. 1968.

[254] Feher EG. The supercritical thermodynamic power cycle. Energy conversion 1968;8:85-90.

[255] Sharan P, Neises T, Turchi C. Thermal desalination via supercritical $CO_2$ Brayton cycle: Optimal system design and techno-economic analysis without reduction in cycle efficiency. Applied Thermal Engineering 2019;152:499-514.

[256] Moore J, Brun K, Evans N, Bueno P, Kalra C. Development of a 1 MWe supercritical $CO_2$ Brayton cycle test loop. 4th international symposium-Supercritical $CO_2$ power cycles2014.

[257] Moore J, Day M, Cich S, Hofer D. Testing of A 10 MWe supercritical $CO_2$ turbine. Proceedings of the 47th Turbomachinery Symposium: Turbomachinery Laboratory, Texas A&M Engineering Experiment Station; 2018.

[258] Sridharan K. Corrosion of Structural Materials for Advanced Supercritical Carbon-Dioxide Brayton Cycle. Univ. of Wisconsin, Madison, WI (United States); 2017.

[259] Pint BA, Lehmusto J, Lance MJ, Keiser JR. Effect of pressure and impurities on oxidation in supercritical $CO_2$. Materials and Corrosion 2019;70:1400-9.

[260] Rouillard F, Moine G, Charton F. Corrosion Behavior Of Different Metallic Materials In Supercritical $CO_2$ At 550°C And 250 Bars. CORROSION 2010: NACE International; 2010.

[261] Rouillard F, Moine G, Martinelli L, Ruiz J. Corrosion of 9Cr steel in $CO_2$ at intermediate temperature I: mechanism of void-induced duplex oxide formation. Oxidation of Metals 2012;77:27-55.

[262] Tan L, Anderson M, Taylor D, Allen TR. Corrosion of austenitic and ferritic-martensitic steels exposed to supercritical carbon dioxide. Corrosion Science 2011;53:3273-80.

[263] Rouillard F, Moine G, Charton F. Corrosion Behavior Of Different Metallic Materials In Supercritical $CO_2$ At 550° C And 250 Bars. CORROSION 2010: NACE International; 2010.

[264] Lim J, McKrell T, Eastwick G, Ballinger R. Corrosion of materials in supercritical carbon dioxide environments. CORROSION 2008: NACE International; 2008.

[265] Cao G, Firouzdor V, Sridharan K, Anderson M, Allen T. Corrosion of austenitic alloys in high temperature supercritical carbon dioxide. Corrosion Science 2012;60:246-55.

[266] Pint BA, Unocic KA, Brese RG, Keiser JR. Characterization of chromia scales formed in supercritical carbon dioxide. Materials at High Temperatures 2018;35:39-49.

[267] Wright IG, Pint BA, Shingledecker JP, Thimsen D. Materials considerations for supercritical $CO_2$ turbine cycles. ASME Turbo Expo 2013: Turbine Technical Conference and Exposition: American Society of Mechanical Engineers; 2013. p. V008T34A10-VT34A10.

[268] Lee HJ, Kim H, Kim SH, Jang C. Corrosion and carburization behavior of chromia-forming heat resistant alloys in a high-temperature supercritical-carbon dioxide environment. Corrosion Science 2015;99:227-39.

[269] Olivares R, Young D, Nguyen T, Marvig P. Resistance of High-Nickel, Heat-Resisting Alloys to Air and to Supercritical $CO_2$ at High Temperatures. Oxidation of Metals 2018;90:1-25.

[270] Pint BA, Unocic KA. The Effect of $CO_2$ Pressure on Chromia Scale Microstructure at 750 °C. JOM 2018;70:1511-9.

[271] Bidabadi MHS, Zheng Y, Rehman A, Yang L, Zhang C, Chen H, et al. Effect of $CO_2$ gas pressure on composition, growth rate, and structure of duplex oxide formed on 9Cr steel at 550 °C. Corrosion Science 2020;163:108252.

[272] Liang Z, Gui Y, Wang Y, Zhao Q. Corrosion performance of heat-resisting steels and alloys in supercritical carbon dioxide at 650 °C and 15 MPa. Energy 2019;175:345-52.

[273] Mahaffey J, Kalra A, Anderson M, Sridharan K. Materials corrosion in high temperature supercritical carbon dioxide.  4th International Symposium-Supercritical $CO_2$ Power Cycles: Citeseer; 2014.

[274] Mahaffey J, Schroeder A, Adam D, Brittan A, Anderson M, Couet A, et al. Effects of CO and $O_2$ Impurities on Supercritical $CO_2$ Corrosion of Alloy 625. Metallurgical and Materials Transactions A 2018;49:3703-14.

[275] Kung S, Shingledecker J, Wright I, Sabau A, Tossey B, Lolla T. Corrosion of heat exchanger alloys in open-fired $sCO_2$ power cycles. Proceedings of the 6th International Symposium on Supercritical $CO_2$ Power Cycles, Pittsburgh, PA2018.

[276] Pint BA, Unocic KA, Keiser J. Effect of impurities on supercritical $CO_2$ compatibility. Oak Ridge National Lab, Oak Ridge, TN (United States); 2019.

[277] Pint BA, Brese RG, Keiser JR. Effect of pressure on supercritical $CO_2$ compatibility of structural alloys at 750 °C. Materials and Corrosion 2017;68:151-8.

[278] Davis JR. Nickel, cobalt, and their alloys: ASM international; 2000.

[279] Lu J, Huang J, Yang Z, Zhou Y, Dang Y, Zhao X, et al. Effect of Cobalt Content on the Oxidation and Corrosion Behavior of Ni–Fe-Based Superalloy for Ultra-Supercritical Boiler Applications. Oxidation of Metals 2018;89:197-209.

[280] WebBook N. Thermophysical properties of fluid systems. http://webbook. nist. gov/chemistry/fluid/2020.

[281] Lee HJ, Subramanian GO, Kim SH, Jang C. Effect of pressure on the corrosion and carburization behavior of chromia-forming heat-resistant alloys in high-temperature carbon dioxide environments. Corrosion Science 2016;111:649-58.

[282] Roine A. HSC 6.0 Chemistry. Chemical reactions and Equilibrium software with extensive thermochemical database and Flowsheet simulation. Pori: Outokumpu research Oy-2006-448 pp 2006.

[283] Regina J, DuPont J, Marder A. The effect of water vapor on passive-layer stability and corrosion behavior of Fe–Al–Cr base alloys. Oxidation of Metals 2004;61:69-90.

[284] Chen H, Wang H, Sun Q, Long C, Wei T, Kim SH, et al. Oxidation behavior of Fe-20Cr-25Ni-Nb austenitic stainless steel in high-temperature environment with small amount of water vapor. Corrosion Science 2018;145:90-9.

[285] Young DJ. High temperature oxidation and corrosion of metals: Elsevier; 2008.

[286] Zhao S, Xie X, Smith GD. The oxidation behavior of the new nickel-based superalloy Inconel 740 with and without $Na_2SO_4$ deposit. Surface and coatings technology 2004;185:178-83.

[287] Wood G, Whittle D. The mechanism of breakthrough of protective chromium oxide scales on Fe-Cr alloys. Corrosion Science 1967;7:763-82.

[288] Furukawa T, Rouillard F. Oxidation and carburizing of FBR structural materials in carbon dioxide. Progress in Nuclear Energy 2015;82:136-41.

[289] Young DJ, Nguyen TD, Felfer P, Zhang J, Cairney JM. Penetration of protective chromia scales by carbon. Scripta Materialia 2014;77:29-32.

[290] Mikkelsen L, Linderoth S. High temperature oxidation of Fe–Cr alloy in $O_2$–$H_2$–$H_2O$ atmospheres; microstructure and kinetics. Materials Science and Engineering: A 2003;361:198-212.

[291] Meier GH, Jung K, Mu N, Yanar NM, Pettit FS, Abellán JP, et al. Effect of alloy composition and exposure conditions on the selective oxidation behavior of ferritic Fe–Cr and Fe–Cr–X alloys. Oxidation of Metals 2010;74:319-40.

[292] Subramanian GO, Lee HJ, Kim SH, Jang C. Corrosion and carburization behaviour of Ni-xCr binary alloys in a high-temperature supercritical-carbon dioxide environment. Oxidation of Metals 2018;89:683-97.

[293] Atkinson A. Transport processes during the growth of oxide films at elevated temperature. Reviews of Modern Physics 1985;57:437.

[294] Li W, Huang X, Li J, Woo OT, Sanchez R, Bibby CD. Effect of Pressures on the Corrosion Behaviours of Materials at 625°C. JOM 2017;69:207-16.

[295] Zeng Y, Li J, Amirkhiz BS, Zheng W, Matchim M, Podlesny M. Corrosion and stress corrosion cracking of UNS S31008 and UNS N08810 alloys in supercritical water. CORROSION 2015: NACE International; 2015.

[296] Amirkhiz BS, Xu S. TEM examination of precipitation behaviour of $M_{23}C_6$ and sigma phases and dislocations in SS 310S under creep deformation at 800 °C. Microscopy and Microanalysis 2015;21:585-6.

[297] Sourmail T. Precipitation in creep resistant austenitic stainless steels. Materials science and technology 2001;17:1-14.

[298] Quadakkers WJ, Olszewski T, Piron-Abellan J, Shemet V, Singheiser L. Oxidation of metallic materials in simulated $CO_2/H_2O$-rich service environments relevant to an oxyfuel plant. Materials Science Forum: Trans Tech Publ; 2011. p. 194-9.

[299] Zheng X, Young D. High-temperature corrosion of $Cr_2O_3$-forming alloys in CO-$CO_2$-$N_2$ atmospheres. Oxidation of Metals 1994;42:163-90.

[300] Rouillard F, Furukawa T. Corrosion of 9-12Cr ferritic–martensitic steels in high-temperature $CO_2$. Corrosion Science 2016;105:120-32.

[301] Ruther W, Schlueter R, Lee R, Hart R. Corrosion behavior of steels and nickel alloys in superheated steam. Corrosion 1966;22:147-55.

[302] Oleksak RP, Baltrus JP, Nakano J, Nakano A, Holcomb GR, Doğan ÖN. Mechanistic insights into the oxidation behavior of Ni alloys in high-temperature $CO_2$. Corrosion Science 2017;125:77-86.

[303] Nguyen T, Zhang J, Young D. Microstructures of chromia scales grown in $CO_2$. Materials at High Temperatures 2015;32:16-21.

[304] Terentyev D, He X, Zhurkin E, Bakaev A. Segregation of Cr at tilt grain boundaries in Fe–Cr alloys: A Metropolis Monte Carlo study. Journal of Nuclear Materials 2011;408:161-70.

[305] Wolf I, Grabke H. A study on the solubility and distribution of carbon in oxides. Solid state communications 1985;54:5-10.

[306] Chyrkin A, Huczkowski P, Shemet V, Singheiser L, Quadakkers W. Sub-scale depletion and enrichment processes during high temperature oxidation of the nickel base alloy 625 in the temperature range 900–1000 °C. Oxidation of Metals 2011;75:143-66.

[307] Chyrkin A, Sloof W, Pillai R, Galiullin T, Grüner D, Singheiser L, et al. Modelling compositional changes in nickel base alloy 602 CA during high temperature oxidation. Materials at high temperatures 2015;32:102-12.

[308] Abbasi M, Kim D-I, Shim J-H, Jung W-S. Effects of alloyed aluminum and titanium on the oxidation behavior of INCONEL 740 superalloy. Journal of Alloys and Compounds 2016;658:210-21.

[309] Oleksak RP, Carney CS, Holcomb GR, Doğan ÖN. Structural evolution of a Ni alloy surface during high-temperature oxidation. Oxidation of Metals 2018;90:27-42.

[310] Olivares R, Young D, Marvig P, Stein W. Alloys SS316 and Hastelloy-C276 in supercritical $CO_2$ at high temperature. Oxidation of Metals 2015;84:585-606.

[311] Chang K-H, Chen S-M, Yeh T-K, Kai J-J. Effect of dissolved oxygen content on the oxide structure of Alloy 625 in supercritical water environments at 700 °C. Corrosion science 2014;81:21-6.

[312] Baker BA. A New Alloy Designed for Superheater Tubing in Coal-Fired Ultra Supercritical Boilers. Superalloys2005. p. 601-11.

[313] Jablonski PD, Hawk JA, Cowen CJ, Maziasz PJ. Processing of Advanced Cast Alloys for A-USC Steam Turbine Applications. JOM 2012;64:271-9.

[314] Xu S, Amirkhiz BS. Mechanical properties of fuel cladding candidate alloys for Canadian SCWR concept. JOM 2016;68:469-74.

[315] Zeng Y, Guzonas D. Corrosion assessment of candidate materials for fuel cladding in Canadian SCWR. JOM 2016;68:475-9.

[316] Vamshi M, Singh SK, Sateesh N, Nagaraju DS, Subbiah R. A review on influence of carburizing on ferritic stainless steel. Materials Today: Proceedings 2020.

[317] Gheno T, Monceau D, Zhang J, Young DJ. Carburisation of ferritic Fe–Cr alloys by low carbon activity gases. Corrosion Science 2011;53:2767-77.

[318] Rutkowski B, Gil A, Agüero A, González V, Czyrska-Filemonowicz A. Microstructure, Chemical-and Phase Composition of Sanicro 25 Austenitic Steel After Oxidation in Steam at 700° C. Oxidation of Metals 2018;89:183-95.

[319] Dudziak T, Hussain T, Simms NJ, Syed A, Oakey J. Fireside corrosion degradation of ferritic alloys at 600 °C in oxy-fired conditions. Corrosion science 2014;79:184-91.

[320] Chandra K, Kranzmann A, Neumann RS, Oder G, Rizzo F. High temperature oxidation behavior of 9–12% Cr ferritic/martensitic steels in a simulated dry oxyfuel environment. Oxidation of Metals 2015;83:291-316.

[321] Hünert D, Kranzmann A. Impact of oxyfuel atmospheres $H_2O/CO_2/O_2$ and $H_2O/CO_2$ on the oxidation of ferritic–martensitic and austenitic steels. Corrosion Science 2011;53:2306-17.

[322] Schulz W, Huenert D, Nitschke H, Saliwan-Neumann R, Kranzmann A. Comparison Of The Corrosion Behaviour Of 9-12 % Cr Steels In $H_2O$, $H_2O$-$CO_2$ And $H_2O$-$CO_2$-$O_2$. CORROSION 2009. Atlanta, Georgia: NACE International; 2009. p. 10.

[323] Sayyar N, Shamanian M, Niroumand B. Arc weldability of Incoloy 825 to AISI 321 stainless steel welds. Journal of Materials Processing Technology 2018;262:562-70.

[324] Zhang N, Lior N. Two novel oxy-fuel power cycles integrated with natural gas reforming and $CO_2$ capture. Energy 2008;33:340-51.

[325] Lasek JA, Głód K, Janusz M, Kazalski K, Zuwała J. Pressurized oxy-fuel combustion: A Study of selected parameters. Energy & Fuels 2012;26:6492-500.

[326] Viswanathan R, Henry JF, Tanzosh J, Stanko G, Shingledecker J, Vitalis B, et al. U.S. Program on materials technology for ultra-supercritical coal power plants. Journal of Materials Engineering and Performance 2005;14:281-92.

[327] ASTM. ASTM G16-13(2019), Standard guide for applying statistics to analysis of corrosion data. West Conshohocken, PA: ASTM International; 2019.

[328] Ehlers J, Young D, Smaardijk E, Tyagi A, Penkalla H, Singheiser L, et al. Enhanced oxidation of the 9% Cr steel P91 in water vapour containing environments. Corrosion science 2006;48:3428-54.

[329] Otsuka N. Carburization of 9% Cr steels in a simulated oxyfuel corrosion environment. Oxidation of metals 2013;80:565-75.

[330] Pint BA, Keiser JR. The effect of temperature and pressure on supercritical $CO_2$ compatibility of conventional structural alloys. Oak Ridge National Lab.(ORNL), Oak Ridge, TN (United States); 2016.

[331] Hussain T, Simms NJ, Nicholls JR, Oakey JE. Fireside corrosion degradation of HVOF thermal sprayed FeCrAl coating at 700–800°C. Surface and Coatings Technology 2015;268:165-72.

[332] Momber A. Colour-based assessment of atmospheric corrosion products, namely of flash rust, on steel. Materials and Corrosion 2012;63:333-42.

[333] Pujilaksono B, Jonsson T, Halvarsson M, Svensson J-E, Johansson L-G. Oxidation of iron at 400–600 °C in dry and wet $O_2$. Corrosion Science 2010;52:1560-9.

[334] Kuang W, Wu X, Han E-H. Influence of dissolved oxygen concentration on the oxide film formed on Alloy 690 in high temperature water. Corrosion science 2013;69:197-204.

[335] Raynaud G, Rapp R. In situ observation of whiskers, pyramids and pits during the high-temperature oxidation of metals. Oxidation of Metals 1984;21:89-102.

[336] Mu N, Jung K, Yanar N, Meier G, Pettit F, Holcomb G. Water vapor effects on the oxidation behavior of Fe–Cr and Ni–Cr alloys in atmospheres relevant to oxy-fuel combustion. Oxidation of metals 2012;78:221-37.

[337] Nguyen TD, Zhang J, Young DJ. Growth of $Cr_2O_3$ blades during alloy scaling in wet $CO_2$ gas. Corrosion Science 2018;133:432-42.

[338] Polman E, Fransen T, Gellings P. Oxidation kinetics of chromium and morphological phenomena. Oxidation of metals 1989;32:433-47.

[339] Rutkowski B, Gil A, Agüero A, González V, Czyrska-Filemonowicz A. Microstructure, Chemical-and Phase Composition of Sanicro 25 Austenitic Steel After Oxidation in Steam at 700 °C. Oxidation of Metals 2018;89:183-95.

[340] Gheno T, Monceau D, Young DJ. Mechanism of breakaway oxidation of Fe–Cr and Fe–Cr–Ni alloys in dry and wet carbon dioxide. Corrosion Science 2012;64:222-33.

[341] Sand T, Geers C, Cao Y, Svensson J, Johansson L. Effective Reduction of Chromium-oxy-hydroxide Evaporation from Ni-Base Alloy 690. Oxidation of Metals 2019;92:259-79.

[342] Xie Y, Nguyen TD, Zhang J, Young DJ. Corrosion behaviour of Ni-Cr alloys in wet $CO_2$ atmosphere at 700 and 800 °C. Corrosion Science 2019;146:28-43.

[343] Halvarsson M, Tang JE, Asteman H, Svensson J-E, Johansson L-G. Microstructural investigation of the breakdown of the protective oxide scale on a 304 steel in the presence of oxygen and water vapour at 600 °C. Corrosion Science 2006;48:2014-35.

[344] Asteman H, Svensson J-E, Johansson L-G, Norell M. Indication of chromium oxide hydroxide evaporation during oxidation of 304L at 873 K in the presence of 10% water vapor. Oxidation of Metals 1999;52:95-111.

[345] Asteman H, Svensson J-E, Norell M, Johansson L-G. Influence of water vapor and flow rate on the high-temperature oxidation of 304L; effect of chromium oxide hydroxide evaporation. Oxidation of Metals 2000;54:11-26.

[346] Abe F, Araki H, Yoshida H, Okada M. The role of aluminum and titanium on the oxidation process of a nickel-base superalloy in steam at 800°C. Oxidation of Metals 1987;27:21-36.

[347] Nguyen TD, Zhang J, Young DJ. Effects of silicon on high temperature corrosion of Fe–Cr and Fe–Cr–Ni alloys in carbon dioxide. Oxidation of metals 2014;81:549-74.

[348] Chen JH, Rogers PM, Little JA. Oxidation behavior of several chromia-forming commercial nickel-base superalloys. Oxidation of Metals 1997;47:381-410.

[349] Hong J, Field R, Gazzino M, Ghoniem AF. Operating pressure dependence of the pressurized oxy-fuel combustion power cycle. Energy 2010;35:5391-9.

[350] Sanchez DL, Nelson JH, Johnston J, Mileva A, Kammen DM. Biomass enables the transition to a carbon-negative power system across western North America. Nature Climate Change 2015;5:230-4.

[351] Riaza J, Gil M, Álvarez L, Pevida C, Pis J, Rubiera F. Oxy-fuel combustion of coal and biomass blends. Energy 2012;41:429-35.

[352] Demirbas A. Potential applications of renewable energy sources, biomass combustion problems in boiler power systems and combustion related environmental issues. Progress in energy and combustion science 2005;31:171-92.

[353] Koppejan J, Van Loo S. The handbook of biomass combustion and co-firing: Routledge; 2012.

[354] Veijonen K, Vainikka P, Järvinen T, Alakangas E. Biomass co-firing–an efficient way to reduce greenhouse gas emissions. VTT Processes, March 2003;28:A1.

[355] Jurado N, Darabkhani H, Anthony E, Oakey J. Oxy-combustion studies into the co-firing of coal and biomass blends: effects on heat transfer, gas and ash compositions. Energy Procedia 2014;63:440-52.

[356] Tan Y, Jia L, Wu Y. Some combustion characteristics of biomass and coal cofiring under oxy-fuel conditions in a pilot-scale circulating fluidized combustor. Energy & fuels 2013;27:7000-7.

[357] Lupiáñez C, Mayoral MC, Guedea I, Espatolero S, Díez LI, Laguarta S, et al. Effect of co-firing on emissions and deposition during fluidized bed oxy-combustion. Fuel 2016;184:261-8.

[358] Holcomb GR, Carney C, Doğan ÖN. Oxidation of alloys for energy applications in supercritical $CO_2$ and $H_2O$. Corrosion Science 2016;109:22-35.

[359] Stringer J, Wright IG. Current limitations of high-temperature alloys in practical applications. Oxidation of Metals 1995;44:265-308.

[360] Holcomb GR, Tylczak J, Meier G, Lutz B, Yanar N, Pettit F, et al. Oxy-Combustion Environment Characterization: Fire-and Steam-Side Corrosion in Advanced Combustion. National Energy Technology Lab.(NETL), Pittsburgh, PA, and Morgantown, WV …; 2012.

[361] Stein-Brzozowska G, Maier J, Scheffknecht G. Impact of the oxy-fuel combustion on the corrosion behavior of advanced austenitic superheater materials. Energy procedia 2011;4:2035-42.

[362] Zeng Z, Natesan K, Cai Z, Rink D. Effect of coal ash on the performance of alloys in simulated oxy-fuel environments. Fuel 2014;117:133-45.

[363] Hussain T, Syed A, Simms NJ. Trends in fireside corrosion damage to superheaters in air and oxy-firing of coal/biomass. Fuel 2013;113:787-97.

[364] Geddes B, Leon H, Huang X. Superalloys: alloying and performance: Asm International; 2010.

[365] Shibli A. Coal Power Plant Materials and Life Assessment: Developments and Applications: Elsevier; 2014.

[366] Baker B. A new alloy designed for superheater tubing in coal-fired ultra supercritical boilers. Superalloys 2005;718:625-706.

[367] Syed A, Simms N, Oakey J. Fireside corrosion of superheaters: Effects of air and oxy-firing of coal and biomass. Fuel 2012;101:62-73.

[368] O'Hagan CP, O'Brien BJ, Griffin F, Hooper B, Leen SB, Monaghan RF. Porosity-based corrosion model for alkali halide ash deposits during biomass co-firing. Energy & Fuels 2015;29:3082-95.

[369] Niu Y, Tan H. Ash-related issues during biomass combustion: Alkali-induced slagging, silicate melt-induced slagging (ash fusion), agglomeration, corrosion, ash utilization, and related countermeasures. Progress in Energy and Combustion Science 2016;52:1-61.

[370] Talbot DE, Talbot JD. Corrosion science and technology: CRC press; 2018.

[371] Guo S, Zhang J, Wu W, Zhou W. Corrosion in the molten fluoride and chloride salts and materials development for nuclear applications. Progress in Materials Science 2018;97:448-87.

[372] Leistikow S, Wolf I, Grabke H. Effects of cold work on the oxidation behavior and carburization resistance of Alloy 800. Materials and Corrosion 1987;38:556-62.

[373] Yang X-y, Peng X, Wang F-h. Hot corrosion of a novel electrodeposited Ni–6Cr–7Al nanocomposite under molten (0.9 Na, 0.1 K)$_2$SO$_4$ at 900 °C. Scripta Materialia 2007;56:891-4.

[374] Yuan L, Wang H. Hot corrosion behaviors of a Cr$_{13}$Ni$_5$Si$_2$-based metal silicide alloy in Na$_2$SO$_4$+ 25 wt.% K$_2$SO$_4$ and Na$_2$SO$_4$+ 25 wt.% NaCl molten salts. Intermetallics 2010;18:324-9.

[375] Sidhu T, Malik A, Prakash S, Agrawal R. Cyclic oxidation behavior of Ni-and Fe-based superalloys in air and Na$_2$SO$_4$-25% NaCl molten salt environment at 800 °C. International Journal of Physical Sciences 2006;1:27-33.

[376] Li Y, Spiegel M, Shimada S. Corrosion behaviour of various model alloys with NaCl–KCl coating. Materials Chemistry and Physics 2005;93:217-23.

[377] Tsaur C-C, Rock JC, Wang C-J, Su Y-H. The hot corrosion of 310 stainless steel with pre-coated NaCl/Na$_2$SO$_4$ mixtures at 750 °C. Materials chemistry and physics 2005;89:445-53.